ANTINEUTRINO SPECTRUM CHARACTERIZATION OF THE HIGH FLUX ISOTOPE REACTOR USING NEUTRONIC SIMULATIONS

A Dissertation
Presented to
The Academic Faculty

By

Andrew Conant

In Partial Fulfillment
of the Requirements for the Degree
Doctor of Philosophy in the
School of Mechanical Engineering

Georgia Institute of Technology

August 2019

ANTINEUTRINO SPECTRUM CHARACTERIZATION OF THE HIGH FLUX ISOTOPE REACTOR USING NEUTRONIC SIMULATIONS

Approved by:

Dr. Anna Erickson, Advisor
School of Mechanical Engineering
Georgia Institute of Technology

Dr. Bojan Petrovic
School of Mechanical Engineering
Georgia Institute of Technology

Dr. Rachel Whitlark
Sam Nunn School of International Affairs
Georgia Institute of Technology

Dr. Steven Biegalski
School of Mechanical Engineering
Georgia Institute of Technology

Dr. David Chandler
Research Reactor Division
Oak Ridge National Laboratory

Dr. Nathaniel Bowden
Nuclear and Chemical Sciences Division
Lawrence Livermore National Laboratory

Date Approved: July 10, 2019

Good judgement comes from experience. Experience comes from bad judgement.

Unknown

I would like to dedicate this to my parents, Joan and Ken Conant, who have encouraged and inspired me every step of the way to accomplish what I have so far.

ACKNOWLEDGEMENTS

I would like to thank all of my committee members for taking their time to advise and guide me throughout the way in working on interesting research. Dr. Anna Erickson has been a trusted longtime advisor for me and has been supportive of me in all aspects. Dr. Bojan Petrovic deserves credit for teaching me the fundamentals of reactor physics and modeling and simulation fundamentals. Dr. Steven Biegalski has asked critical questions and helped in my understanding of safeguards applications. Dr. Rachel Whitlark has helped me frame my thinking away from solely through the technical lens. Dr. Nathaniel Bowden has been a role model in helping bridge the gap between neutrino detection technology and safeguards applications, and I appreciate his guidance. Dr. David Chandler has been instrumental in drilling his expertise of the High Flux Isotope Reactor (HFIR) into my mind and has provided ample resources and advice throughout this work.

My education would not have been successful without the direct and indirect help of my fellow Georgia Tech students throughout the years. My classmates from freshman year through qualifying exams aided my understanding of my field and others. I am extremely proud to be an alumnus of Georgia Tech. Go Jackets!

The Precision Reactor Oscillation and Spectrum Experiment (PROSPECT) collaboration has been instrumental in introducing me to the field of neutrino physics. I would specifically like to thank PROSPECT collaborators Pranava Surukuchi, Bryce Littlejohn, Tom Langford, Pieter Mumm, and Nathaniel Bowden for their patient teaching in neutrino physics and detection. Being a part of such a unique and groundbreaking experiment broadened my experiences from just traditional nuclear engineering challenges.

My long-term internship at Oak Ridge National Laboratory (ORNL) contributed to the quality and expediency of this work as well. I learned a lot while onsite at the High Flux Isotope Reactor (HFIR) and had the opportunity to contribute to interesting work on reactor safety. I would like to thank my mentor David Chandler, the leader for the HFIR Nuclear

Safety and Experiment Analysis (NSEA) group Charles Carathers, and the NSEA group members who increased my knowledge of HFIR and its operation.

Penultimately, my funding sources have been a large motivator for keeping me in school for all these years. The Department of Energy (DOE) Nuclear Energy University Programs (NEUP) Integrated University Program (IUP) Fellowship supported me for my first three years of graduate school. The DOE and National Nuclear Security Administration (NNSA) Nuclear Nonproliferation International Safeguards (NNIS) Fellowship allowed me to finish out my graduate studies. I am ecstatic that the DOE and NNSA have been supportive of my work and future career in the nuclear industry.

Lastly, and most importantly, I would like to thank my family. My mother Joan continues to show faith in me and encourages me to keep pushing even when I do not have faith in myself. My father Ken always instilled the desire for excellence in academic achievements. My brother Steven and his new wife Lizzie have been amazing at taking my mind off work when I have needed it most. Without this core support group, I could not have accomplished this work.

TABLE OF CONTENTS

LIST OF TABLES

LIST OF FIGURES

SUMMARY

Antineutrino detectors have matured significantly over the past two decades. They have demonstrated the capability to measure the operating status, power level, and fuel burnup of nuclear reactors. Monitoring nuclear reactors with antineutrino detectors provide advantages over current safeguards technology in that they can: operate remotely and unattended, provide real-time information, remain non-intrusive and unconnected to internal plant systems, and reduce reliance on operator declarations. However, current anomalies lead to mismatches between the theoretical and measured spectrum and are one of the factors in preventing antineutrino safeguards implementation. The current Precision Reactor Oscillation and Spectrum Experiment (PROSPECT) seeks to address these issues by making a modern short-baseline measurement of the ^{235}U spectrum and searching for neutrino oscillations. PROSPECT has constructed a ton-scale liquid scintillator detector to measure the antineutrino flux from the High Flux Isotope Reactor (HFIR) at Oak Ridge National Laboratory (ORNL) and has already recorded tens of thousands of antineutrinos attributed to fission events in HFIR.

To aid PROSPECT in its high-precision measurement, reactor simulations are performed to characterize the antineutrino spectrum from HFIR. Neutronic simulations using MCNP and other nuclear engineering codes such as SCALE are used to quantify key reactor parameters related to neutrino production. Modeling and simulation allowed for high-fidelity quantification of fission rates, fractions, and spatial distributions that all impact the signal at a short-baseline detector. The design and missions of HFIR permit antineutrino emissions from non-fuel sources; a methodology for identifying such sources is developed and is evaluated for different materials in the reactor. Work on spent fuel, reactor power, and simulations for theoretical antineutrino predictions are also discussed. All of these factors contribute to the measurement of the antineutrino spectrum from HFIR and advancing antineutrino detectors as a viable safeguards technology.

CHAPTER 1
INTRODUCTION

Nuclear reactors constitute a large part of the world electricity production. As of July 2018, there were 453 operable commercial nuclear reactors that produced 397 GW of electricity (GWe) [1]. An additional 57 commercial reactors are under construction around the world to contribute another 57 GWe. This does not include the 227 research reactors in more than 50 countries that are used for education, training, isotope production, neutron experiments, and other purposes [2]. The worldwide energy demand and consumption is increasing quickly, e.g. 2.3% in 2018 [3]. Nuclear energy provides an excellent opportunity to meet some of these needs by producing electricity without contributing significantly to the carbon emissions affecting climate change.

Meeting national and global needs for low-carbon sources of electricity requires the deployment of new reactors as many current ones have retired or will do so in the coming decades. Additionally, research reactors in the United States need to be modified and developed to maintain national science and security missions. Critically increasing demand for nuclear reactors, whether of similar light water reactor (LWR) designs or advanced Generation IV designs [4], requires the proper scaling in instrumentation and the nuclear security enterprise to maintain accordance with nonproliferation and safeguards agreements, e.g. the Treaty on the Non-Proliferation of Nuclear Weapons (NPT). Many non-Organisation for Economic Co-operation and Development (OECD) countries have expressed new or renewed interest in nuclear power to meet their energy needs. The third pillar of the NPT guarantees these countries the peaceful use of nuclear technology, which includes power reactors for electricity and research reactors for other science and security missions. With increasing demand for nuclear energy and its benefits, the spread of peaceful technology is inevitable.

The international community, under the NPT, has concerns over the proliferation of sensitive nuclear material and information as they can also be utilized for military purposes, i.e. nuclear weapons. The US, particularly the Department of Energy (DOE) and National Nuclear Security Administration (NNSA), have a vested interest to "prevent, counter, and respond to nuclear nonproliferation, counter-proliferation, and nuclear security threats" involving any nuclear facilities and material [5]. The International Atomic Energy Agency (IAEA) also has a vital role in applying safeguards to peaceful nuclear facilities for countries that have signed the NPT. The potential large increase in nuclear energy development in non-OECD, developing states (which largely overlap with NPT non-weapons states) raises concerns over safety and security of the material [5].

The inherent dual-use nature of nuclear technology comes with security concerns over the accountability of nuclear and radiological material and necessitates the implementation of safeguards processes. In the case of nuclear reactors, one of the key pieces of the nuclear fuel cycle process, the fuel material is of the most concern as fissile material itself is necessary for a nuclear weapon. The IAEA identifies 25 kg of highly-enriched uranium (HEU) and 8 kg of plutonium as a significant quantity, or the "approximate amount of nuclear materials with the possibility of manufacturing a nuclear device cannot be excluded" [6]. Various actors have taken actions to mitigate the probability of proliferation and potential weapons production of non-weapons states on constraining both the uranium and plutonium path. The former has seen success in limiting the spread of enrichment technology needed to make an HEU weapon and constraining the nuclear fuel fabrication process to only a few countries. The latter has relied on preventing proliferation of plutonium-producing reactors and subsequent reprocessing capabilities, such as through export controls within the Nuclear Suppliers Group (NSG).

Ultimately, the IAEA is responsible for enabling enforcement of international safeguards and ensures this primarily through material accountancy at nuclear facilities, e.g. the commercial and research reactors under the NPT umbrella. It does so by forming com-

prehensive safeguards agreements (CSAs) with member states to ensure that all nuclear material is used peacefully within a state. The Additional Protocol (AP) provides for further abilities by the IAEA to increase its efficiency and ensure absence of any undeclared nuclear material production. The IAEA uses several types of technologies in parallel to confirm the lack of nuclear fuel diversion to military applications and absence of clandestine facilities (under the AP). Techniques include non-destructive analysis (NDA), destructive analysis (DA), unattended and remote monitoring, containment and surveillance, and environmental sampling [7]. Each of these techniques pose unique challenges; for example, environmental sampling and DA incur significant technological, timeliness, and personnel costs while NDA may require advanced instrumentation or on-site inspectors to be present at the facility. The IAEA utilizes all of these these technologies concurrently to ensure its safeguards missions, but is continually looking to improve its capabilities through R&D [8].

The IAEA is continuously searching for methods and technologies to enhance capabilities to verify that states are meeting their obligations and to promptly detect misuse of civilian nuclear material. The DOE/NNSA express full support in "modernizing nuclear verification capabilities" and actively encourage technological maturation of new technologies [5]. Improvement in IAEA capabilities can increase efficiency, reduce costs, and standardize implementation of safeguards throughout all facilities worldwide. The IAEA Department of Safeguards outlined their desired technological capabilities in their Long-Term R&D Plan 2012-2023 [8]. Among the thirteen long-term capabilities needed, some significant technological requirements include the "ability to make maximum efficiency savings by the use of remote monitoring of operators and unattended IAEA equipment" and the "ability to safeguard new types of [facilities]."

For decades it has been suggested that antineutrino detectors (ADs) can be used to monitor current and future nuclear reactors [9, 10, 11]. In the past several decades, they have demonstrated capabilities to measure the operational status, power level, and fissile content

in real-time [11]. Antineutrino detectors can operate passively, remotely, and outside of the reactor core. These features contrast with current methods that implement neutron flux detectors, thermocouples, and pressure and flow sensors to measure operational parameters of the reactor. These signals have low-tamper resistance, need to be connected to plant systems within the core, and rely heavily on operator declarations. Antineutrino detectors have the potential to measure signatures from the fission rates in the core that do not have such disadvantages.

The IAEA has expressed interest by hosting a focused workshop on AD application in 2008 [12] and concluded that safeguards integration of antineutrino detectors is possible but at that time practical. Antineutrino detectors need to improve in cost, efficiency, and deploy-ability at a variety of reactor sites. Some of the reports suggestions include application of antineutrino detectors in a wider set of environments (such as different reactors), deployment at near-ground level, and a wider base of integrated simulation software to decrease reliance of power and fissile content information on operator declarations.

The state of the art in antineutrino detection still stands to gain in the understanding of neutrino physics to enable safeguards integration. Flux deficit and spectral deviations observed by recent experiments (discussed in more detail in Chapter 2) show disagreement between the theoretical predictions and experimental measurements at nuclear reactors. However, the recent Precision Reactor Oscillation and Spectrum Experiment (PROSPECT) seeks to address some of these anomalies by measuring the antineutrino flux at the High Flux Isotope Reactor (HFIR) at Oak Ridge National Laboratory (ORNL). PROSPECT seeks to advance the field of antineutrino detection, which can potentially meet current and future IAEA needs. Development can help safeguard new types of reactors, especially ones that may need out-of-core instrumentation due to materials limits or need to verify the inventory of long-lived cores.

With the current understanding of antineutrino spectra, high-precision measurements are necessary to further development of ADs. PROSPECT seeks such a high-resolution

spectrum measurement to make definitive statements about the antineutrino spectrum and associated anomalies. It has been suggested that reactor modeling and simulation is still necessary for understanding the measurement of antineutrinos from a nuclear reactor [12, 13]. Several works have examined the role of reactor modeling in understanding antineutrino spectra and uncertainties from current and future nuclear reactors [14, 15, 16]. Reactor modeling provides the capability to characterize the nuclear reactor as a source of antineutrinos and understand systematic uncertainties that can increase precision on the measured spectrum. The PROSPECT experiment needs more detailed understanding of its spectrum from HFIR. Reactor modeling of operating and future reactors is a necessary tool for the understanding of spectra and deployment of antineutrino detectors as a safeguards technology.

CHAPTER 2
BACKGROUND

This chapter addresses background information that is necessary to understand research performed. Section 2.1 introduces the concept of antineutrino physics and detection. Background on the PROSPECT experiment is then discussed in Section 2.2. Finally, design information on the High Flux Isotope Reactor is presented in Section 2.3.

2.1 Antineutrino Physics

Neutrinos (ν) are neutral, nearly massless particles that travel at close to the speed of light and were instrumental in the creation of the universe. Hypothesized by Wolfgang Pauli in 1930, neutrinos were the particle that account for the previously-unresolved missing momentum in three-body beta decay to explain the continuous energy spectrum of resulting electrons. According to the Standard Model, neutrinos come in three flavors: electron (ν_e), muon (ν_μ), and tau (ν_τ), each deriving from their respective partner lepton associated with their creation. Each neutrino also has an associated anti-particle called an antineutrino ($\overline{\nu}$). The electron neutrino (ν_e) is created in positron (β^+) decay while the electron antineutrino ($\overline{\nu}_e$) is created in beta (β^-) decay. Both of these are common products that are created in nuclear reactions.

Nuclear reactors are a copious source of electron antineutrinos ($\overline{\nu}_e$). Neutron-induced fissions that drive the nuclear chain reaction creates neutron-rich fission products that are prone to beta decay and emit an antineutrino:

$$ {}^{A}_{Z}X \rightarrow {}^{A}_{Z+1}\,Y^* + \beta^- + \bar{\nu}_e \tag{2.1} $$

where an element X with an atomic number Z and mass number A transmutes to the next

highest element along with an electron (β^-), antineutrino ($\overline{\nu}_e$), and kinetic energy that is carried away by the products. Nearly all of the energy is carried away by the β^- and $\overline{\nu}_e$. A typical commercial nuclear reactor with 1 GWe of power produces about 10^{20} $\overline{\nu}_e$ per second and 6 $\overline{\nu}_e$ per fission reaction [17].

2.1.1 Antineutrino Detection

In 1956, Reines and Cowan confirmed Pauli's hypothesis with the experimental discovery of electron antineutrinos at the P Reactor at the Savannah River Site in the 1950s [18]. It was discovered that antineutrinos can be detected with the inverse beta decay (IBD) reaction using a ton-scale liquid scintillator detector. The experimental confirmation of the neutrino earned the work a Nobel Prize in Physics in 1995. The IBD reaction [19] has a 1.8 MeV threshold for the $\overline{\nu}_e$:

$$\bar{\nu}_e + {}^1_1 p \rightarrow {}^1_0 n + \beta^+ \tag{2.2}$$

Antineutrino detectors (ADs) operate by matching the coincidence of the prompt positron annihilation (two 0.511 MeV γ's) and delayed neutron absorption to verify an IBD interaction. Most recent experiments have used liquid scintillator detectors to count the subsequent photon and neutron interactions. ADs require significant background rejection to minimize cosmogenic and accidental production of neutrino-like signatures. Due to the low cross-section of the IBD reaction ($\approx 10^{-22} cm^{-2}$), it is most beneficial to place an antineutrino detector close to the reactor core as the signal falls off with the inverse square distance from the reactor core, also called the baseline of the detector.

Figure 2.1 shows the emitted spectrum, IBD cross-section, and expected detected spectrum for $\overline{\nu}_e$'s coming from a nuclear reactor. The $\overline{\nu}_e$ spectrum is monotonically decreasing with energy while the cross-section is monotonically increasing. The expected detected spectrum, a product of the two, shows a characteristic peak in the 3-4 MeV range. The distribution falls off heavily after 8 MeV; few reactor $\overline{\nu}_e$ are detected above this energy. It

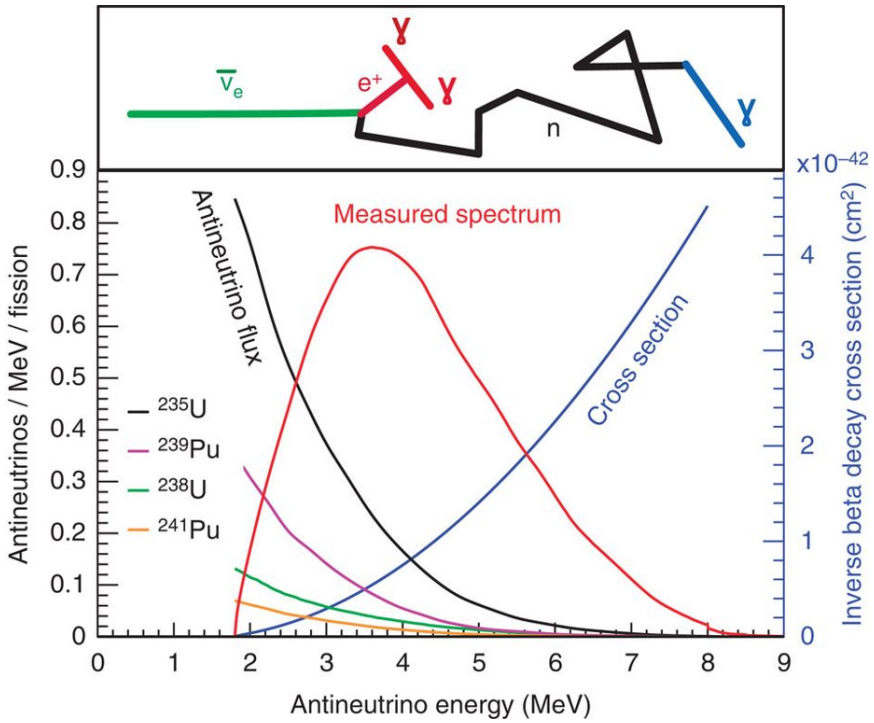

Figure 2.1: Inverse beta decay reaction and spectrum from major isotopes in a commercial reactor, reproduced from Ref. [17]

can also be seen that the yield and spectrum of $\overline{\nu}_e$ varies significantly with different parent fissioning isotope.

Experiments have measured the $\overline{\nu}_e$ flux and spectrum from nuclear reactors for several decades [20, 21]. These experiments have taken place at a wide variety of reactor types and baselines (meters to kilometers) from the reactor core; a summary of them can be found in Table 2.1 [22]. Several have measured the $\overline{\nu}_e$ flux coming from more than one nuclear reactor, and a majority of them have been at commercial nuclear reactors. Experiments seek to constrain the mass splitting (Δm^2) and neutrino mixing angle (θ) parameters that help define the parameters defining the Standard Model [23]. Several experiments have made recent strides in fundamental understanding of the last unknown neutrino mixing angle (θ_{13}). These long-baseline experiments include RENO [24], Double Chooz [25], and Daya Bay [26].

These experiments seek to gain understanding of the Standard Model from reactor $\overline{\nu}_e$'s.

Table 2.1: Summary of neutrino experiments at nuclear reactors, reproduced from Ref. [22]

Table 2 – A summary table for the experiments conducted until 2015 to measure reactor neutrinos.

Exp	P (GW)	Fuel ^{235}U %	Detector	Shielding	Mass (ton or L)	Depth MWE	L m	Time (d) on–off	ε %	No. of events #/day On–Off	S/B	Ref.
Bugey3	2.8		^{6}Li(0.15%) + LS	8 cm LS	0.556	23	15	72–60	~20	1,285–62	21	[11]
			(NE320)	4 mm B_4C	(600 L)	9.5	40	129–72		251–66	3.8	
			Seg. 98	25 cm water			95	28–6		67–37	1.8	
				10 cm Pb								
Bugey4	2.8		^{3}He + H_2O	10 cm LS	1.48	25	15	88–39	54.9	5,621–2,599	1.16	[12]
				4 mm B_4C								
				25 cm water								
				10 cm Pb								
Goesgen	2.8		^{3}He + LS(NE235C)	5 mm B_4C	377 L	5	38	143	16.7	76–	~4	[13]
			SEG. 30	20 cm water			46	204	16.5	52–	~3	
				15 cm iron			65	359	16.8	24–	~1.5	
				2 m concrete								
ILL	0.057	93	^{3}He + LS(NE235C)	12 cm LS	0.325	8	8.76	129–49	19.4	38–	1~2	[14]
			SEG. 30	15 cm PE	(377 L)							
				20 cm Pb								
Palo Verde	11.63		Gd-LS (0.1%)	1 m H_2O	11.34	32	750	350–	11.2	~50–	~1	[15]
			(seg.,66)				890					
Chooz	8.5	3.1	Gd-LS	1–2 m LS	5	300	1,000	64–143	69.8	25–1.4	18	[16]
				75 cm SAND								
				14 cm FE								
SRP	2.0	–	Gd-LS	~10 inches LS veto	275 L	–	18.2	172–	37.7	419–	–	[17]
			(0.5%)	2 inches Pb			23.8	208–		260–		
			NE313	3 inches plastic veto								
				8 inches Pb								
SONGS	3.4		Gd-LS (0.1%)	0.5 m H_2O	0.64	25	25	–	~10	564–105	5.5	[18]
			Seg. 4									
KamLAND		–	Spherical LS	180 cm oil veto	1,000	2,700	~180,000	~1,930–	~90	0.83–0.14	5.8	[19]
			(diam. 13 m)	~1 m water								
Double Chooz	8.5	4	Gd-LS	55 cm LS	8	300	1,050	461–	91.5	37.7–1.6	23.6	[20]
				105 cm oil								
				50 cm LS								
				15 m steel								
Daya Bay	17.4	4	Gd-LS	45 cm LS	20	250	360	565–	80	664–13	51	[21]
				50 cm oil		265	500	568–	83.7	595–9.5	63	
				2.5 m water		860	1,580	562–	96.3	74–2.2	34	
RENO	16.8	4	Gd-LS	60 cm LS	16	120	290	500–	64.7	617–17.5	35	[22]
				70 cm oil		450	1,380	500–	74.5	61.2–3.1	19.7	
				150 cm water								
NEOS	3.0	4	Gd-LS	10 cm Bo-PE	1	30	23.6	30	~50	1,946–84	22	[23]
				10 cm Pb								

Gd-LS, gadolinium-loaded liquid scintillator; ILL, Institut Laue-Langevin; NEOS, Neutrino Experiment for Oscillation at Short baseline; S/B, signal/background; SONGS, San Onofre Nuclear Generating Station; SRP, Savannah River Plant.

At a nuclear reactor, the emitted $\overline{\nu}_e$ spectra *S* follows as [27]:

$$\frac{d^2\phi(E_{\overline{\nu}_e},t)}{dE_{\overline{\nu}_e}dt} = \sum_i f_i(t)S_i(E_{\overline{\nu}_e}) = \sum_i f_i(t)\frac{dN_i}{dE_{\overline{\nu}_e}} \tag{2.3}$$

where S is the reactor emitted source spectrum, f_i is the fission rate of isotope *i* and $dN_i/dE_{\overline{\nu}_e}$ is the $\overline{\nu}_e$ spectrum of that isotope. Equation 2.4 can also include a normalization to reactor power if fission fractions are used instead of fission rates. The $\overline{\nu}_e$ spectra are typically presented per unit energy so that it can be integrated over various energy ranges. Precise knowledge of the reactor fission rates by isotope is necessary to characterize the

$\overline{\nu}_e$ spectrum from the reactor. Equation 2.4 has been modified to include additional terms based on current knowledge and approximations [28]:

$$\frac{d^2\phi(E_{\overline{\nu}_e},t)}{dE_{\overline{\nu}_e}dt} = \sum_i f_i(t)\frac{dN_i}{dE_{\overline{\nu}_e}}c_i^{ne}(E_{\overline{\nu}_e}) + s_{SNF}(E_{\overline{\nu}_e},t) \tag{2.4}$$

where c_i^{ne} is the contribution of non-equilibrium isotopes [29, 30] and s_{SNF} is the contribution of spent fuel.

The $\overline{\nu}_e$ (or ν) flux measured at the detector can be described by Equation 2.5 [28]:

$$\frac{d^2N(E_\nu,t)}{dE_\nu dt} = N_p\sigma_{IBD}(E_\nu)\eta\frac{P(E_\nu,L)}{4\pi L^2}\frac{d^2\phi(E_\nu,t)}{dE_\nu dt} \tag{2.5}$$

where *N* is the number of neutrinos detected in the active volume, N_p is the number of target protons in the detector, σ_{IBD} is the energy-dependent inverse beta decay cross-section, P is the oscillation survival probability from reactor to detector, and L is the distance from fission site to detector segment. The last term accounts for the relative change in the emitted spectrum from the source.

Equation 2.5 can be greatly simplified by integrating over the energy domain and encompassing all constants and detector-related terms into one factor γ [9]:

$$\frac{dN_{\overline{\nu}_e}}{dt} = \gamma[1+k(t)]P_{th} \tag{2.6}$$

where P_{th} is the thermal power of the reactor and $k(t)$ is a term that account for the time-varying fission rates in fractions in the reactor. The detected spectrum is proportional to $\overline{\nu}_e$ physical and detector-related parameters, reactor power, and any time-varying term that changes over a reactor cycle.

2.1.2 Predicted Antineutrino Spectra

Theoretical predictions of reactor $\overline{\nu}_e$ spectra rely on well-known spectra for each fissile isotope. Thus it is important to quantify the $\frac{dN_i}{dE_{\overline{\nu}_e}}$ term in Equation 2.4. Predictions can

be grouped into two categories: those using the summation method and those using the conversion method.

Summation Method

The first method is the summation method, also called the *ab initio* approach. This method takes the aggregate $\overline{\nu}$ spectrum by taking the sum of the spectra from each fission product weighted by its fission yield [27]:

$$\frac{dN_i}{dE_{\overline{\nu}_e}} = \sum_n Y_n(Z, A, t) \sum_{n,i} b_{n,i}(E_0^i) P_{\overline{\nu}}(E_{\overline{\nu}}, E_0^i, Z) \tag{2.7}$$

where Y is the yield of β^- decays, n accounts for all the ground and excited states of the daughter, b is the branching ratio of the transition, E_0 is the endpoint energy, and $P_{\overline{\nu}}$ is the normalized $\overline{\nu}_e$ spectrum for that transition. This method is straightforward intuitively, however it comes with some issues.

It is evident that accuracy with this method depends greatly on the accuracy of transition, decay, and fission yield data of thousands of fission product nuclides and their subsequent daughters. Much work has gone into understanding the $\overline{\nu}_e$ spectrum from the summation method and the associated electron spectrum to decrease uncertainties [27, 31, 32]. Many transitions, particularly those that are short-lived, are not included in the nuclear data. Therefore approximations have been made to account for missing transition data. Summation method predictions have results with errors of approximately 10%. The summation method predictions for these four isotopes is shown in Figure 2.2 [27].

Conversion Method

The second method is the conversion of reactor electron to $\overline{\nu}_e$ spectra. Problems with the summation-predicted spectra have necessitated utilizing well-known beta spectra to predict $\overline{\nu}_e$ spectra. Because the daughter atom carries away a negligible amount of energy, nearly

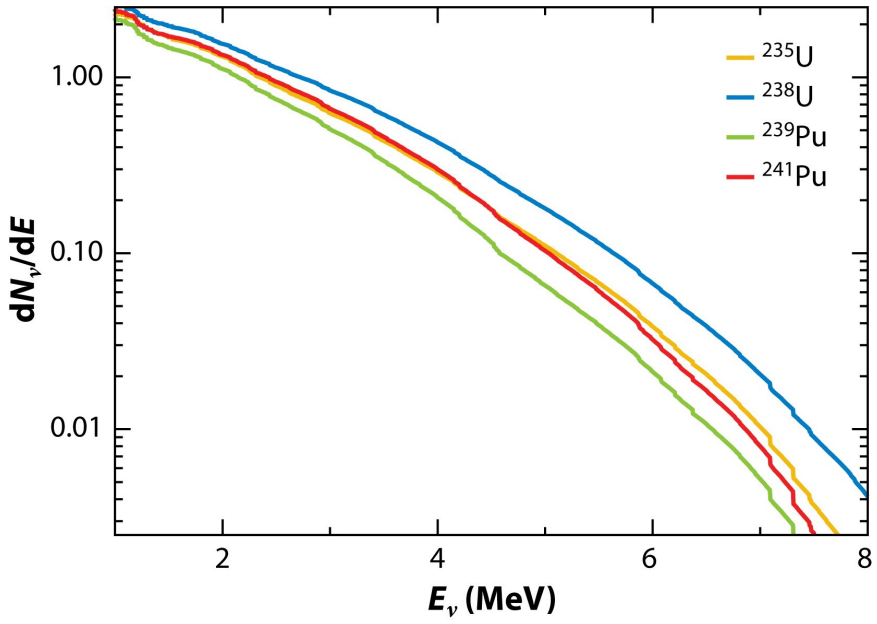

Figure 2.2: Summation-predicted $\overline{\nu}_e$ spectra of the primary fissile isotopes in a commercial nuclear reactor, reproduced from Ref. [27]

all the kinetic energy is shared by the β^- and $\overline{\nu}_e$. In other words:

$$E_0 \approx E_e + E_{\bar{\nu}} \tag{2.8}$$

where E_0 is the same endpoint energy as in Equation 2.7.

This method relies on the inversion of reactor β^- spectra to obtain the $\overline{\nu}_e$ spectrum. Virtual β^- branches are used to convert the total β^- spectra from a reactor into a finite number of approximate fits, usually around 30. This method requires several approximations and assumptions. Some of these include corrections in several physical phenomena, the choice of a regularization scheme, and neglect or other treatment of forbidden transitions [33].

The β^- spectra that is most widely used as an input to conversion procedures today was measured at the Institut Laue-Langevin (ILL) High Flux Reactor (RHF) in the 1980s by Shreckenbach *et al.* [34, 35, 36]. This includes beta spectra for the three fissile isotopes: ^{235}U, ^{239}Pu, and ^{241}Pu.

The most widely-used predictions for conversion-predicted $\overline{\nu}_e$ spectra are those by Hu-

ber [33]. He calculated the $\overline{\nu}_e$ spectrum from the electron spectra of ^{235}U, ^{239}Pu, and ^{241}Pu. The spectra for ^{238}U, the only one of the four isotopes that undergoes fission primarily from fast neutrons, has been predicted in [29] with an updated version in [37]. However, summation predictions are also commonly used for ^{238}U.

2.1.3 Antineutrino Anomalies

Several recent experiments have made significant progress in monitoring nuclear reactors with neutrino detectors, including Double Chooz [25], RENO [24], and Daya Bay [26]. Across these experiments and others, flux deficits and spectral deviations have been observed in the $\overline{\nu}_e$ spectra compared to theoretical predictions. Recent experiments have indicated a roughly 6% deficiency in detected $\overline{\nu}_e$ flux. This phenomenon has been called the "reactor antineutrino anomaly" and has been extensively studied in the past decade [38, 39, 40]. The anomaly across many experiments is shown in Figure 2.3. Analysis of the anomaly has suggested the potential existence of a fourth type of neutrino, the "sterile" neutrino that does not interact weakly as the other three neutrino flavors do.

The other unexplained phenomenon in the spectrum is what is called the "bump" or "shoulder" in the 5-7 MeV range of $\overline{\nu}_e$ energy. This phenomenon is more pronounced in summation predictions. The Daya Bay experiment saw a several percent increase in this range (Figure 2.3) [26]. This shoulder was initially not found in the electron spectra, but some papers have found a similarly-shaped bump [31].

The anomaly and bump have been extensively explored by the neutrino physics community [41, 42]. Variations in the decay and fission yield databases, such as JEFF-3.1.1 [43] and ENDF/B-VII.1 [44], provide complications that need to be resolved. The hypothesis of the sterile neutrino still remains and has motivated short-baseline experiments to test directly for its existence. Different studies have shown certain isotopes may be responsible for deficiencies in the flux predictions themselves, most recently the Daya Bay result suggested that ^{235}U may be responsible for the anomaly. Regardless of the source of physical

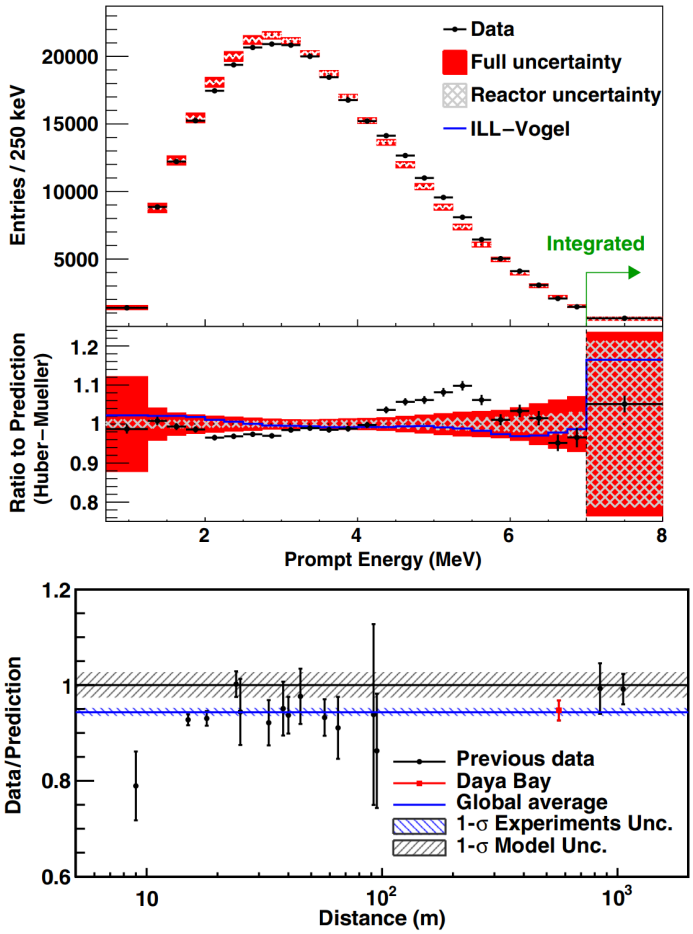

Figure 2.3: "Bump" in the $\overline{\nu}_e$ spectrum in the 4-6 MeV range (top) and deficit of experimental to theoretical data (bottom), reproduced from Ref. [26]

anomalies, the disagreement between theoretical predictions and measured $\overline{\nu}_e$ spectra need to be studied further to accurately measure the flux from nuclear reactors.

2.2 PROSPECT

The Precision Reactor Oscillation and Spectrum Measurement (PROSPECT) [45] attempts to answer remaining questions about the $\overline{\nu}_e$ spectrum from nuclear reactors. It has two main goals: 1) perform a precise measurement of the ^{235}U $\overline{\nu}_e$ flux and 2) search for sterile neutrino oscillations at short baseline. The PROSPECT experiment is measuring the $\overline{\nu}_e$ flux at the High Flux Isotope Reactor (HFIR) at Oak Ridge National Laboratory (ORNL).

HFIR is a high-powered, compact research reactor fueled with highly-enriched uranium (HEU). The HEU fuel of the reactor provides for a large contribution of ^{235}U fissions with little fuel isotopic evolution. The HFIR site also allows for the PROSPECT detector to be located close to the reactor core; this setup is ideal for searching for sterile neutrino oscillations. More details on HFIR will be discussed in Section 2.3.

2.2.1 Detector Design

PROSPECT has constructed a four-ton, segmented, ^{6}Li-doped liquid scintillator detector [46]. The detector contains an array of 14 horizontal by 11 vertical segments (154 total), each with a photomultiplier tube (PMT) at each end. A schematic of the detector and segmentation is shown in Figure 2.4 The center of each segment is located between 7-10 meters from the reactor core center. Each segment is optically separated from the others using an optical grid. The PMTs at the ends seek the gamma rays that are emitted from the positron (β^+) annihilation and neutron capture:

$$\beta^+ + \beta^- \rightarrow \gamma + \gamma \tag{2.9}$$

$$^{1}_{0}n +^{6} Li \rightarrow^{4}_{2} He +^{3}_{1} H \tag{2.10}$$

The ^{6}Li-doped liquid scintillator used is similar to the Eljen Technology's EJ-309 liquid scintillator, which is widely used in the field of radiation detection today. The scintillator produces visible light when ionizing radiation interacts. In the IBD reaction, this involves the gamma rays from the positron interaction (prompt) and neutron capture (delayed), which are shown in Figure 2.5. These signals can be correlated to differentiate reactor IBD-like events from accidental rates from backgrounds.

One challenge with PROSPECT is background rejection. The detector is situated close to ground level, with less than one meter of water equivalent overburden. Thus, the detec-

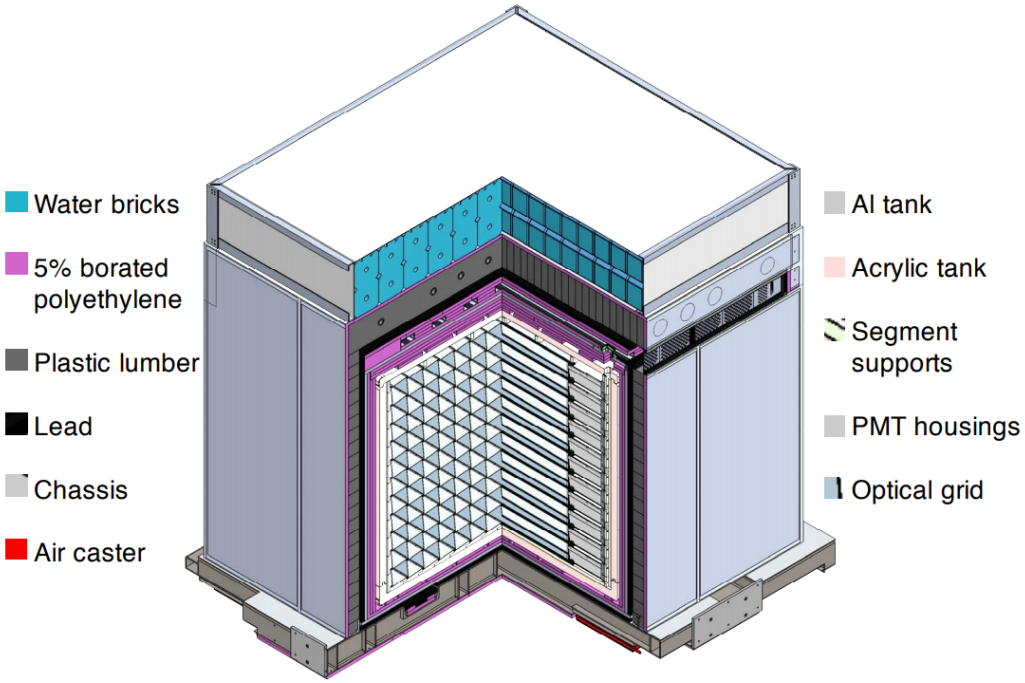

Figure 2.4: Schematic of PROSPECT detector and shielding assembly [47]

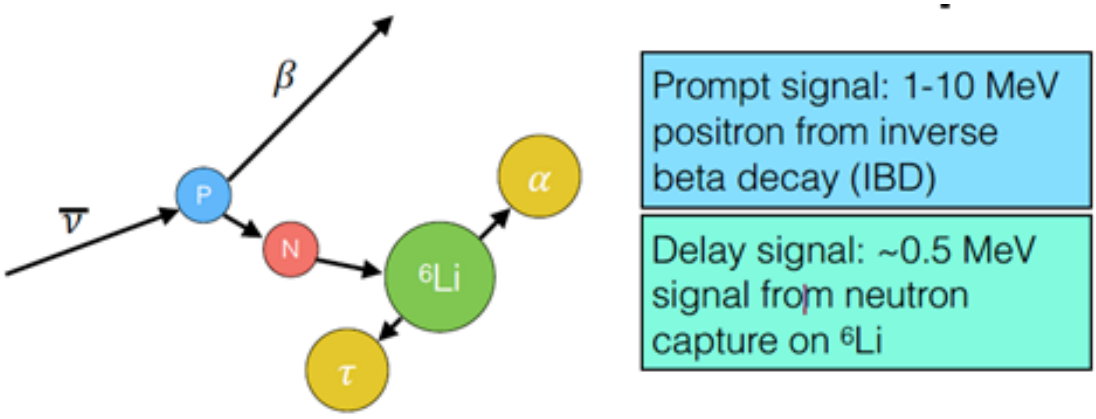

Figure 2.5: Inverse beta decay (IBD) reaction showing the production of the prompt and delayed signal

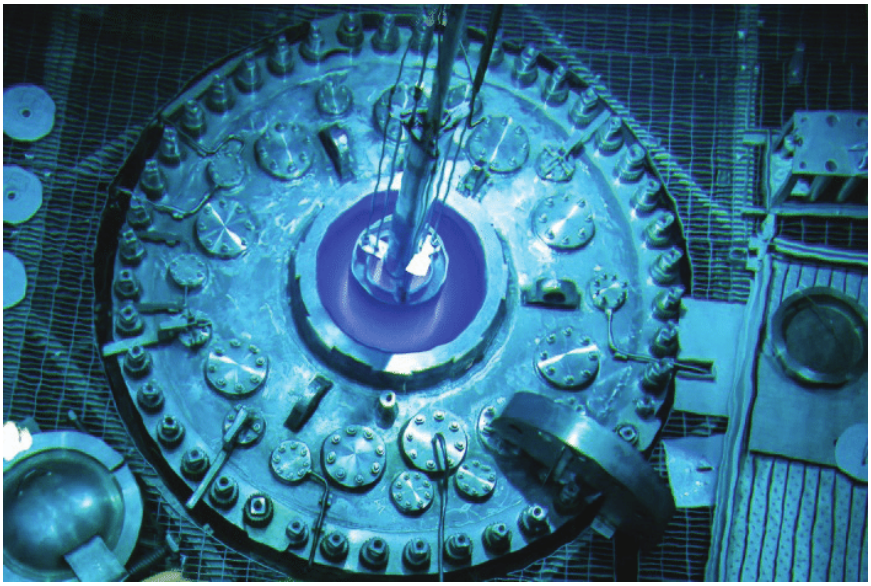

Figure 2.6: Aerial view of the HFIR core during defueling

tor has to be able to reject efficiently cosmogenic and reactor backgrounds. Cosmogenic neutrons give the biggest challenge for the PROSPECT detector. The detector has various levels of containment and shielding made of: aluminum, acrylic, and polyethylene. Water and lead bricks are used to reduce the background from cosmogenic neutrons and reactor-related gamma rays, respectively.

2.3 High Flux Isotope Reactor (HFIR)

The High Flux Isotope Reactor (HFIR) is a major research reactor with missions of neutron scattering, isotope production, materials irradiation, and neutron activation analysis. It is one of the few HEU fueled research reactors in the United States. HFIR is a compact reactor that can attain high thermal neutron fluxes, over 2×10^{15} n/cm^2/s, in its central region. It nominally operates at a power of 85 MWt for a cycle length of 23-26 days (1955 - 2210 MWd of operation). HFIR currently operates seven cycles annually Table 2.2 shows the nominal core, fuel, and coolant parameters. The PROSPECT experiment has taken data for much of cycles 478-482, the five most recent cycles to date. An image of HFIR is shown in Figure 2.6.

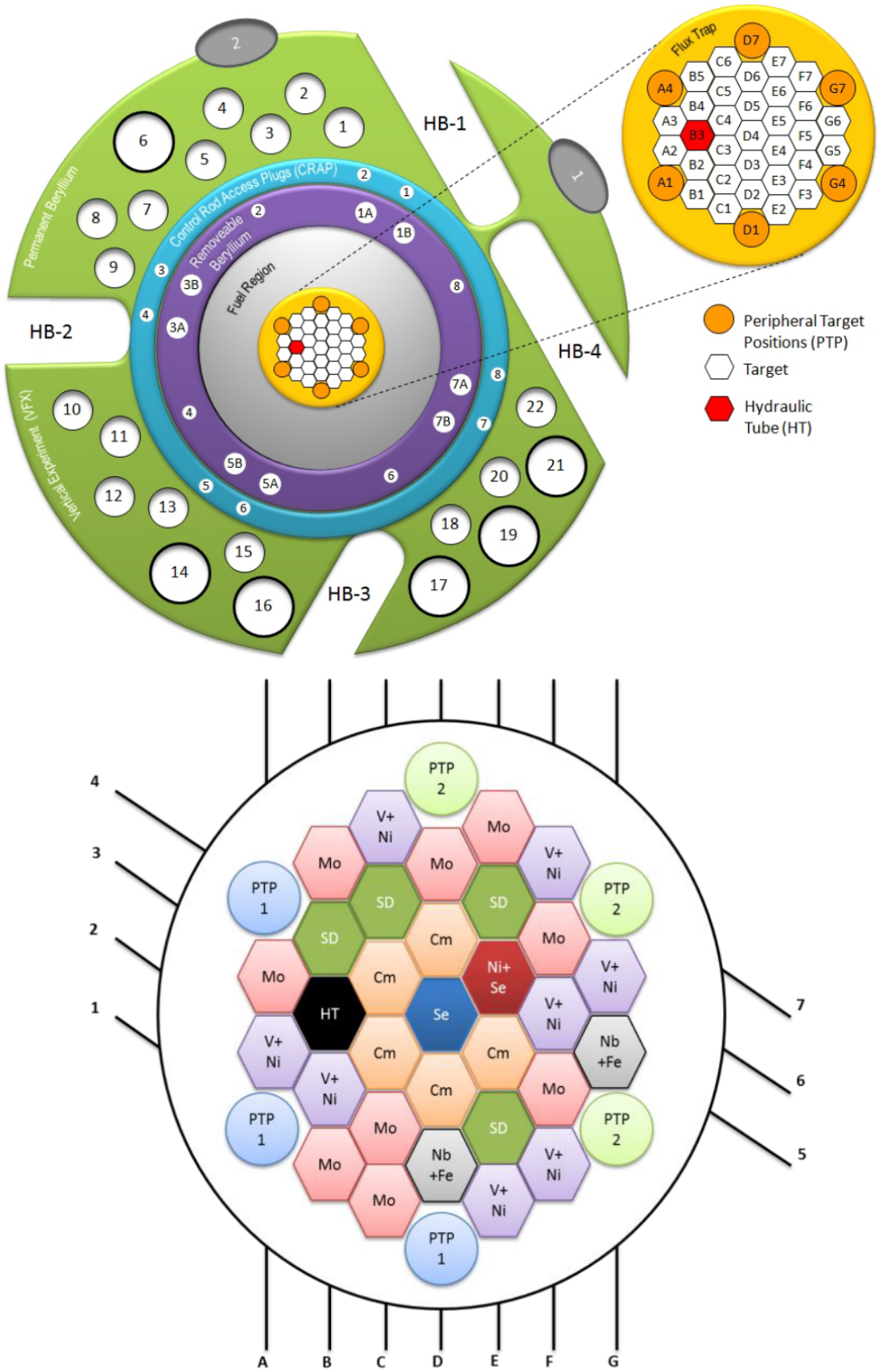

Figure 2.7: HFIR experiment locations in the flux trap and beryllium reflector (top) and loading of the flux trap in the representative model (bottom), reproduced from Ref. [48]

Table 2.2: HFIR nominal design and operating parameters

Fuel	
Composition	U_3O_8-Al
Enrichment	93%
Plate Thickness (cm)	0.127
Number of Plates	540
Core ^{235}U Loading (kg)	9.4
Total ^{235}U+^{238}U loading (kg)	10.4
Core	
Diameter (m)	0.435
Height (m)	0.769
Active Fuel Height (m)	0.508
Power (MWt)	85
Cycle length (days)	23-26
Peak Thermal Flux (n/cm^2/s)	2.5e+15
Moderator	H_2O
Reflector	Be
Control Element Materials	Eu,Ta,Al
Coolant	
Flow rate (gpm)	16,000
Inlet temperature (F)	120
Exit temperature (F)	156
Operating pressure (psig)	468
Pressure drop (psi)	110

2.3.1 HFIR Region Description

HFIR is a versatile research reactor with a flux-trap style design. The flux trap style means that it is designed to maximize or "trap" thermal neutron flux at the center annulus of the core. The purpose of this is for maximizing neutrons available for materials irradiations and isotope production purposes. The HFIR core can be grouped into four major neutronic regions: the flux trap, fuel, control element, and reflector. Outside of these four major regions are the pool, reactor vessel, and support structures. All of the design choices are outlined in the HFIR Core Nuclear Design report [49].

Flux Trap

The central region is the flux trap target (FTT) region. The FTT region contains a total of 37 target positions, which include 30 interior positions, 6 peripheral target positions (PTPs), and one hyrdraulic tube (HT). Figure 2.7 shows the experiment positions in the core. The contents of the FTT vary from cycle to cycle depending on experimental demand for isotope production and materials irradiation. The model with a representative loading [48], for example, contains target materials composed of vanadium, nickel, molybdenum, tungsten, selenium, niobium, iron, nickel (^{62}Ni), and curium. The curium targets are used to produce ^{252}Cf, which results in its spontaneous fission and other neutron-induced fission of higher actinides. In more recent cycles since that report, experiments have included previously mentioned isotopes as well as silicon carbide, steels, and other ferritic alloys. These isotopes have more importance for PROSPECT since the implementation of the detector at HFIR in early 2018.

2.3.2 Fuel

Radially outward of the FTT is the fuel region. The fuel is a U_3O_8-Al dispersion fuel enriched to approximately 93% by weight ^{235}U (5-6% ^{238}U and 1% ^{236}U) and manufactured in the form of involute plates. The fuel meat region is contoured along the arc of the involute to minimize the peak-to-average power density ratio and allow for sufficient thermal safety margin. The fuel meat thickness as a function of distance along a flat fuel plate is shown in Figure 2.8.

The fuel elements are grouped into two different regions, the inner and outer fuel elements (IFE/OFE). The IFE and OFE contain 171 and 369 fuel plates, respectively, arranged in a symmetric fashion azimuthally. The filler material of all IFE plates combined contain several grams of boron carbide, which contains ^{10}B that acts as a burnable absorber to even out the neutron flux distribution throughout the cycle, elongating the cycle and providing shutdown margin. The IFE and OFE plates are each separated by approximately 0.05

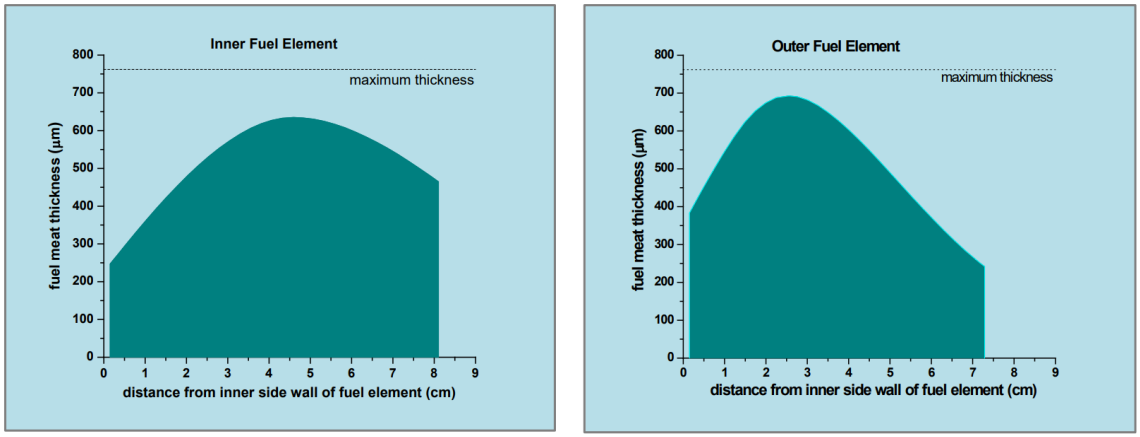

Figure 2.8: Flat plate fuel meat thickness profiles for the IFE and OFE, reproduced from Ref. [50]

inches in between which water flows to moderate neutrons and cool the fuel.

The IFE and OFE fuel plates are each attached into the sidewalls of their assemblies. The IFE and OFE assemblies are independently manufactured, tracked, and inserted into the core. A fresh IFE and OFE assembly are used in the core for every cycle, unlike most commercial reactors in which fuels are irradiated in batches that remain in core for future cycles contain plutonium.

Control Elements

The fuel regions are surrounded by two concentric control elements (CEs). Both control elements are partially inserted at the beginning of cycle (BOC) and are gradually withdrawn in opposite directions throughout the cycle. The inner control element (ICE) is the control cylinder that withdraws downward throughout the cycle; the outer control element (OCE) is a set of four safety plates, each of which can individually scram the reactor, move upward throughout the cycle. Both control elements contain europium, tantalum, and aluminum in their absorbing regions [48]. The end of cycle (EOC) occurs when both elements are fully withdrawn and the reactor can no longer maintain criticality. Both the ICE and OCE are replaced approximately every 100,000 MWd of reactor operation (approximately 50 cycles).

The control element withdrawal scheme and approximate position as a function of length in the cycle are shown in Figure 2.9. The control element moves at the highest rate early in the cycle; its removal rate is more constant over the remainder of the cycle. Typically for most analysis, day 15 is considered to be the middle of cycle from a neutron flux perspective whereas day 13 is usually closer to the arithmetic average.

Beryllium Reflector

The most radially outward region is the beryllium reflector region which serves to moderate neutrons to be transported down beam tubes and reflect them back into the core active region to sustain the chain reaction. The reflector region is split up into three regions: the removable (RB), semi-permanent (SPB), and permanent (PB) beryllium regions. The RB is replaced every several years (83,700 MWd) while the SPB and PB are replaced every few decades (167,400 and 279,000 MWd, respectively). The PB contains 22 vertical experimental facilities (VXFs), including inner small, outer small, and large VXFs. The four horizontal beam tubes (HBs) penetrate the outer radial areas in order to support cold and thermal scattering experiments, the primary mission of HFIR today. Recent cycles have included NpO_2 targets to produce ^{238}Pu for the National Aeronautics and Space Administration (NASA) [51, 52, 53].

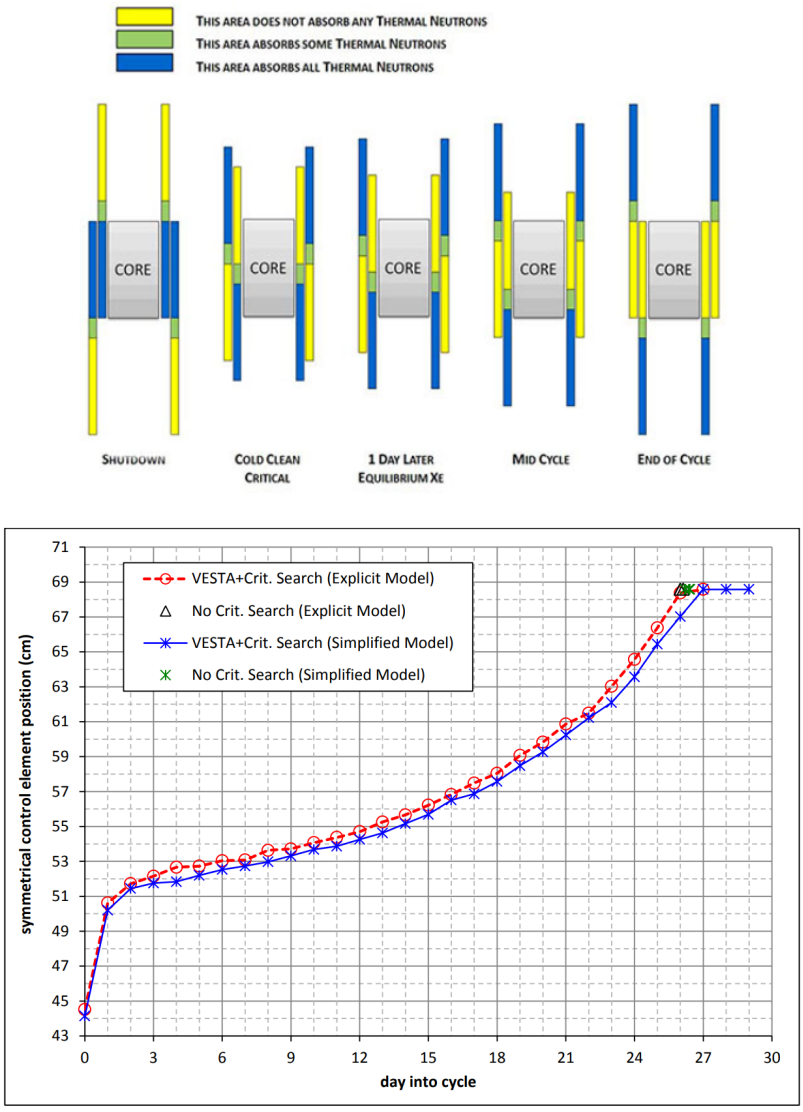

Figure 2.9: Drawing of control element positions at different times in the reactor cycle (top) and position as a function of time in the cycle according to the representative model [48] (bottom)

CHAPTER 3
OBJECTIVE AND APPROACH

The goal of this work is to perform high-fidelity modeling and simulation of HFIR for the determination of its antineutrino flux and uncertainties associated with its operation. Despite significant advancements in antineutrino detectors in the past several decades, understanding of the antineutrino flux from nuclear reactors is incomplete. It is important to have understanding of the reactor as a neutrino source. Reactor simulations serve as a method to quantify changes in reactor operating parameters and to calculate perturbations without full experimental replication. The objective of this work is to tie the novel task of employing modeling and simulation of a research reactor to quantify sensitivities of antineutrino emission rates from a reactor with a unique experiment, PROSPECT.

There are three main focus areas of this work. They can be summarized through the following research questions:

1. How does the antineutrino flux, spectrum, and baseline change throughout a cycle of HFIR?

2. How much of an impact do reactions in aluminum structures, the beryllium reflector, and target materials contribute to the antineutrino flux and spectrum?

3. How can the research reactor nature of HFIR be leveraged along with computational tools to understand spent fuel, power determination, and theoretical antineutrino predictions?

The first question addresses the precision to which the antineutrino flux can be calculated and measured. This includes the spatial and temporal distributions of fission rates by isotopic breakdown. This also includes the distance from the fission site to detector seg-

ments, which can be represented by several measures. Work that addresses this question is discussed in Chapters 4-5.

The second question addresses a unique challenge specific to HFIR as a research reactor. HFIR is driven by its missions of neutron scattering, materials irradiation, and isotope production, several of which can have an impact on antineutrinos produced from non-fuel related reactions in the core. This work develops a methodology for candidate selection and analyzes the relevant isotopes to quantify their contributions. Work that addresses this question is discussed in Chapters 6.

The third question addresses the broader impact of this work in advancing antineutrino detectors to be implemented as a safeguards technology. Many previous antineutrino experiments have taken place at power reactors. The unique nature of HFIR as a research reactor in combination with modeling tools can be leveraged to help bridge the gap between simulation and experiment. Knowledge of the reactor facility is necessary to reduce the uncertainty in analysis of the antineutrino spectra. Work that addresses this question is discussed in Chapters 7-8.

In summary, the first question seeks to characterize the antineutrino flux from HFIR. The second question seeks to address a complication in the measurement due to unique design and operation of HFIR. The third question seeks to further identify other factors associated with the spectrum measurement at HFIR that broaden the context of the PROSPECT experiment in spectral predictions and safeguards application.

3.1 Computational Tools

3.1.1 MCNP

The Monte Carlo N-Particle (MCNP) code [54] is a three-dimensional continuous-energy Monte Carlo transport code used for radiation transport and shielding calculations. It has also grown in the past decade in its capabilities for criticality eigenvalue calculations. This is the main code used for generating reaction rates and fission distributions. The most

Table 3.1: Typical HFIR reactor physics parameters for BOC, EOC, and their arithmetic average from [48, 58]

Parameter	BOC	EOC	Average
Q (MeV)	200.51	200.92	200.71
β	0.00745	0.00734	0.00740
ν	2.44	2.442	2.441
Λ (μs)	37.75	69.52	53.63
S (10^{18} n/s)	6.456	6.449	6.452

common version used in this work is MCNP 5 versions 1.51 and 1.60 [55], although some work was also done in MCNP 6.1.1 [54]. The older version of the code is most frequently used by HFIR staff for nuclear safety and experiment analysis.

The HFIR reactor models date back many years and have been used for simulation of key reactor parameters for safety analysis. In 2004, a HFIR MCNP model was created based off Cycle 400 of HFIR [56]. The model included representation of the as-built core configuration with modifications out through the beryllium reflector but with a homogenized representation of the fuel plate and coolant channels. Various iterations of the model have existed over the past several years. In 2015, a model of HFIR Cycle 400 was created due to extensive documentation of the cycle [50]. The model was then improved upon in 2016 to include explicit modeling of the involute-shaped fuel plates and a representative target loading [48]. The models exist for beginning- and end-of-cycle (BOC and EOC) and in single day time steps for each day in the cycle; the isotopics for each day were calculated in Ref. [48] with the VESTA depletion code [57]. Views of the MCNP models are shown in Figure 3.1. Iterations of this most recent model is what will be used for this analysis, with one exception in modeling plutonium targets. Table 3.1 shows some of the relevant neutronic parameters for HFIR from various calculations.

Statistical Error

MCNP is a Monte Carlo code that comes with inherent statistical uncertainty in its calculations. For most of the results, the uncertainty associated with each value may not be

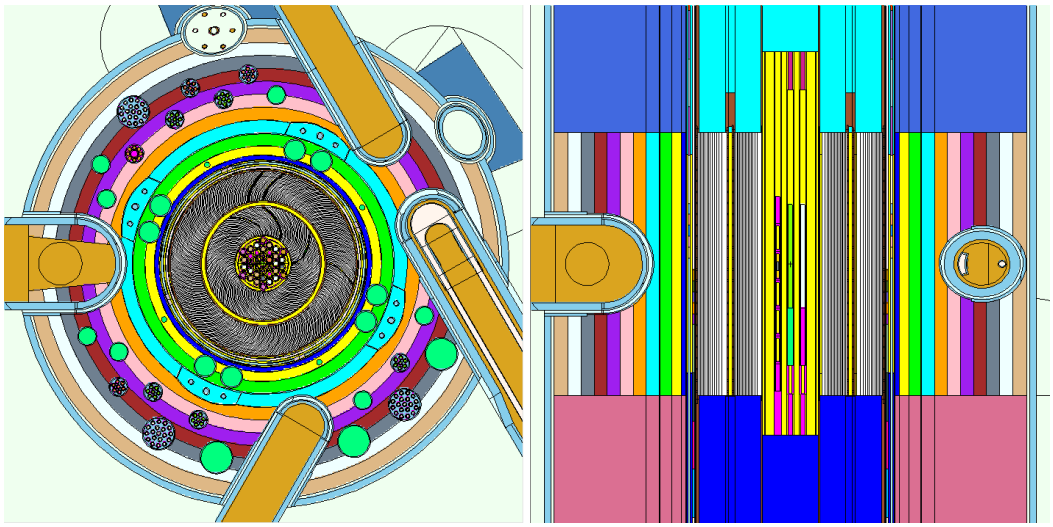

Figure 3.1: Top-down (left) and side (right) view of the HFIR core in the MCNP model [48]

discussed directly. In almost all cases, the MCNP statistical uncertainties were no more than 0.1-0.3% for neutron flux spectra. Depending on the specific reaction, tallies for reaction rates tended to have higher uncertainty, sometimes in the range of 1-3%, but often it was lower than that and on the same order of magnitude as the flux spectra uncertainties. The listing and propagation of these uncertainties is not discussed explicitly in every section. It is noted that these uncertainties are often too small to bias the results significantly.

3.1.2 SCALE

SCALE [59] is Oak Ridge National Laboratory's comprehensive modeling and simulation suite with many applications in nuclear science and technology. The COUPLE [60] and ORIGEN [61] modules were most frequently used in this work. The COUPLE sequence is a cross-section processor that generates cross-section data based on user input neutron flux spectra or otherwise calculated cross-sections. The Oak Ridge Isotope Generation (ORIGEN) code is a depletion module that can be used for neutron activation analysis, actinide transmutation, fission product generation, and source term analysis.

3.1.3 ADVANTG

The Automated Variance Reduction Generator (ADVANTG) [62] is a software also developed by ORNL to decrease statistical uncertainty in MCNP tallies using weight windows and source biasing. ADVANTG uses the three-dimentionsal discrete ordinates transport solver Denovo. ADVANTG employs the Consistent Adjoint Driven Importance Sampling (CADIS) and Forward-weighted (FW-CADIS) methods to provide space- and energy-dependent weight windows for each individual tally. ADVANTG is used in combination with MCNP to increase precision on tallies. Currently, ADVANTG is only suitable for use with MCNP5 version 1.60 in fixed source (i.e. not criticality) mode.

3.1.4 HFIRCON

Recent work at ORNL has gone into developing HFIRCON, an automated and integrated code package used for quick analysis for HFIR-specific neutronics calculations [63]. The development of HFIRCON allows for rapid simulations of multi-cycle depletion and analysis. The HFIRCON driver module utilizes several existing tools: ADVANTG [62], ORIGEN [59], and ORNL-TN, which includes modifications to the MCNP5 version 1.60 source code and data processing from MCNP6.2. HFIRCON was originally developed to solve problem types involveing: cycle length calculations, single-cycle target depletions, and multi-cycle target depletions.

The HFIRCON code contains many user-friendly functionalities that help simulate one or more HFIR cycle(s) with user-input time steps. It allows for fast geometry initialization and stochastic volume calculation using LAVAMINT for any input [64]. It dynamically searches for the critical rod position for each time step. The code creates HDF5 files for tallies and cell information that can easily be post-processed with a viewing utility or Python interface. These functionalities improve greatly in time and headache from many current methods of HFIR depletion simulations.

It produces relevant nuclide concentrations, reaction rates, and neutron flux for any

user-defined energy group structures. The code can also deplete target materials and calculate reaction and heat generation rates, which can be used for safety analysis. The current default setting for HFIRCON allows for tracking of 2237 isotopes and can generate tally cards in fuel and target materials. The default for fission and capture tallies includes 82 and 422 nuclides, respectively. Overall, the code provides the opportunity to perform quick neutronic transport and depletion simulations.

3.1.5 Neutrino Spectra Generation

As previously described, $\overline{\nu}_e$ spectra are primarily generated in two different ways. The main method has been the conversion of measured electron spectra, which has parametrized data for ^{235}U, ^{238}U, and ^{239}Pu from Huber [33] and ^{238}U data from Mueller and Haag [29, 37]. This data is arranged into 250 keV bins. The second method used in this thesis is the summation method using the Oklo nuclide modeling toolkit [65]. Oklo generates summation-predicted from Evaluated Nuclear Data File (ENDF) fission yields and Evaluated Nuclear Structure Data File (ENSDF) beta decay and transition data.

The two major methods are compared prior to use in generating $\overline{\nu}_e$ spectra from HFIR fission rates. Figure 3.2 shows the spectra from Huber/Mueller spectra and the ^{235}U spectra compared to the Oklo-generated data. The Oklo data tends to agree well with the Huber data for most of the energy ranges except for energies less than 4 MeV. The advantage with the Oklo data is that it is available in 10 keV bins; the Huber data is only published for 250 keV bins. As previously mentioned, each fission produces approximately 6 $\overline{\nu}_e$ per fission. Only a fraction of these are above the IBD threshold of 1.8 MeV. Table 3.2 compares these values for both methods.

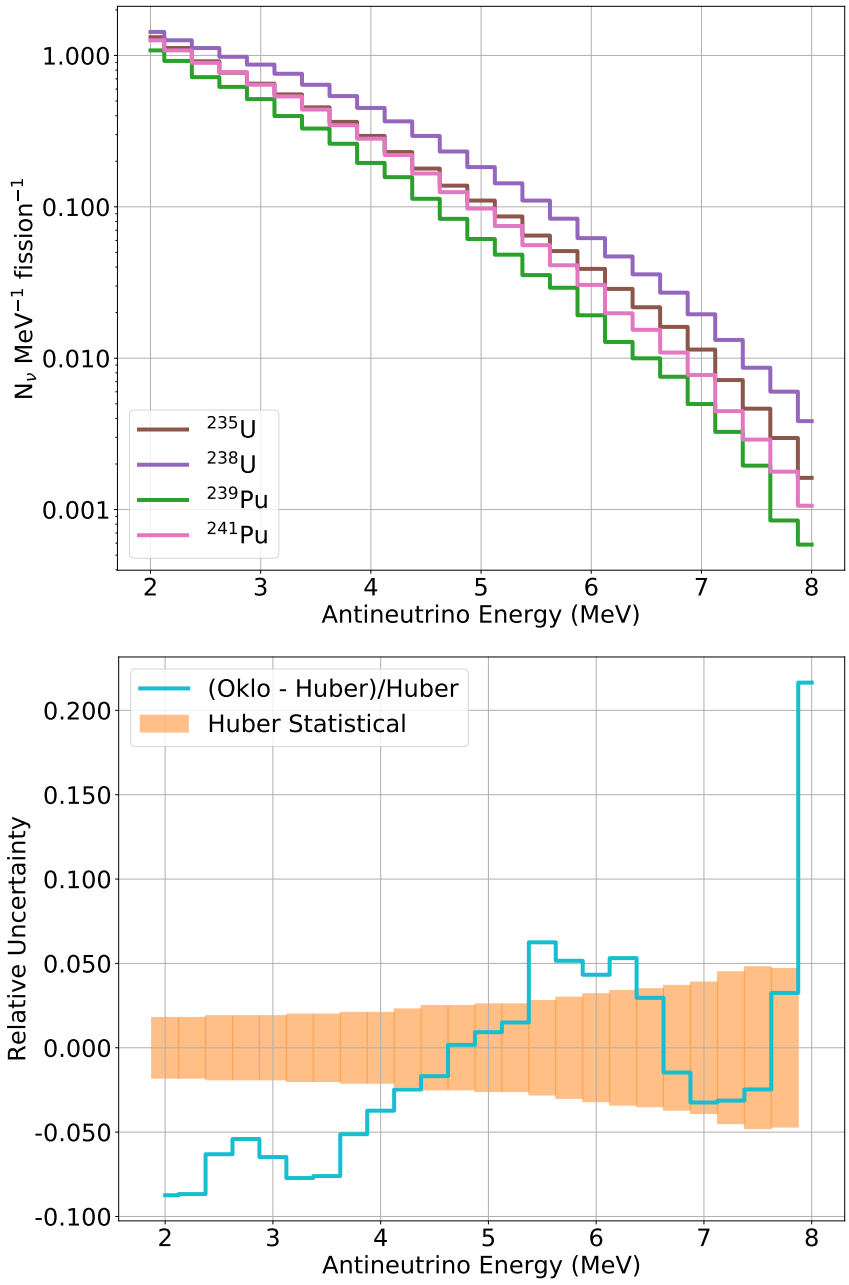

Figure 3.2: Huber/Mueller $\overline{\nu}_e$ spectra (top) and the relative difference between Huber and Oklo ^{235}U data with Huber total statistical uncertainty for comparison (bottom)

Table 3.2: Average number of $\overline{\nu}_e$ emitted per fission above IBD threshold according to Oklo-generated data and the standard Huber model

Isotope	Oklo	Huber [66]
^{235}U	1.841	1.974
^{238}U	2.265	2.535
^{239}Pu	1.497	1.501
^{241}Pu	1.827	1.885

CHAPTER 4

FISSION RATES AND ANTINEUTRINO SPECTRUM

In this chapter, the isotope-dependent fission rates and fractions are quantified for a typical HFIR cycle. It is necessary to calculate the fission rates and fractions to understand how much the neutrino spectrum will change as a function of burnup, or, in other words, fuel evolution. These rates are used to calculate and generate antineutrino spectra from state-of-the-art methods.

Various neutronic models are used to generate these rates. The main model used is a variation of the MCNP representative model, and an input is ran for each day in the cycle. Each of these is run as a static (time-independent) criticality calculation. The day-by-day models contain isotopics in fuel materials based on the VESTA depletion code [57] and updated control element positions; this is heavily outlined in the description of the depletion simulations of the representative model [48]. ADVANTG is used to generate energy-dependent weight windows for the fuel cells.

The models are primarily run in MCNP5 version 1.60. This version of the code is the primary one used for neutronic analysis at HFIR for safety calculations because it has been passed through the software quality assurance (SQA) approval process. MCNP5 is currently the only version that has been consistently effective at running the representative model; MCNP6 sometimes experiences segmentation faults or lost particle errors when running the models successfully ran with MCNP5. The one exception achieved in this work was at running the model with perturbation cards (PERT) added, a new capability in MCNP6, which is discussed in Section 4.4.

First, ENDF/B-VII cross-sections are used for all isotopes. For each day in the cycle, MCNP is run with 100,000 source particles, 50 skipped cycles, and 500 active cycles. The k_{eff} for the simulations as a function of day in the cycle is shown in Figure 4.1. The 1σ

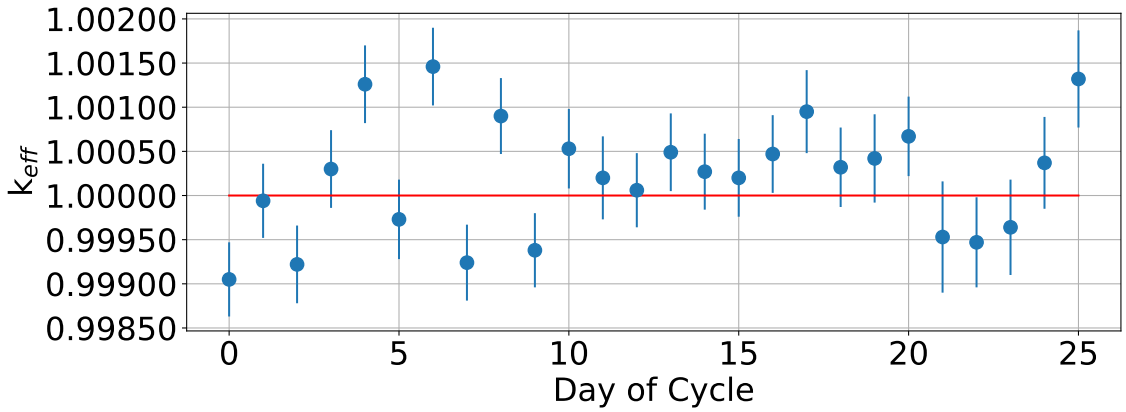

Figure 4.1: Criticality eigenvalue with 1σ error from the MCNP calculations for each day in the cycle

error was in the range of 10-20 per cent mille (pcm) or less.

4.1 Fission Rates and Fractions

As previously discussed, the $\overline{\nu}_e$ source is produced from the byproducts of fission, previously displayed in Table 3.2. The $\overline{\nu}_e$ spectrum can be calculated using the fission rates f and fission fractions F of a fissile isotope i:

$$S(E_{\overline{\nu}_e}, t) = \sum_i f_i(t) \frac{dN_i}{dE_{\overline{\nu}_e}} = f(t) \sum_i F_i(t) \frac{dN_i}{dE_{\overline{\nu}_e}} \tag{4.1}$$

The HFIR fuel contains about 9.4 kg of ^{235}U, or over 10 kg of total uranium metal, distributed between the IFE and OFE fuel regions. The HFIR fuel assembly is replaced every cycle, such that each cycle starts with fresh fuel elements in both the IFE and OFE. The replacement of the elements means that, contrary to traditional commercial reactors, the HFIR core starts each cycle with no plutonium in the fuel contributing to the fission rate and therefore zero fission fraction. The $\overline{\nu}_e$ flux is derived from those that are generated through the fission process, primarily via the beta decays of neutron-rich fission products.

Because the $\overline{\nu}_e$ yield and spectrum differs among the main fissile isotopes common in nuclear fuel, isotope-dependent reaction rates are required to generate predicted $\overline{\nu}_e$ spectra

coming from HFIR. The current version of MCNP [54] does not possess the functionality to output isotope-dependent fission rates, therefore tallies with phantom materials have to be added. A phantom material is one that may not fill a particular cell of the problem but whose reaction multiplier (such as cross-section) can be used in a flux tally to generate reaction rates in that cell for that material alone. A phantom material for each relevant fissile isotope is created to get the desired reaction rates. The total reaction rate *R* and reaction rate of isotope *i* (R_i) can be calculated from MCNP F4 and FM4 cards and the number density *N*:

$$R = N\phi\sigma = N \times F4 \times FM4 \tag{4.2}$$

$$R_i = N_i\phi\sigma_i = N_i \times F4 \times FM4_i \tag{4.3}$$

where $FM4_i$ is the phantom material. Equation 4.2 would calculate the total fission rate of all isotopes while Equation 4.3 calculates the reaction rate of the primary actinides. Post-processing Python scripts are used to multiply the tally results by the time- and cell-dependent concentrations for each isotope.

The tally results can be used to calculate core absolute reaction rates of each isotope using the power normalization factor (PNF), also called the neutron source term *S*, shown in Equation 4.4.

$$PNF(neutrons/sec) = S = \frac{P\nu}{k_{eff}Q_{fiss}} \tag{4.4}$$

The fission fractions are calculated as the sum of fission rates of each isotope over the total fission rate of all isotopes, as shown in Equation 4.5 Equation 4.5 can be calculated from simulation results without normalization to the absolute power, but it is needed to obtain an absolute emission rate of antineutrinos. This normalization can be done with the power normalization factor (PNF) that is a function of simulation outputs and/or nominal

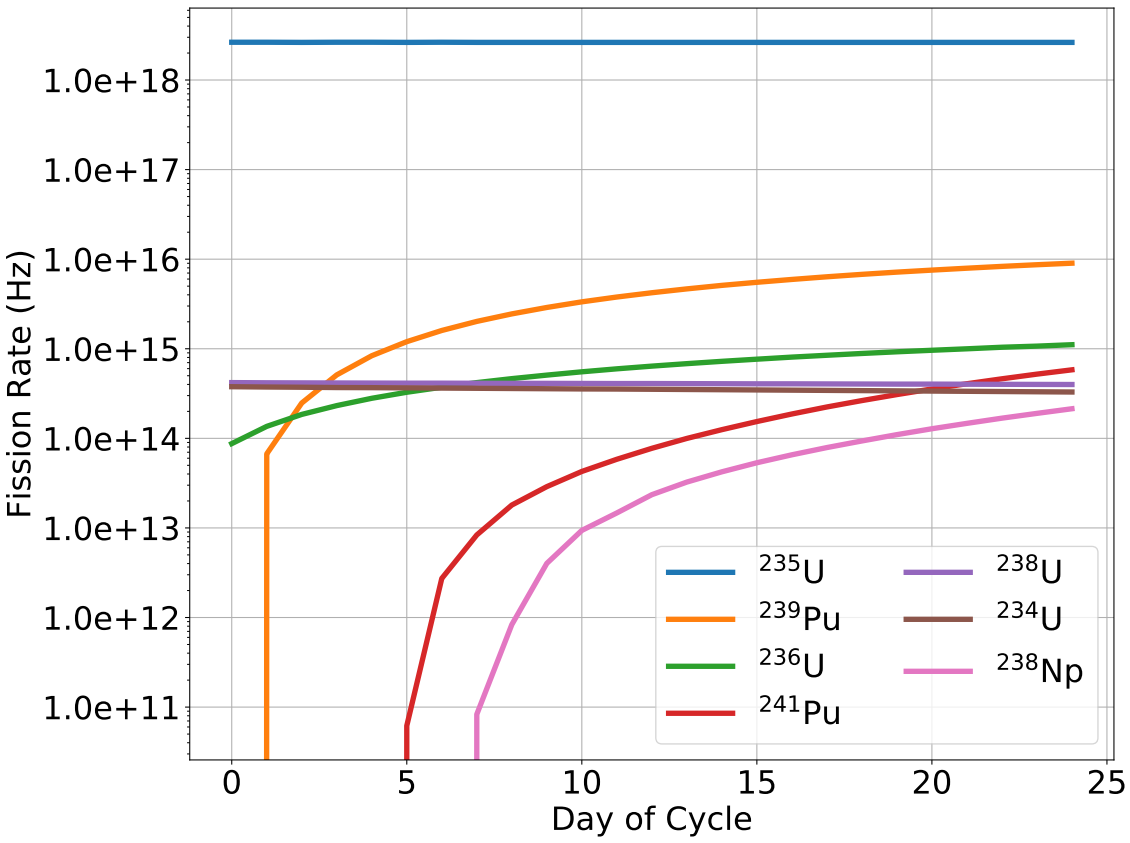

Figure 4.2: Total core isotopic fission rates from MCNP representative model

reactor parameters [67, 68]. Equation 4.4 shows the PNF, also called the neutron source term *S* as a function of reactor power *P*, the neutron multiplicity ν, the effective criticality k_{eff}, and fission energy release Q_{fiss}. As shown in Table 3.1, the PNF, often called the source term *S*, this factor increases by less than 0.3% from BOC to EOC.

$$F_i = \frac{\int_{\vec{r}} \int_E N_i(\vec{r}) \phi(\vec{r}) \sigma_{f,i} d^3\vec{r} dE}{\sum_i \int_{\vec{r}} \int_E N_j(\vec{r}) \phi(\vec{r}) \sigma_{f,j} d^3\vec{r} dE} = \frac{R_i}{\sum_j R_j} \tag{4.5}$$

Table 4.1 shows the fission rates and fractions from simulations of the representative model. The ^{235}U fraction decreases with time as the ^{239}Pu fraction linearly increases with cycle time. The ^{238}U and ^{236}U fractions remain roughly constant throughout the entire cycle. Table 4.1 also includes the cycle average for all of the isotopes studied and those normalized to the primary 4 isotopes typically considered for reactor $\overline{\nu}_e$ analysis. The fission fraction of ^{235}U stays above 0.995 for the entire cycle. The average value is above 0.997, and higher if it is only normalized to the other three primary isotopes.

Figure 4.2 shows the fission rates for the seven-largest contributing isotopes. The primary four isotopes are in the top five on an average basis. ^{236}U is the third largest contributor to the total fission rate on a cycle average basis. The average ^{236}U fraction is greater than ^{238}U and ^{241}Pu. The buildup and subsequent fission of ^{236}U can be explained by the initial inventory and neutron capture on ^{235}U consistently throughout the cycle; this makes sense because the capture cross-section of ^{235}U is only about an order of magnitude less than that of fission. The ^{236}U fission rate still pales in comparison to the ^{235}U fission rate by a factor of 1000.

4.1.1 Fission Fraction Uncertainty

As a Monte Carlo code, the fission rates and uncertainties inherent statistical uncertainties. Parallelization on computer clusters allows the statistical uncertainty of these calculations to be drastically reduced. The uncertainty of the fission fractions is important for understanding the variation in the $\overline{\nu}_e$ flux.

Table 4.1: Fission rate and fractions for each day in the cycle from MCNP representative model, with cycle average for all isotopes and the four-isotope only calculation

Day	Rate (10^{18} Hz)	^{235}U	^{238}U	^{239}Pu	^{241}Pu	^{236}U	^{234}U	^{238}Np
0	2.644	0.99967	0.00016	0.00000	0.00000	0.00003	0.00014	0.00000
1	2.644	0.99962	0.00016	0.00003	0.00000	0.00005	0.00014	0.00000
2	2.645	0.99954	0.00016	0.00009	0.00000	0.00007	0.00014	0.00000
3	2.645	0.99942	0.00016	0.00019	0.00000	0.00009	0.00014	0.00000
4	2.645	0.99928	0.00016	0.00032	0.00000	0.00011	0.00014	0.00000
5	2.645	0.99912	0.00016	0.00046	0.00000	0.00012	0.00014	0.00000
6	2.645	0.99896	0.00016	0.00061	0.00000	0.00014	0.00014	0.00000
7	2.646	0.99878	0.00016	0.00077	0.00000	0.00016	0.00014	0.00000
8	2.646	0.99860	0.00016	0.00093	0.00001	0.00018	0.00014	0.00000
9	2.646	0.99841	0.00016	0.00110	0.00001	0.00019	0.00014	0.00000
10	2.646	0.99821	0.00016	0.00127	0.00002	0.00021	0.00014	0.00000
11	2.646	0.99802	0.00016	0.00143	0.00002	0.00023	0.00013	0.00001
12	2.647	0.99783	0.00016	0.00160	0.00003	0.00024	0.00013	0.00001
13	2.647	0.99764	0.00015	0.00177	0.00004	0.00026	0.00013	0.00001
14	2.647	0.99744	0.00015	0.00193	0.00005	0.00027	0.00013	0.00002
15	2.647	0.99725	0.00015	0.00209	0.00006	0.00029	0.00013	0.00002
16	2.648	0.99706	0.00015	0.00225	0.00007	0.00031	0.00013	0.00002
17	2.648	0.99687	0.00015	0.00241	0.00008	0.00032	0.00013	0.00003
18	2.648	0.99668	0.00015	0.00257	0.00010	0.00034	0.00013	0.00004
19	2.648	0.99649	0.00015	0.00272	0.00012	0.00035	0.00013	0.00004
20	2.648	0.99631	0.00015	0.00286	0.00013	0.00036	0.00013	0.00005
21	2.649	0.99612	0.00015	0.00301	0.00015	0.00038	0.00013	0.00006
22	2.649	0.99594	0.00015	0.00315	0.00018	0.00039	0.00013	0.00006
23	2.649	0.99576	0.00015	0.00329	0.00020	0.00041	0.00013	0.00007
24	2.649	0.99558	0.00015	0.00342	0.00022	0.00042	0.00012	0.00008
25	2.649	0.99541	0.00015	0.00354	0.00024	0.00043	0.00012	0.00009
Average	2.647	0.99769	0.00016	0.00169	0.00007	0.00024	0.00013	0.00002
4 Only	2.647	0.99809	0.00016	0.00169	0.00007			

The uncertainty of fission fractions can be calculated from error propagation shown in Equations **??** and **??**. For the fission rates (f) and fission fractions (F) of N isotopes, the uncertainty (σ) can be calculated as:

$$F_i = \frac{f_i}{\sum_{k=1}^{N} f_k} = \frac{f_i}{f_{total}} \tag{4.6}$$

$$\sigma_{F_i} = F_i \sqrt{\left(\frac{\sigma_{f_i}}{f_i}\right)^2 + \left(\sum_{k=1}^{N} \left(\frac{\sigma_{f_k}}{f_{total}}\right)^2\right) - \frac{2\sigma_{f_i}\sigma_{f_{total}}\rho_{f_i,f_{total}}}{f_i f_{total}}} \tag{4.7}$$

The first term inside the square root, the relative uncertainty of the fission rate of a particular isotope, tends to be comparable for all fissile isotopes but linearly increases with thermal fission cross-section. The summation in the second term is dominated by the ^{235}U term in HFIR as the magnitude of the absolute error, $\sigma_{f_{235}}$, is the largest in the numerator due to the fission rate being considerably larger. The last term in the square root is a negative term also dominated by the ^{235}U fission rate and uncertainty. The correlation coefficient $\rho_{f_i,f_{total}}$ is unity because the fission rate of a particular isotope has a direct linear relationship with the total fission rate.

The results of the error propagation calculation show that the uncertainty in the fission fraction is near zero for ^{235}U and for most of the cycle for ^{239}Pu, less than 1% after its buildup over the first two days of the cycle. Because the fission rates of ^{238}U, ^{241}Pu, ^{234}U, and ^{236}U are of much smaller magnitudes, their relative fission fraction uncertainty is nearly 100% due to the dominant middle term from the absolute ^{235}U uncertainty, $\sigma_{f_{235}}$. These fission fractions are dominated by the uncertainty in the ^{235}U fission rate uncertainty, i.e. the statistical precision of the ^{235}U rates are near the same order of magnitude as the fission rates of these lower-contributing actinides.

4.1.2 Comparison of ENDF/B-VII.1 and ENDF/B-VII Cross Sections

Here, the effect of different neutron cross-section libraries is considered. The model is updated to use ENDF/B-VII.1 cross-sections when available. The ENDF/B-VII.1 release [69] states that most major actinide cross-sections (^{235}U, ^{238}U, and ^{239}Pu) were not modified but other minor actinides were modified. However, there were changes in thermal reactions on fission products and absorber materials (Eu, Sm, Mo, Mn, Cd, Gd) and resonance matrix analyses of light isotopes (He, Li, Be). In the HFIR model, all cross-sections were updated to ENDF/B-VII.1 with the exception of two elements, V and Zn, which required isotope concentration breakdown. These elements had cross-sections available in ENDF/B-VII but were not isotope dependent. Instead of assuming their isotopic dependence at various points in time in the core, the ENDF/B-VII were used for the element. The S(α,β) cards remained the same fir both cases.

Table 4.2 shows the ratio of the ENDF/B-VII.1 to ENDF/B-VII fission rate for the isotopes contributing most to the fission rate in HFIR. The ratios are almost all near unity within uncertainty. The results suggest that the changes to cross-sections in minor actinide fission, neutron absorbers, materials in the flux trap, and light materials in the beryllium reflector do not impact the fission rates and fractions significantly. The k_{eff} remained about the same between using both cross-seciton libraries.

4.2 Antineutrino Spectrum and Evolution

The antineutrino yield and spectrum varies with each fissile isotope produced. At a commercial power reactor, the fission rate changes throughout the cycle, and more importantly the fission fraction changes greatly. At a single power reactor, the fission fraction can start or evolve to be above 30% depending on the fuel loading at the beginning of cycle and batch scheme. HFIR is different in that its HEU fuel results in a high ^{235}U fission fraction, greater than 99.5% throughout the cycle as calculated in the previous section. The goal of

Table 4.2: Ratio of fission rates using ENDF/B-VII.1 to ENDF/B-VII data in MCNP simulations. Note that the uncertainty in the fission rates is $\leq 0.1\%$.

Day	^{235}U	^{238}U	^{239}Pu	^{241}Pu	^{236}U	^{234}U
0	1.001	0.998			0.999	0.999
1	1.001	1.000	1.001		1.001	1.000
2	1.001	0.999	1.000		0.999	0.999
3	1.000	0.999	1.000		1.000	1.000
4	0.998	0.998	0.999		0.996	0.998
5	1.001	0.999	1.001	1.000	0.999	0.999
6	0.999	0.999	0.999	0.997	1.001	0.999
7	1.001	1.000	1.000	0.999	1.000	1.000
8	0.999	0.998	0.999	0.998	0.999	0.998
9	1.001	0.999	1.000	1.000	1.002	0.999
10	1.000	0.999	0.999	0.998	0.999	0.999
11	1.000	1.000	0.999	0.998	1.000	1.000
12	1.000	0.999	0.999	0.999	1.000	0.999
13	0.999	0.999	1.000	1.000	1.000	0.999
14	0.999	0.999	0.999	0.998	1.000	0.999
15	0.999	0.999	0.999	0.999	1.000	0.999
16	0.999	0.999	0.999	0.999	1.000	0.999
17	0.999	0.999	0.999	0.999	1.000	0.999
18	1.000	0.999	1.000	0.999	1.000	0.999
19	0.999	0.998	0.999	0.999	0.999	0.999
20	0.999	0.999	1.000	1.000	1.001	0.999
21	1.000	0.999	0.999	0.999	1.001	0.999
22	1.000	1.000	1.001	1.000	1.002	1.001
23	1.000	1.000	1.000	1.000	1.001	1.000
24	0.999	1.000	1.000	1.000	1.000	1.000
25	0.999	1.000	1.000	1.000	1.001	1.000

this section is to examine the changes in the $\overline{\nu}_e$ spectrum at HFIR from the high-precision calculations of fission rates and fractions.

Here, the $\overline{\nu}_e$ spectrum for HFIR are generated from the fission rates and fractions using the two main methods described previously. The conversion method relies on the Huber/Mueller [33, 29] data from the measured β^- spectra. The summation method relies on the summation of ENDF fission yield and ENSDF transition data in the Oklo code [65]. The fission $\overline{\nu}_e$ spectra is calculated from the fission fractions and total fission rate from the PNF (Equation 4.5).

The $\overline{\nu}_e$ spectrum per fission is calculated from the fission fractions of each isotope $F_i(t)$ and the $\overline{\nu}_e$ produced per energy bin for each isotope:

$$S_{\overline{\nu}_e}(E,t) = \sum_i F_i(t) \frac{\partial N_i}{\partial E} \tag{4.8}$$

where N_i is the energy-dependent number of $\overline{\nu}_e$ emitted (MeV^{-1}). The value of N_i can be obtained from either the conversion or summation method.

4.2.1 Conversion Method

The conversion method takes the standard Huber/Mueller $\overline{\nu}_e$ spectra for ^{235}U, ^{238}U, ^{239}Pu, and ^{241}Pu. These are the standard isotopes that account for more than 99% of fissions in most thermal nuclear reactors. Because these are the only isotopes with widely-referenced data, only the fission rates for these isotopes are calculated with this method according to the 4-only fractions in Table 4.1.

4.2.2 Summation Method

The summation method utilizes the Oklo code [65] that generates the $\overline{\nu}_e$ spectra for each isotope. The current available version of Oklo on Github comes with the available fission product yield data for only ^{235}U, ^{238}U, ^{239}Pu, and ^{241}Pu. The fission product yield information is obtained from the ENDF/B-VII database [44]. The spectra are compared to that

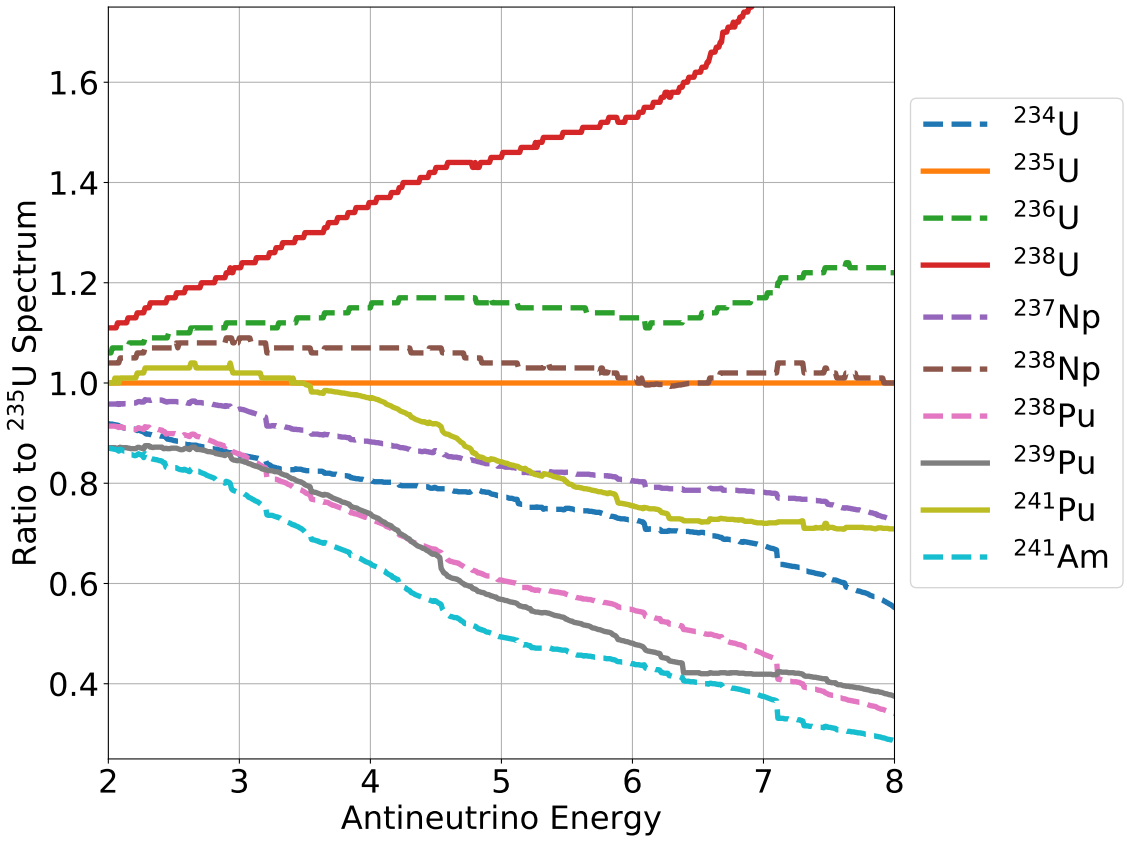

Figure 4.3: Calculated fission $\overline{\nu}_e$ spectra from the Oklo code relative to the ^{235}U spectrum. Solid lines represent the standard four isotopes that fission in a nuclear reactor.

of ^{235}U, the dominant contributor in HFIR. Figure 4.3 shows the spectra for many isotopes that were added. Other than the previously mentioned four top isotopes, the ^{234}U and ^{236}U have the highest fission fractions. ^{236}U has a higher yield while ^{234}U has a lower yield compared to ^{235}U. The fission fractions for all isotopes in Table 4.1.

4.2.3 Evolution of Antineutrino Spectrum

The $\overline{\nu}_e$ spectrum for both methods as a function of time is shown in Figure 4.4. As suggested by the high ^{235}U fission fraction, the spectrum is similar to that of ^{235}U by Huber on a per fission basis. The summation-generated spectra have lower yields for all isotopes.

Therefore the spectra for each method is compared to the relative ^{235}U generated from its own method. Figure 4.5 shows the relative change in $\overline{\nu}_e$ flux by energy bin for several

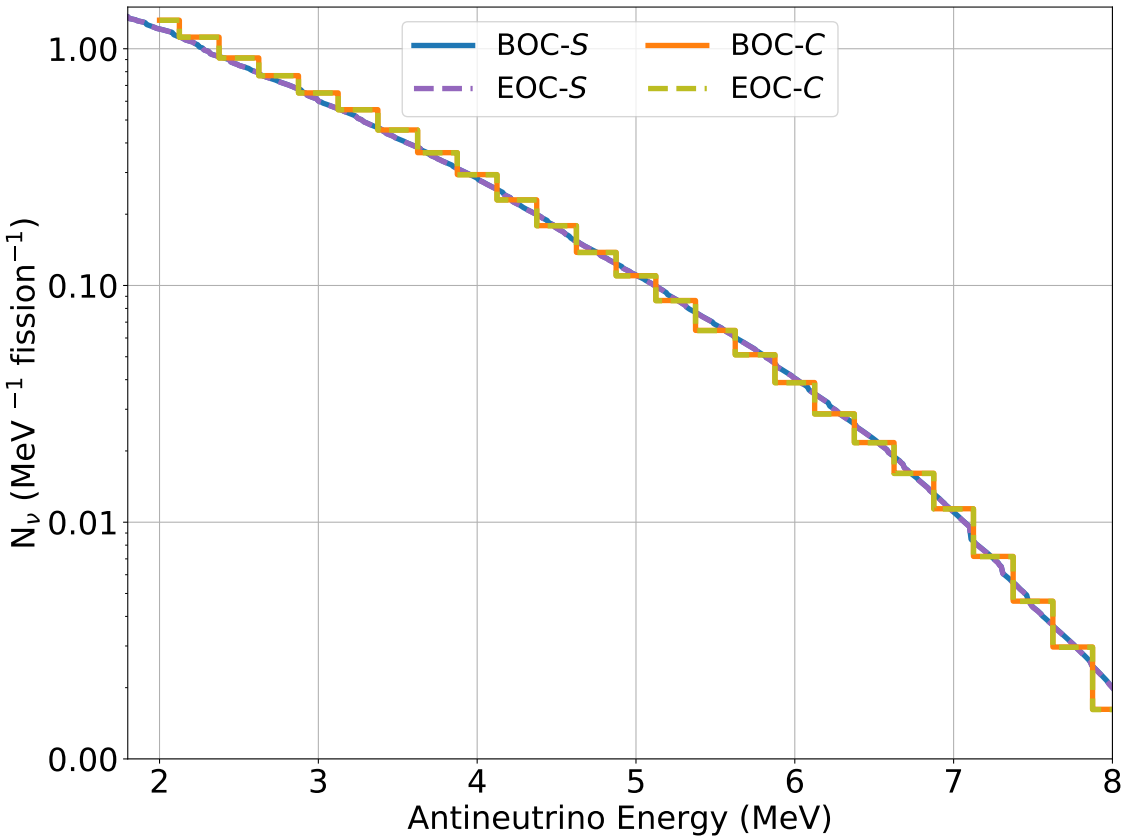

Figure 4.4: Difference from BOC $\overline{\nu}_e$ yield for multiple days in the cycle for the conversion (*C*) and summation (*S*) methods

points of time in a cycle relative to the nominal pure ^{235}U $\overline{\nu}_e$ spectra. The emitted spectra calculated by the two methods follow similarly to their differences as shown in Figure 3.2, i.e. lower prediction by Oklo (*S*) below 5 MeV and higher prediction by Oklo in the 5-7 MeV range. For each of the methods described, the spectrum changes negligibly from BOC to EOC, with only a 0.3% change in the higher energy bins at EOC predicted by Oklo.

4.2.4 Fission Fraction Uncertainty Propagation

The uncertainty of the fission rates and fractions is to be propagated through for each energy bin with the Huber/Mueller data. The uncertainty can be propagated from Equation 4.8:

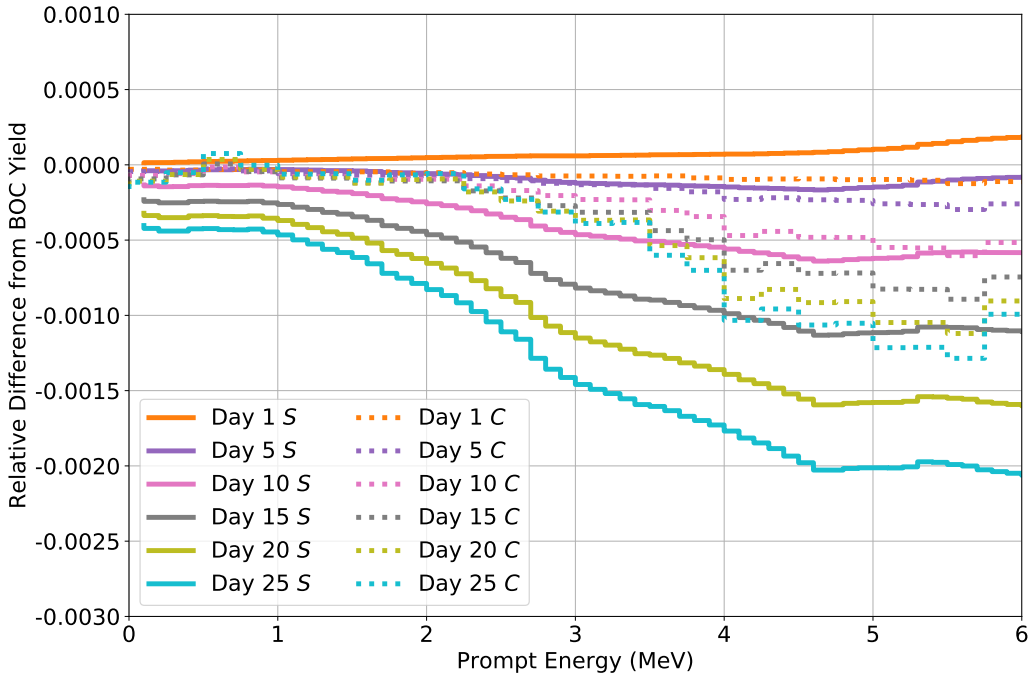

Figure 4.5: Difference from BOC $\overline{\nu}_e$yield for multiple days in the cycle for the conversion (*C*) and summation (*S*) methods

Table 4.3: Description of fission fraction uncertainty propagation

Reference Spectra	Change in F_i	Isotopes Changed (+/-)
Average Huber	$+2\sigma$ -1σ	+ (^{238}U,^{241}Pu) / - (^{235}U) - (^{238}U,^{241}Pu) / + (^{235}U)
Average Oklo	$+2\sigma$ -1σ	+ (^{238}U,^{241}Pu,^{234}U,^{236}U) / - (^{235}U) - (^{238}U,^{241}Pu,^{234}U,^{236}U) / + (^{235}U)

$$S_{\overline{\nu}_e}(E,t) = \sum_i F_i(t) N_i(E) \tag{4.9}$$

$$\sigma_S = \sqrt{\sum_i \sigma_{F_i}^2 N_i^2 + F_i^2 \sigma_{N_i}^2} \tag{4.10}$$

where the first term in the square root contains the uncertainty of the fission fraction and the second term contains the uncertainty in the $\overline{\nu}_e$ spectrum, whether that be predicted from the summation or conversion method.

The goal of this section is to understand how the uncertainty in fission fraction can be compared to those of the theoretical predictions. As stated in Section 4.1.1, the uncertainties for ^{235}U and ^{239}Pu fission fractions are nearly zero while the rest of the isotopes are 100%. Cases of $\overline{\nu}_e$ spectra are created from the two methods combined with the -1σ and $+2\sigma$ uncertainty of their fission fractions to create binding cases of the propagated $\overline{\nu}_e$ spectrum, i.e. the first term in Equation 4.10. The -1σ sigma is created as opposed to -2σ for the minor actinides because their relative uncertainty is 100% and fission fractions cannot be negative.

The cases are outlined in Table 4.3. In these cases, when the fission fractions are increased/decreased from the non-^{235}U isotopes, the ^{235}U fraction alone is assumed to decrease/increase to make the total of the fission fractions equal to unity.

In both of the average Huber and Oklo cases, the $\overline{\nu}_e$ fission spectra changed negligibly from the nominal spectrum with cycle-average fission fractions. All bins had a deviation

from the nominal of $\leq 1\%$, which is almost negligible. The highest deviation was in the highest energy range, near 8 MeV for Huber and Oklo data. The propagation of fission fraction uncertainty shows that the fuel evolution and the uncertainty in its modeling is not a large issue for the measurement of the HFIR $\overline{\nu}_e$ spectrum.

Due to the small statistical uncertainty with the Monte Carlo generated rates and fractions, the errors were much smaller than those associated with the theoretical $\overline{\nu}_e$ spectra. Theoretical uncertainties for the Huber model are in the range of 2-7% for ^{235}U and about the same or higher for the plutonium isotopes. The summation-predicted Oklo spectra have higher uncertainties due to the lack of sufficient nuclear data. Attempts at addressing this will be discussed in Chapter 7.

4.3 HFIRCON: Code Testing

Some recent work at ORNL has gone into the development of HFIRCON [63], an automated and integrated parallel performance-tuned depletion tool for HFIR analysis. The functionality of HFIRCON allows for relatively quick calculations of fission rates with depletion. With MCNP alone, it takes much more time to gain relevant statistics of actinides with lower fission fractions. HFIRCON is therefore used to check the MCNP generated rates, to more easily examine the fission rates from minor actinides, and to test more of the functionality of HFIRCON. This work also serves to benchmark HFIRCON for a different purpose than for what it was originally intended.

The HFIRCON main driver file is a controller JSON file to input user parameters alongside an MCNP input file. It outputs HDF5 files that can be processed with an HDF5 viewer or Python post-processing scripts. The current default setting for HFIRCON tracks of 2237 isotopes and automatically generates tally cards in fuel and target materials using phantom materials as discussed previously. The default for fission and capture tallies includes 82 and 422 nuclides, respectively.

First, a version of the Cycle 400 model, based on [50], was modified to be run in

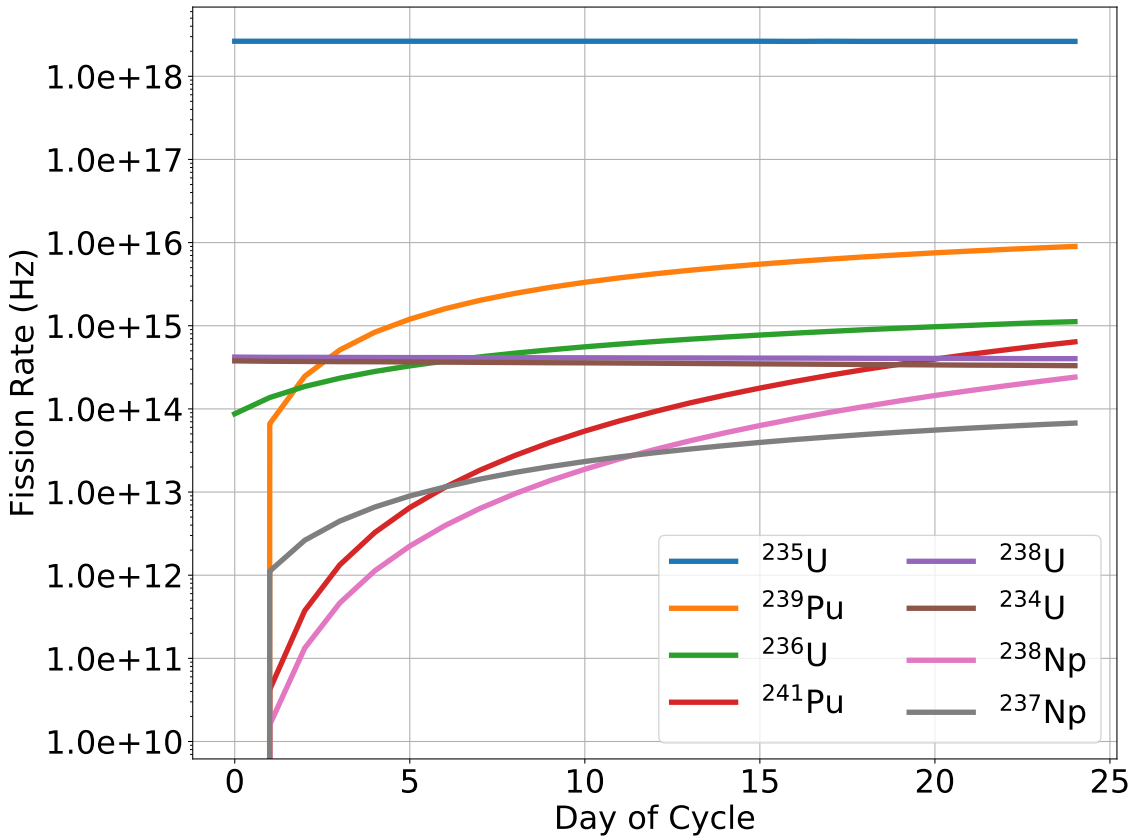

Figure 4.6: Total core isotopic fission rates from MCNP representative model run in HFIR-CON

HFIRCON. The full core depletion model with 5 time steps (day 1, 5, 10, 15, 25) was used for testing. This run took approximately 12 hours using the CADES platform at ORNL. The analysis involved post-processing scripts to read and analyze the HDF5 files for reaction rates and isotopic concentrations. Eventually, an explicit model with some slight modifications was run for 1-day time steps in HFIRCON. The modifications involved changing cell and material numbers to satisfy definition limitations in HFIRCON.

The fission rates for the explicit model run in HFIRCON are shown in Figure 4.6. It can be seen that the fission rate evolution is slightly smoother than that shown in Figure 4.2. The fission rates are all comparable to those predicted in MCNP. Small differences between MCNP and HFIRCON fission rates can be attributed in part to the use of VESTA vs. ORIGEN and the fact that HFIRCON requires a user input value for the average energy

released per fission (Q in Equation 4.4 or $\bar{E}_f$. The value for this parameter slowly increases from 200.51 to 200.92 MeV in HFIR due to the small buildup of plutonium; the value used in HFIRCON is the suggested value of 200.71.

The fission fractions are also compared. The ranking of the isotope's fission fractions is the same as it is for MCNP. The relative differences for the same six isotopes discussed previously, four uranium and two plutonium, are shown in Table 4.4. It shows a small increase in the ^{235}U and decrease in ^{241}Pu. HFIRCON shows a quicker buildup of ^{241}Pu that explains its large relative differences. Due to the increase in fission fraction of ^{235}U, HFIRCON would predict a $\overline{\nu}_e$ spectrum even more consistent with that of ^{235}U.

Table 4.4: Relative difference (%) between HFIRCON and MCNP fission fractions relative to MCNP for the six largest fission contributors in the representative model

Day	^{235}U	^{238}U	^{239}Pu	^{241}Pu	^{236}U	^{234}U
0	0.22	0.08			0.02	0.10
1	0.22	0.12	-1.27		0.29	0.16
2	0.34	0.21	-0.34		0.53	0.22
3	0.28	0.22	-0.11		0.71	0.27
4	0.21	0.27	-0.07		0.67	0.27
5	0.45	0.28	0.11	> 100	0.81	0.29
6	0.20	0.34	-0.09	> 100	0.99	0.34
7	0.52	0.32	0.11	> 100	0.79	0.31
8	0.34	0.32	0.05	53.02	0.95	0.31
9	0.40	0.24	-0.05	36.16	0.93	0.25
10	0.36	0.33	-0.14	26.73	0.87	0.32
11	0.39	0.30	-0.14	23.21	0.83	0.29
12	0.26	0.37	-0.25	20.26	0.94	0.32
13	0.26	0.35	-0.20	17.87	0.97	0.34
14	0.20	0.41	-0.42	16.34	1.00	0.35
15	0.20	0.48	-0.37	15.41	1.07	0.40
16	0.18	0.47	-0.37	14.47	1.02	0.41
17	0.17	0.46	-0.40	13.51	1.09	0.39
18	0.17	0.45	-0.43	12.70	1.11	0.38
19	0.16	0.49	-0.46	12.12	1.09	0.42
20	0.22	0.51	-0.31	11.70	1.15	0.43
21	0.26	0.53	-0.35	11.24	1.29	0.45
22	0.28	0.57	-0.35	10.77	1.18	0.47
23	0.27	0.64	-0.30	10.39	1.27	0.52
24	0.19	0.67	-0.32	10.07	1.30	0.55

4.4 Fuel Density Perturbations

New capabilities in MCNP6 [54] allow for the user to define perturbations through the PERT card. The PERT card uses Taylor series approximations to calculate the response of an MCNP tally [70]. The card calculates the first and second moments of some response from the change in a multiplicative constant to a tally, often a cross-section. The options on the card allow for the changing of a cell's density or the changing of an isotope's relative concentration to affect its macroscopic cross-section in the material.

Fuel density perturbations are performed for HFIR to understand the effect of fuel loading uncertainty as well as to test the model in MCNP6 with new capabilities. These runs were performed on the Teller cluster at Georgia Tech to test the new capability, but to the author's knowledge runs with the explicit HFIR models on MCNP6 have not been successful on an ORNL cluster.

The PERT cards are added for a single fuel cell at various percent changes for two cases, cell density and ^{235}U relative concentration. The fuel cell chosen is an OFE fuel cell near the center at BOC to maximize the change of ^{235}U fission rate. It is recommended that the number of PERT cards be kept to a minimum [54], hence only one cell is chosen. Both the first and second order terms are calculated using separate perturbation cards.

Figure 4.7 shows the change in the fission rate as a function of perturbed density of the fuel cell. It can be seen that the relationship is nearly linear with change in ^{235}U concentration or cell density. This signifies that there is little self-shielding of the ^{235}U when adding a marginal amount more in the cell. For comparison, the uncertainty of gram loading of ^{235}U in a fuel plate is $\pm$ 1%. The increase or decrease in density could become an issue from a power peaking perspective, however internal procedures at HFIR have requirements in place to signal if a plate does not meet certain standards in fuel plate homogeneity. However, this is not seen to be an issue. HFIR also has ample safety margin to allow for a small change in fuel density.

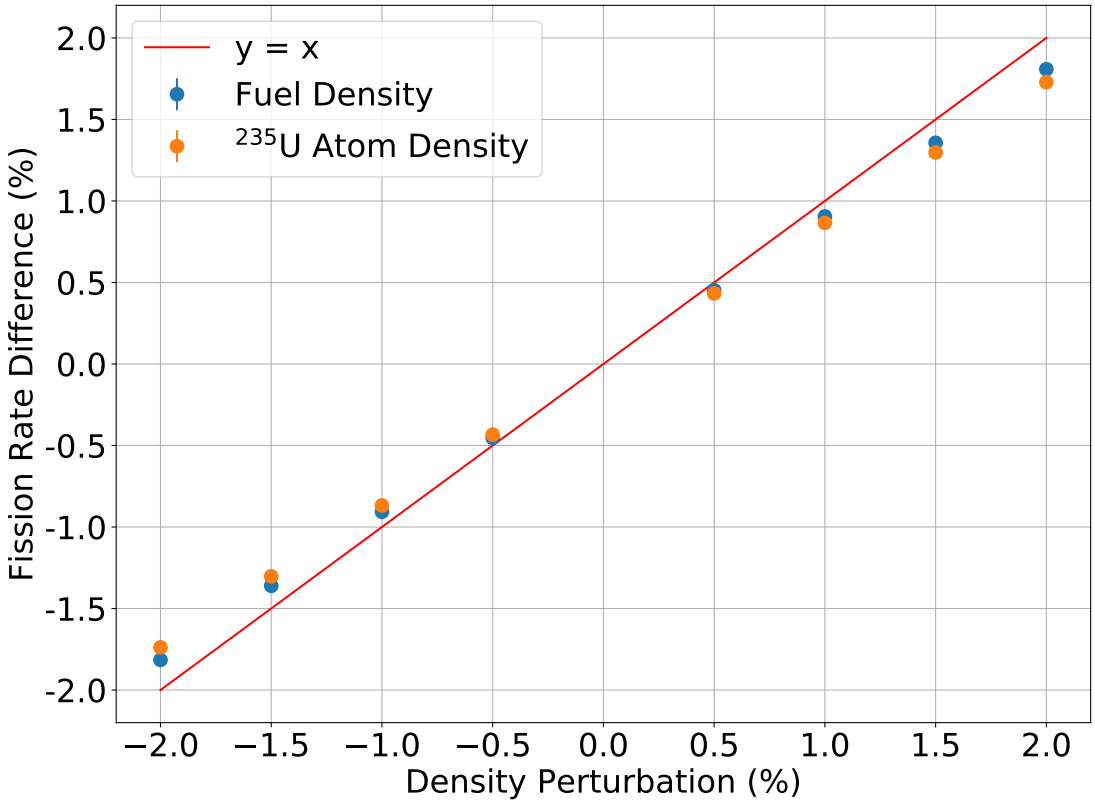

Figure 4.7: Perturbed fission rate from input density perturbations

The main purpose of this section was to test out a new functionality in MCNP6 and to test its applicability to HFIR fuel. The study of this capability showed linearity and therefore little self-shielding in the uncertainty bands of fuel loading. Furthermore, local changes in power density would be mitigated by the total thermal power of the reactor, which to a greater extent quantifies the core fission rate and fractions that are significant to predicting the $\overline{\nu}_e$ spectrum. The effect of power level will be discussed in Chapter 8.

4.5 Summary

The fission rate in HFIR is dominated by ^{235}U. Within uncertainty, the fission fraction is over 99.5% throughout the entire cycle. The ^{239}Pu is the second highest contributor which steadily increases throughout the cycle. The ^{236}U was found to be the third largest

contribution on a cycle average. The rates are compared and found to have small differences between using different cross-section libraries and a newer code HFIRCON.

CHAPTER 5

FISSION DISTRIBUTION AND EFFECT ON BASELINE

PROSPECT is able to test the sterile neutrino hypothesis with a short baseline from the detector to the reactor core. The PROSPECT detector sees a variation in spatial- and energy-dependent $\overline{\nu}_e$ flux in the detector due to high frequency oscillations. The experiment relies on the compact core to produce a constant distribution of $\overline{\nu}_e$ to the detector. The PROSPECT detector is segmented into a grid of optical segments, 14 horizontally and 11 vertically. The baseline of the individual segments of the detector vary in baseline between 6.7 and 9.2 meters from the center of the core, as shown in Table 5.1. It is important that the baseline not change much over the course of a cycle for time-independent oscillation analysis. Calculating fission rate distributions aids in ensuring that the baseline to the detector segments does not change significantly throughout the cycle.

Table 5.1: Baselines (m) for each individual detector segment to the center of the reactor

y\x	0	1	2	3	4	5	6	7	8	9	10
13	8.262	8.339	8.419	8.501	8.584	8.669	8.755	8.843	8.933	9.024	9.116
12	8.140	8.219	8.300	8.382	8.467	8.553	8.640	8.729	8.820	8.912	9.006
11	8.019	8.099	8.181	8.265	8.350	8.437	8.526	8.617	8.709	8.802	8.897
10	7.898	7.980	8.063	8.148	8.235	8.323	8.413	8.505	8.598	8.692	8.788
9	7.779	7.862	7.946	8.032	8.120	8.210	8.301	8.394	8.488	8.584	8.681
8	7.660	7.744	7.830	7.918	8.007	8.098	8.190	8.284	8.380	8.477	8.575
7	7.543	7.628	7.715	7.804	7.895	7.987	8.081	8.176	8.273	8.371	8.471
6	7.426	7.513	7.601	7.692	7.783	7.877	7.972	8.069	8.167	8.266	8.367
5	7.311	7.399	7.489	7.580	7.673	7.768	7.865	7.962	8.062	8.163	8.265
4	7.197	7.286	7.377	7.470	7.565	7.661	7.758	7.858	7.958	8.060	8.164
3	7.084	7.174	7.267	7.361	7.457	7.555	7.654	7.754	7.856	7.960	8.064
2	6.972	7.064	7.158	7.253	7.351	7.450	7.550	7.652	7.755	7.860	7.966
1	6.861	6.955	7.050	7.147	7.246	7.346	7.448	7.551	7.656	7.762	7.869
0	6.752	6.847	6.944	7.042	7.143	7.244	7.348	7.452	7.558	7.666	7.774

5.1 Fission Rate Distribution

The fission rate distribution represents the volumetric (fissions/cm^3/s) fuel fission rate spatially in the reactor. The fission rate distribution can be calculated from the tallies that were calculated in Chapter 4. The version of the HFIR representative model used is discretized into several axial and radial zones. The IFE and OFE contain 21 and 14 radial (r) regions, respectively; both fuel elements are discretized into 19 axial (z) regions. Each cell in rz uses a single fuel material that is individually depleted, however this does not include azimuthal angular dependence around the core. While individual plates are explicitly modeled, utilizing one material for several radial and axial zones in each plate would be too memory-intensive with current tools and clusters.

The fission rate distribution is calculated for each day in the cycle. Figure 5.1 shows the relative volumetric fission rate distribution at the beginning-, middle-, and end-of-cycle (BOC, MOC, EOC). At BOC, the rates peak at the outer edge of the IFE and inner edge of the OFE near the axial center (i.e. midplane) with a max-to-average value of 1.6. The distribution flattens out throughout the cycle, with no cell deviation greater than 20% of the average volumetric fission rate at EOC. The withdrawal of the control rods explains the low relative rate at the outer edge of the OFE at BOC, but the full withdrawal of the neutron absorbing regions by EOC brings these values closer to the average. The distribution for each day in the cycle is shown in Appendix A.

5.2 Fission Epicenter

One of the advantages in using HFIR for PROSPECT is that it has a relatively compact core. Often in $\overline{\nu}_e$ calculations for such a small core, the reactor is treated as a point source. The average location of $\overline{\nu}_e$ production is important for oscillation analysis. In this section it is tested to see if the center of the core is the location of the fission epicenter, or the average location of all fissions.

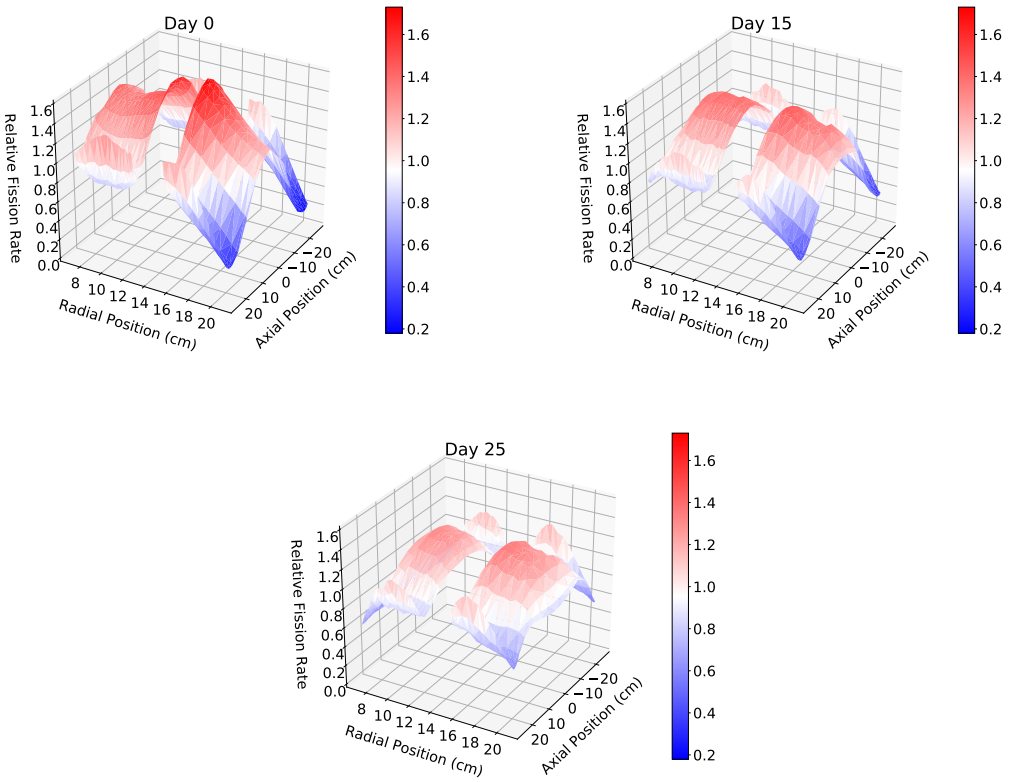

Figure 5.1: Relative fission rate distribution for BOC, MOC, and EOC

Detailed MCNP FMESH tallies are used to calculate finer flux and fission distributions. FMESH tallies can discretize coordinate systems into a much finer mesh than what is capable with traditional tallies, which are only for calculations within user-defined surfaces or cells. The calculation time increases significantly with the incorporation of more cells, but to a lesser degree with more meshes in an FMESH tally. Here, the fuel meat is split into 100 meshes per dimension in r, z, θ, totaling to $O(10^6)$ meshes. This provides the capability to calculate neutron fluxes and fission rate in a finer distribution than what was calculated in the previous section.

The FMESH tallies are used to calculate the average fission location in HFIR across multiple dimensions. The average location of fission can be calculated as integrating the fission rate over all active fuel geometry, shown in Equation 5.1:

$$\vec{r}_{avg} = \frac{\int \vec{r} f(\vec{r}) d\vec{r}}{\int f(\vec{r}) d\vec{r}} \tag{5.1}$$

In discretized cells or meshes *i*, the average fission location is calculated as shown in Equation 5.3:

$$\vec{r}_{avg} = \frac{\sum_i \vec{r}_i f_i}{\sum_i f_i} \tag{5.2}$$

Here the $\vec{r}$ is the centroid of the cell or mesh. The uncertainty associated with this approximation is assumed to be negligible as the meshes are relatively small; in the fuel cells, the meshes along the fuel plate vary between 0.5 at the axial end to 5 cm [48]. The covariance between the numerator and denominator of Equation 5.3 is assumed to be small as the magnitude of the fission rate has little effect the location of the average fission location. Assuming these are true, the uncertainty can be calculated in a single scalar dimension *r* (which can be r, x, y, z):

$$\sigma_{r_{avg}} = r_{avg} \sqrt{\left(\frac{\sigma_{\sum_i r_i f_i}}{\sum_i r_i f_i}\right)^2 + \left(\frac{\sigma_{\sum_i f_i}}{\sum_i f_i}\right)^2} \tag{5.3}$$

Figure 5.2 shows the average axial and radial location as a function of time in the cycle. This is shown using both the cell fission rates from last chapter and the mesh fission rates using FMESH. The two methods are in good agreement, and the FMESH method has lower relative errors. The average axial location is near the midplane, up to 0.25 cm above the midplane. The reason for this is the loading of more neutron-absorbing targets in the lower half of the flux trap, resulting in slightly higher fission rates in the upper half of the fuel. Additionally, the black region of the outer control element is located in the upper half of the core while the black region of the inner control element is located in the lower half of the core. An example of this can be seen in the side view of Figure 2.9. The average radial location occurs between 0.5 and 1 cm into the OFE fuel meat. This makes sense as the OFE contributes to a higher fraction of the fissions in total, but not always volumetrically.

The fission axial epicenter remains only 0.25 cm above the core midplane. Therefore the average fission location is at the core centerline just above the midplane. Because the HFIR fuel elements are annular, the average fission location in Cartesian coordinates will be near the core centerline, whereas the average radial location will be in/near the fuel meat, approximately 15 cm as shown in Figure 5.2.

5.3 Azimuthal Fission Dependence

The calculation of the fission distribution in the representative model has no azimuthal dependence in the fuel cells as it uses materials independent of angle during depletion. The mesh method provides the opportunity to obtain angle-dependent fission rates. To accomplish this, the fuel regions are split up into 2 degree increments to get finer precision than in the previous section.

Figure 5.3 shows the relative fission rate azimuthally around the core. The fission rates include an average over all axial and radial segments in that angular slice. Relative errors were approximately 0.07%. The relative fission rate peaks at 2.5% above the average in the angles that correspond to the gaps between the control element plates. The angle of the

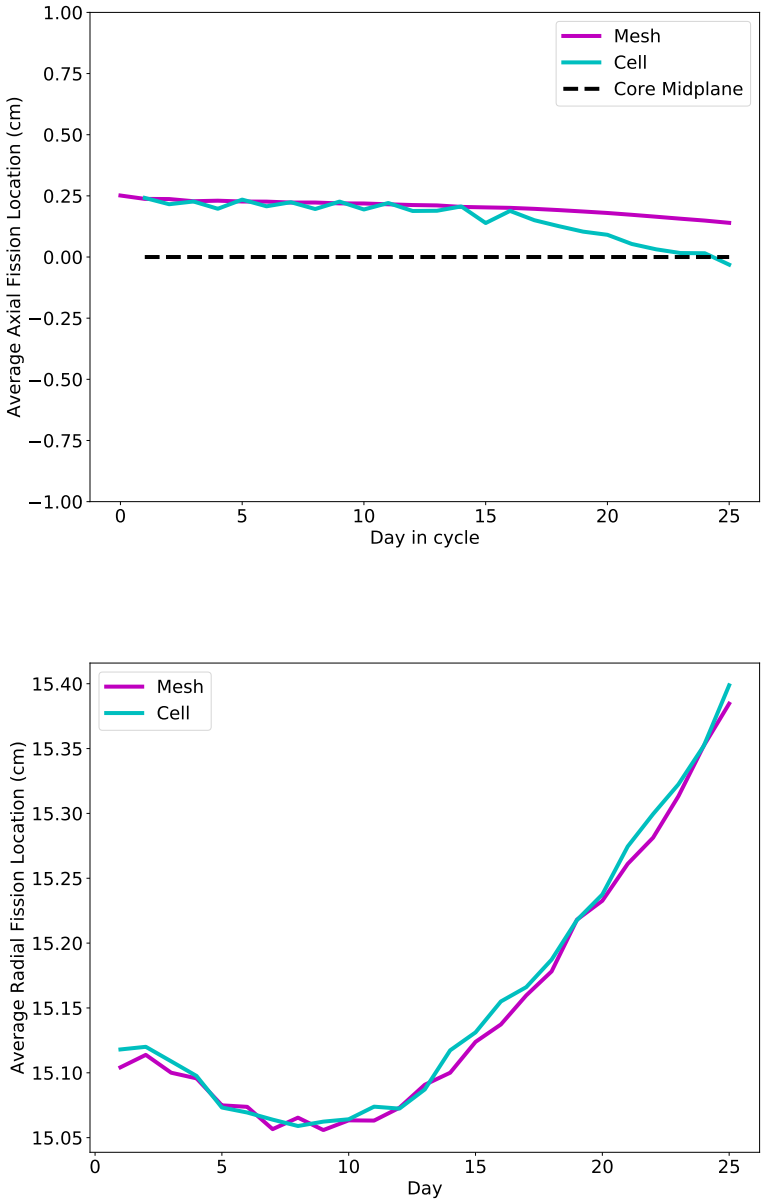

Figure 5.2: Average axial (top) and radial (bottom) fission location in the HFIR representative model as a function of time

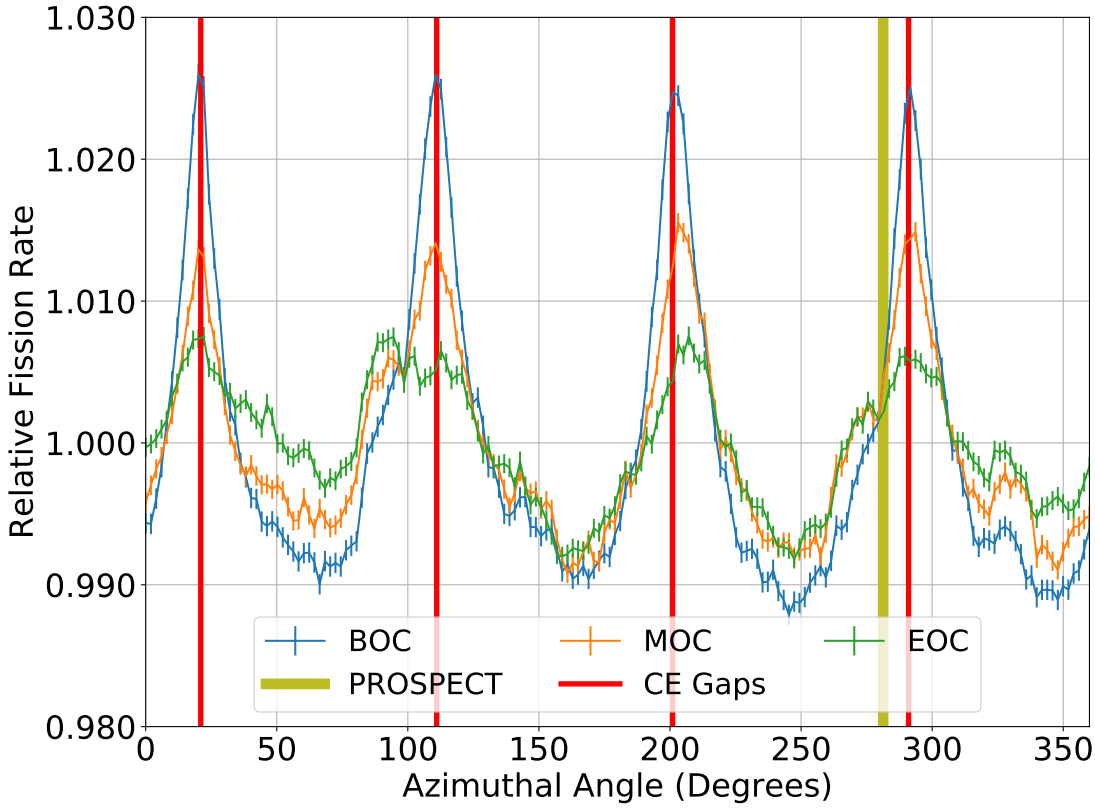

Figure 5.3: Radially- and axially-averaged relative fission rate as a function of angle around the reactor, showing control element (CE) gaps and the direction of the PROSPECT detector

PROSPECT detector is shown for reference as well.

5.4 Baseline

The baseline is the distance from the reactor to detector, i.e. the location of fission to the location to the $\overline{\nu}_e$ detection. The baseline is important for two reasons. First, the number of $\overline{\nu}_e$ detected is inversely proportional to the square of the baseline. A shorter baseline is optimal for $\overline{\nu}_e$ flux at the detector. Second, the oscillation probability changes as a function of baseline and $\overline{\nu}_e$ energy, as shown in Figure 5.4. The proportionality can be described by

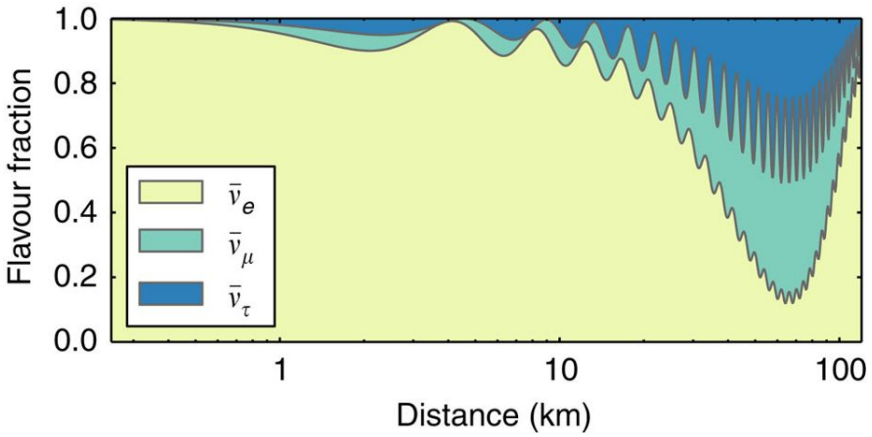

Figure 5.4: Flavor fraction of 4 MeV $\overline{\nu}_e$ oscillation as a function of baseline from the reactor, reproduced from Ref. [17]

Equation 5.4:

$$\frac{d^2N(E_\nu,t)}{dE_\nu dt} \;\alpha\; \frac{P(E_\nu,L)}{4\pi L^2} \tag{5.4}$$

A precise quantification of the baseline is important for PROSPECT because it relies on a short baseline from the HFIR core. Because the PROSPECT detector is segmented, the baseline for each segment is different. The values of the baselines vary between 6.7 and 9.1 meters from the center of the reactor core. The average baseline for a segment is 7.9 $\pm$ 0.5 meters, where all segments fall within 2σ of the average value.

The fission rate distributions from the previous section are used to calculate the distance from the fission location to the detector. Here it is assumed that the fission products do not diffuse significantly through the fuel, i.e. the location of the fission is also where the $\overline{\nu}_e$'s are emitted. The reactor to detector center-to-center distance is used to calculate the average baseline to the center of the detector for different points in the cycle. The center-to-center distances from reactor to detector are shown in Figure 5.5.

Figure 5.6 shows the baseline from HFIR to the PROSPECT detector at BOC, MOC, and EOC. It can be seen that the baseline distribution flattens out slightly over the course of the cycle. This agrees with the flattening of the fission distribution from BOC to EOC

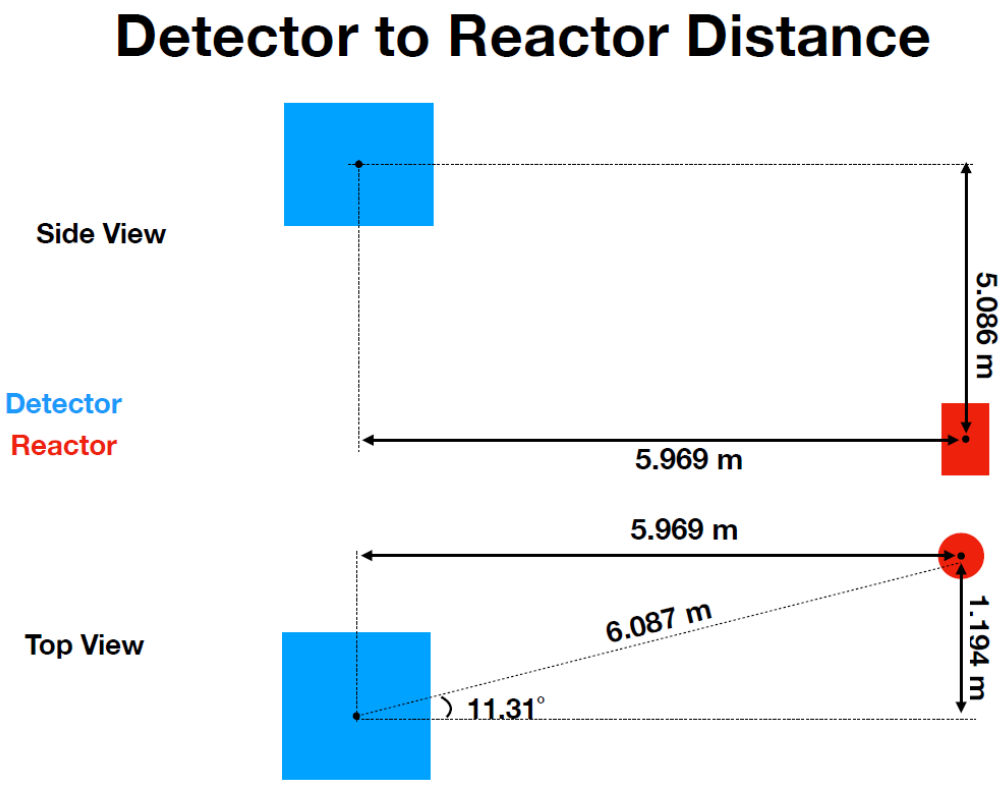

Figure 5.5: Center-to-center baseline from HFIR core to PROSPECT detector

as shown in Figure 5.1.

5.5 Fission-Weighted Baseline

A more precise metric is desired to understand the change in expected signal for each detector segment. A concept called the "fission-weighted baseline" is created to understand this change relative to the physical baseline and change within a cycle. The goal of this metric is to quantify the average distance that a $\overline{\nu}_e$ travels to each detector segment. In this calculation, the coordinate system is oriented such that the reactor center is the origin. The scalar baseline *B* of a particular segment *j* from the fission site *i* is calculated as:

$$B_j = |\vec{r}_{ij}| = |\vec{r}_i - \vec{r}_j| \tag{5.5}$$

For a simple approximation of a compact core like HFIR, the reactor could be considered

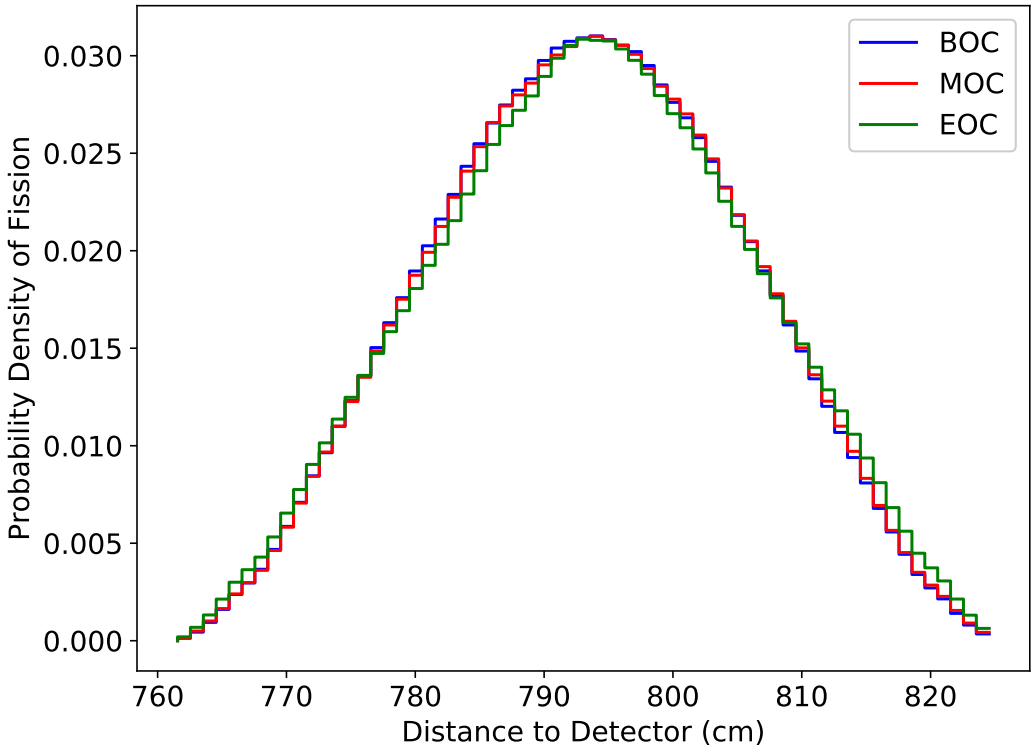

Figure 5.6: Distribution of center-to-center reactor to detector baselines

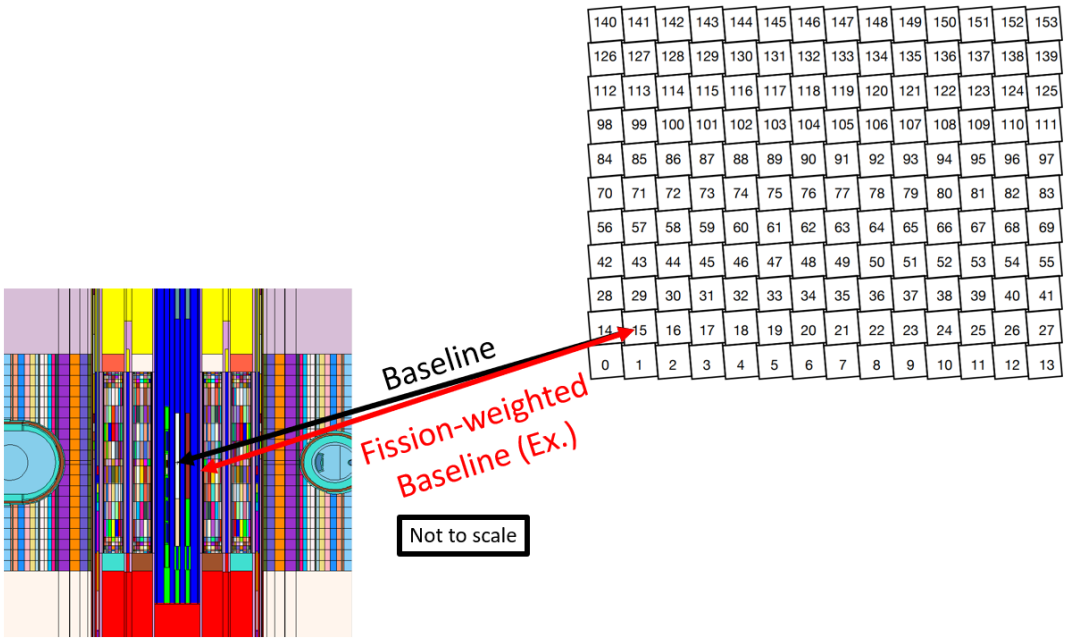

Figure 5.7: Example illustration of the difference between the physical, center-to-center baseline with the fission-weighted baseline

as a point source:

$$B_{center-to-center} = |\vec{r}_{core,center} - \vec{r}_j| = |\vec{r}_j| \tag{5.6}$$

This value $B_{center-to-center}$ is the distance between the center of the reactor to the center of detector segment *j*. The fission-weighted baseline $\bar{B}_j$ accounts for the fission rate in each cell including for the solid angle between the fission site and detector segment:

$$\bar{B}_j = \frac{\sum_i^{N_{cell}} |\vec{r}_{ij}| \frac{F_i}{4\pi|\vec{r}_{ij}|^2}}{\sum_i^{N_{cell}} \frac{F_i}{4\pi|\vec{r}_{ij}|^2}} \tag{5.7}$$

Figure 5.7 shows an example of what the different between the baseline (B_j) and fission-weighted baseline ($\bar{B}_j$) could look like for a particular segment *j*.

The baseline of each physical segment varies from 6.75 meters at the lower, adjacent corner to 9.12 meters at the upper, opposite corner. The difference between the physical

baseline and fission-weighted baseline, $B_j - \bar{B}_j$, is shown in Tables 5.2 and 5.3 for BOC and EOC, respectively. Note that the values in Table 5.1 are in meters but the values in Tables 5.2 and 5.3 are in centimeters. Note that the errors for the values listed in Tables 5.2 and 5.3 are relatively small. If one considers the difference between the values presented in Tables 5.2 and 5.3, the change within a cycle would be even smaller, i.e. subtracting values in Tables 5.2 and 5.3 would decrease to nearly zero. In any case, the baseline for any particular segment is less than 1 cm.

Table 5.2: Segment-dependent difference between center-to-center baseline and fission-weighted baseline, $B_j - \bar{B}_j$, at BOC (cm)

y\x	0	1	2	3	4	5	6	7	8	9	10
13	0.5	0.5	0.6	0.6	0.6	0.6	0.6	0.6	0.6	0.6	0.6
12	0.5	0.5	0.6	0.6	0.6	0.6	0.6	0.6	0.6	0.6	0.6
11	0.5	0.6	0.6	0.6	0.6	0.6	0.6	0.6	0.6	0.6	0.7
10	0.5	0.6	0.6	0.6	0.6	0.6	0.6	0.6	0.6	0.6	0.7
9	0.5	0.6	0.6	0.6	0.6	0.6	0.6	0.6	0.6	0.7	0.7
8	0.6	0.6	0.6	0.6	0.6	0.6	0.6	0.6	0.6	0.7	0.7
7	0.6	0.6	0.6	0.6	0.6	0.6	0.6	0.6	0.7	0.7	0.7
6	0.6	0.6	0.6	0.6	0.6	0.6	0.6	0.6	0.7	0.7	0.7
5	0.6	0.6	0.6	0.6	0.6	0.6	0.6	0.7	0.7	0.7	0.7
4	0.6	0.6	0.6	0.6	0.6	0.6	0.6	0.7	0.7	0.7	0.7
3	0.6	0.6	0.6	0.6	0.6	0.6	0.7	0.7	0.7	0.7	0.7
2	0.6	0.6	0.6	0.6	0.6	0.6	0.7	0.7	0.7	0.7	0.7
1	0.6	0.6	0.6	0.6	0.6	0.6	0.7	0.7	0.7	0.7	0.7
0	0.6	0.6	0.6	0.6	0.6	0.7	0.7	0.7	0.7	0.7	0.7

5.6 PROSPECT Solid Angle

The solid angle of the detector is important for the magnitude of $\overline{\nu}_e$ that reach the detector. The solid angle is inversely proportional to square of the reactor-to-detector distance ($1/4\pi L^2$). Using the HFIR and PROSPECT detector geometries, a solid angle factor is calculated so that it can be used for future calculations. This factor is conceptualized as the geometrical solid angle of the active volume of the detector with respect to the reactor not accounting for oscillation.

Table 5.3: Segment-dependent difference between center-to-center baseline and fission-weighted baseline, $B_j - \bar{B}_j$, at EOC (cm)

y\x	0	1	2	3	4	5	6	7	8	9	10
13	0.4	0.4	0.4	0.4	0.5	0.5	0.5	0.5	0.5	0.5	0.5
12	0.4	0.4	0.4	0.4	0.5	0.5	0.5	0.5	0.5	0.5	0.5
11	0.4	0.4	0.4	0.5	0.5	0.5	0.5	0.5	0.5	0.5	0.5
10	0.4	0.4	0.5	0.5	0.5	0.5	0.5	0.5	0.5	0.5	0.5
9	0.4	0.4	0.5	0.5	0.5	0.5	0.5	0.5	0.5	0.5	0.5
8	0.4	0.4	0.5	0.5	0.5	0.5	0.5	0.5	0.5	0.5	0.5
7	0.4	0.5	0.5	0.5	0.5	0.5	0.5	0.5	0.5	0.5	0.5
6	0.4	0.5	0.5	0.5	0.5	0.5	0.5	0.5	0.5	0.5	0.5
5	0.4	0.5	0.5	0.5	0.5	0.5	0.5	0.5	0.5	0.5	0.5
4	0.5	0.5	0.5	0.5	0.5	0.5	0.5	0.5	0.5	0.5	0.5
3	0.5	0.5	0.5	0.5	0.5	0.5	0.5	0.5	0.5	0.5	0.5
2	0.5	0.5	0.5	0.5	0.5	0.5	0.5	0.5	0.5	0.5	0.6
1	0.5	0.5	0.5	0.5	0.5	0.5	0.5	0.5	0.5	0.5	0.6
0	0.5	0.5	0.5	0.5	0.5	0.5	0.5	0.5	0.5	0.5	0.6

A simple voided MCNP model is created to calculate the approximate solid angle of the detector, as used in stochastic volume calculations [55]. This voided model assumes the geometry of the detector [46] and its distance according to Figure 5.5. The distribution of the fissions in the reactor and actual dimensions of the active volume of the PROSPECT detector. The number calculated is found to be consistent with the solid angle using the simple formula.

$$\frac{1}{4\pi\bar{L}^2} = 1.283 \times 10^{-7} cm^{-2} \pm 0.18\% \tag{5.8}$$

5.7 Summary

The results of this section show that the fission distribution changes negligibly throughout the cycle for the purposes of PROSPECT detector analysis. The fission distribution peaks most drastically at BOC and slowly flattens out over the cycle. The fission epicenter is only 0.25 cm away from the geometrical center of the reactor, although this can change with target loading in the flux trap and VXFs. The fission-weighted baseline concept is

created and found to be consistent with the other measures as it is less than 1 cm from the reactor center. These results do not account for the $\overline{\nu}_e$ probability of oscillation, which are accounted for in PROSPECT analysis. These results show that the baseline does not change significantly for the whole detector and for individual segments. Therefore the oscillation probability should be negligibly impacted as well.

CHAPTER 6

NON-FUEL SOURCES OF ANTINEUTRINOS

Antineutrino detectors seek to measure the antineutrino flux coming from the beta decay of fission products to obtain information on the reactor spectrum. The measurement of fission rates from an antinuetrino detector depends on the correlation between fissions and antineutirnos produced. However, other neutron-induced reactions produce antineutrinos via beta decay. Therefore the detected antineutrinos are a confluence of the fission-derived and non-fission-derived antineutrinos. As previously described, the $\overline{\nu}_e$ production rate has been assumed to be linearly related with the reactor power, which is proportional to the fission rate:

$$\frac{dN_{\bar{\nu}_e}}{dt} = \gamma[1 + k(t)]P_{th} \tag{6.1}$$

$dN_{\bar{\nu}_e}/dt$ is the expected detection rate, γ is a constant that reflects the size, location, and efficiency of the detector, $k(t)$ is a term that takes into account the burnup of the fuel, and P_{th} is the thermal power of the reactor. It has been shown that the term $k(t)$ is negligible for HFIR, therefore making the detection rate directly proportional to the power of the reactor. Both of these quantities should be time-independent.

ADs rely on the direct correlation of the power and fission rate to the total $\overline{\nu}_e$ spectrum. The presence of non-fuel sources of $\overline{\nu}_e$ have the potential to disrupt this linear relationship if produced in a large enough quantity. From theoretical models, the detected $\overline{\nu}_e$ are assumed to come from the β^- decay of neutron-rich fission products only. However, other neutron-induced reactions can produce unstable isotopes that are prone to undergo a β^- transition.

One such reaction is neutron capture, also called neutron activation:

$$ {}^{A}_{Z}X + {}^{1}_{0}\,n \rightarrow {}^{A+1}_{Z}\,X^{*} \rightarrow {}^{A+1}_{Z+1}\,Y^{*} + \beta^{-} + \bar{\nu}_{e} \tag{6.2} $$

The $\overline{\nu}_e$ produced from this reaction is not taken into account for most $\overline{\nu}_e$ spectrum calculations and measurements.

Others have identified non-fuel sources as a potential explanation for anomalies in the $\overline{\nu}_e$ spectrum at commercial reactors [41, 71]. This theory has mostly been ruled out due to the lack of sufficient transitions above IBD threshold. However, it has been discovered that there are some differences between theoretical spectrum compared to that from ILL due to the difference in irradiation time [30, 29]. Some isotopes have a β^- half-life that take over 12 hours to build up. This contribution is commonly called the non-equilibrium effects and are mostly due to ^{100}Tc, ^{104}Rh, and ^{142}Pr [30]. These isotopes are still fission products and are taken into account as an additional uncertainty term for $\overline{\nu}_e$ measurements.

This portion of the analysis seeks to understand the contribution of non-fission-derived antineutrinos from HFIR. In other words, the $\overline{\nu}_e$ sources cannot be derived from fission or fission product decay chains. The HFIR design and missions result in the presence of many materials in the high-flux regions which can transmute to β^--decaying isotopes via activation and other reactions. This analysis does not include the previously-mentioned non-equilibrium isotopes.

One part of the uniqueness of HFIR is the capability to intentionally irradiate numerous elements as well as unintentionally irradiate the gamut of materials already existing in the reactor due to its design. Typical commercial reactors, e.g. pressurized water reactors (PWRs), contain few materials in the core other than the fuel, cladding, moderator, and neutron poisons. In commercial PWRs, the largest components are typically made of zirconium (e.g. zircaloy cladding) or stainless steels in their support structures. Previous analyses have found that the contribution of these materials in typical reactors are negligible [41, 72].

While fission reactions typically produce multiple antineutrinos due to the fission product decay chains, the number of $\overline{\nu}_e$ from a candidate is directly proportional to the activity of the beta-decaying parent. In other words:

$$N_{\overline{\nu}}(Hz) = A_{\beta^-}(Bq) \tag{6.3}$$

Each beta-decay of a non-fission-derived neutron reaction will produce exactly one antineutrino at a rate equal to the activity of the daughter product.

The main code used to generate antineutrino spectra from beta spectra is the Oklo nuclide toolkit [65]. The Oklo code reads in the Evaluated Nuclear Structure Data File (ENSDF). The ENSDF contains information on the beta decay information of isotopes and energy levels of the daughter. Because of the nature of the three-body decay, the maximum antineutrino energy is limited by the beta endpoint energy. The beta endpoint energy depends on the energy level of the daughter isotope, which is the energy released (Q-value) less the energy of the gamma from the excited state.

$$E_\beta = Q - E_\gamma \tag{6.4}$$

The antineutrino energy needs to be above the IBD threshold of 1.8 MeV in order to produce a detector signal. Therefore the beta endpoint (maximum) energy also must be higher than 1.8 MeV.

6.1 Selection of Antineutrino Candidates

The unique missions, operation, and design of HFIR allow for a large number of materials to be present and irradiated during a given cycle. In searching for candidate isotopes that could contribute to the $\overline{\nu}_e$ spectrum, all areas of the reactor discussed in Section 2.3 are considered. This includes isotopes in the materials that make up the structural, control element, and reflector regions in addition to the large variety of target materials that are

typically irradiated in the FTT positions or VXFs in the reflector region.

The isotopes that would be of most concern for predicting an accurate fission $\overline{\nu}_e$ spectrum would be isotopes that contribute largely to the antineutrino flux coming from the core materials in excess of those from fission. Absorption reactions release significantly less heat than fission reactions, therefore they contribute insignificantly to the power level. $\overline{\nu}_e$ production that is not tracked via the power level disrupts the predicted linear relationship between detected $\overline{\nu}_e$and power level [73]. Selecting candidate isotopes can then be thought of as selecting the "worst case scenario" isotopes for $\overline{\nu}_e$production as excess contributions to the fission spectrum as they negatively affect the predictability of the power level from the $\overline{\nu}_e$detection rate. These potentially highly-contributing $\overline{\nu}_e$ sources are what will be referred to as "antineutrino candidates."

To contribute significantly to the spectrum, the combination of parent and daughter isotopes of the neutron reaction must fulfill several criteria. Again, this criteria serves to find the maximized potential contributors to the antineutrino flux. Each isotope does not necessarily need to fulfill all the criteria, as there are some trade-offs in the factors. Table 6.1 contains a summary of the isotopes considered, with criteria described in the following paragraphs.

First, an antineutrino candidate must have a relatively high concentration in the core. It cannot be contained in trace amounts or be an isotope that is not routinely irradiated in the HFIR experiment regions. In addition, a high abundance in the core relative to other isotopes with the same Z is ideal. All the isotopes in Table 6.1 are considered to be present at a sufficient quantity in the core, and the natural isotopic abundance is listed.

Second, the neutron-induced reaction must have a non-negligible neutron cross-section to produce the daughter. Because the neutron-induced reaction rate (R) is a product of the concentration and energy-dependent cross-section and flux, it is necessary to have a

maximum of this product:

$$R = N_i(t) \int \phi(E,t)\sigma_i(E)dE \tag{6.5}$$

For example, aluminum has a relatively high atomic concentration in the core but a low cross-section, while the poisons in the CEs have the inverse. Both of these can still be considered as $\overline{\nu}_e$candidates. All of the cross sections listed in Table 6.1 are the ENDF/B-VII.1 [44] thermal neutron cross-section (0.0253 eV), unless otherwise noted.

Third, the daughter product must β^- decay with a low half-life relative to the cycle of the reactor such that the daughter generates a large enough activity. If the half-life is too long, it will not decay with a high enough frequency, i.e. to produce a significant amount of $\overline{\nu}_e$. The relative magnitude of half-life to cycle length will determine how quickly, if at all, the activity will reach secular equilibrium with its production rate. Isotopes with half-lives of up to several hours are considered such that they would reach a large enough value early into the HFIR cycle, i.e. within a day of operation, and therefore have a considerable contribution for much of the cycle duration.

Fourth, the β^- transition must release enough energy lesser the excited state of its product (or the β^- endpoint energy) to be greater than the IBD threshold of 1.8 MeV. The antineutrino will not be detected without meeting this requirement. The energy released and final state energy are retrieved from the Evaluated Nuclear Structure Data File (ENSDF) database [74] maintained by the National Nuclear Data Center (NNDC). Some of the daughter isotopes in Table 6.1 have several final states; only the ones that generate a β^- endpoint energy above the IBD threshold are considered.

The activity of the antineutrino candidate, i.e. its $\overline{\nu}_e$production rate, as a function of time follows its creation rate, usually (n,γ), in the reactor minus its decay rate:

$$A_i(t) = N_i(t)\left(1 - e^{-\lambda t}\right) \int \phi(E,t)\sigma_i(E)dE \tag{6.6}$$

If the half-life of the product is small enough relative to the irradiation period, the decay term quickly declines and the activity becomes time-independent. The third criteria allows for the exclusion of time-dependence for most isotopes.

Candidate isotopes included materials that were found in the representative model [48]. Table 6.1 shows a non-comprehensive list of the main isotopes considered. The potential candidate isotopes with atomic mass number are shown in the left-most column. The first two criteria are displayed in columns 2-3 to see if the isotope meets the abundance and cross-section requirements. The third criteria is displayed in columns 4-5 to examine if the isotope meets the β^- transition and half-life requirements according to ENSDF data [74]. The fourth criteria is displayed in columns 6-8 and shows if the the isotope transition that results in a β^- endpoint above 1.8 MeV. A hyphen in the table means that the candidate does not meet the criteria and is therefore no longer considered. Therefore the screened antineutrino candidates can be seen by the non-empty fields in the last column of Table 6.1. All isotopes with a value above 1.8 MeV in the last column are examined for this analysis.

The next step for the antineutrino candidates is to calculate the reaction rates and $\overline{\nu}_e$ spectra for the candidate isotopes. The β^- decays of antineutrino candidates that are to be considered include three main regions. The first is structural, which includes ^{28}Al, ^{55}Cr, ^{66}Cu, and ^{27}Mn. The second is the beryllium reflector, which includes ^{6}He and ^{8}Li. The last is the target materials, which include ^{52}V in the FTT and two actinide targets, curium in the FTT and neptunium in the VXFs.

6.2 Calculation Process

The calculation methodology for obtaining the $\overline{\nu}_e$ yield and spectra is shown in Figure 6.1. MCNP is used to generate the flux spectrum and magnitude. The flux spectrum in all cells containing each candidate is obtained in 44-groups as this is a collapsed version of the SCALE standard 238-group flux and is commonly used in activation problems. The 252-group flux is also obtained for several cases as this is used more commonly in the most

Table 6.1: A summary list of the antineutrino candidates in HFIR. The requirements for $\overline{\nu}_e$candidate selection previously described are bolded in the second row of the table. A hyphen symbolizes that the isotope is no longer considered due to not fulfilling criteria.

	El.	A	Abundance (%)	ENDF/B-VII.1 σ (b)	Daughter	$t_{1/2}$ (s)	Q (MeV)	E_{final} (MeV)	E_β Max (MeV)
Requirement			**High**	**High**	**β^-decay**	**Low**	**High**		**$>$ 1.8 MeV**
Structural	Al	27	100.0	0.23	^{28}Al	1.34E+02	4.64	1.78	2.86
	Fe	54	2.8	2.25	^{55}Fe	-			
		56	91.8	2.59	^{56}Fe	-			
		57	2.1	2.43	^{58}Fe	-			
		58	0.3	1.00	^{59}Fe	3.84E+06	1.57	-	
	Cr	50	4.3	15.40	^{51}Cr	-			
		52	83.8	0.86	^{53}Cr	-			
		53	9.5	18.09	^{54}Cr	-			
		54	2.4	0.41	^{55}Cr	2.10E+02	2.60	0.00	2.60
	Cu	63	69.2	4.47	^{64}Cu	-			
		65	30.8	2.15	^{66}Cu	3.07E+02	2.64	0.00	2.64
	Mg	24	79.0	0.05	^{25}Mg	-			
		25	10.0	0.19	^{26}Mg	-			
		26	11.0	0.19	^{27}Mg	5.73E+02	2.61	0.84	1.77
	Mn	55	100.0	13.27	^{56}Mn	9.28E+03	3.70	Various	0.25, 2.85
Reflector	Be	9	100.0	0.04[a]	^{6}He	8.07E-01	3.50	0.00	3.50
		10	trace	-	^{10}B	4.75E+13	0.55	-	
	Li	7	92.41	0.04	^{8}Li	8.40E-01	16.00	3.03	12.97
Poisons (CE)	B	10	80.1	3842.56	^{7}Li	-			
		11	19.9	0.01	-				
	Eu	151	47.8	9200.73	^{152}Eu	4.22E+08	-		
		153	52.2	358.00	^{154}Eu	2.71E+08	-		
	Nb	93	7.59	1.16	^{94}Nb	6.41E+11	2.04		
	Ta	181	99.99	8250.44	^{182}Ta	9.89E+06	1.81	Various	
Targets (FTT + VXFs)	V	51	100.0	4.92	^{52}V	2.25E+02	3.97	1.434	2.54
	Mo	98	24.4	0.13	^{99}Mo	2.38E+05	1.36	-	
	Se	78	23.8	0.43	^{79}Se	-			
		80	49.6	0.61	^{81}Se	1.11E+03	1.59	-	
	Ni	58	68.1	4.22	^{59}Ni	-			
	Np	Various			Various[b]				Various[b]
	Cm	Various			Various[b]				Various[b]
Moderator	O	16	99.75	0.03	^{16}N	7.13E+00	10.42		4.29, 10.42

[a]The cross-section listed is in the fast region due to the high energy threshold ^{9}Be(n,α) or ^{16}O(n,p) reaction

[b]Np and Cm and products to which they transmute are fissile and produce fission $\overline{\nu}_e$ spectra

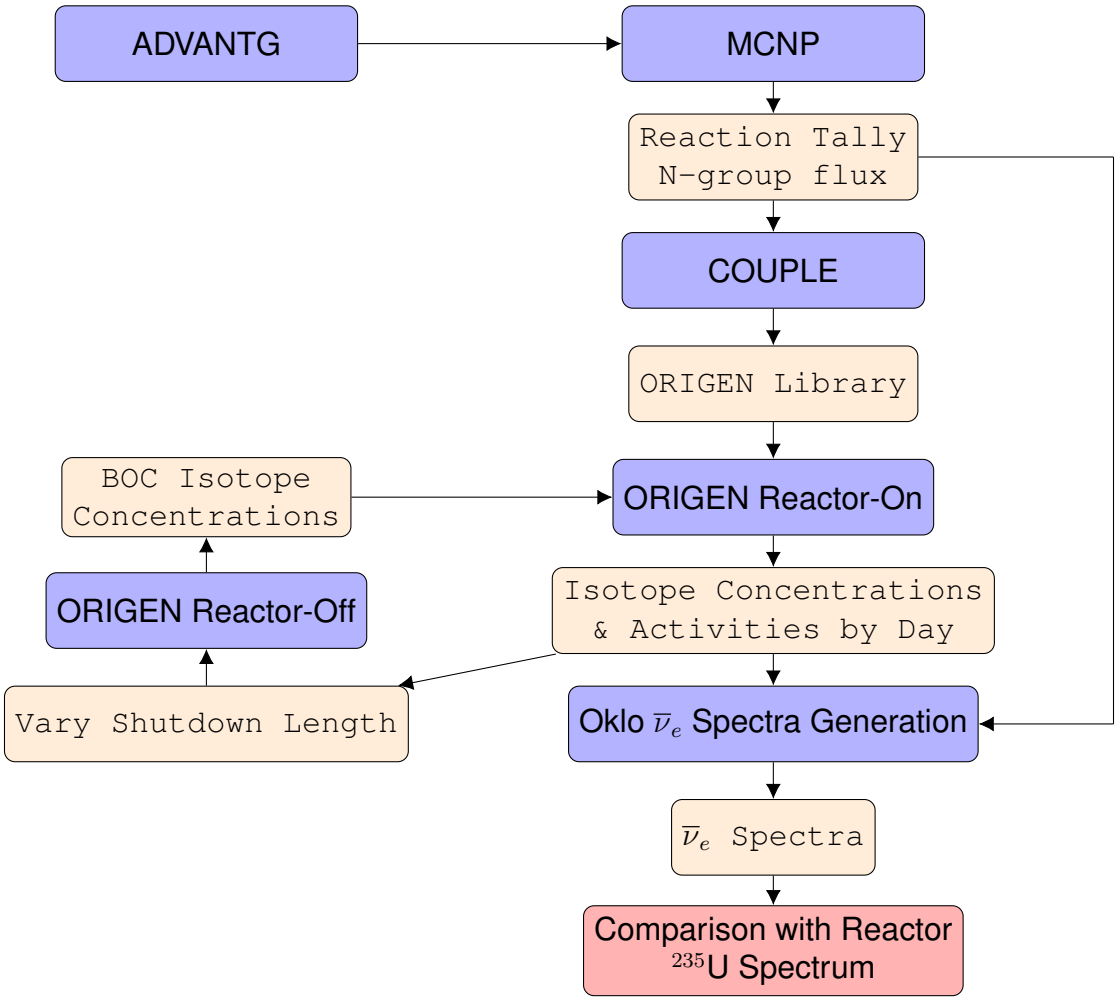

Figure 6.1: Calculation methodology for $\overline{\nu}_e$ candidate spectra generation using MCNP, SCALE modules COUPLE and ORIGEN, and $\overline{\nu}_e$ spectra

recent release SCALE 6.2.3. The flux is calculated in MCNP for each day in the cycle, for days 0 through 25.

The flux is plugged into the SCALE COUPLE module to generate an ORIGEN library. COUPLE generates a binary format data library that calculates weighted multi-group cross-sections that are problem-dependent. COUPLE modifies ORIGEN libraries and updates cross-sections and fission yields to become problem-dependent based on the transport calculation in MCNP. Only the neutron cross-sections are updated. The result is an ORIGEN library for each cell containing a candidate for each day in the cycle.

The ORIGEN library is used for an ORIGEN reactor-on input for each cell. A full cycle input is generated with the library for each day in the cycle. The absolute flux magnitude is used from each day in the cycle using the PNF (Equation 4.4). This flux magnitude is assumed to be cycle-independent, meaning it was only calculated for each day in the representative model.

For certain candidates, the shutdown time needs to be factored in for multi-cycle analysis. The decay time leads to the destruction of isotopes depending on how long of a shutdown is required for HFIR. The most prominent region for this is the beryllium reflector, where the poison concentrations change as a function of decay time.

Finally, the daily- and cycle-dependent rates are plugged into Oklo to generate the $\overline{\nu}_e$ spectra. The probability density function (PDF) of the $\overline{\nu}_e$ spectra for the non-fissile candidates are shown in Figure 6.2. The PDF is analogous to the number of $\overline{\nu}_e$ emitted per unit energy (MeV) as each decay emits one $\overline{\nu}_e$. The only isotopes with an endpoint above 3.5 MeV is ^{8}Li.

The spectra of each candidate is compared to the nearly pure ^{235}U spectra from HFIR. The ratio of $\overline{\nu}_e$ from the candidate versus ^{235}U can be considered an "excess" in that energy range.

$$\frac{\bar{\nu}_{cand}(E)}{\bar{\nu}_{fuel}(E)} = \frac{^{A}_{Z}X(n, capture)}{^{235}U(n, fission)} \frac{N_{\bar{\nu},X}(E)}{N_{\bar{\nu},^{235}U}(E)} \tag{6.7}$$

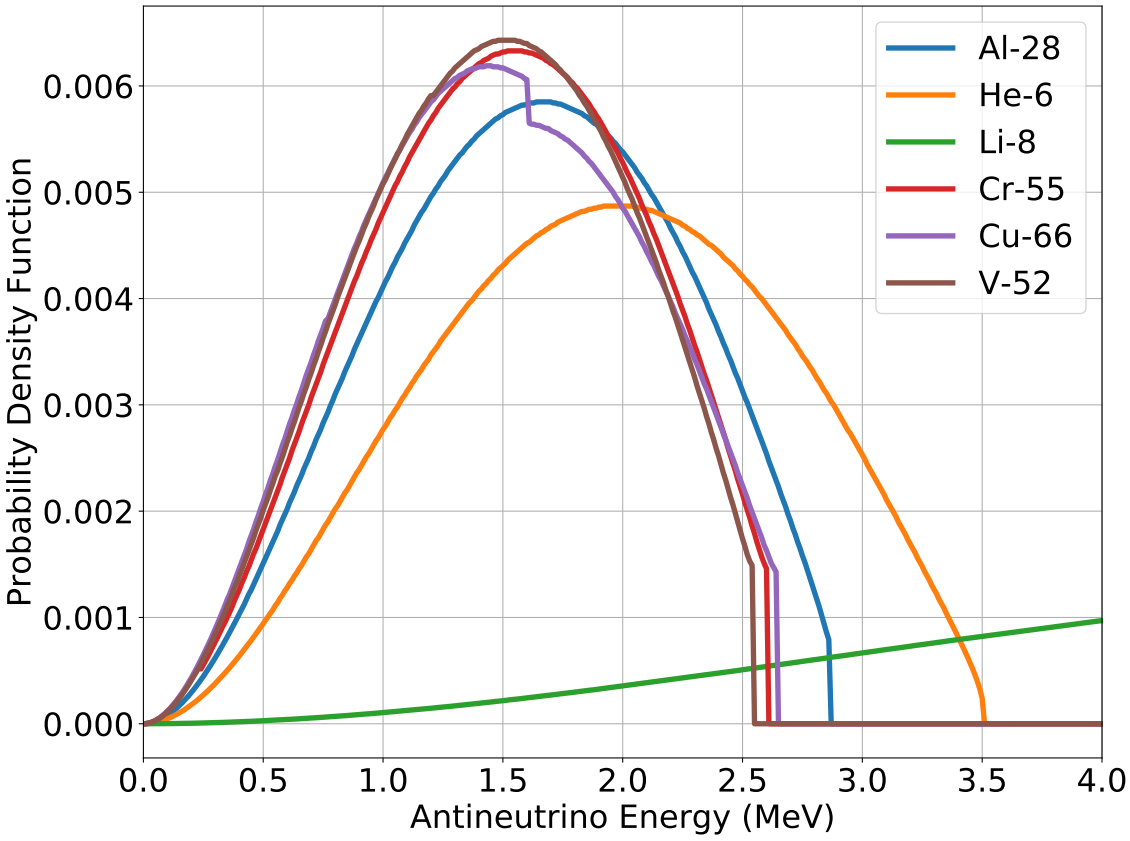

Figure 6.2: Oklo-generated $\overline{\nu}_e$ spectra for candidate isotopes

where $N_{\overline{\nu}}$ is the number of $\overline{\nu}_e$ produced above the IBD threshold per reaction. Because the fission rate is evidently the most frequent neutron-induced transmutation in a reactor and the fact that fission always produces more $\overline{\nu}_e$ than a single β^- decay, both ratios will always be less than one. The result will be a fraction, or excess, of $\overline{\nu}_e$ above threshold produced by the candidate versus those from fission.

6.3 Structural Candidates

The most prominent structural materials in HFIR include aluminum, iron, copper, chromium, and manganese. Aluminum is included in the form of Al-6061, Al-1100, and several others. Aluminum was selected initially in the design of HFIR due to its low fabrication and reprocessing costs [49]. It also has a lower neutronic penalty than other structural materials; the only exception is zirconium which is much more expensive but typically used in commercial reactors. Copper, chromium, and manganese have much lower quantities in the core than aluminum.

6.3.1 Aluminum

Aluminum is the most prominent structural material in HFIR. The natural abundance of aluminum is 100% ^{27}Al. In the FTT region, aluminum makes up dummy targets, target rod rabbit holders (TRRH) in the target positions, and capsule bodies. In the IFE and OFE, it is the largest atomic contributor in the U_3O_8-Al fuel and constitutes most of the filler material, which is the non-fuelled region located within the aluminum cladding [50]. The un-fueled regions of the fuel plates and side walls of the IFE/OFE are also predominately composed of aluminum. It exists in all regions of the control elements, although absorption is dominated by neutron poisons. Some of the reflector and HB tube cells are of relevance, although aluminum reactions are less dominant due to the lower neutron flux in these outer regions.

The reaction of interest for aluminum is ^{27}Al(n,γ)^{28}Al with a β^- transition to ^{28}Si [75].

The transition releases 4.642 MeV and results in an excited state of ^{28}Si at 1.779 MeV; therefore the β^- endpoint energy is 2.864 MeV [75]. The half-life of ^{28}Al is 2.245 $\pm$ 0.002 minutes, therefore it is assumed the ^{28}Al production reaches equilibrium with its production quickly into the cycle.

$$^{27}Al +^{1}_{0} n \rightarrow^{28} Al \tag{6.8}$$

$$^{28}Al \rightarrow^{28} Si* + \beta^- + \bar{\nu}_e + 2.86MeV \tag{6.9}$$

6.3.2 Activity of ^{28}Al

The activity of ^{28}Al is calculated from tallies in MCNP alone according to Equations 4.2-4.3. In the explicit representative HFIR MCNP model, aluminum is contained in 1967 cells and the mass totals to 250 kg. A phantom material for ^{27}Al is created to get its isotopic absorption rate. Again, the ^{28}Al activity is assumed to be equal to the capture rate (i.e. ^{27}Al(n,γ) $\approx A_{Al-28}$). The flux is also tallied in both 44-group and 252-group for input into the SCALE module COUPLE for library creation.

Figure 6.3 shows the results of the ^{28}Al activity for the different methods. The relative error in the MCNP flux and reaction rates was $\leq 0.3\%$. The inclusion of COUPLE and ORIGEN tended to produce different results towards EOC. The MCNP methods grows to a higher EOC value of 5.48×10^{17} Hz while the 44-group ORIGEN case extended to 4.85×10^{17} Hz. However, the average value of the MCNP-predicted ^{28}Al activity is about 2.6% higher than the COUPLE+ORIGEN prediction.

The breakdown of some of the most prominent cells in the MCNP model with aluminum captures are shown in Table 6.2. The reflector container has the highest contribution at over 5% of the total ^{28}Al activity. Some of the other sturctures with the highest contributions include the sidewalls of both the IFE and OFE, white regions of the outer control element, and structures in the flux trap. Aluminum captures in the fuel meat and filler is a

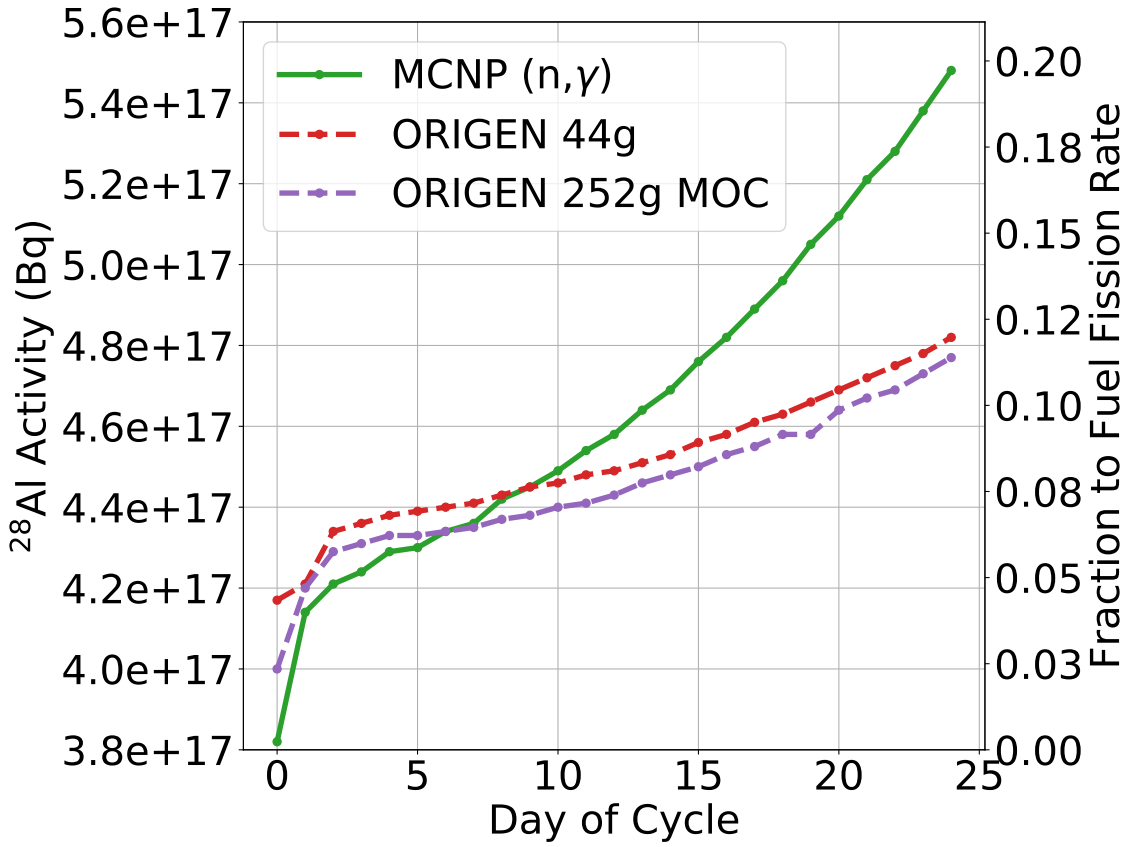

Figure 6.3: ^{28}Al activity for the MCNP-only method and the ORIGEN depletion for two different energy bin schemes. The 252-group used the middle-of-cycle spectra with daily flux magnitudes, therefore displaying a more average value. The values are compared as a ratio to the core average fission rate on the right y-axis.

lower contribution ($\approx 12\%$ total) due to the dominance of the ^{235}U cross-section and the relatively thin filler region.

Table 6.2: Listing of top 20 most-contributing cells in the representative model to the ^{28}Al core activity

Cell	Rate (10^{16} Hz)	Fraction	Cell Description
4120	2.72	5.84%	Beryllium Reflector Container
3111	1.88	4.29%	White region of ICE
50016	1.24	2.96%	OFE Sidewall
2500	1.18	2.89%	OFE Sidewall
4010	1.12	2.83%	Beryllium Reflector Clad
10023	0.95	2.46%	IFE Sidewall
9121	0.88	2.34%	HB Tube
2300	0.82	2.24%	OFE Sidewall
50001	0.82	2.30%	OFE Sidewall
10001	0.71	2.02%	IFE Sidewall
2200	0.69	2.01%	IFE Sidewall
50150	0.68	2.04%	OFE Sidewall
10150	0.55	1.66%	White region of OCE
804	0.54	1.66%	White region of OCE
3511	0.54	1.69%	White region of OCE
3811	0.53	1.70%	White region of OCE
3711	0.53	1.73%	IFE Sidewall
3611	0.52	1.74%	Target basket
1660	0.49	1.64%	HB Tube
9588	0.48	1.63%	Al holder of Pu targets
Total	17.9	47.66%	

The reaction rates can then be converted to $\overline{\nu}_e$ spectra according to Equation 6.7. The excess of $\overline{\nu}_e$ from ^{28}Al versus those from ^{235}U fission according to Oklo predictions are shown in Figure 6.4. The ratio is between 6-8% in the 0.5 MeV above IBD threshold. The ratio drops sharply after this point to 2-3% at EOC due to the energy approaching the β^- endpoint of ^{28}Al. The ratio is largest at the lower energies due to this being near the peak of its spectrum.

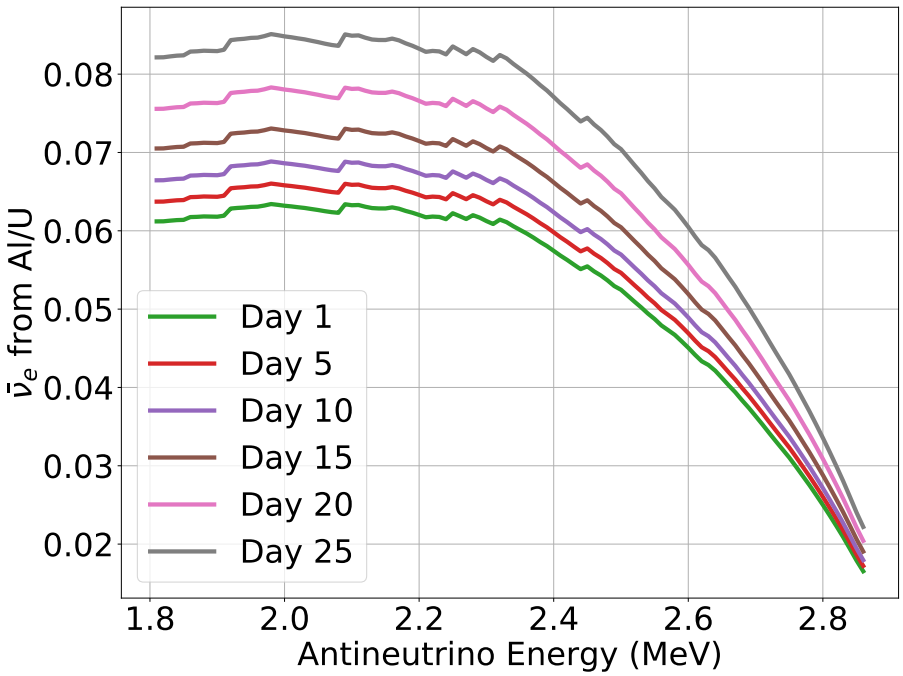

Figure 6.4: Ratio of $\overline{\nu}_e$ from ^{28}Al via ^{27}Al(n,γ) to those from ^{235}U(n,fission) based on the 44-group ORIGEN activities and Oklo spectra

Differences between MCNP and ORIGEN Models

It is clear that there are some difference between the MCNP and ORIGEN generated results for ^{28}Al (Figure 6.3). One of the possibilities is the depletion of aluminum could cause a decrease in the reaction rate. To examine this, the EOC concentrations of ^{27}Al are compared to those from BOC. The results shown in Figure 6.5 are the EOC/BOC ratios. The closer to unity the value, the less the fractional depletion of the cell. Almost all cells depleted less than 0.2%. The main exceptions are the IFE and OFE filler and clad material. The IFE clad and filler cells deplete between 2-6% while the same for the OFE range from 2-10%. While these values are higher than expected, the IFE and OFE are replaced every cycle. Additionally, the clad and filler cells have some of the lowest contributions percentage-wise to the overall ^{28}Al activity. Therefore the depletion of these from cycle to cycle should not have much of an impact on the ^{27}Al capture rate into ^{28}Al activity.

Next, the cross-sections for each method are compared. In COUPLE, it calculates and

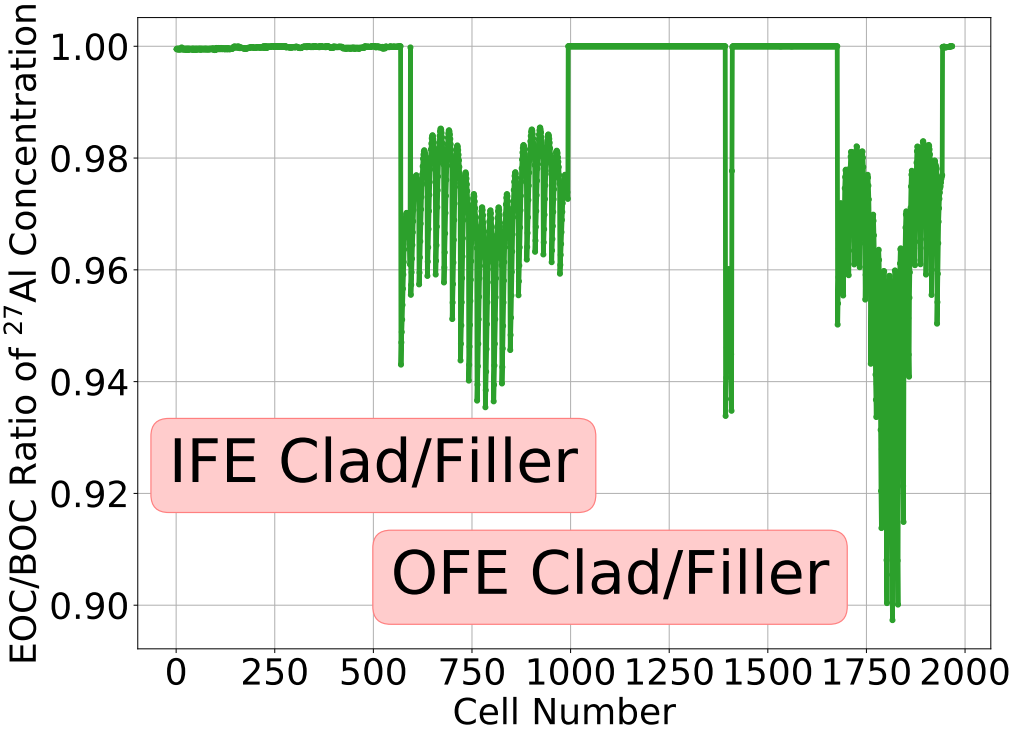

Figure 6.5: EOC/BOC concentration of ^{27}Al

updates the 1-group cross-sections based on the input flux when generating an ORIGEN library. In MCNP, the one-group cross-section can be calculated from the F4 and FM4 tallies (similar to Equation 4.3):

$$\sigma_\gamma = \frac{\int dE\phi(E)\sigma\gamma(E)}{\int dE\phi(E)} = \frac{\langle\phi\sigma\rangle}{\langle\phi\rangle} = \frac{F4\ FM4_\gamma}{F4} \tag{6.10}$$

Table 6.3 shows the calculated 1-group cross-section from ^{27}Al for the reflector container, the cell with the largest contribution to the ^{28}Al activity. The higher cross-section is calculated with MCNP, about 10% higher than that those calculated with COUPLE using either the 44-group or 252-group structure. This difference is consistent for almost all ^{27}Al-bearing cells, displaying calculation differences that are independent of cell. The relatively large difference in these cross-sections can help explain the difference in increases of ^{28}Al activity that is displayed in Figure 6.3.

Table 6.3: One-group cross-section for ^{27}Al(n,γ) for three different methods calculated for the reflector container at MOC

Method	σ_γ (barns)
MCNP	0.186
COUPLE 44g	0.169
COUPLE 252g	0.169

Because the MCNP and COUPLE cross-sections disagree for the same flux spectrum, the available cross-sections in the databases are compared. Table 6.4 shows the ^{27}Al thermal capture cross-section retrieved from ENDF/B-VII.1 and JEFF-3.3 alongside that from the 252-group activation library available in SCALE. That from the 252-group library is 9.2% higher than either un-collapsed library. This excess is likely the cause for the different reaction rates calculated using MCNP and MCNP with COUPLE and ORIGEN.

Table 6.4: Thermal (0.0253 eV) neutron capture cross section for ^{27}Al for the ENDF/B-VII.1 and JEFF-3.3 databases and JEFF 252-group activation library in SCALE

Case	σ_γ	Ratio to ENDF/B-VII.1
ENDF/B-VII.1	0.233463	1.000
JEFF-3.3	0.233463	1.000
JEFF-252g (SCALE)	0.255036	1.092

Comparison of Aluminum Activation with NBSR

It was discovered that the $\overline{\nu}_e$ contribution from ^{27}Al activation in HFIR has a significant contribution. HFIR shares a similar design and missions to other high-performance research reactors around the world. To check the aluminum results, a similar reactor is chosen to calculate and compare the activation rates.

One such similar reactor is the National Bureau of Standards Reactor (NBSR) at the National Institute of Standards and Technology (NIST). The NBSR has similar fuel design to HFIR [76]. The NBSR is a similar user facility that is also dedicated to neutron scattering experiments, including a cold source. The fuel is a 93% enriched U_3O_8 aluminum powder dispersion fuel in involute plate form. As opposed to having two concentric fuel elements,

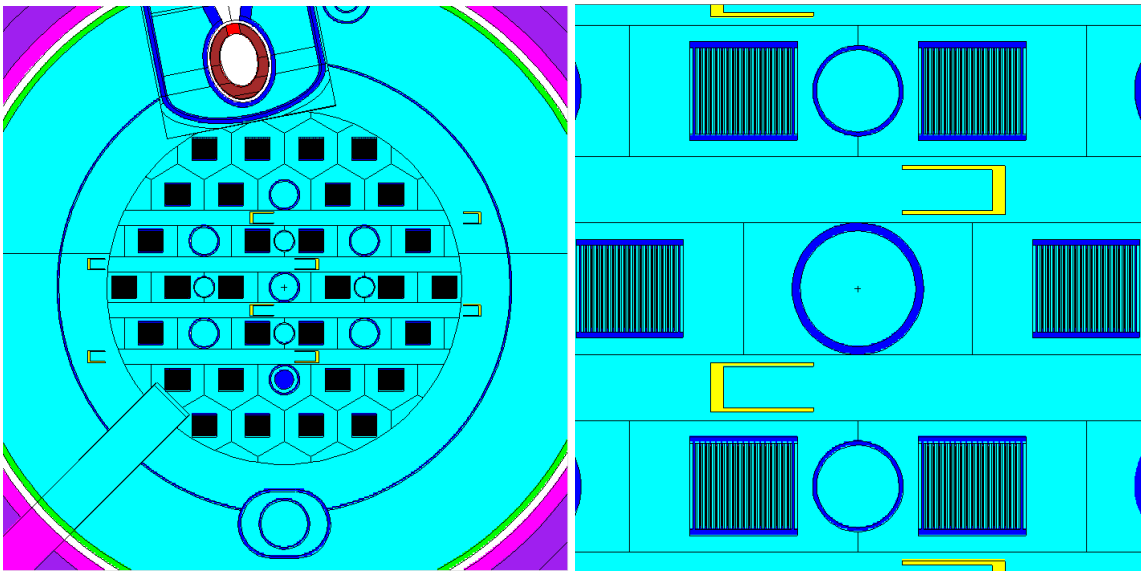

Figure 6.6: Aerial view of the NBSR core model (left) with a close-up of the assemblies and fuel plates (right)

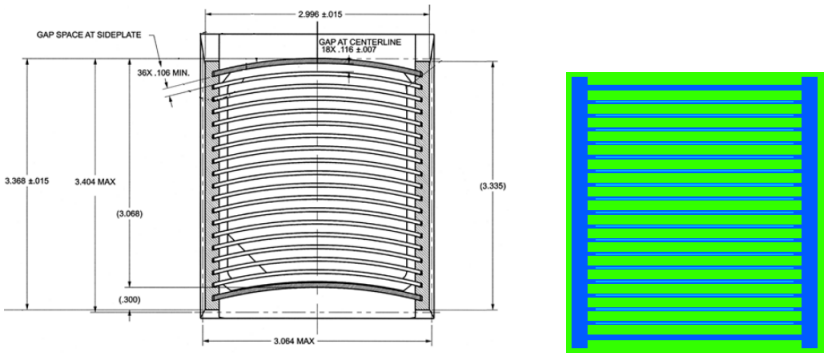

Figure 6.7: Top-down view of NBSR fuel element with 17 fuel plates (left) and MCNP representation (right)

the NBSR has 34 plates in assemblies split into upper and lower regions.

The NBSR also has a well-benchmarked model of its core in MCNP [77]. This model was made available for both BOC and EOC. Figure 6.6 shows the NBSR reactor model and the representation of its assemblies and fuel plates. It can be seen that the NBSR model also represents structures and facilities far from the reactor core, including sample irradiation locations, beam tubes, and thermal shielding. The major difference is that the plates are not modeled with curvature. Figure 6.7 shows a top-down drawing of an NBSR elements and its representation in MCNP.

Table 6.5 compares the nominal parameters between HFIR and NBSR. Significant differences include the moderator, core size, operating power, cycle length, and configuration of the fuel elements/assemblies. The HFIR fuel is less spatially distributed. It contains two concentric fuel regions in which each element's separation is nearly 0.1 cm. While the spacing of fuel plates in the NBSR is similar, the fuel elements themselves are spread apart more than two orders of magnitude further apart than those in HFIR. As a consequence of this, the NBSR is not able to achieve a higher thermal flux despite similar loading of ^{235}U.

Table 6.5: HFIR and NBSR nominal reactor parameters

	HFIR	**NBSR**
Fuel		
Composition	U_3O_8-Al	U_3O_8-Al
Enrichment	93%	93%
Plate Thickness (cm)	0.127	0.051
Number of Plates	540	1020
Core ^{235}U Loading (kg)	9.4	10.5
Core		
Diameter (m)	0.432	0.74
Height (m)	0.76	1.12
Power (MWt)	85	20
Cycle Length (days)	24	38.5
Peak Thermal Flux (n/cm^2/s)	2.5e+15	1.5e+14
Moderator	H_2O	D_2O
Reflector	Be	D_2O
Control Element Materials	Eu,Ta,Al	Cd,Al

The same process is used with HFIR to generate the ^{27}Al capture rates in the NBSR. Here, only MCNP is used to generate the reaction rates. The F4 and FM4 tallies are again used for the BOC and EOC models of the NBSR. Table 6.6 shows the reaction rates calculated in MCNP for HFIR and NBSR and their ratio to each core's respective fission rate. The NBSR experiences a much larger ratio to the fission rate, by a factor of 3-4. The NBSR experiences more parasitic absorption by aluminum than in HFIR. Studies of the neutron

Table 6.6: Comparison of ^{27}Al activation rates for HFIR and NBSR at BOC and EOC

Reactor	Time	^{27}Al(n,γ) (Hz)	Ratio to ^{235}U(n,f) (%)
HFIR	BOC	4.14×10^{17}	15.6
	EOC	5.48×10^{17}	20.6
NBSR	BOC	3.77×10^{17}	60.1
	EOC	3.79×10^{17}	60.4

energy were examined to see if the moderator difference had an impact. The average energy of a neutron causing ^{27}Al capture is only slightly higher for HFIR, 0.04 eV, than it is for NBSR, 0.03 eV. This suggests that the spectral effects from the different moderators is not the main contributor to the factor of 3-4 difference in the reaction rate.

Because the reactors are of similar design, the reactor regions containing aluminum are grouped into rough categories according to their function in the reactor. The fraction of aluminum captures in these regions is calculated relative to the core total rate. The structural components are largest for both reactors. NBSR has a 56% contribution in its structural elements while HFIR is lower at 40%. HFIR has much higher ^{27}Al captures in the beam tube and reflector regions, areas that are further away from the fuel meat than other regions. HFIR also has a much higher contribution in the fuel, while the NBSR has more captures in its filler and clad material. The smaller core and beryllium reflector result in a more spatially varying distribution of ^{28}Al compared to NBSR relative to their own sizes.

Table 6.7: Fractional contribution (%) of aluminum activation rates by category in HFIR and NBSR cores at the beginning of cycle (BOC)

Structural Category	HFIR	NBSR
Core Structural	39.92	56.19
Beam Tube	18.81	9.24
Reflector	17.47	5.67
Control Elements	10.88	13.23
Fuel	7.42	1.96
Fuel Filler/Clad	5.50	13.70

The $\overline{\nu}_e$ spectrum for the NBSR from its fissions and ^{28}Al contributions are calculated. Figure 6.8 shows the ratio of $\overline{\nu}_e$ from ^{28}Al to those from ^{235}U fission. The amount from the

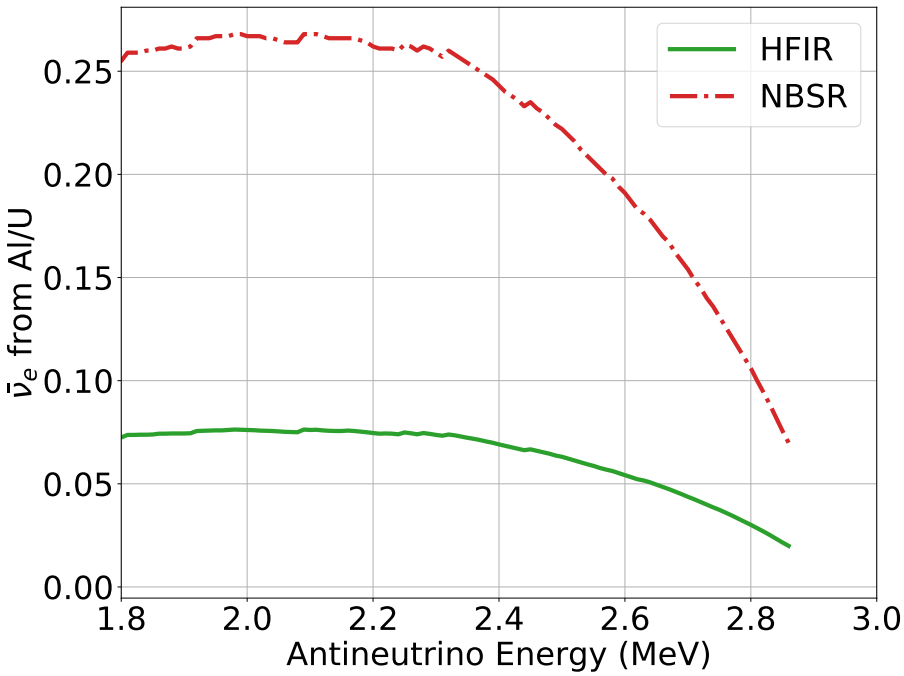

Figure 6.8: Ratio of $\overline{\nu}_e$ from aluminum activation to those from fission in HFIR and NBSR

NBSR is upwards of 25% in the low energy range. This is a much larger contribution and would give larger uncertainties in a $\overline{\nu}_e$ measurement at NBSR.

The key takeaway from this section is that HFIR and NBSR have similar fuel design and missions, yet their reaction rate ratios of ^{27}Al(n,γ)/^{235}U(n,fission) are vastly different. The main differences are attributed to the wider spacing of fuel elements, larger core, and harder neutron spectrum in NBSR. The effects of ^{28}Al activation would have been exacerbated if the NBSR was chosen for a PROSPECT-like experiment.

6.3.3 Chromium, Copper, and Manganese

Chromium, copper, and manganese are also structural material candidates. Most of these are included in the steel of the TRRH-bearing capsules, the stainless steel ends, and trace amounts in Al-6061 materials in HB tubes and IFE/OFE sidewalls. For these particular elements, only the EOC reaction rates are calculated in MCNP. Due to the fact that the flux in most core regions is higher at EOC than BOC and that most non-fuel materials

are not depleted significantly from BOC to EOC, these calculations are considered to be a conservative over-estimate of their average $\overline{\nu}_e$ emissions.

^{55}Cr is produced from the (n,γ) reaction on ^{54}Cr, which has the lowest abundance and cross-section of its four naturally-occurring isotopes. The half-life of ^{55}Cr is 3.497 minutes, which is low compared to the cycle length of HFIR. The β^- transition releases 2.603 MeV. Although ^{55}Cr decays to several excited states of ^{55}Mn, the most probable ($> 99.5\%$) is the ground state [78]. The β^- endpoint energy is thus assumed to be 2.603 MeV. Chromium is contained in 221 cells of the model, totalling 16 grams. The EOC ^{55}Cr production rate is found to be 1.6×10^{13} Hz, which is lower than the fission rate by a factor of 10^5.

^{66}Cu is produced from the (n,γ) reaction on ^{65}Cu, which has the lower abundance and cross-section of its two naturally-occurring isotopes. The half-life of ^{66}Cu is 5.120 minutes, which is again low compared to the cycle length. The β^- transition releases 2.640 MeV. The only transition to the ground state of ^{66}Zn, the only transition that has a β^- endpoint energy above IBD threshold, occurs approximately 90.77% of the time [79]. Copper is contained in 869 cells of the model, totalling 161 grams. The EOC ^{66}Cu production rate is 1.13×10^{15} Hz. This is approximately 0.04% of the fission rate. This results in a peak excess ratio in any energy bin of no more than 0.02%.

^{27}Mn is produced from the (n,γ) reaction on ^{55}Mn, which is the sole naturally-occurring isotope. The half-life of ^{27}Mn is 2.578 hours, relatively low compared to the cycle length. The β^- transition releases 3.695 MeV. The main transition of interest from ^{27}Mn to ^{56}Fe is to the 0.846 MeV excited state, which occurs 56.6% of the time [80]. The β^- endpoint energy for this transition is therefore 2.849 MeV. Manganese is present in 226 cells of the model, totalling 109 grams. The EOC ^{27}Mn production rate is 5.16×10^{15} Hz.

In summary, the copper, chromium, and manganese isotopes of interest result in EOC activities listed in Table 6.8. The ^{55}Cr activity is too small compared to the fission rate. The ^{66}Cu and ^{27}Mn have activities on the same order of magnitude at 10^3 less than the fision rate. These both result in $\overline{\nu}_e$ contributions that are negligible compared to those from

Table 6.8: EOC activities of non-aluminum structural products

Isotope	EOC Activity (Bq)
^{55}Cr	1.60×10^{13}
^{66}Cu	1.13×10^{15}
^{27}Mn	5.16×10^{15}

fission and even those from ^{28}Al. Therefore these three structural isotopes are no longer considered as $\overline{\nu}_e$ candidates for HFIR.

6.4 Beryllium Reflector

The primary purpose of the beryllium reflector is to moderate neutrons to thermal energies and reflect them back into the core to maintain criticality of the reactor. This region also contains the many experimental facilities at HFIR, such as the horizontal beam tubes and vertical experiment facilities (VXF). The reflector also contains some coolant holes to allow for sufficient cooling of experiments.

The beryllium reflector is split up into three regions, the removable (RB), semi-permanent (SPB), and permanent (PB). The RB is replaced approximately every few years (83,700 MWd) while the SPB and PB are replaced after more than one decade (167,400 and 279,000 MWd, respectively). All regions, when fresh, contain $> 99\%$ atomically ^{9}Be. HFIR is expected to have a long outage in the mid-2020s to replace the PB. The reflector regions extend axially an extra two inches on the top and bottom of the fuel meat region. The flux in many beryllium reflector regions increases as the the control elements are gradually withdrawn throughout the cycle.

The dominant reaction in ^{9}Be for all neutron energies is elastic scattering, as shown in Figure 6.9. The (n,γ) reaction follows the 1/v behavior, but its cross-section is approximately three orders of magnitude less at 0.025 eV. In the fast region, the (n,2n) and (n,α) threshold reactions are between 1-2 orders of magnitude less than that for scattering at 0.0253 eV. These two fast-region reactions produce two beta-decaying products of interest for antineutrino generation as well as gaseous products and neutron poisons that are im-

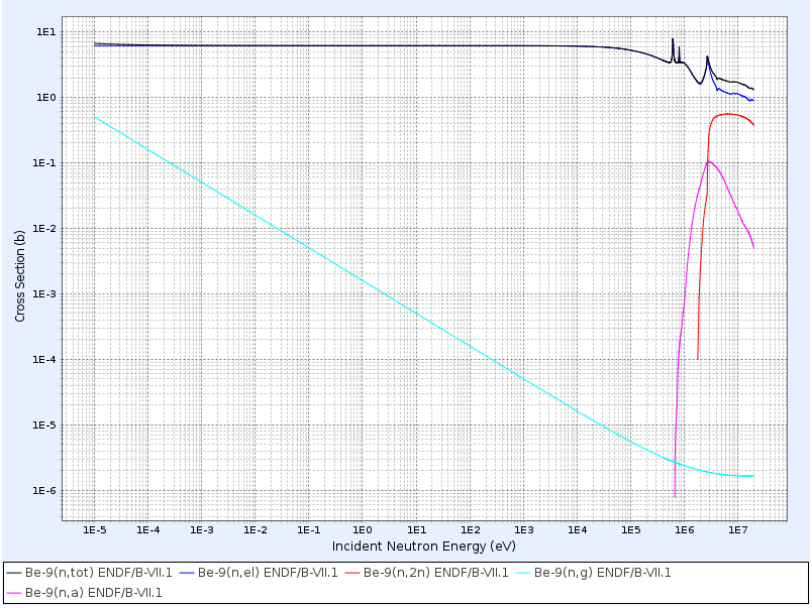

Figure 6.9: Cross-sections of ^{9}Be

portant for HFIR safety and performance. Figure 6.10 shows the transmutation chain and relevant isotopes of interest.

The first product of interest is ^{6}He, which is a short-lived gaseous product formed directly from the (n,α) reaction on ^{9}Be. It has a half life of 0.81 seconds and decays to the ground state of ^{6}Li. This transition releases 3.507 MeV of energy, which is also the β^{-} endpoint energy [81]. Its short half-life results in its complete decay just seconds after the reactor shuts down. Therefore, it would only contribute to the antineutrino signal while the reactor is on.

$$^{9}Be +^{1}_{0} n + 0.597keV \rightarrow^{4} He +^{6} He \tag{6.11}$$

$$^{6}He \rightarrow^{6} Li + \beta^{-} + \bar{\nu}_{e} + 3.51MeV \tag{6.12}$$

The second product of interest in ^{8}Li, which has a half-life of 0.84 seconds, similar to that of ^{6}He. Its decay releases 16.004 MeV, resulting in a 3.03 MeV excited state of ^{8}Be, which quickly decays into two α particles. Therefore the β^{-} endpoint of the ^{8}Li is

approximately 12.97 MeV. This is a high endpoint which results in a harder spectrum of $\overline{\nu}_e$ compared to that of fission.

$$^{7}Li +^{1}_{0} n \rightarrow^{8} Li \tag{6.13}$$

$$^{8}Li \rightarrow^{8} Be* + \beta^{-} + \bar{\nu}_e + 12.97MeV \tag{6.14}$$

The precursor of ^{6}He does not change much from cycle to cycle, i.e. the beryllium does not deplete significantly. ^{8}Li is produced by two subsequent neutron captures on ^{6}Li, the daughter of the ^{6}He β^{-} decay. The ^{6}Li concentration in the reflector regions builds up over the first few cycles of a fresh reflector region [82, 83].

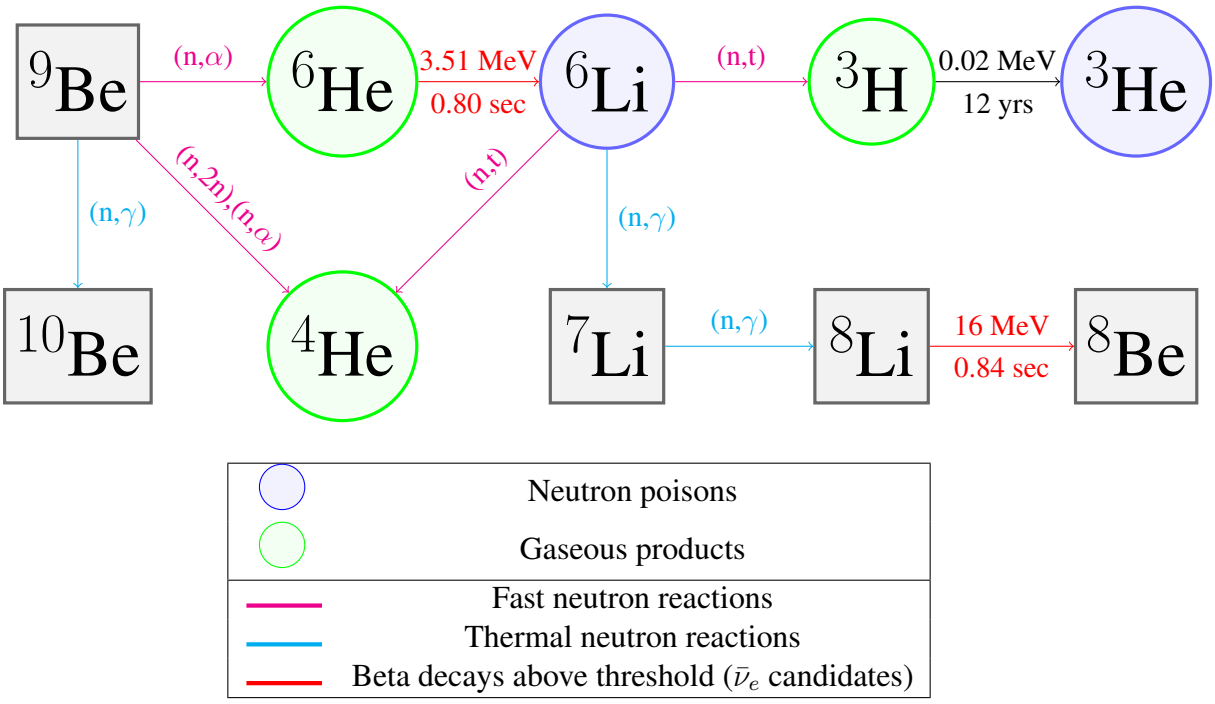

Figure 6.10: Isotopes and reactions in the beryllium reflector

6.4.1 Multi-Cycle Model

The approach to generating activities of ^{6}He and ^{8}Li involved the generation of flux using neutron transport in MCNP followed by depletion in ORIGEN/SCALE, as shown in Figure

6.1. The multi-cycle model is necessary to account for the buildup of neutron poisons with increasing irradiation of a fresh reflector. The effect of this will be discussed later.

The MCNP model has an updated discretization of the beryllium reflector regions compared to the representative model. The discretization contains 17 radial regions and 21 axial regions (357 total), shown in Tables 6.9-6.10. In the RB and SPB regions, the model includes the water gaps in between the different regions. Therefore the inner radius of those regions does not equal the outer radius of the previous region.

Table 6.9: Radial discretization of beryllium reflector regions

Region	Number	Outer R (cm)	Inner R (cm)
RB	1	25.1155	24.1211
	2	27.3202	25.1760
	3	30.1198	27.3710
SPB	4	33.3077	30.3327
PB	5	34.2875	33.3375
	6	35.2875	34.2875
	7	36.3375	35.2875
	8	37.4375	36.3375
	9	38.6375	37.4375
	10	39.9375	38.6375
	11	41.3875	39.9375
	12	42.9875	41.3875
	13	44.7875	42.9875
	14	46.7875	44.7875
	15	49.0875	46.7875
	16	51.6875	49.0875
	17	54.61	51.6875

The preferred energy grouping for neutron activation applications in the current SCALE 6.2 release is 252-group structure, however the 44-group has been used in the past for activation problems. The two energy-binning groups are compared to determine which may be more viable. The 252-group structure is preferable but more challenging to obtain the necessary statistics in each group. Figure 6.11 shows the comparison of flux for the innermost RB cell (40211) at the midplane with the 44-group and 252-group Be(n,α) cross-section obtained from SCALE libraries [59]. Because neither method is evidently superior

Table 6.10: Axial discretization of beryllium reflector regions

Segment Number	Top (cm)	Bottom (cm)
1	30.48	27.5
2	27.5	24.5
3	24.5	21.5
4	21.5	18.5
5	18.5	15.5
6	15.5	12.5
7	12.5	9.5
8	9.5	6.5
9	6.5	3.5
10	3.5	0.5
11 (midplane)	0.5	-0.5
12	-0.5	-3.5
13	-3.5	-6.5
14	-6.5	-9.5
15	-9.5	-12.5
16	-12.5	-15.5
17	-15.5	-18.5
18	-18.5	-21.5
19	-21.5	-24.5
20	-24.5	-27.5
21	-27.5	-30.48

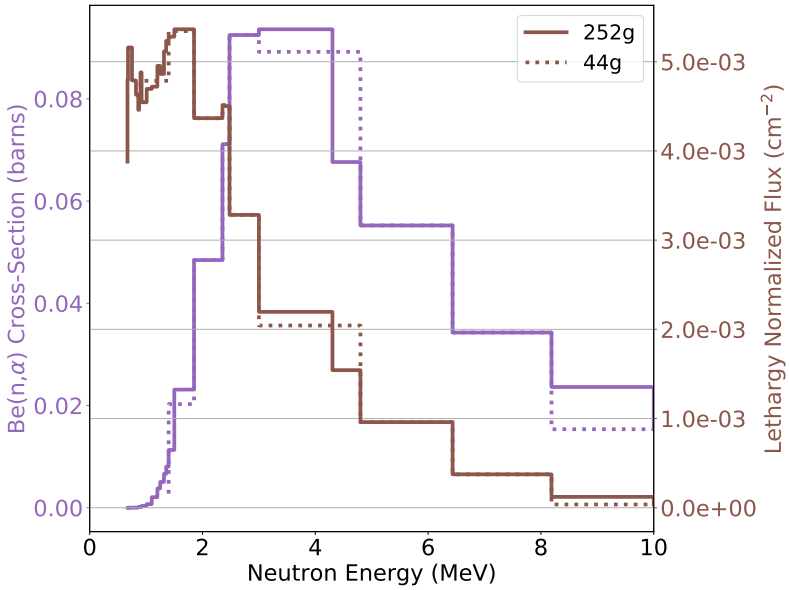

Figure 6.11: Flux at MOC for the innermost RB cell at the midplane compared with the 44-g and 252-g cross-section for Be(n,α) in SCALE libraries [59]

to the other, the 44-group method is primarily pursued due to the higher statistics gained in the lower energy groups.

The process outlined in Figure 6.1 is used to calculate concentrations of isotopes in the beryllium reflector. The 44-group flux is calculated in MCNP for all 357 regions for each day in a representative cycle. The group fluxes and magnitudes from proper normalization (Equation 4.4) are used for each region for each day in the cycle. An assumption is made that the neutron flux spectrum and magnitude changes negligibly with the buildup of poisons in the reflector. Since the concentration of the ^{6}Li and ^{3}He is relatively small compared to that of beryllium, this assumption is believed to be justified. The HFIR cycle is assumed to be 25 days, followed by a 25 day shutdown (the effect of this will be discussed later). This pattern is repeated for at least 10 cycles.

Figure 6.12 shows the calculated 1-group cross-sections for the ^{6}He production from the Be(n,α) reaction. These can be used to calculate the ^{6}He production rate more easily in the future. It can be seen that the cross-section is the highest in the inner regions of the reflector and decreases with each successive radial region due to the softening of the

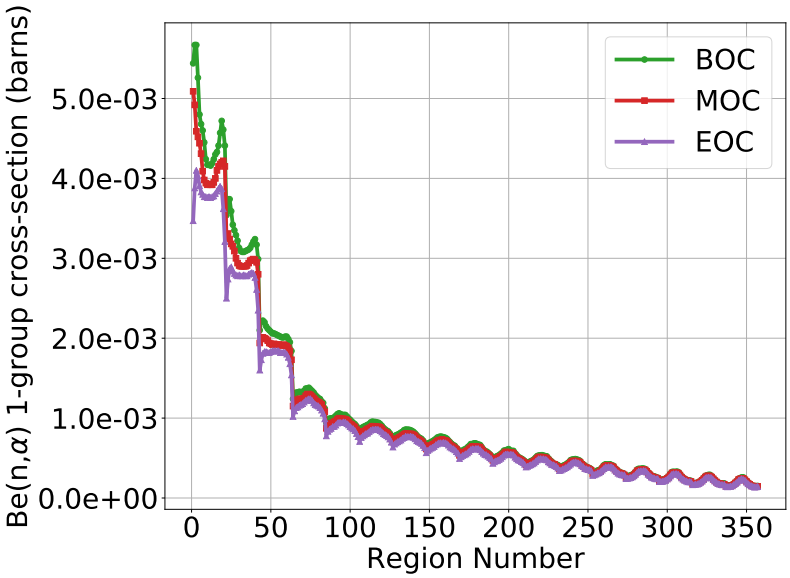

Figure 6.12: ORIGEN-calculated 1-group Be(n,γ) cross-section for each region of the reflector using a 44-group structure at middle of cycle. The region number proceeds from the top- and innermost-cell, moving downward first and then outward.

Table 6.11: Fraction of ^{9}Be(n,α) and ^{6}He activity by region of the reflector

Region	Fraction (%)
RB	69.2
SPB	11.0
PB	19.2

spectrum with increasing radius. It also shows a higher cross-section in the higher regions of the RB than their axial counterparts at the bottom of the RB.

6.4.2 Helium-6

^{6}He is produced directly from the (n,α) reaction on ^{9}Be. It is the precursor reaction to the production of both neutron poisons. The half-life of ^{6}He is 0.806 seconds. The released and β^{-} endpoint energy are both 3.507 MeV as all ^{6}He decays to the ground state of ^{6}Li [81]. The ^{9}Be(n,α) rate during the cycle in the entire reflector ranges from 3.80 to 4.05×10^{15} Hz, shown in Figure 6.13. This increase is largely driven by the control rod withdrawal because more fast neutrons traverse to the axial ends of the reflector and induce the (n,α) reaction.

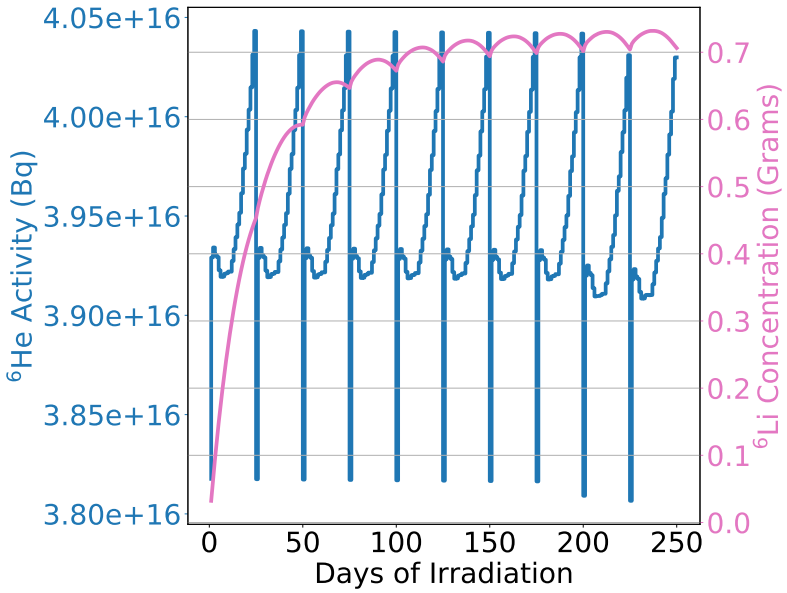

Figure 6.13: Activity of ^{6}He for first 10 cycles of irradiation if all regions are assumed fresh, with buildup of ^{6}Li shown to negligibly impact the rate

The distribution by reflector region is shown in Table 6.11, with the RB contributing almost 70% of the total rate due to the radial drop-off of fast flux further into the reflector. This rate is found to be relatively cycle independent. All ^{6}He decays quickly upon shutdown and the ^{9}Be does not deplete significantly. The buildup of ^{6}Li if all regions are assumed fresh decreases to total core Be(n,α) rate by less than 1%.

The ^{6}He activity can be translated to $\overline{\nu}_e$ spectra assuming the production rate equals its activity. The ratio of $\overline{\nu}_e$ from ^{6}He to those from fission is shown in Figure 6.14. The ratio peaks around 0.75% around 2.5 MeV. Similar to the spectrum from ^{28}Al, the spectrum falls off sharply as the energy approaches the β^- endpoint energy.

6.4.3 Lithium-8

The ^{8}Li contribution is found to vary as a function of time. While the ^{6}Li reaches equilibrium as a function of irradiation time, the ^{7}Li does not; it continues to climb from with increased exposure. Therefore the multi-cycle model is increased from 10 cycles to 50 cycles. This calculation is conservative due to the RB being replaced approximately every

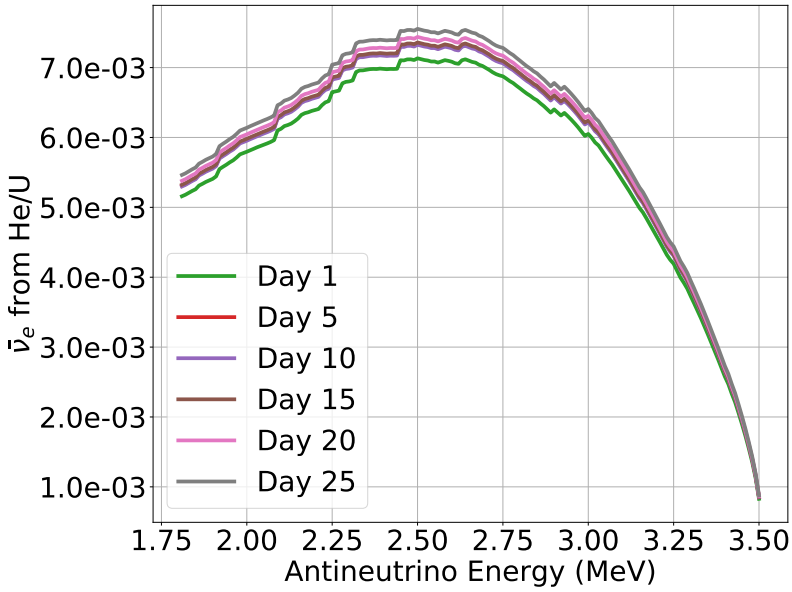

Figure 6.14: Ratio of $\overline{\nu}_e$ from ^{6}He via ^{9}Be(n,α) to those from ^{235}U(n,fission) based on the 44-group ORIGEN activities and Oklo spectra

40 cycles instead of 50. Figure 6.15 shows the activity of ^{8}Li with irradiation time in the reflector region. Three cases are considered due to the replacement frequency of the reflector regions: only the RB is fresh, the RB and SPB are fresh, and all regions are fresh. The regions that are not fresh have reached their equilibrium concentration of ^{6}Li in all radial and axial regions. All cases converge toward a value of approximately 4×10^{12} Hz. This value is nearly 10^{6} lower than the fission rate. The buildup of ^{6}Li decreases the ^{6}He activity by approximately 1%, which shows its buildup has a relatively negligible on the ^{6}He activity.

The $\overline{\nu}_e$ spectra and magnitude for ^{8}Li is shown in Figure 6.16. The data is compared to the Oklo spectra for ^{235}U because there are not theoretical predictions for $\overline{\nu}_e$ above 8 MeV with the Huber data. The ^{8}Li has little significance up until the high energy range. Its contribution above 10 MeV is as high as 20-30%, however few $\overline{\nu}_e$'s are detected above that energy. Because of its low magnitude and low rate rate compared to ^{235}U fission, ^{8}Li can be safely ignored as a candidate due to the natural buildup in the reflector. However, the intentional loading of lithium to generate ^{8}Li $\overline{\nu}_e$'s is discussed in Section 8.3.

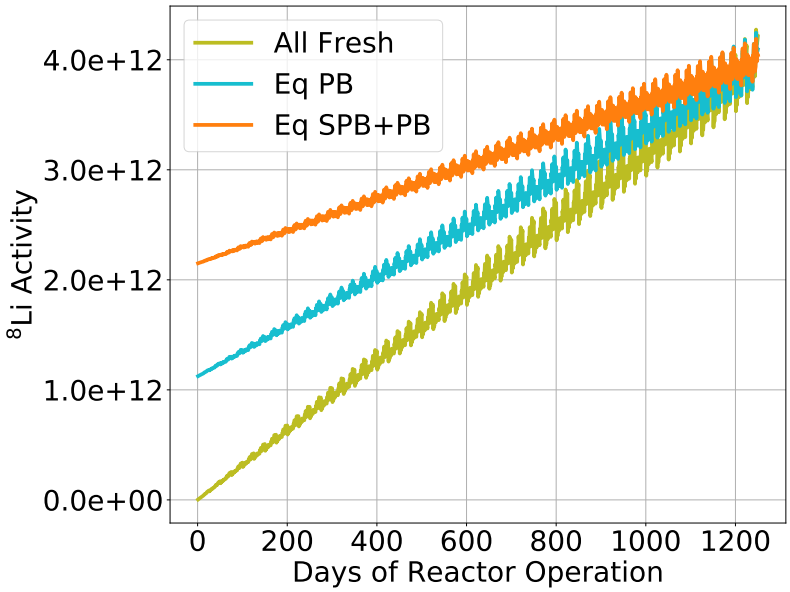

Figure 6.15: Activity of ^{8}Li as a function of irradiation time for 50 cycles with assumptions of no ^{6}Li in all reflector regions (fresh), ^{6}Li having reached equilibrium in the PB, and ^{6}Li having reached equilibrium in the SPB and PB

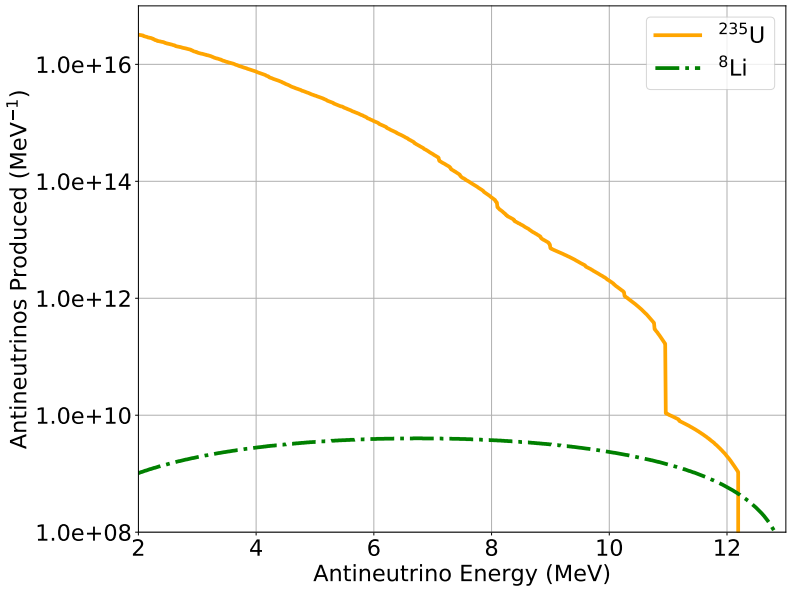

Figure 6.16: Cycle-average $\overline{\nu}_e$ emissions shown for the Oklo-predicted ^{235}U and ^{8}Li contributions

6.4.4 Poison Concentrations and Shutdown Length

It has been discussed that the two isotopes of interest in the reflector for $\overline{\nu}_e$ contributions are ^{6}He and ^{8}Li. The effect of ^{6}He is significant and is relatively independent of shutdown length. The ^{8}Li contribution is negligible due to its low order of magnitude. In either case, the reactions of interest do produce neutron poisons, as shown in Figure 6.10. While this is not discussed here due to the lack of impact on $\overline{\nu}_e$ production, the impact of shutdown length on the poison concentrations, primarily ^{3}He, is discussed in Appendix B. Buildup of poison concentrations have an impact on reactivity penalty of an irradiated reflector, while gaseous buildup leads to increased stresses and reduced thermal conductivity. Both of these are important for nuclear safety analysis of HFIR.

6.5 Target Materials

6.5.1 Vanadium

Vanadium is a target material that is primarily irradiated in the FTT region. The representative model [48] contains many vanadium-bearing targets. Many of these targets are not solely composed of vanadium as a target material; the representative model contains many generic homogeneous targets to obtain representative loading of elements. The FTT region also has some vanadium capsules in the PTPs and TRRHs that make up part of its composition. Since PROSPECT has begun taking data, the loading of vanadium in the FTT region has not changed drastically.

The amount of vanadium in the flux trap typically varies between 200 and 300 grams. This number is tracked for reactivity changes associated with changing mass of elements in the FTT for the estimated symmetric critical control element position (ESCCEP) calculation. Table 6.12 shows the gram-loading of vanadium in the flux trap for the previous 5 HFIR cycles; the values range from 228.2 at a minimum to 274.0 at a maximum. The data is obtained from HFIR calculations of the ESCCEP performed prior to each cycle startup

[84].

Table 6.12: Gram loading of vanadium in the flux trap for the previous 5 HFIR cycles

Cycle Number	Vanadium in FTT (grams)	
478	274.0	*Max*
479	260.0	
480	228.2	*Min*
481	248.0	
482	234.3	

^{52}V is produced from the (n,γ) reaction on ^{51}V, which is the main naturally-occurring isotope. The only other naturally-occurring isotope is ^{50}V, which constitutes 0.25% of vanadium in nature and is not a candidate. The cross-section for neutron capture on ^{50}V is approximately an order of magnitude higher than that of ^{51}V. Capture tallies in vanadium materials showed that the ratio of captures in ^{50}V to ^{51}V roughly follows this product of abundance and cross-section, i.e. ^{50}V(n,γ)/^{51}V(n,γ) is approximately 2.5%. Therefore, assuming natural abundance, over 97% of the neutron captures in vanadium still occur in ^{51}V despite the higher cross-section of ^{50}V.

$$^{51}V + ^{1}_{0}\,n \xrightarrow[\sigma_{\gamma,t}]{4.92b} ^{52}V \tag{6.15}$$

$$^{52}V \xrightarrow{3.74min} ^{52}Cr^{*} + \beta^{-} + \bar{\nu}_e + 2.54MeV \tag{6.16}$$

The half-life of ^{52}V is 3.743 minutes, again low compared to the cycle length. The β^- transition releases 3.974 MeV. The main transition is to a 1.434 MeV excited state of ^{52}Cr, the only transition that has a β^- endpoint energy above IBD threshold, occurs approximately 99.2% of the time [85]. The endpoint energy of this transition is 2.540 MeV.

Calculation Process

To calculate approximate $\overline{\nu}_e$ rates from ^{52}V, several loadings of vanadium-bearing generic targets are loaded into several positions in the flux trap; these targets contain vanadium in a similar concentration to that in the V+Ni targets in the representative model [48]. Several cases are created with full-axial vanadium targets loaded into between 1 and 10 FTT positions. The loading in the simulation cases created here have vanadium masses of between 150 and 370 grams, which includes the range of values listed in Table 6.12.

The capture rates of ^{51}V (and ^{50}V) are calculated on a per-gram basis for the various cases at both BOC and EOC. Linear regression is performed for the capture rate of ^{51}V as a function of grams in the FTT region for both BOC and EOC:

$$A_V = aM_V + b \tag{6.17}$$

where $A_V$and M_V are the activity and mass of the vanadium loading in the FTT. Then, a and b are the slope and intercept of the linear fit. The $R^2 > 0.99$ for both the BOC and EOC fits.

The number of grams from the 5 cycles can be used to calculate approximate ^{52}V activities from the linear regression, as shown in Figure 6.17. The rates range from 1.58 to 1.82×10^{16} Hz for the minimum gram loading and from 1.70 to 1.95×10^{16} Hz for the maximum gram loading of the previous 5 cycles at BOC and EOC.

The fractional increase in the spectrum for the lower and upper loadings of vanadium is calculated in the 1.8 - 2.54 MeV range from the two separate linear regressions created from BOC and EOC simulations. The $\overline{\nu}_e$ spectrum increases in that range from 0.26-0.51%. The increase from BOC to EOC can be explained in a similar fashion to that for the ^{28}Al, with the thermal flux increase in most regions of the core and particularly the flux trap. Although depletion of the targets from BOC to EOC is not performed, this is suspected to negligibly change the results.

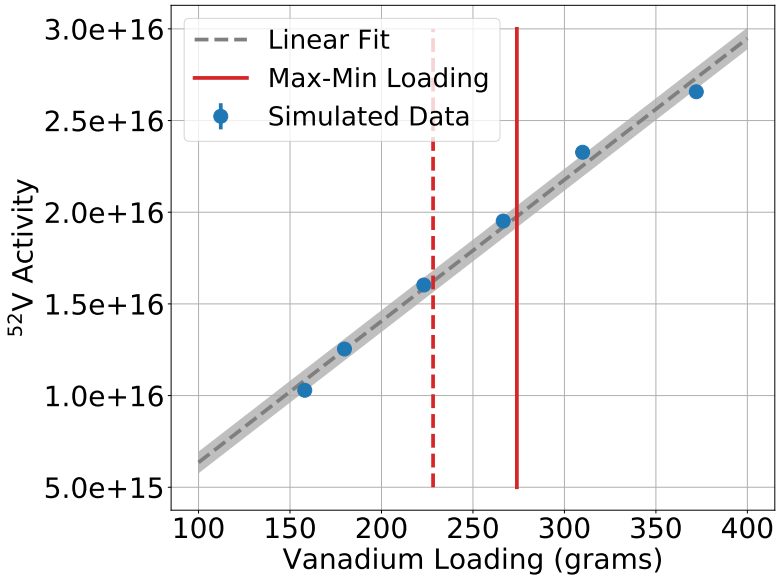

Figure 6.17: Activity of ^{52}V as a function of grams loaded into the core for the six cases. A linear fit of the data with 1σ error is shown with associated error. The red lines show the minimum (dashed) and maximum (solid) loadings of vanadium in the previous five cycles [84].

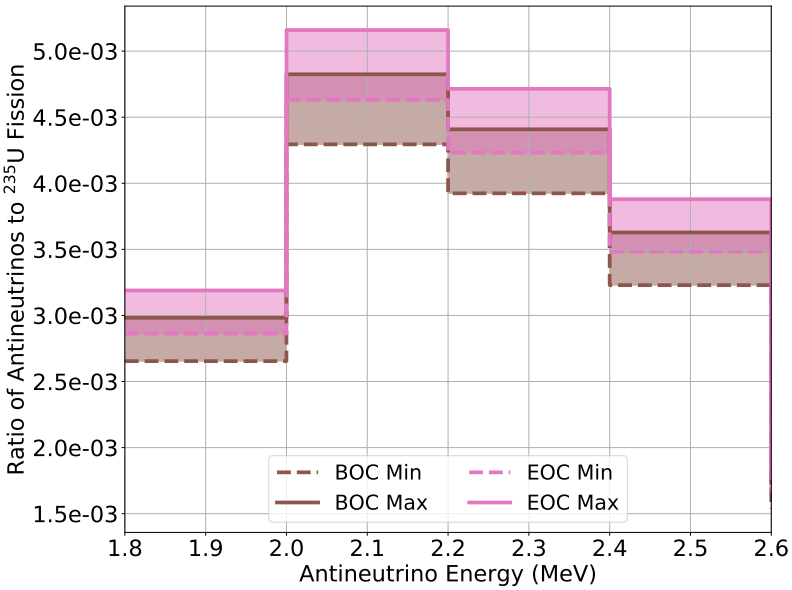

Figure 6.18: Excess $\overline{\nu}_e$ from ^{52}V for the maximum and minimum loading of vanadium in the FTT with actual loadings in previous five HFIR cycles

6.5.2 Curium

Targets made of curium oxide (CmO) have been irradiated in the FTT region to produce ^{252}Cf in many recent cycles. The CmO targets take up the full length of the active fuel region. Although the primary acitinide composition in the targets is curium, they also contain smaller concentrations of plutonium and americium [48].

Calculations of CmO fission and heat generation rates have been performed at HFIR for safety analysis. The cycle-dependent fission rates of the CmO targets is obtained and analyzed. The fission rates in the targets is dominated by the fission of ^{245}Cm and ^{247}Cm, which account for over two thirds of the CmO fission rates. ^{241}Pu and ^{251}Cf also contribute at the 5-12% level each. The fission yield data is not available for ^{247}Cm in ENDF or other databases.

Five CmO targets were in the FTT starting in cycle 479. The same targets were subsequently irradiated during the next 3 cycles (through 482). The fission rate of the total of the five targets is shown in Figure 6.19. The rates decrease with each subsequent cycle, i.e. the fission rate is the highest in cycle 479. The peak of the fission rate is approximately 2×10^{15} Hz near at BOC.

During the first irradiation cycle, the fission fraction is over 80% ^{245}Cm, which drops towards 50% at EOC. The ^{247}Cm fraction increases from 5% to 15%. The ^{241}Pu fraction slowly increases to about 12%. These EOC1 fission fractions remain roughly constant for these three isotopes with the ^{251}Cf fraction building to slowly increasing to 10%. This rounds out the majority of isotopes, with other Cm isotopes having percent-level contributions.

The maximum isotope contributor, ^{245}Cm, has a fission rate of less than a 1×10^{15} Hz. This is less than 0.01% of the fuel fission rate. The relatively small differences between isotopic $\overline{\nu}_e$ emissions combined with this fission rate ratio suggest that irradiation of curium targets will not impact the HFIR $\overline{\nu}_e$ spectrum.

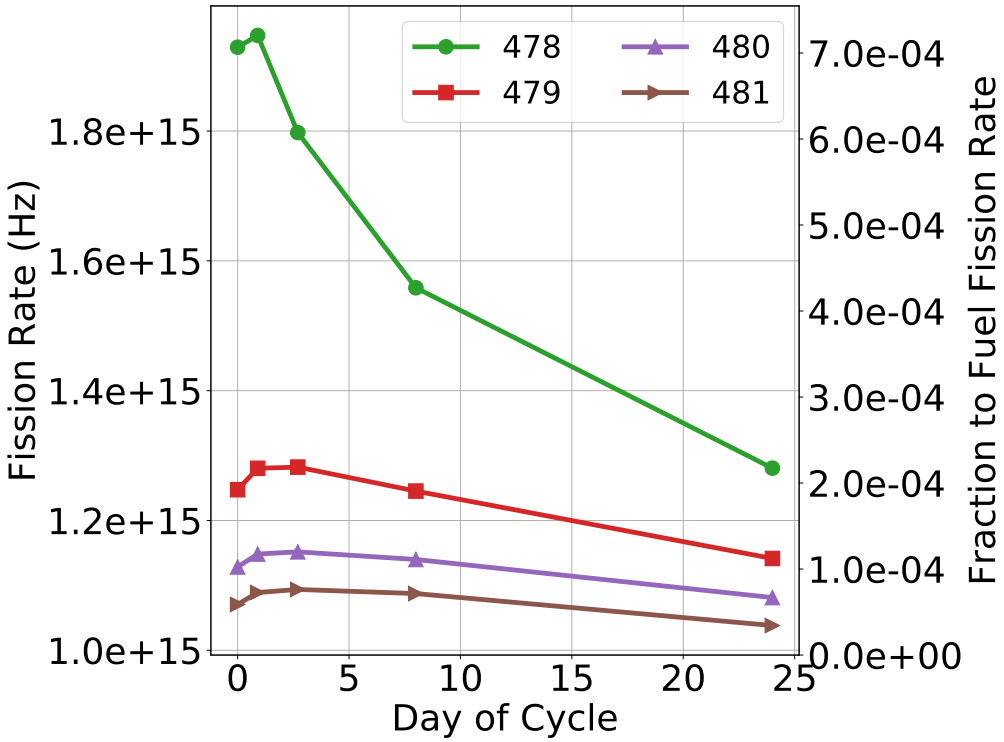

Figure 6.19: Total fission rates in CmO targets and comparison to fuel fission rate

6.5.3 Neptunium/Plutonium

Neptunium oxide (NpO_2) targets have been irradiated in several past cycles to produce for the National Aeronautics and Space Administration (NASA) [53, 52]. The targets are irradiated in the VXFs in the PB nominally for three cycles; the same targets are irradiated in successive cycles. The PROSPECT experiment took data during three NpO_2 irradiation cycles. Nine VXFs were filled with NpO_2 targets starting in Cycle 479 and continued into Cycle 480. Cycle 481 contained zero targets with Np/Pu. Cycle 482 continued with the targets' third and final irradiation cycle to date. This is summarized in Table 6.13.

Previous work has quantified fission and heat generation rates in order to support safety analysis of the NpO_2 targets [86, 87]. These models used the homogenized representation of the fuel, cladding, and coolant as in the representative model [48]. Two VXF positions, VXF-3 and VXF-15, are fully axially filled with an array of NpO_2-Al pellets. These two

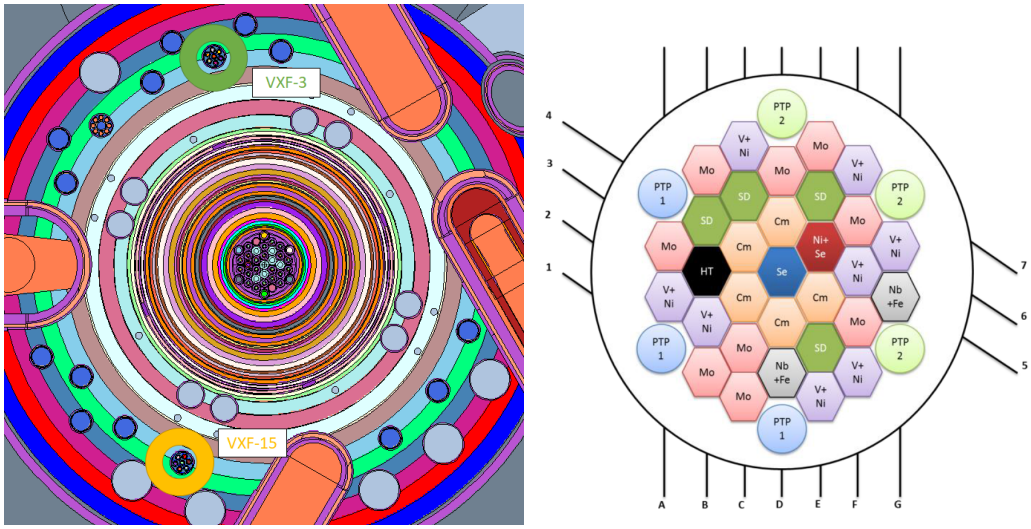

Figure 6.20: Top-down (left) and side (right) view of the HFIR core in the homogenized MCNP model with NpO_2 targets in VXF-3 and VXF-15 [86, 87]

locations are chosen because they typically have the lowest and highest neutron flux level of the inner small VXFs. The representation of the NpO_2 targets from a top and side view are shown in Figure 6.20. The pellets are irradiated for three cycles with a shutdown length of 25 days in between. These previous models are the basis for this calculation.

Table 6.13: Number of VXFs fully-loaded with NpO_2 pellets for the previous 5 cycles arranged by their Nth cycle of irradiation

Cycle	Operation Dates (2018)	Cycle Number				Total
		1	2	3	4	
478	2/20 - 3/16	0	1	2	1	4
479	5/1 - 5/25	9	0	3	0	12
480	6/17 - 7/6	0	9	0	1	10
481	7/24/ - 8/17	0	0	0	0	0
482	9/4 - 9/28	0	0	9	0	9

The fission rates are calculated for the three-cycle irradiations of NpO_2 in the two VXF positions. The fission rates in the NpO_2 targets are dominated by two isotopes: ^{239}Pu and ^{238}Np. Figure 6.21 shows the fission rates in the two targets over three cycles. The ^{238}Np dominates for the first 2 cycles, and ^{239}Pu becomes the dominant contributor in the third cycle.

Figure 6.22 shows the fission rates using an average value of the fission rates in VXF-

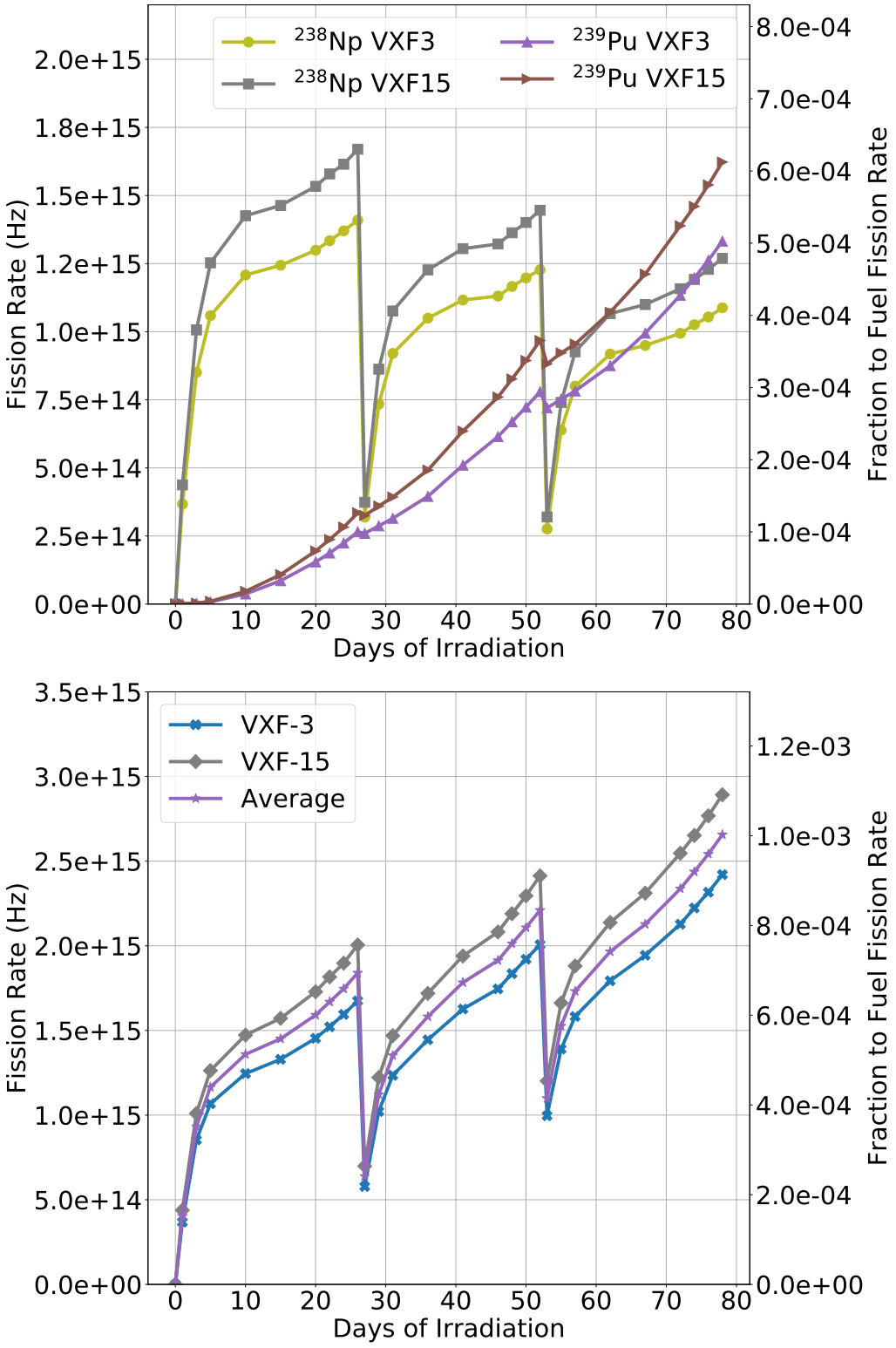

Figure 6.21: Fission rate with irradiation time of fully-loaded NpO_2 targets for 3 cycles in VXF-3 and VXF-15 for ^{238}Np and ^{239}Pu (top) and both combined (bottom)

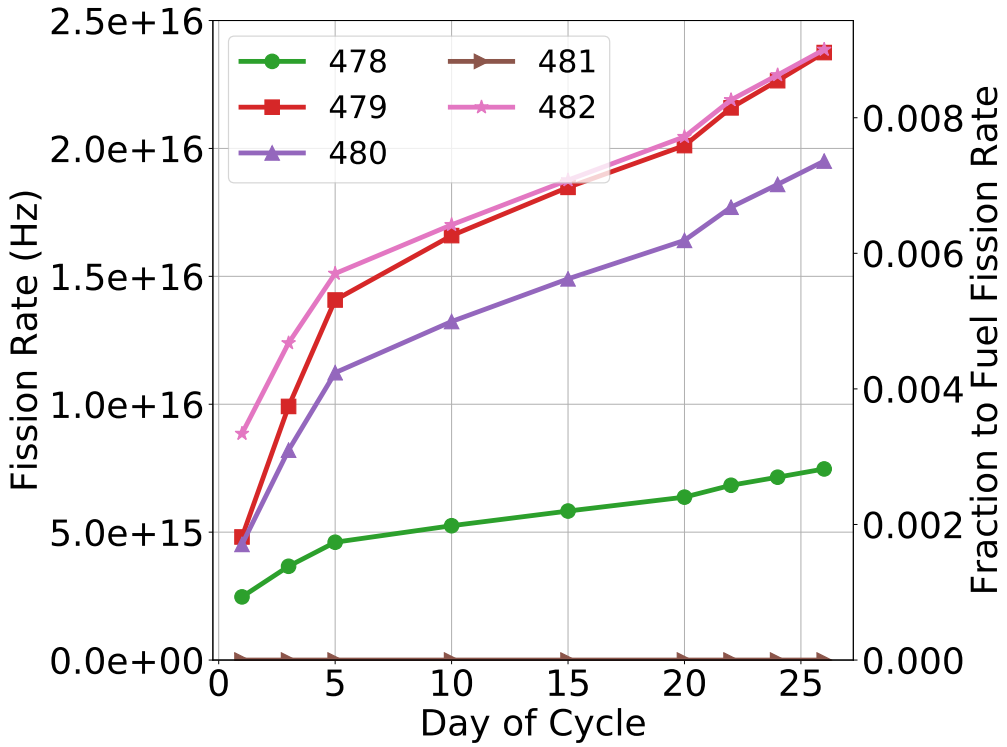

Figure 6.22: Fission rate of NpO_2 targets for cycles 478-482 based on their loading from Table 6.13 and fission rates in Figure 6.21

3 and VXF-15 for the number of targets and the cycle during which they were irradiated according to Table 6.13. Cycle 482 had the highest contribution due to nine VXFs with fully-loaded targets being in their third irradiation cycle. Cycle 479 was comparable as it had nine VXFs with fully-loaded targets in their first irradiation cycle and three in their third irradiation cycle.

To calculate the impact of the fission rates of the targets on the $\overline{\nu}_e$ spectrum, an assumption has to made regarding their heat generation as it impacts total heat power of the core. Because the total core power is conserved to 85 MW, the total fission energy released needs to be conserved. The small difference in energy release per fission due to the different isotopes is relatively small. Therefore the increase in fission rate in the NpO_2 targets is assumed to decrease the fission rate in the fuel by the same amount.

Figure 6.23 shows the relative difference to the nominal ^{235}U $\overline{\nu}_e$ spectrum with the

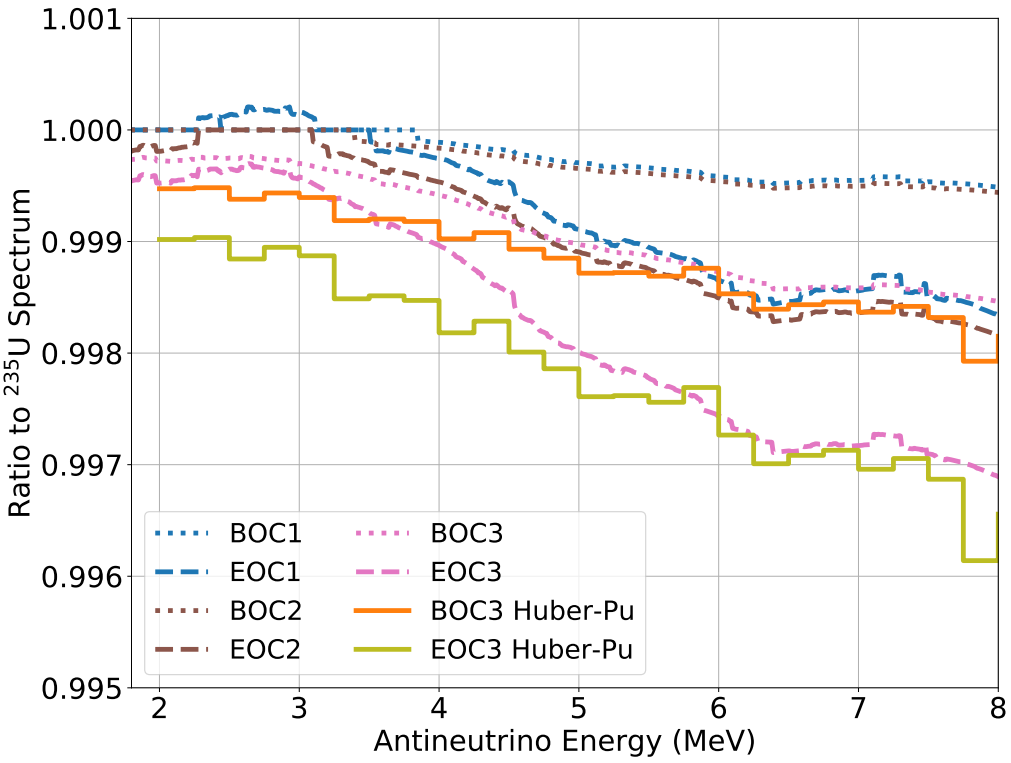

Figure 6.23: Fission rate of NpO_2 targets for cycles 478-482 based on their loading from Table 6.13 and fission rates in Figure 6.21

inclusion of the neptunium targets. The BOC/EOC curves reflect the impact of the inclusion of nine VXFs with fully-loaded targets in their first, second, or third irradiation cycle. This includes the contributions due to the increased fission rate of ^{238}Np and ^{239}Pu from the summation method (Oklo). The final series with "Huber-Pu" is almost the same calculation using the conversion data from Huber. However, because only the $\overline{\nu}_e$ spectrum for ^{238}Np is not available, only the ^{239}Pu fission rate is considered. The BOC/EOC1, BOC/EOC2, and BOC/EOC3, are analogous to Cycles 479, 480, and 482, respectively. Cycle 482 sees the largest decrease in the $\overline{\nu}_e$ spectrum due to the high ^{239}Pu fission rates from the targets being in their third irradiation cycle. According to Huber model predictions, the drop in the spectra increases with $\overline{\nu}_e$ energy from 0.1% to 0.4%.

Increase in Helium-6 Contribution

The irradiation of fissile targets in the reflector has a drastic impact on the local flux and heat generation rates. The increase in plutonium fissions hardens the spectrum in the reflector areas surrounding the VXFs bearing these targets. FMESH tallies are used to calculate the relative increase in fast flux and the ^{9}Be(n,α) reaction rate with the presence of NpO_2 targets.

Figure 6.24 shows the relative increase in the axially-averaged ^{9}Be(n,α) rate radially and azimuthally near the targets. The relative increase in these reaction rates locally is as high as 25-30% just outside the target basket. In the model, this increase is almost all in the second and third radial regions of the PB, shown in Table 6.9. Considering the PB regions account for just under 20% of the ^{6}He activity, this effect will be less than 5%. The expected number will be much lower due to the targets only increasing the flux in the nearest 5 cm around the target.

6.6 Water

Water also has the potential to be a $\overline{\nu}_e$ candidate from its (n,p) reaction. Water activation from this reaction is the primary production mechanism for radiation in the primary coolant system of commercial nuclear reactors. Extra shielding is required from the high-energy γ's that is created from the subsequent β^- decay. This reaction creates ^{16}N, which β^- decays with a half-life of only 7.13 seconds [88].

$$^{16}O +_0^1 n \rightarrow^{16} N +_1^1 p \tag{6.18}$$

$$^{16}N \rightarrow^{16} O + \beta^- + \bar{\nu}_e + 10.42MeV \tag{6.19}$$

Note that the 10.42 MeV is the release energy, however it results in several potential excited states of ^{16}O. The three most prominent result in β^- endpoint energies of 4.289 (66.2%),

10.419 (28.0%), and 3.302 MeV (4.8%) [88].

Water tallies are added to the representative model to calculate the ^{16}O(n,p) reaction rate at BOC and EOC. The tallies that calculate the reaction rate are analogous to the activity due to the short half-life of ^{16}N. The activity of ^{16}N is calculated to be 9.19 and 9.13×10^{12} Hz for BOC and EOC, respectively. The relative error for both was 0.7%. This activity is comparable to the ^{8}Li activity and five orders of magnitude less than the ^{235}U fission rate. This reaction for the purpose of HFIR is safely ignored.

6.7 Note on LWR Comparisons

A vast majority of $\overline{\nu}_e$ measurements have taken place at large-scale commercial nuclear power plants, mainly light water reactors (LWRs). The natural question arises of how non-fuel $\overline{\nu}_e$ production may impact the spectrum for a commercial LWR compared to HFIR. While a full analysis of all of the products is not done here, some insight can be provided based on this analysis. The larger core size and lack of significant experimental facilities of commercial reactors results in less neutron leakage to non-fuel elements and fewer relative neutrons activating non-fuel materials (i.e. potential $\overline{\nu}_e$ candidates) in the core. Commercial LWRs also have a small variety of materials that are contained in the core. The primary non-fuel materials that exist in commercial LWRs include zircaloy as a cladding material and variations of stainless steels.

All of the main LWR isotopes of iron and zirconium would be ruled out by the $\overline{\nu}_e$ candidate selection process (Section 6.1, Table 6.1); the only exception is ^{96}Zr, the isotope of zirconium with the lowest natural abundance (2.8%). The ^{96}Zr(n,γ)^{97}Zr transition has only one, albeit dominant, transition that results in a β^- endpoint (1.915 MeV) slightly higher than IBD threshold [89]. It has a half-life of 16.749 hours, which is not negligible but much larger than many of the isotopes considered in this work. The endpoint of 1.915 MeV is only slightly larger than the IBD threshold of 1.8 MeV which means that relatively few would be detected due to the β^- endpoint being at the tail end of the distribution.

Similarly, chromium only has one isotope that fulfills the $\overline{\nu}_e$ selection criteria, ^{55}Cr, which was previously discussed for HFIR. It also has a low natural abundance, similar to ^{97}Zr, and a half-life and β^- endpoint similar to that of ^{28}Al. The chromium composition in stainless steels is expected to be small and not an issue for LWRs.

Detailed studies of isotopes such as ^{97}Zr and those of chromium are not performed here due to the lack of available data of exact composition and the hypothesis that the effects are small. Further studies can be done to examine the activation of zirconium and chromium composition in steels. Furthermore, this effect is hypothesized to be small due to the significantly larger fission rate in a power reactor and the lack of large quantities of chromium in the higher flux regions of the core.

6.8 Summary

This rigorous approach involved examining many isotopes which could contribute to the $\overline{\nu}_e$ spectrum above the IBD threshold. A methodology was developed for investigating the most problematic $\overline{\nu}_e$ candidates that are most problematic in quantity for systematic uncertainties. The three largest-contributing isotopes were ^{28}Al, ^{6}He, and ^{52}V. Most of the other isotopes had a much smaller or negligible effect. The one exception was the NpO_2 targets that had as high as a 0.8% effect on the fission rate, but this has a small effect on the $\overline{\nu}_e$ spectrum because the ^{238}Np or ^{239}Pu fission rates are not high enough to perturb it.

The average values for the top three isotopes are used to calculate average excess contributions for a nominal cycle. For aluminum and helium, this means the cycle average as their activities were calculated as a function of length into the cycle. For vanadium, the average value from the loading cases was taken. Figure 6.25 shows the excess contributions as a step function by energy range for the three largest contributions. ^{28}Al contributes over 8% in the low-energy range and all thre isotopes combine to over 9%. The ^{28}Al had by far the largest contribution between 1.8 and 2.86 MeV, its β^- endpoint. The ^{6}He has a peak contribution of 0.5-0.75% effect around 2.5 MeV but drops off towards its endpoint

of endpoint of 3.5 MeV. The ^{52}V contribution peaks at about 0.5%.

Figure 6.26 shows the most updated PROSPECT results according to its recent Physical Review Letter [90]. The contribution of from the ^{28}Al and ^{6}He can be seen in the upper panel of the figure, below the 2.5 MeV in reconstructable energy. The results show that there are some disagreements between the Huber model and the PROSPECT data in two energy ranges. This will not be discussed further here, but Ref. [90] can be viewed for more information.

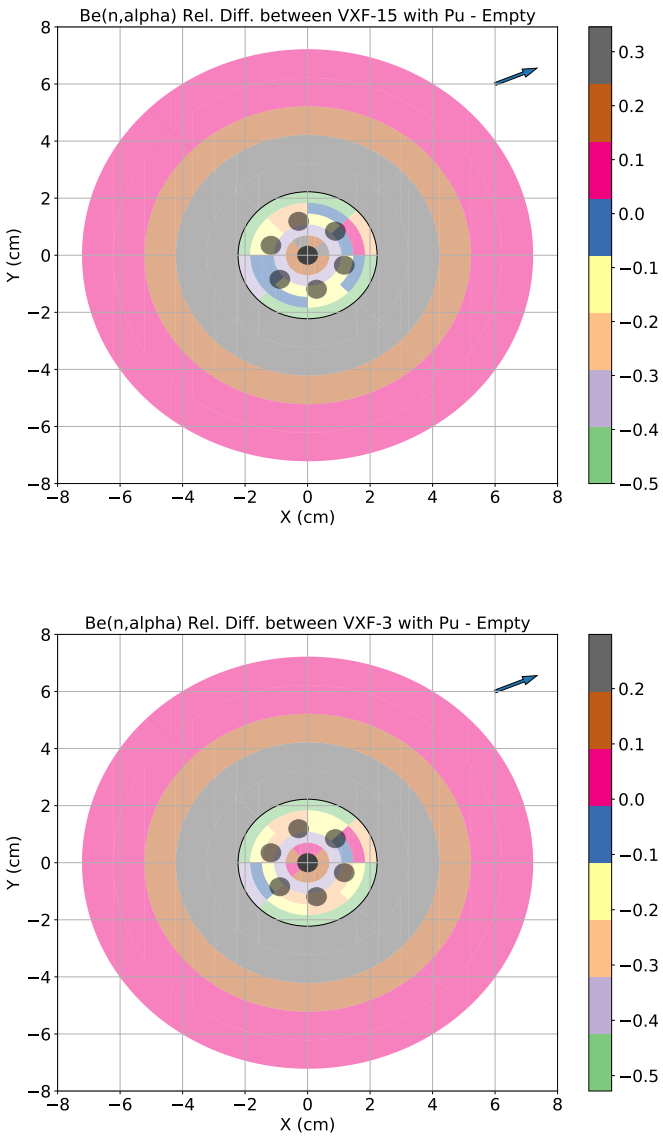

Figure 6.24: Relative increase in the axially-averaged ^{9}Be(n,α) reaction rate due to the presence of NpO_2 targets in the VXFs with the arrow pointing towards the core. The top is the higher cases for VXF-15. The bottom is lower case for VXF-3. Note that the scales are different.

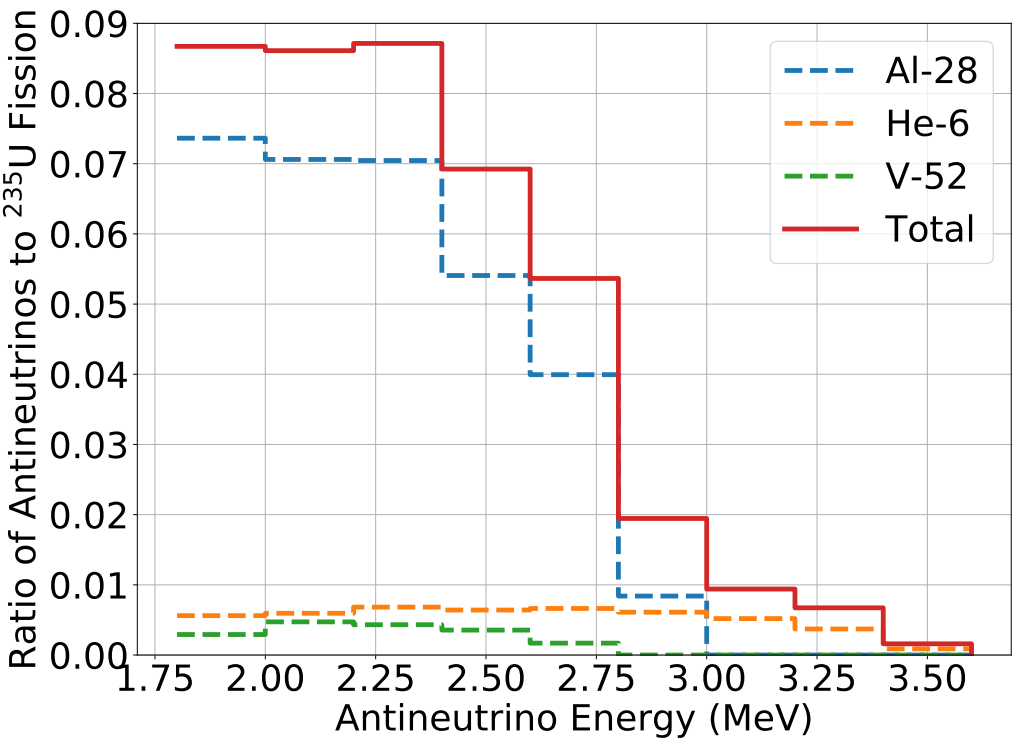

Figure 6.25: Average excess of ^{28}Al, ^{6}He, and ^{52}V contributions to the $\overline{\nu}_e$ spectrum

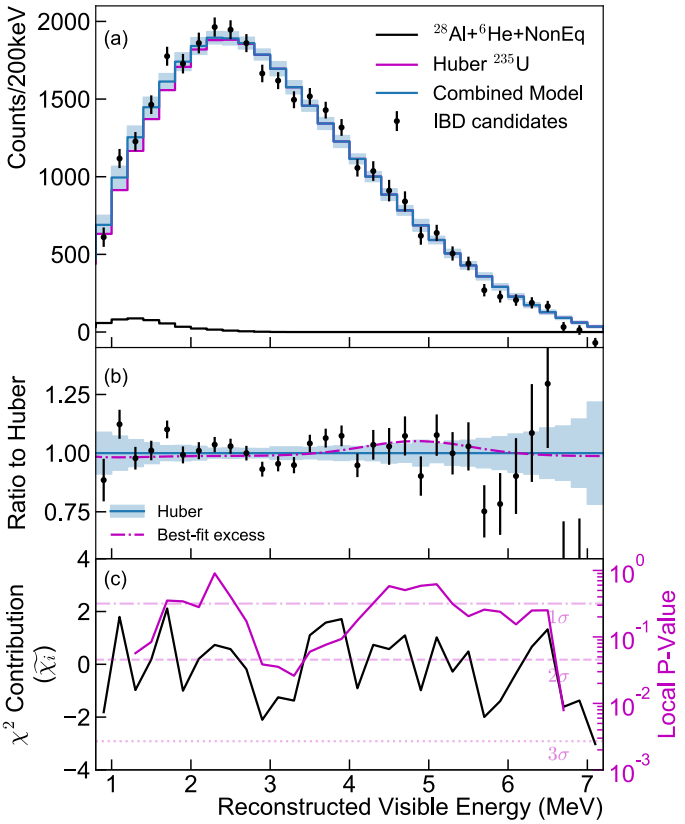

Figure 6.26: Measured prompt energy spectrum of IBD events compared to Huber predictions for ^{235}U with contributions from ^{28}Al, ^{6}He, and non-equilibrium isotopes (a) along with the ratio to the Huber model and best fit from LEU experiments (b) and χ^2 and local p-value of results, reproduced from Ref. [90]

CHAPTER 7
SPENT FUEL AND THEORETICAL PREDICTIONS

The goal of this chapter is to discuss other relevant work that contributes to understanding of predictions to the $\overline{\nu}_e$ spectrum. The approaches used in this chapter take a hybrid of approaches from using nuclear engineering tools to neutrino physics correlations. This chapter is split up into three sections. First, the impact of spent fuel will be discussed. Then, work on understanding the impact of fission neutron energy will be explored. Finally, the beta spectrum capability in the ORIGEN code will be utilized to generate new insights as well. These findings can be useful in understanding the theoretical predictions of $\overline{\nu}_e$ spectra and their applications.

7.1 Spent Fuel Contribution

HFIR, as with most nuclear reactors, needs to have sufficient capabilities to store spent nuclear fuel (SNF) for at least for the short-term. Spent fuel pools to store discharged fuel serve dual purposes: to carry away thermally the decay heat and maintain shielding between until the fuel is safe to remove. Most commercial reactors remove discharged fuel from the spent fuel pool after 5-10 years to be stored in temporary dry casks. At HFIR, the spent fuel is kept in approximately dozens in numbers before it may be shipped to the Savannah River Site (SRS). Because so many spent fuel assemblies are stored on site at HFIR, some analysis should be performed to quantify the extent of their contribution.

Recent work has gone into characterizing the $\overline{\nu}_e$ contributions from spent fuel, both at Daya Bay and for safeguards applications [91, 92, 93]. The Daya Bay calculation showed that in their power reactor experiment was on the order of 0.26-0.34% [91]. The recent study focusing on safeguards from Brdar study [92] found a roughly empirical solution for

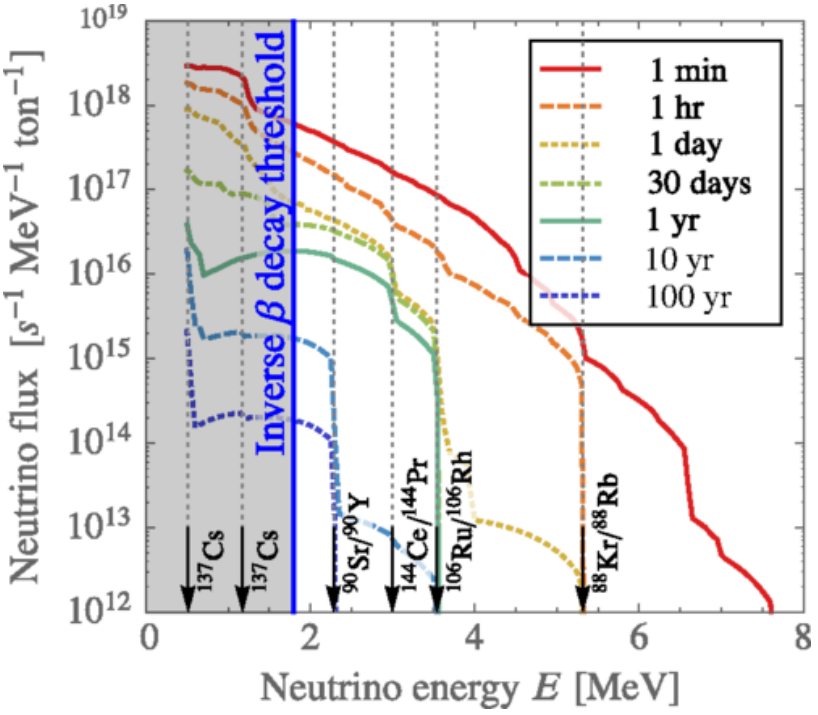

Figure 7.1: Spectrum of $\overline{\nu}_e$ emitted from spent nuclear fuel as a function of time, reproduced from [92]

a particular case of commercial nuclear fuel. Their formulation is:

$$N_\nu = 5.17 yr^{-1} ton^{-1} MTU^{-1} \times \left(\frac{10m}{d}\right)^2 \tag{7.1}$$

where the source of $\overline{\nu}_e$'s produced is N_ν, d is the distance between the source and detector, and the values are reported per year, per unit mass of the detector (in tons), and per unit burnup of fuel (in metric tons of uranium or MTU). They also published supplemental data with $\overline{\nu}_e$ spectra for various decay times. Figure 7.1 shows the $\overline{\nu}_e$ from the spent fuel at a select few of those decay times.

7.1.1 Spent Fuel Assumption Justifications

The result from the Brdar study came with several assumptions that are not relevant for HFIR or its fuel. First, the fuel was low-enriched uranium (LEU), which is typical to commercial nuclear reactors. It has been established that the HEU HFIR fuel leaves little

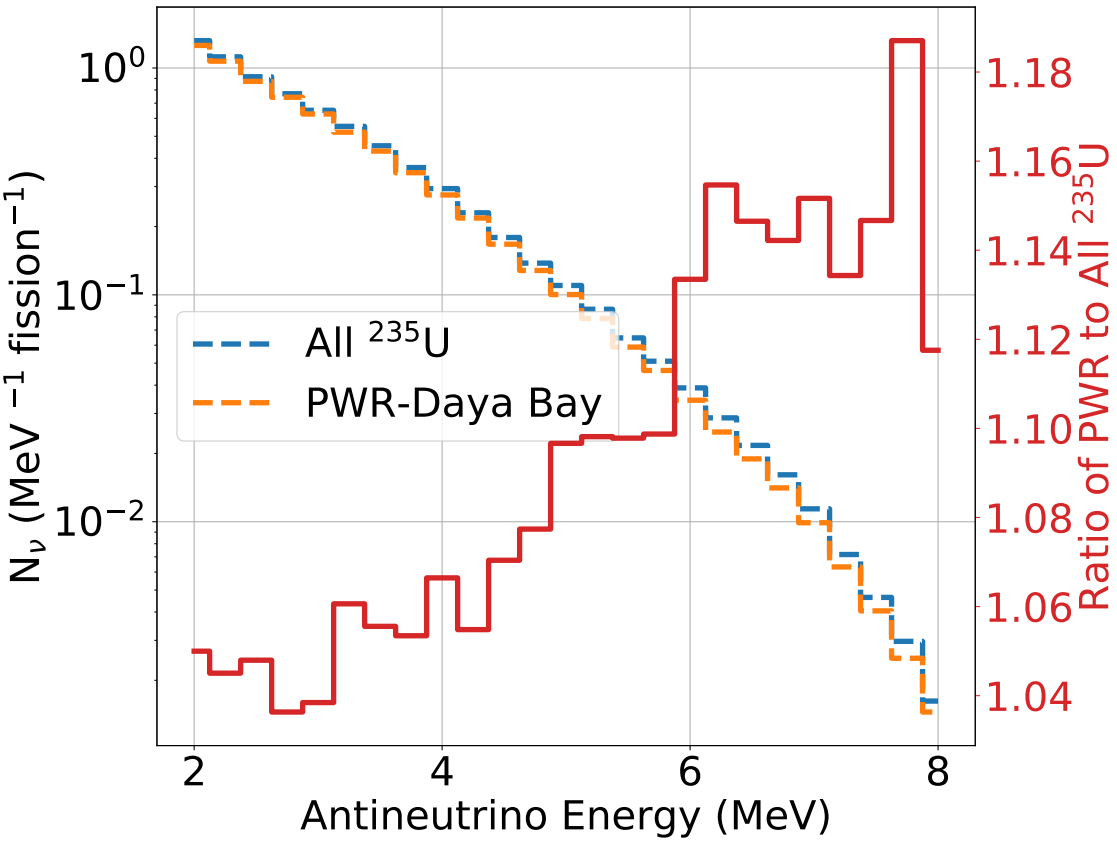

Figure 7.2: Spectrum for all ^{235}U spectrum compared to that of fission fractions with Daya Bay averages [28] with the ratio of the latter to former on the right axis

fission fraction from other isotopes. Second, the data is for a reference at 45 GWd/MTU. The HFIR fuel achieves a burnup of approximately 2000 MWd (85 MW for 24 days) with its loading of 10.4 kg. This equates to about 200 GWd/MTU, a factor of 4-5 higher than that of a commercial reactor. While these are not valid for HFIR, their approximate correction factors can be calculated.

To account for the difference among fission fractions, nominal fission fractions for a PWR are taken from Daya Bay analysis [28]; the fission fractions used are (0.571, 0.076, 0.299, 0.054) for (^{235}U, ^{238}U, ^{239}Pu, and ^{241}Pu). The relatively small difference between the energy released per fission shows that the total core fission rate should negligibly decrease due to plutonium buildup. Figure 7.2 shows the difference between a pure ^{235}U spectrum and one with these fission fractions. The ratio between the two is also shown, with in-

Table 7.1: Energy released per fission for the four primary isotopes [94]

Isotope	$\bar{E}_f$ (MeV)
^{235}U	203.19 ± 0.06
^{238}U	206.32 ± 0.17
^{239}Pu	207.58 ± 0.07
^{241}Pu	211.33 ± 0.08

creasing disparity, up to 18% at the higher ends of the spectrum; however the $\overline{\nu}_e$ detected spectrum is dominated by the lower energies. The effect of using the PWR-reactor-derived correlation is estimated to have a 5-6% difference.

Table 7.1 shows the difference between the energy released per fission among the four primary isotopes in a commercial reactor [94]. All of the energy releases are similar; the ^{241}Pu is the highest relative to ^{235}U and only by less than 5%. This can be explained by the following equation for burnup (BU), or the energy released per unit initial mass (M_{init}):

$$BU = \frac{\int dt \sum_i f_i(t)\bar{E}_i(t)}{M_{init}} = \frac{\int dt f(t) \sum_i F_i(t)\bar{E}_i(t)}{M_{init}} \tag{7.2}$$

with the fission rate f and fraction F. This, combined with Equation 7.1, gives an approximation for the $\overline{\nu}_e$ productions as a function of burnup, of the change in fission rates and energy released over time. The small differences in energy release per fission and $\overline{\nu}_e$ production per fission based on fission fractions lead to the assumption that the $\overline{\nu}_e$ spectra should change negligibly from a commercial PWR to HFIR on a per fission basis. The error associated with fission rates, fractions, and energy releases are relatively small; the total error associated with this should be no more than a few percent.

The error with the difference in burnup is a potentially larger issue as its correlation with $\overline{\nu}_e$ production rates is not straightforward. It is hypothesized that the $\overline{\nu}_e$ (and β^-) spectra per mass loading are not substantially different as a function of burnup. The proxy measurement used for this is the decay heat power, which combines the β^- and γ energies produces from fission products following the fission event, i.e. not including the kinetic energy of the fragments.

To understand the impact of burnup, it is first considered if the decay heat, proportional to the β^- activity, changes as a function of burnup. For this, the ANSI/ANS standard decay heat equation from Todreas is used [95]:

$$\frac{P}{P_0} = 0.066[t_s^{-0.2} - (t_s + \tau_s)^{-0.2}] \tag{7.3}$$

where P/P_0 is the ratio of decay heat to reactor power, t_s is the time since shutdown, and τ_s is the amount of reactor operating time. When calculating the decay heat power as a function of shutdown time for a PWR, an irradiation time of 540 days (18 months) is used as this is the typical cycle time for a 3-batch scheme. The HFIR decay heat data is taken from a calculation that examined the effects of safety plate insertions; the calculation includes detailed, time-dependent fission and decay heat power for ample time steps following the scram [96].

Figure 7.3 shows the decay heat comparison based on two HFIR safety analyses and typical values for a PWR from the empirical correlation. The relative decay heat does not change much between the PWR and higher-burnup HFIR fuel. Because HFIR has a similar decay heat but higher burnup, a scale factor should be applied in that it is more efficient per unit mass at achieving the same decay heat because Equation 7.1 is per metric ton of fuel. A scale factor for the HFIR fuel compared to the Ref. [92] will be applied based on the ratio of burnup. This ratio of burnup for HFIR versus a commercial PWR is 204/45 = 4.53.

7.1.2 Spent Fuel Pool Description

HFIR has two main areas for storage of spent fuel. These include the center and east pool, whereas the reactor is in the west pool. Each pool is approximately 20 feet long and separated from the other pools by a separation gate. HFIR has the availability to store spent fuel for 5 years or longer. Upon finished irradiation, the spent fuel assemblies are placed in a jacket assembly. The jacket assemblies are placed in arrays in either a “diamond” or “hourglass” cluster. Figure 7.4 shows the arrangement of a set of spent assemblies.

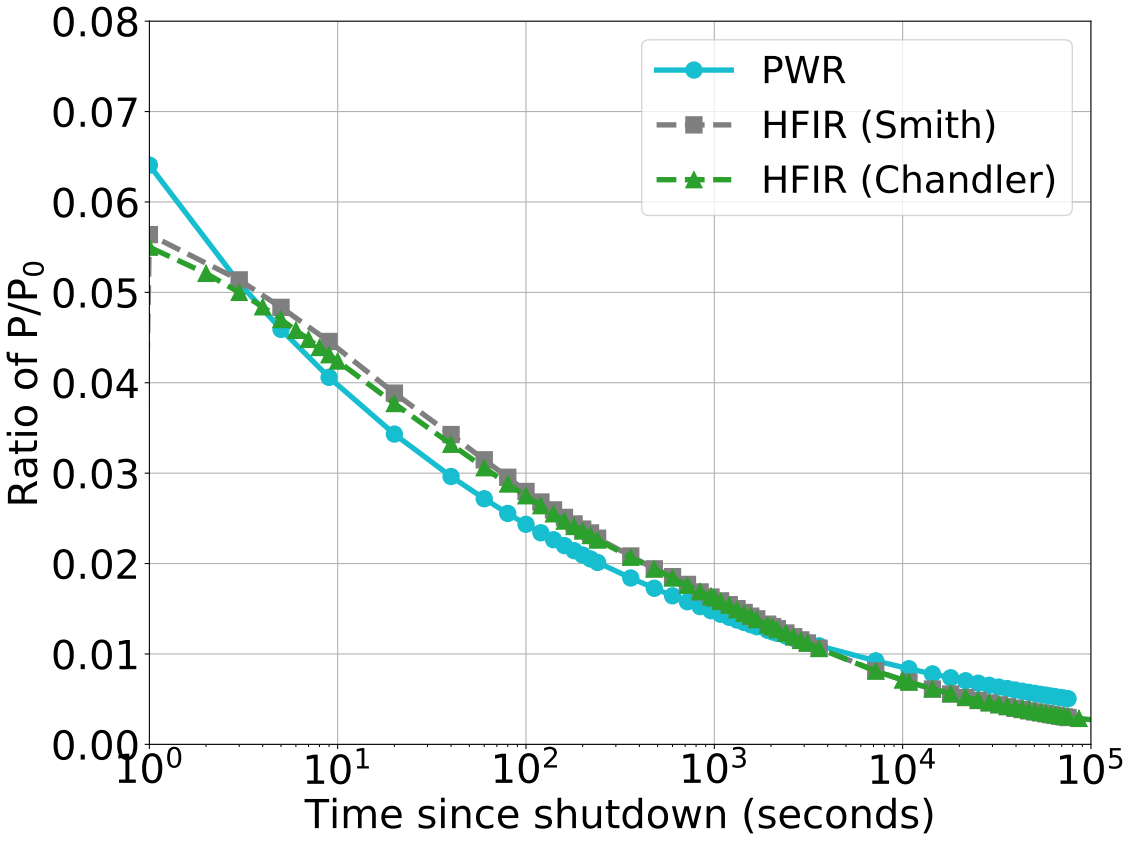

Figure 7.3: Decay heat relative to reactor power as a function of shutdown time from PWR correlation [95] and two HFIR calculations [96, 97]

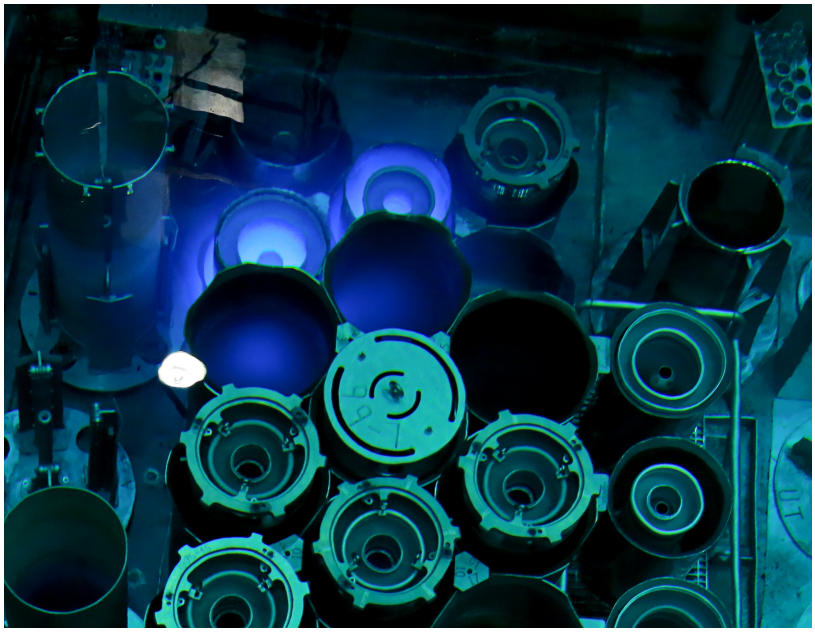

Figure 7.4: Spent fuel assembly in the HFIR pool

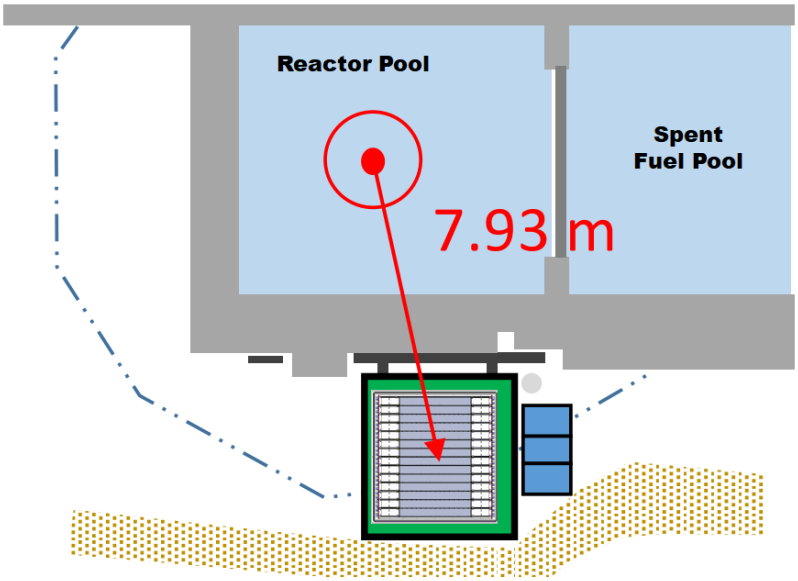

Figure 7.5: Diagram of the PROSPECT detector in its relative proximity to the reactor and spent fuel pool, modified from an image in Ref. [47]

A reference point of September 2018 is used for which the locations of all the spent fuel assemblies are known. The center pool, which is adjacent to the reactor pool and closest to the detector, contained several of the more recently discharged spent fuel assemblies. The east pool contained far more assemblies, although many of these were irradiated over 10 cycles prior. Due to export controls, detailed images and identification numbers are not shown here. Most of the spent fuel assembly positions are within 15 meters of the PROSPECT detector. Figure 7.5 shows the rough orientation, with the baseline of the detector to the reactor as 7.9 meters.

7.1.3 Spent Fuel $\overline{\nu}_e$ Calculation

The actual snapshot of spent fuel assembly locations from September 21, 2018 is used as a first order approximation. Based on locations of the assemblies and several drawings of the reactor building and detector, distances to the center of the detector are calculated. The closest assembly in the center and east pools are 10.8 and 11.2 meters, respectively, from the center of the detector. Solid angles to the detector are calculated for each position.

The identification number and cycle in which assemblies were irradiated is identified. Assemblies in the center pool include those irradiated in HFIR cycles 474-482 (1 month to one year prior). These assemblies are closer to the PROSPECT detector. Assemblies in the east pool ranged from those irradiated in the 420s to the most recent being 472 (1.5 to 10 years prior). The end-of-cycle date is obtained and the date between the retrieval data and irradiation completion is calculated. The $\overline{\nu}_e$ emissions are calculated by logarithmic interpolation of the energy-dependent spent fuel $\overline{\nu}_e$ data [92]:

$$\frac{\ln N(E,t_{des}) - \ln N(E,t_i)}{t_{des} - t_i} = \frac{\ln N(E,t_{i+1}) - \ln N(E,t_i)}{t_{i+1} - t_i} \tag{7.4}$$

where $N(E,t)$ refers to the $\overline{\nu}_e$ source term at the desired discharge time (t_{des}) or at its left (i) or right ($i+1$) boundary and t is the time in days since discharge. This interpolation can be rearranged to obtain the desired $\overline{\nu}_e$ spectrum at the time of discharge:

$$N(E,t_{des}) = N(E,t_i)\left(\frac{N(E,t_{i+1})}{N(E,t_i)}\right)^{\frac{t_{des}-t_i}{t_{i+1}-t_i}} \tag{7.5}$$

The $\overline{\nu}_e$ source flux from both the reactor, using the Huber ^{235}U spectrum, and the spent fuel at each position can be translated to the flux in the detector with some modifications to Equation 2.5 to incorporate several spent fuel source position and assuming constants in detector properties:

$$\frac{dN_{\bar{\nu}}}{dE} = \sum_i \gamma \frac{p(E_{\bar{\nu}}, L_i)}{4\pi L_i^2} \frac{d\phi_{\bar{\nu}}}{dE} \tag{7.6}$$

where γ is the constant detector term and $p(E_{\bar{\nu}}, L)$ is the oscillation probability, which will not be considered for this analysis. Dividing both sides by the detector efficiency term, it becomes the flux inside the detector from the reactor, $\phi_{det,Rx}$:

$$\frac{d\phi_{det,Rx}}{dE} = \frac{1}{4\pi L^2} \frac{d\phi_{\bar{\nu}}}{dE} \tag{7.7}$$

The reactor spectrum used is the Huber spectrum multiplied by this solid angle. For simplification, the baseline term L is assumed to be constant for the reactor, i.e. it is treated as a point source ($i = 1$).

The spent fuel is summed over the many storage locations in the pools. To account for the difference in burnup, the HFIR emissions are scaled based on their relative burnup to the reference PWR case. In other words, the burnup factor b = 204 GWd / 45 GWd = 4.53, discussed previously, is applied. The spent fuel version of the equation for the flux due to SNF in the detector, $\phi_{det,SNF}$, can be written as:

$$\frac{d\phi_{det,SNF}}{dE} = b \sum_i \frac{1}{4\pi L_i^2} \frac{d\phi_{\bar{\nu}}}{dE} \tag{7.8}$$

This is a first order approximation and can be calculated in more sophisticated ways in the future.

To exacerbate the potential SNF effects, the contribution of a recently discharged fuel element is approximated. This assembly is assumed to be in the core for one day following reactor shutdown. In other words, this would be the background from SNF if reactor has been shutdown for 24 hours and that core has not been moved elsewhere in the pool. This is to examine the effect of what the nearly worst case SNF term could be as the reactor is closer to the detector than any SNF assembly location.

Figure 7.6 shows the calculated flux at the detector for the reactor with SNF at this particular date for the nominal case and with the 1-day spent assembly still in the reactor core with respect to the nominal reactor-on $\overline{\nu}_e$ spectrum. The rates differ by 2-3 orders of magnitude. The SNF spectrum is zero above 3.5 MeV, which is consistent with the results from Ref. [92].

Table 7.2 shows the ratio of SNF to reactor $\overline{\nu}_e$ spectrum for the single time step and one exacerbated by a recently shutdown core. The exacerbated case sees slight increases due to the recently discharged element. Even this worst case is no more than 0.25% of the reactor spectrum for any energy bin. The effect of including a recently discharged element has a

significant impact on the SNF contribution. The element that finished irradiation one day prior contributed upwards of 50% in many energy bins relative to the nominal amount of spent fuel. This value decreases to 40% when considering all $\overline{\nu}_e$ above IBD threshold. In any case, the recently irradiated core contributes half as much as the previous three dozen spent assemblies.

Table 7.2: Ratio of $\overline{\nu}_e$ spectrum (%) from SNF to reactor-on for a nominal and worst case, with 1-day old assembly still in the core

Energy (MeV)	Nominal	Worst Case
2	0.161	0.233
2.25	0.161	0.227
2.5	0.149	0.210
2.75	0.135	0.189
3	0.081	0.110
3.25	0.038	0.051
3.5	0.024	0.032

This method takes advantage of recent work and the ability to obtain information on spent fuel assemblies from HFIR at a particular point in time. The most prominent uncertainty is with the assumption that the $\overline{\nu}_e$ spectrum is similar in yield and in spectrum for fuel with burnups of 45 and 200 GWd/MTU. Testing this assumption further would be useful. This method does not take into account oscillation, which suffices for this purpose but may need to be considered in future analysis.

7.2 Fission Neutron Energy

As discussed in Section 2.1, anomalies still contribute to uncertainty in the understanding of $\overline{\nu}_e$ measurements and subsequent spectral calculations. One hypothesis about the mismatch between experiments and predictions for the "bump" in the spectrum has to deal with the impact of neutron energy causing fission. The harder neutron spectrum in a typical PWR where many experiments have taken place is different than that in the ILL HEU-fueled reactor. This could be a problem due to the relatively large component of fissions that take place in the resonance region [41]. Some early work by Cowan *et al.* showed some

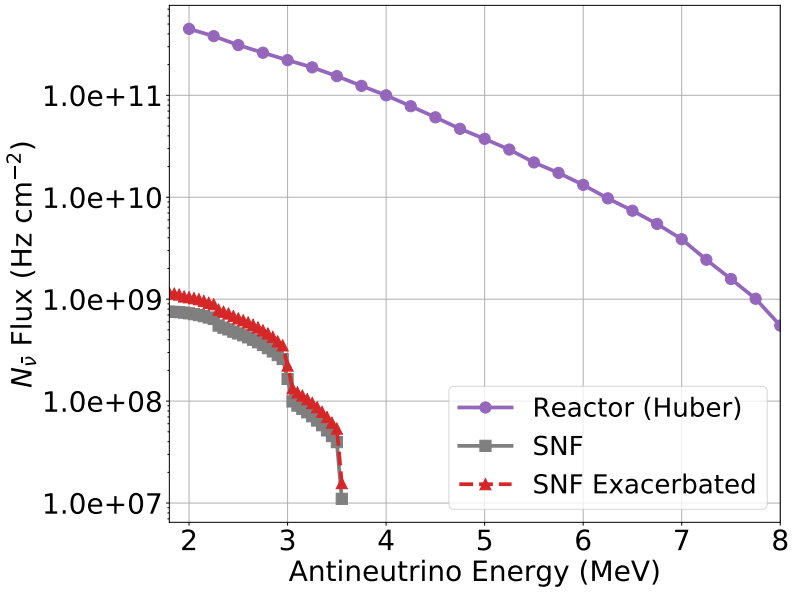

Figure 7.6: Calculated flux at the PROSPECT detector for fission rate with Huber $\overline{\nu}_e$ conversion and SNF estimations from September 2018 and an exacerbated case with an element 1 day after irradiation finishes

asymmetries in the resonances of ^{235}U and ^{239}Pu [98, 99, 100, 101]. The following work is detailed in Ref. [102].

For this section, models of various reactors will be used to examine the impact of fission neutron energy dependence on the $\overline{\nu}_e$ spectrum. The first two are the HFIR model and the NBSR model, detailed in Section 6.3.2. The third is a typical PWR model, similar to that in the OECD/NEA benchmark [103].

The PWR model is an eighth-core model with radial reflection that is based on a typical 4-loop Westinghouse design with a thermal power of 3565 MW. The core barrel is approximately 3.67 meters in length and contains 193 fuel assemblies. The fuel is in the form of UO_2 pellets with an outer diameter of 0.4096 cm. These pellets are stacked in assemblies with a core active fuel height of 3.66 m. The fuel assemblies have a target cycle and discharge burnup of 21 and 40-50 GWd/MTU. All of these are pretty typical values for a commercial plant of this type.

Figure 7.8 shows the ENDF/B-VII.1 fission cross-sections for the major uranium and

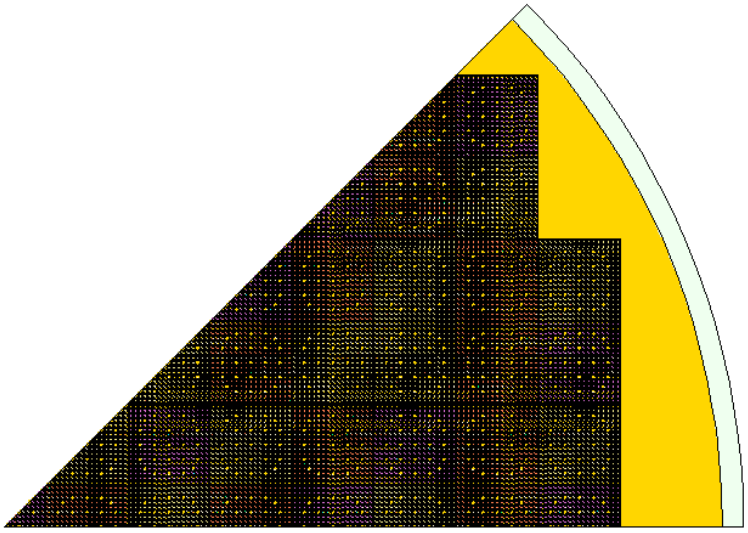

Figure 7.7: Standard model of an eight-core pressurized water reactor based off the Westinghouse design for the OECD/NEA benchmark [103]

Table 7.3: Cutoff energies typically used in three-group structure and for the fission neutron energy work

Group Name	Typical Upper Energy Cutoff	This Work Upper Energy Cutoff
Fast	20 MeV	20 MeV
Epithermal	100 keV	100 keV
Thermal	0.625 eV	0.1 keV

plutonium isotopes. It can be seen that the odd-numbered isotopes (^{235}U, ^{239}Pu, ^{241}Pu), which have a higher tendency to fission, all have resonances in their cross-sections in the 0.1 - 1 eV range. Typically for reactor calculations using three groups, the upper cutoff in the thermal range is 0.625 eV due to that being the cadmium cutoff energy. For this work, the upper energy range for the thermal is assumed to be 0.1 eV to capture the effect of the resonances in the "epithermal" range. The typical cutoffs versus those used in this work are compared in Table 7.3. The goal of choosing this is to exacerbate the effects of the resonance peaks in this range, particularly ^{239}Pu and ^{241}Pu.

The fission tally for all fuel materials is calculated in the HFIR, NBSR, and PWR models. This is achieved using a F4 tally with FM4 cards added for phantom materials, de-

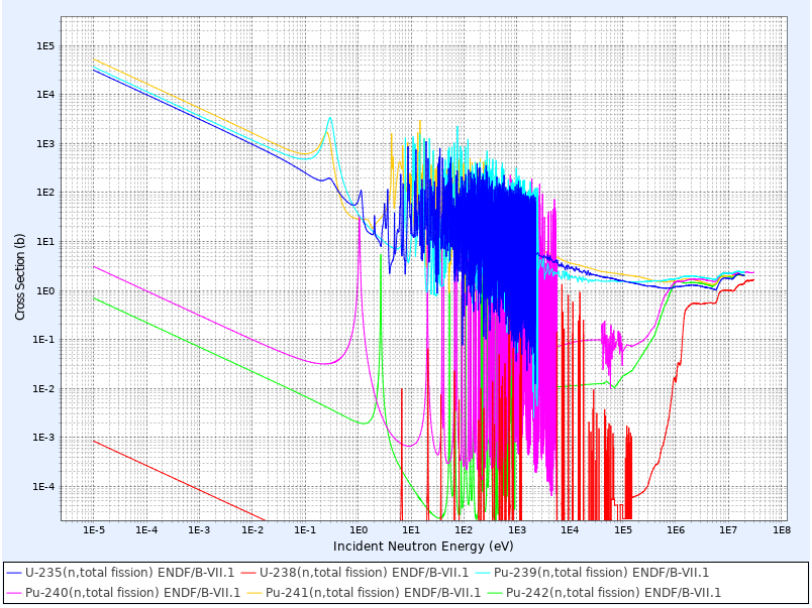

Figure 7.8: Fission cross-sections for the primary fissile isotopes in a nuclear reactor

scribed in Section 4.1, to obtain the fission tally for each isotope. The tallies use a more generic 130-group structure to get more finely detailed energy structure of the neutrons causing fission.

Figure 7.9 shows the normalized distribution and cumulative distributions of neutrons causing fission for the three reactors. Only the ^{235}U components are shared for the two HEU reactors while the two major plutonium isotopes are shown only for the commercial PWR. It can be seen that the D_2O moderation of the NBSR leads to a wider thermal distribution. The ^{235}U for HFIR and commercial PWR are both similar although the latter shows its slightly harder spectrum.

The cumulative distribution in Figure 7.9 highlights the fractions of fissions that are caused by neutrons of a certain energy. For example, approximately 48% of fissions in ^{235}U for the commercial reactor are caused by neutrons of energy 0.1 eV (10^{-7} MeV) or lower. This number is over 66% for the two HEU reactors. For fissions of ^{239}Pu and ^{241}Pu in the PWR, only 32% and 36%, respectively, are caused by neutrons lower than the 0.1 eV cutoff.

When converting neutron-induced fission to its fission products, there are only thermal

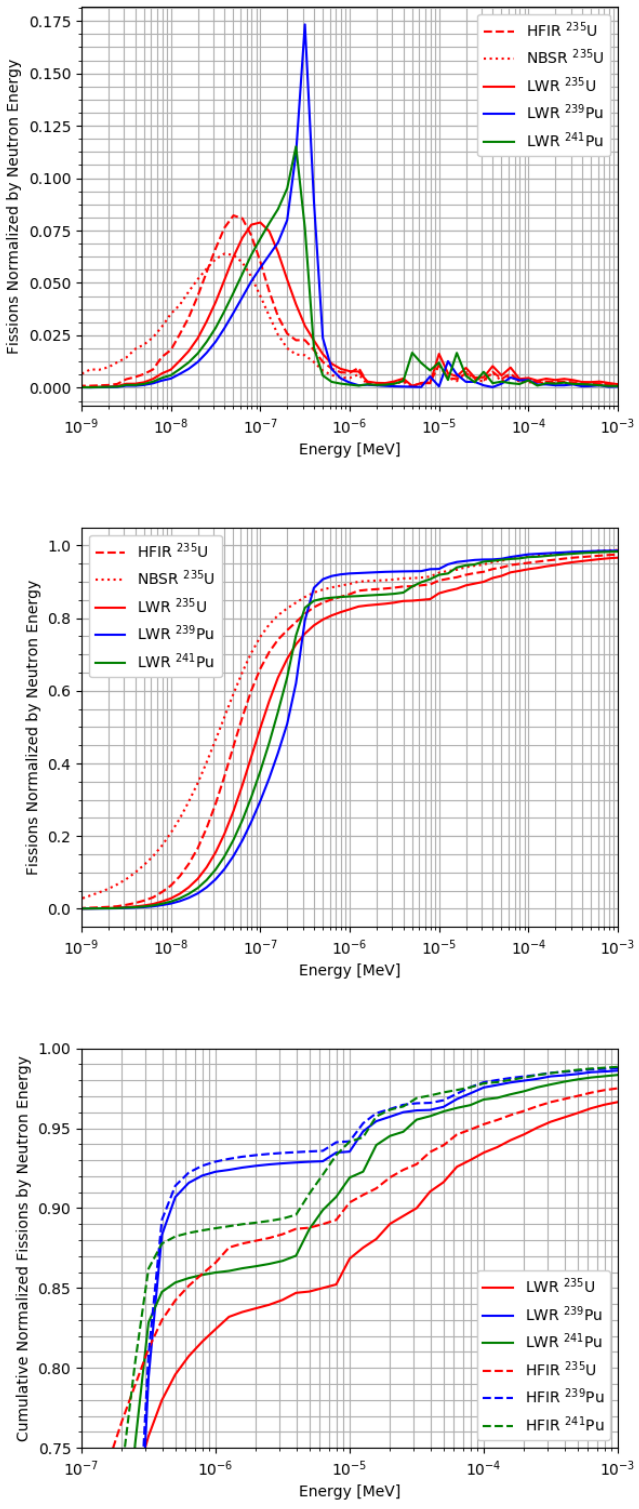

Figure 7.9: (Top) Fission distribution normalized by energy of neutron causing fission. (Middle) Cumulative distribution of fissions by energy of neutron causing fission. (Bottom) Cumulative distribution with focus on resonance region.

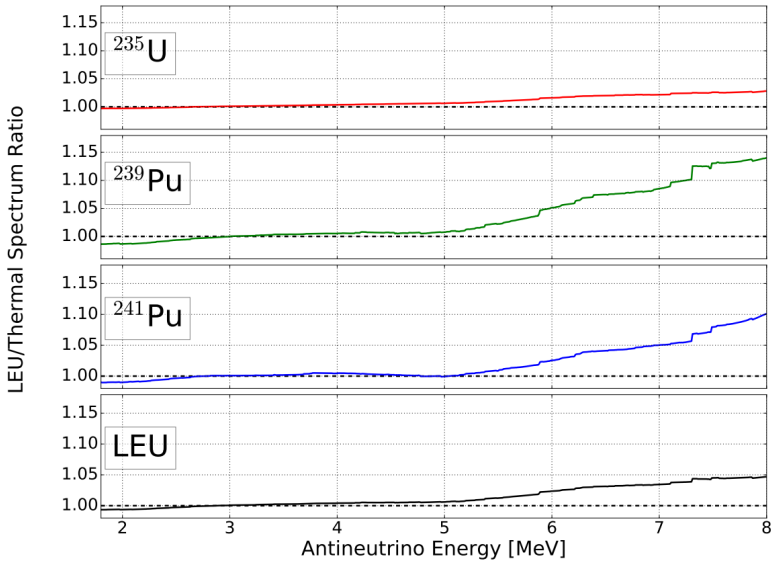

Figure 7.10: Reactor $\overline{\nu}_e$ spectrum ratios for LEU/thermal for ^{235}U, ^{239}Pu, and ^{241}Pu with unity fission fractions in their respective panels and Daya Bay-reported fission fractions for the bottom panel

or fast neutron-induced fission yield libraries when it comes to ENDF7 [44] or JEFF-3.1 [104]. In quantifying the impacts of neutron energy on fission $\overline{\nu}_e$ spectra, two bounding cases are created. One case is where all fissions of ^{235}U, ^{239}Pu, and ^{241}Pu are treated as thermal fissions; this case is called the ILL case as the $\overline{\nu}_e$ produced at the ILL beamline were all thermal. In the second case, the neutron fission energy is chosen to match that of typical reactor $\overline{\nu}_e$ experiments; this case is called the LEU case due to the LEU fuel in a typical commercial PWR.

Figure 7.10 shows the difference between the LEU and thermal cases for the three thermal neutron-inudced isotopes as well as an LEU case with fission fractions similar those in the previous Section 7.1. It can be noted that for the pure ^{235}U and LEU cases that the increase in the 5-7 MeV range averages to no more than 3.5% when treating the resonant fissions as coming from thermal versus fast neutrons. This suggests that the treatment of neutron energy has little to do with the bump.

While the treatment of all resonant fissions as fast fissions may not be entirely accurate, it does provide a good set of binding cases from which to test the fission yield databases.

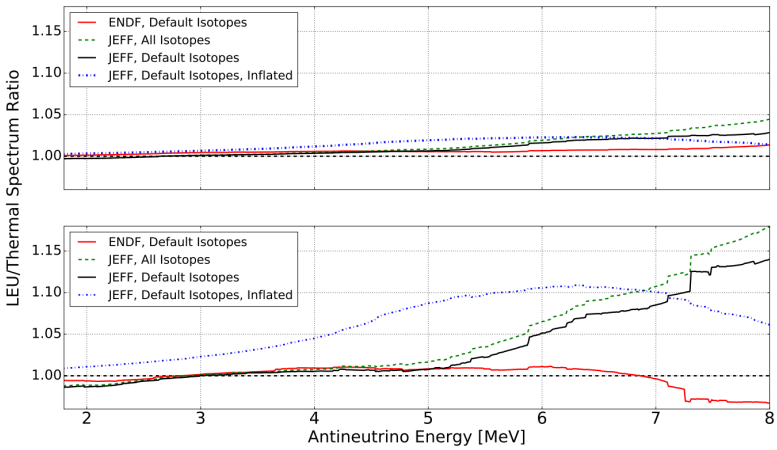

Figure 7.11: Reactor $\overline{\nu}_e$ spectrum ratios for the LEU/thermal case with the inflated spectrum for the top 10 isotopes contributing to the bump for ^{235}U (top) and ^{239}Pu (bottom)

While large deviations in resonant fission yieldF on the order of 20% in specific isotopes, such as ^{115}Cd, have been observed in the previous literature [41, 98, 99, 100, 101], it has been suggested that the isotopes that contribute the most significantly to the bump range, among them ^{96}Y and ^{92}Rb, are not likely to have an impact of that magnitude [102]. More measurements of resonant fission yields are necessary to create a more rigorous approach.

To account for the worst case scenario in which isotopes that contribute most largely to the bump all see increased magnitude of fission yields, they are inflated by 20%. These isotopes that include the aforementioned ^{96}Y and ^{92}Rb account for more than 50% of the yields in the 5-7 MeV $\overline{\nu}_e$ range (full list in Ref. [102]). Figure 7.11 shows the effect of this inflated spectrum for ^{235}U and ^{239}Pu in both the ENDF and JEFF fission yield databases. Small differences were noted in using the default versus all isotopes in JEFF (discussed in Ref. [102]). The ^{235}U LEU/thermal ratio saw almost no change in the $\overline{\nu}_e$ spectrum, often within 2.5% for JEFF. The ^{239}Pu LEU/thermal ratio sees an average of 11% in the bump region. Therefore this extreme inflation approach provides an unlikely explanation for the cause of the bump.

7.3 Beta Spectra Using ORIGEN

The Oak Ridge Isotope Generation (ORIGEN) sequence in the SCALE code [59] has the capability to produce beta spectra. The most recent large update to the sequence that generates electron spectra, BETA-S, was performed back in 2008 [105]. BETA-S calculates the β^- source term and energy spectrum that was meant for spent fuel calculations as well as applications to safety and severe accident scenarios (e.g. loss of coolant accidents). The current release of SCALE (6.2.3) still contains that release of BETA-S.

The implementation of BETA-S comes with a couple of important implications. First, the data library used for beta transition and energy level data is ENSDF-95, released in 1995. The ENSDF-95 database contains approximately 8500 individual beta transitions from over 700 isotopes. Many more recent evaluations have made measurements of then-lacking transitions; most of these are published in Nuclear Data Sheets rather than coming in bulk releases. The current ENSDF website lists transitions, albeit not all of those are β^- transitions.

Second, the BETA-S code uses a simplification for approximating spectra for isotopes which did not have detailed level information. It treats all isotopes with missing decay data as having an allowed transition. In other words, the average β^- energy is approximated as 1/3 of the endpoint energy, a common approximation in this case.

7.3.1 Identification of Missing Beta Spectra in ORIGEN

The ORIGEN depletion code currently maintains the capability to calculate beta spectra in user-defined energy bins. The functionality used to be a separate implementation of a code called BETA-S. The capability was integrated several decades ago has last updated its transition data with the release of ENSDF-95.1 (1995).

BETA-S is able to calculate β^- energy distributions for allowed and first-, second-, and third-forbidden transitions. The ENSDF-95.1 database includes decay data evaluations

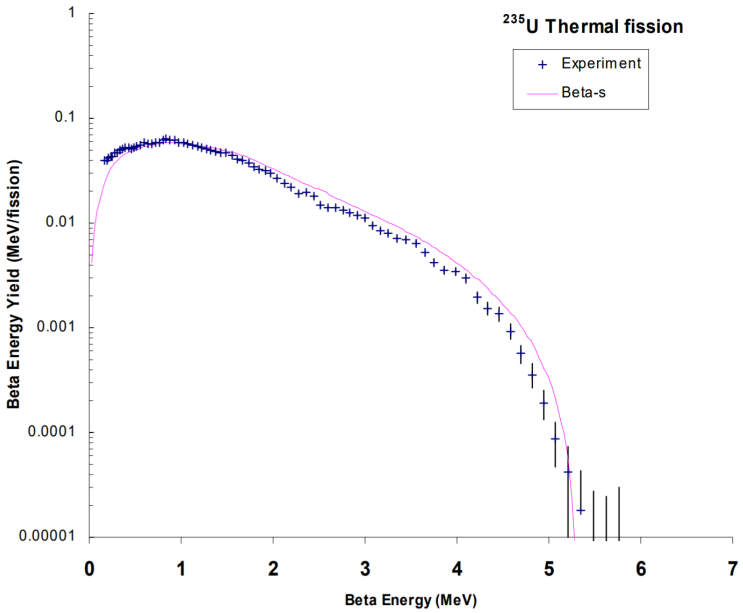

Figure 7.12: Beta spectra produced for the thermal fission of ^{235}U following one second of irradiation, reproduced from Ref. [105]

to adjust the spectra energy based on the average β^- energy. Some transitions for which the β^- type is known are still lacking detailed transition or level data in ENSDF. These transitions are assumed to have one transition of the allowed type in BETA-S. This means that the average energy is a third of the endpoint energy ($E_{avg} = E_{max}/3$). While this may be incorrect, this may skew the spectrum in the high energy region.

The BETA model has been benchmarked against data that was measured from samples irradiated in the Oak Ridge Research Reactor back in 1979, available as the KDDK data set available from the Radiation Safety Information Computational Center (RSICC) [106]. This data is widely used for decay heat data that is used by Standards for loss-of-coolant accident (LOCA) analysis. Figure 7.12 shows the agreement of BETA-S with this KDDK experimental data. However, this data only contains irradiation times of up to 100 seconds, whereas the typical Schreckenbach measurements had their foils irradiated for 12 hours. Data that agrees well with the KDDK data is from Tsoulfanidis, who performed similar measurements to Schreckenbach but to higher irradiation times [107].

A simple ORIGEN model of HFIR is created with an averaged flux spectrum and fuel

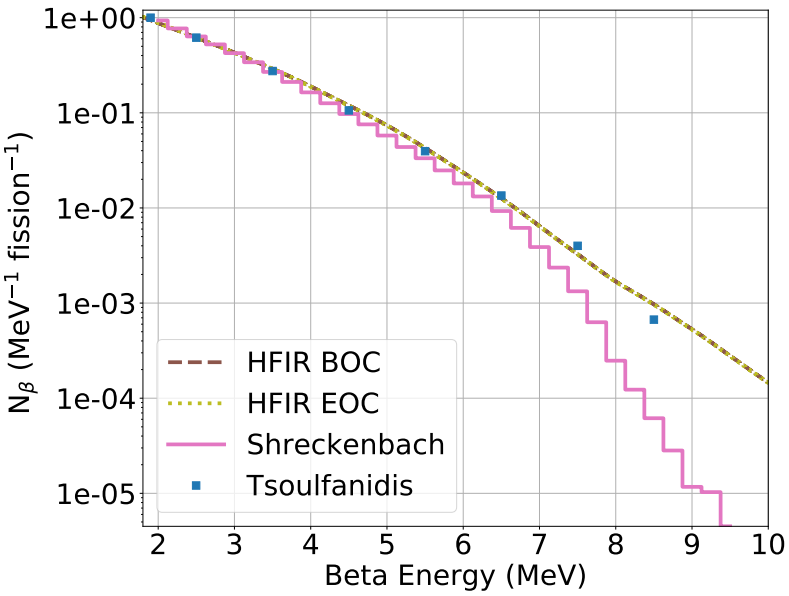

Figure 7.13: Comparison of HFIR β^- spectra for a simple model compared with Schreckenbach data [34] and Tsoulfanidis [107]

composition that approximates a point source. The β^- spectrum is predicted in 10 keV bins and compared to the Schreckenbach data at the ILL reactor [34]. This is also compared with data from Tsoulfanidis that had an irradiation time of about 7 hours [107]. Figure 7.13 shows the β^- spectra for the two data sets with the generated HFIR data in ORIGEN. It can be seen that they all generally agree to the same magnitude up until 7 MeV. Then the Tsoulfanidis data tends to compare better with the HFIR ORIGEN data. The higher HFIR prediction could largely be affected by the simple treatment of allowed β^- decays for which there is unavailable transition data. The general agreement between the methods suggest that they may not contribute to understanding of the reactor anomaly.

To more fully examine the isotopes for which there is missing data, the total β^--decaying fission products are ranked by their activity. The transition information is compared with data currently in the ENSDF database [74]. Table 7.4 shows the largest 20 contributors to the β^- activity of ^{235}U fission for which the spectral and transition data are missing. The Q value utilized by ORIGEN, Q_{ORIGEN} is shown alongside the value currently in ENSDF, Q_{ENSDF} as well as the max value, or endpoint, of the transition. It can be

seen that for several isotopes with max energy values that are higher than what the ENSDF data file says are the endpoint of any transition. The detailed level schemes and updated Q values are now available for several of the isotopes, including ^{101}Nb. The inclusion of some of these extra isotopes has been considered by some papers [32, 108]. The ORIGEN ENSDF file should be updated to include modern evaluations of the transitions.

Table 7.4: Top 20 isotopes with missing ORIGEN β^- decay level data for 12 hours irradiation of HFIR fuel and comparison to current NNDC ENSDF data

Isotope	Activity (Bq)	Fraction of Total Activity (%)	$E_{max,ORIGEN}$ (MeV)	Q_{ENSDF} (MeV)	$E_{max,ENSDF}$ (MeV)
^{101}Nb	1.35E+17	1.12%	5.88	4.569	4.556
^{144}Ba	1.19E+17	0.98%	2.71		
^{133}Te	9.10E+16	0.75%	2.09	2.942	2.63
^{101}Zr	8.33E+16	0.69%	6.54	5.485	5.485
^{103}Mo	8.00E+16	0.66%	3.53		
^{102}Nb	7.70E+16	0.64%	6.47	7.21	6.47
^{103}Nb	5.21E+16	0.43%	5.65		
^{85m}Kr	2.96E+16	0.24%	0.77	0.687	0.536
^{149}Ce	2.11E+16	0.17%	2.27		
i-139	2.11E+16	0.17%	4.97		
ge-86	1.63E+16	0.13%	10.44		
as-86	1.60E+16	0.13%	9.54		
zr-103	1.43E+16	0.12%	7.79		
sn-131	1.27E+16	0.10%	2.12		
sb-129	1.23E+16	0.10%	2.28	2.376	2.271
xe-142	1.19E+16	0.10%	5.46		
cs-144	1.15E+16	0.09%	4.5		
ce-150	1.11E+16	0.09%	3.17		
te-137	1.11E+16	0.09%	1.91		
mo-106	1.02E+16	0.08%	3.96		
nb-104	1.01E+16	0.08%	7.38		
se-88	9.54E+15	0.08%	8.14		
as-83	8.65E+15	0.07%	4.35		
y-102	7.72E+15	0.06%	9.85		
sn-129	7.69E+15	0.06%	3.95	4.022	3.38

7.4 Summary

This section showed how correlations and simulations can affect the PROSPECT measurement specifically and contribute to theoretical predictions. Few studies have quantified spent fuel contributions in great detail. The spent fuel from HFIR contributes less than 0.25% for a given snapshot in time. This effect would be exacerbated for fuel elements that are recently discharged from the core (a day or less). Different reactor models were utilized to evaluate the impact of fission neutron energy on $\overline{\nu}_e$ emissions via fission yields. With an assumption where epithermal fissions are either treated with thermal or fast fission yields, the $\overline{\nu}_e$ spectrum changes negligibly and is unlikely a cause for anomalies. Finally, the beta spectra generation capability in ORIGEN was used and compared to widely-used spectra. Missing data in the code was identified and it is suggested to improve the capability for generating $\overline{\nu}_e$ spectra in ORIGEN.

CHAPTER 8

ABSOLUTE FLUX CORRELATIONS AND MEASUREMENT

In order to apply antineutrino detectors for safeguards applications, the inverse beta decay (IBD) event rate needs to be proportional to the power level and fissile inventory of the reactor to sufficient precision. Given sufficient precision, the detection rate can be ascertained given some knowledge on the burnup evolution of the reactor [9]:

$$N_{\bar{\nu}}(t) = \gamma[(1 + k(t))P_{th}(t)] \tag{8.1}$$

where $N_{\bar{\nu}}$ is the detected $\overline{\nu}_e$ rate, γ is a constant that accounts for the efficiency and baseline of the detector, and $k(t)$ is a time-dependent term depending on the fuel burnup.

The goal of this chapter is to address methods that can help understand the precision of power, which is often one of the larger uncertainties in $\overline{\nu}_e$ measurements. What will be discussed is an absolute flux measurement, correlations with reactor power, and calibration using lithium.

8.1 Absolute Flux Measurement

At HFIR, the time dependence of Equation 8.1 can be ignored and the detection rate can be linearly related to the power. The power is indicative of the overall neutron flux in the reactor at particular locations. It is common to irradiate certain materials in a reactor in order to gain information on the neutron flux or flux ratio at that location, e.g. using indium foils [109, 110]. For a material i in the reactor, the reaction rate for a sample can be calculated from:

$$R_i(t) = N_i(t)\left[1 - e^{-\lambda t}\right]\int \phi(E,t)\sigma_i(E)dE \tag{8.2}$$

In simulation, the neutron flux $\phi(E,t)$ is unknown in absolute terms. The PNF (Equation 4.4) is necessary to be used along with simulation to generate an absolute reaction rate. In MCNP, for example, the neutron flux for an F4 tally is output per source particle and needs the PNF normalization. In other words:

$$R_i(t) = \frac{P\nu}{k_{eff}Q} N_i(t) \left[1 - e^{-\lambda t}\right] \int F4(E,t)\sigma_i(E)dE \tag{8.3}$$

All of the non-power terms can be grouped together as one constant C, as they are well-known for HFIR:

$$R_i(t) = CPN_i(t) \left[1 - e^{-\lambda t}\right] \int F4(E,t)\sigma_i(E)dE \tag{8.4}$$

For an irradiation material, it is assumed that the number density N_i is well known. The decay constant λ should also be well-known. The reaction rate $R_i(t)$ can be precisely determined with counting of the sample following irradiations. With all other terms having relatively low uncertainty, the terms with the largest uncertainties are the power P and tally (integral) term.

Given enough information on the conditions of irradiation and the quantities described above, detailed simulation and sensitivity of the neutron flux spectrum or ratio at a particular location in the core where the sample is irradiated can reduce uncertainty in the tally value. Once that value is well-known, the reactor power can be experimentally determined to high precision. The current precision of the reactor power is around 2%, one of the higher relative uncertainties in $\overline{\nu}_e$ measurements. Such a measurement at HFIR is ideal because of the well-known constants, ability to obtain good counting statistics, and detailed simulation tools available. An absolute flux measurement has been on PROSPECT's laundry list for quite some time.

It was initially discussed to perform an absolute flux measurement using the neutron activation analysis (NAA) laboratory at HFIR to measure the neutron flux precisely at a

particular location. The location intended is the pneumatic tube, from which samples can be inserted and extracted during irradiation. Although some initial data collection has been completed for a set of foils at the beginning of a HFIR cycle, the HFIR event of November 2018 set back the capability for post-processing to be performed [111]. It is anticipated that this data could be available in the coming months and could provide a follow-up to this work.

The procedure for calculating the absolute power would have been as follows:

1. Utilize the NAA counting data to obtain multi-group flux ratios
2. Modify the representative HFIR model to mimic the BOC conditions
3. Calculate the fine-group energy flux in the spatial region in which the measurement was taken with MCNP simulations
4. Perform sensitivity analysis to calculate perturbations of simulated flux
5. Normalize the neutron flux to the reactor power (85 MW)
6. Propagate the uncertainty of the measured data and compare with the calculation and HFIR reported power data

8.2 Thermal Power Correlations

As already discussed, the heat power of the reactor is directly proportional to the expected $\overline{\nu}_e$ detection rate. HFIR maiantains detailed records of its several measures of reactor heat power. PROSPECT has generated tens of thousands of IBD event rates. Due to the relatively small time variation in the reactor parameters and assuming constant detector parameters, the detected $\overline{\nu}_e$ should be directly proportional to the thermal power of the reactor:

$$N_{\bar{\nu}} \, \alpha \, P_{th} \tag{8.5}$$

The goal of this section is to examine the correlation between the two and see what can be learned.

HFIR has several measures of the heat power generated in the core. These include the safety, servo, and computer heat power indications. All power measurement systems have uncertainties of a few megawatts. The operators use a combination of all of these in their procedures for controlling reactor power [112].

Each of the three servo systems independently measure the reactor power level. The input to the servo channel is the neutron flux signal generated in the ionization chambers. The servo instrumentation monitors the flux, flow, inlet temperature, and outlet temperature. The HFIR data heat power recording comes from the individual servo channel indications.

The uncertainties associated with the power measurement instrumentation are outlined in Table 8.1, which shows the uncertainty in the main power instrumentation measurements at HFIR [113]. According to the internal documentation, the average of the three servo channels provides the most accurate measure with an accuracy of $\pm$ 1.82 MW ($\pm$ 2.14%) [113]. The HFIRDATA average reactor heat power has an accuracy of $\pm$ 1.86 MW ($\pm$ 2.19%) [113]. For the servo system, for example, the uncertainty is driven by uncertainties in the analog inputs to the recorder, conversion of the inputs to a heat power measurement, and the calibration accuracy of the instrument itself [113]. The uncertainty in the plant computer is attributable to similar uncertainties.

The heat power data from the three measurements can be obtained from the HFIR internal Proficy Portal database. The three servo channel power average (uncertainty of 1.82 MW) and HFIR DATA average reactor heat power (uncertainty of 1.86 MW) were obtained from each on an hourly basis. Some hours were missing data on the database, so these were not included in the analysis.

Figure 8.1 shows the servo power obtained for several cycles in 2018. These data points coincide with cycles 478-482. The power data is shown on a roughly daily basis for the three different servo channels. The average of the three channels is used in this analysis.

Table 8.1: Uncertainty in thermal power instrumentation measurements for single instrument and their three-channel average [113]

Heat Power Measurement	Single Channel Uncertainty (MW)	Three Channel Average Uncertainty (MW)
Safety		5.70
Servo	3.15	1.82
HFIR Data (Computer)	3.23	1.86

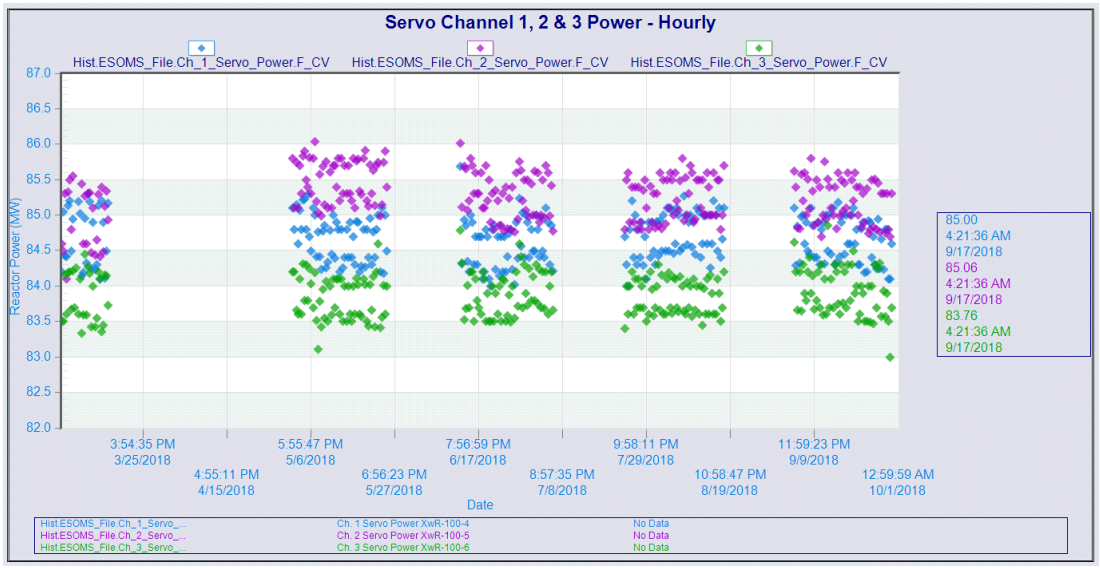

Figure 8.1: Servo power from the HFIR Proficy Portal database coinciding with time since PROSPECT detector installation, cycles 478 (partial) to 482

Table 8.2: Cycle-average power indications for the 5 most recent cycles of HFIR for the servo heat power average and HFIR data heat power average

Cycle Number	Servo ($\pm$ 1.82 MW)	HFIR Data ($\pm$ 1.86 MW)
478	84.53	84.52
479	84.67	84.64
480	84.46	84.66
481	84.59	84.68
482	84.33	84.68

Table 8.2 shows the cycle average of the power data for the two systems. The powers are nearly identical for all four cycles and fit well within the uncertainty of the instrument measurement listed in [113].

$$\bar{P}_{cycle}(MW) = \frac{\int_{t_{start}}^{t_{end}} P(t)dt}{\int_{t_{start}}^{t_{end}} dt} \approx \frac{\sum_{i}^{N_{hours}} P_i}{N_{hours}} \tag{8.6}$$

The distribution of the servo power data for each cycle is shown in Figure 8.2. It should be noted that in the procedure for controlling reactor power, the pool heat power is assumed to be 0.35 MW [112]. It is possible that this can contribute to the lower average cycle powers, although all of the powers are in agreement with the nominal 85 MW within uncertainty limits.

8.2.1 Comparison with Detector Event Rates

For HFIR, where the fuel evolution is relatively small, the IBD rate should be directly proportional to the power level:

$$N_{\overline{\nu}}(t) \; \alpha \; P_{th}(t) \tag{8.7}$$

The PROSPECT experiment has collected tens of thousands of reactor $\overline{\nu}_e$-induced IBDs since its installation [90]. The detected IBD rates can be correlated with the power obtained from the previous section.

The IBD event rate from PROSPECT is taken on a daily average. This IBD event rate

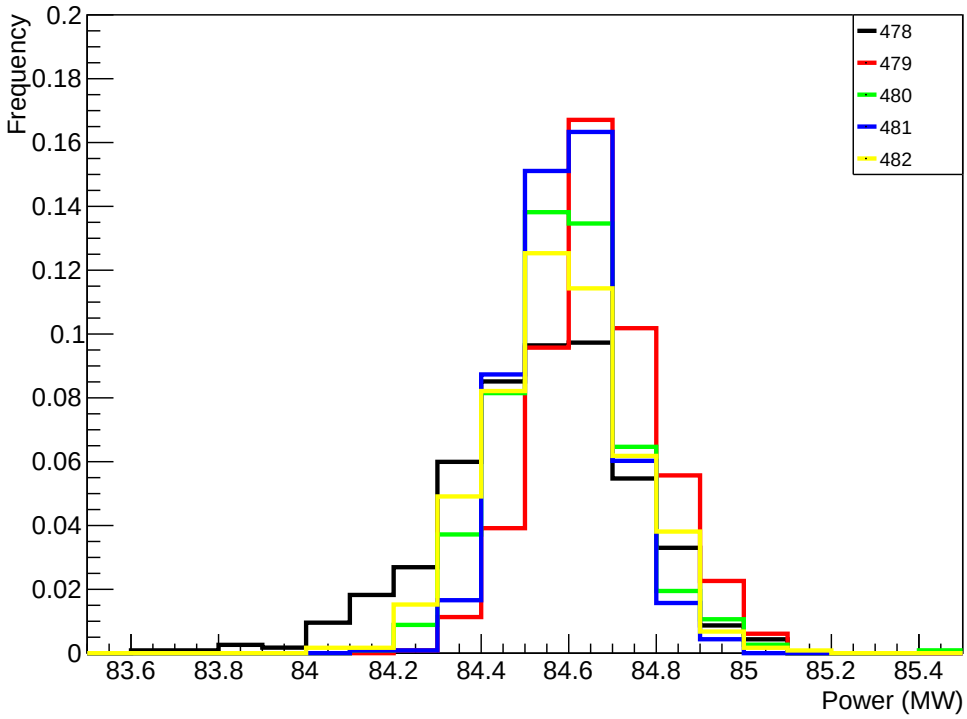

Figure 8.2: Normalized histogram of hourly servo heat power for the 5 most recent cycles of HFIR (478-482)

does not subtract out the accidental rate, i.e. the IBD-like events that are post-analyzed to not represent $\overline{\nu}$ coming from the fission of HFIR. The reactor-on rates vary between 1000 and 1350 IBD events per day, with approximately 750 being attributable to HFIR fissions.

Figure 8.3 shows the servo and HFIR data heat power averages versus IBD event rate over all cycles vs. the PROSPECT data. There is little correlation between the power and IBD event rate at this precision; the correlation coefficient is ≤ 0.1, therefore the correlation is assumed to be insignificant. The uncertainty associated with the power is much higher than that for the $\overline{\nu}_e$ detection rates. The HFIR reactor power tends to read lower than 85 MW; this is true of nearly all data points. One possible explanation is in the procedures for nuclear operations where the pool heat power is assumed to be 0.35 MW. This needs to be investigated further. Nonetheless, the uncertainty band on the power is larger than the data range itself.

These results show that it is difficult to compare the power level, i.e. fission rate, to the IBD detection rate at this level of precision. The uncertainty in the power level seems to be the driver of lacking the capability to detect percent-level changes in reactor power. Advanced instrumentation or an absolute flux measurement may be needed to reduce this uncertainty.

8.3 Calibration using Lithium

While reactors are an ample source of antineutrinos, the detected spectrum falls off significantly past 8 MeV. It has been suggested that lithium can be used to produce high-energy $\overline{\nu}_e$ that can artificially harden the spectrum and help understand neutrino oscillation and high-energy uncertainties [114]. Given a known amount of lithium decays, it is possible to use the increased hard flux to study several things about the $\overline{\nu}_e$ spectrum, detection capability, and oscillation.

Irradiation of lithium in the core permits the study of signal-to-background at high energies. The advantage with the PROSPECT detector is the low cosmogenic backgrounds

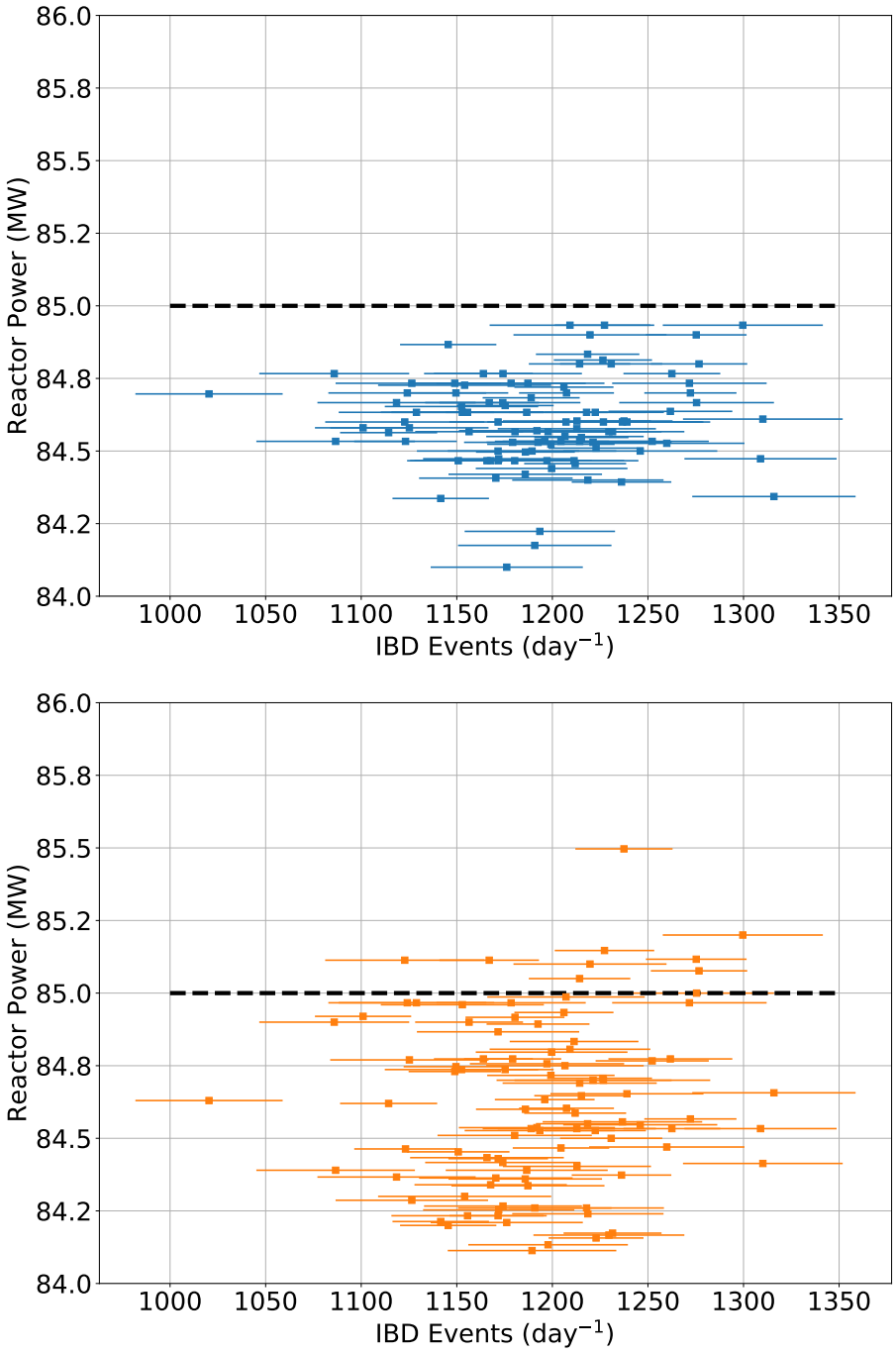

Figure 8.3: Servo (top) and reactor computer heat (bottom) versus IBD daily event rate for cycles 478 to 482. Note that the uncertainty in the IBD event rate is shown but the uncertainty in power level for both cases is larger than the range of the y-axis.

above 8 MeV [115]. This is highlighted in Figure 8.4, which shows the reactor-on and reactor-off count rates for a single HFIR cycle. It can be noted that the reactor IBD candidates fall off significantly in this high-energy range as well.

More importantly for safeguards, low reactor backgrounds in this energy range means that an insertion of a $\overline{\nu}_e$ source can calibrate the detector. If the amount of lithium inserted in the core is known, it is possible to calculate the reaction rate of ^{7}Li(n,g)^{8}Li from a well-characterized neutron flux spectrum and therefore the precise activity of ^{8}Li, as was done in Chapter 6. Reactor simulations provide an opportunity to correlate the activity of ^{8}Li with the power of the reactor. The formulation of the $\overline{\nu}_e$ rate from the reactor power, Equation 8.1, can be modified to include lithium activity A_{Li}:

$$N_{\bar{\nu}}(t) = \gamma[(1 + k(t))P_{th}(t) + A_{Li}(t)] \tag{8.8}$$

$A_{Li}(t)$ would be the time-dependent ^{8}Li activity.

Chapter 6 discusses the quantification of a similar activity term for unwanted material contributions. In this case, the quantification of a well-understood A_{Li} can help quantify the power and uncertainty thereof during a reactor-on period.

First, lithium materials must be selected. One consideration for material selection is the prior inclusion of lithium targets in the core. To the author's knowledge, no primarily lithium-bearing targets have been irradiated in recent history in HFIR, except for the RB-17J and -15J experiments which contained approximately 50 grams of molten lithium as a cover [116]. Common lithium-bearing compounds are analyzed to select test cases. The two compounds selected are lithium carbonate (Li_2CO_3) and lithium fluoride (LiF) due to their larger density compared to other lithium compounds. They are primarily considered due to their high density compared to other lithium compounds without the dominance on molar mass by another bonded element. Lithium hydride (LiH) was also considered but was excluded due to its low atomic density of ^{7}Li relative to that of LiF, for example.

Next, it must be decided where in the core the targets must be placed. The main options

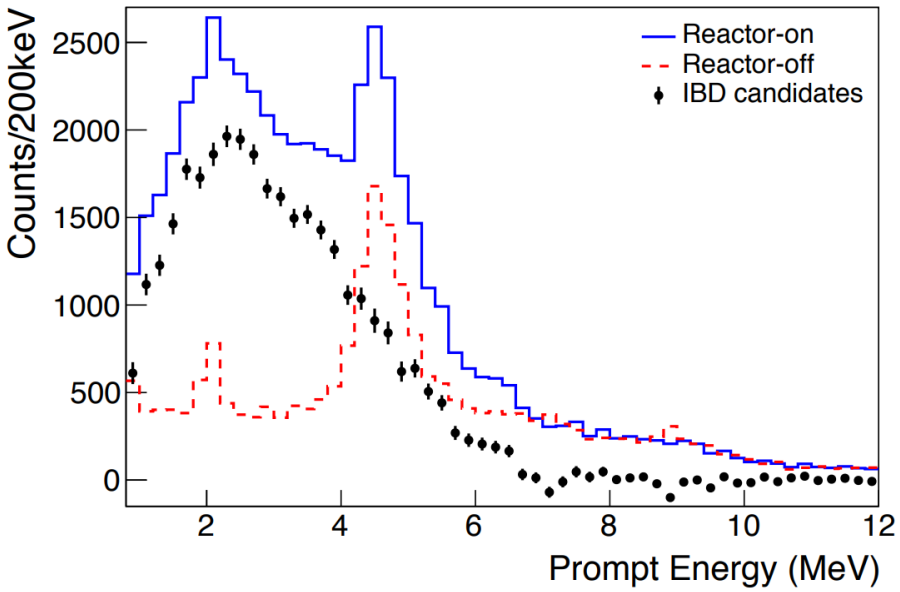

Figure 8.4: Data from the PROSPECT experiment, showing the low background in the high-energy regions [115]

are the flux trap target (FTT) region, removable beryllium (RB) positions, or vertical experiment facilities (VXF). By design, the FTT has the highest total and thermal flux. More importantly, the ^{7}Li competes with ^{6}Li in the thermal region for neutrons. By maximizing the cross-section and flux, the FTT region is selected as the irradiation location. The FTT is also the most central region with an outer diameter of $\approx$ 5 cm, therefore any oscillation in this small core region should be negligible.

Two cases are made with loading of Li_2CO_3 and LiF in the flux trap positions. The cells of the representative model [48] are modified to include the lithium targets in those that receive high flux. For the first case, each material is added into two target positions, one in the inner ring and one on the periphery. For the second case, another target of each is added in a middle ring. The locations are outlined in Figure 8.5.

Figure 8.5: Loading of lithium targets in flux trap for two cases

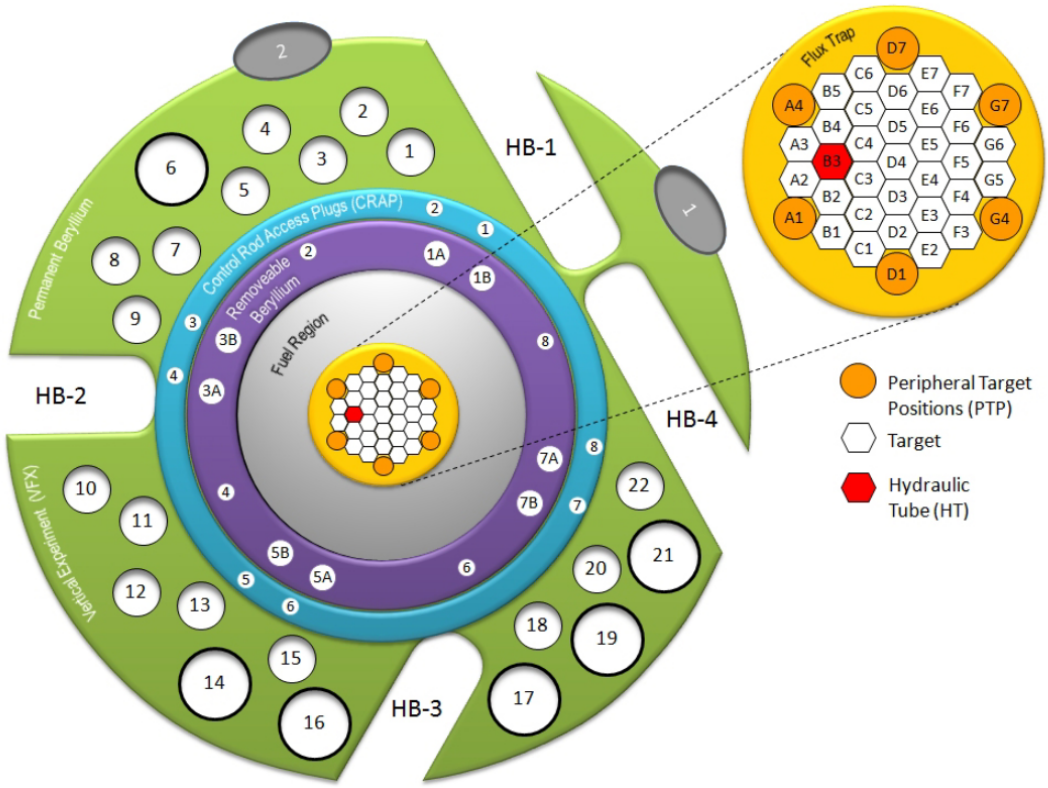

Compound	Case 1	Case 2
Li_2CO_3	D5, G5	D5, G5, F6
Grams ^7Li	22.2	37.7
LiF	A3, D3	A3, D3, B2
Grams ^7Li	19.7	33.5

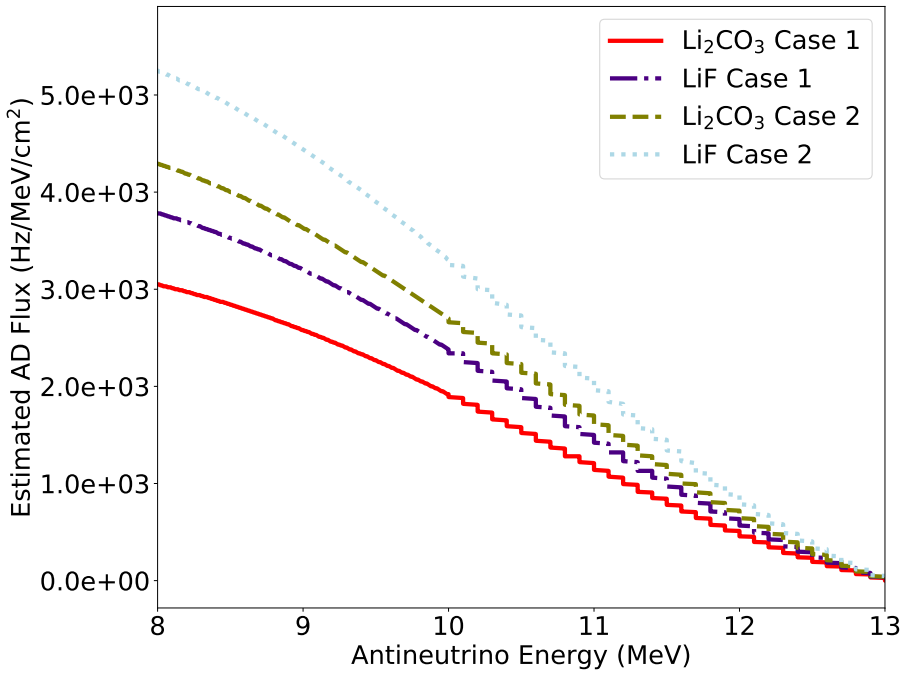

Material (Case)	Flux (E $>$ 8 MeV) (Hz cm^{-2})
Li_2CO3 (1)	7.66×10^5
LiF (1)	9.51×10^5
Li_2CO3 (2)	1.08×10^6
LiF (2)	1.32×10^6

Figure 8.6: Estimated absolute flux of $\overline{\nu}_e$in the detector volume from ^{8}Li

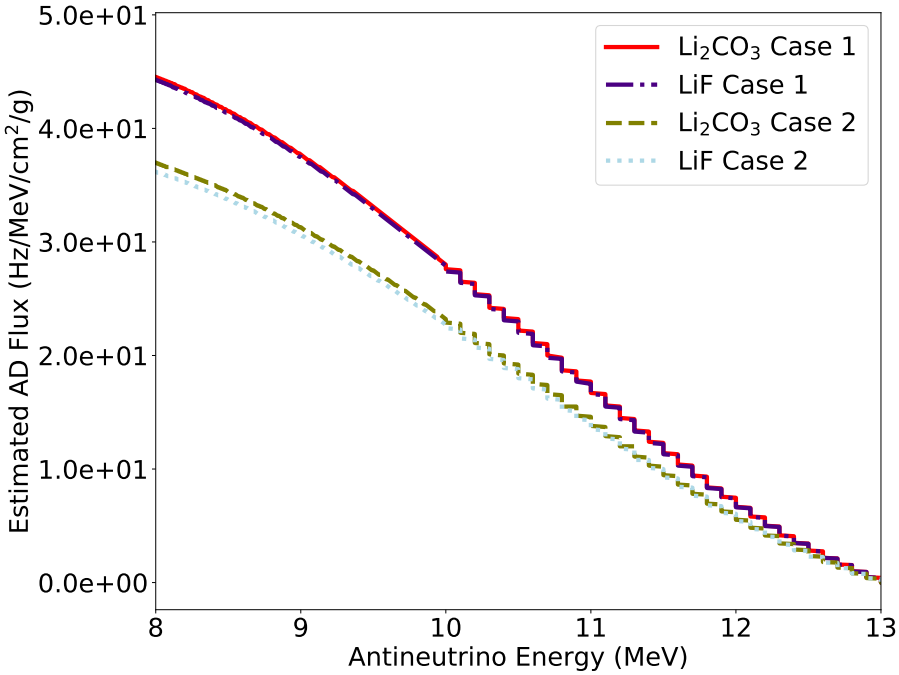

Material (Case)	Flux (E > 8 MeV) (Hz cm^{-2} g^{-1})
Li_2CO3 (1)	1.12×10^4
LiF (1)	1.11×10^4
Li_2CO3 (2)	9.28×10^3
LiF (2)	9.09×10^3

Figure 8.7: Estimated absolute flux of $\overline{\nu}_e$ in the detector volume from ^{8}Li per gram of compound loaded

Table 8.3: Values used for calculation of ^{8}Li $\overline{\nu}_e$ (E $>$ 8 MeV) event rates in PROSPECT-like detector

Parameter	Value Used	Reference
$\left(4\pi\bar{L}^2\right)^{-1}$ (cm^{-2})	1.28 $\times 10^{-7}$	Equation 5.8
S (Hz)	1.32 $\times 10^{6}$	Figure 8.6
N$_{proton}$	2.25 $\times 10^{29}$	[46]
σ_{IBD} (cm^2)	6.8 $\times 10^{-42}$	[117]

8.3.1 Estimated Detector Flux

The ^{8}Li activities are then used to calculate estimated $\overline{\nu}_e$ detection rates in a PROSPECT-like detector. The number of $\overline{\nu}_e$ detected follows the equation:

$$D_{\overline{\nu}_e,det} = \frac{S}{4\pi\bar{L}^2} N_{proton}\sigma_{IBD} \tag{8.9}$$

where $\bar{L}^2$ is the average baseline, *S* is the $\overline{\nu}_e$ source density (Hz), N$_{proton}$ is the total proton density in the active volume, and σ_{IBD} is the IBD cross-section in the energy range of interest.

Figures 8.6 and 8.7 show the spectrum of absolute $\overline{\nu}_e$ flux from the expected target arrangement at the PROSPECT detector. The figures also show the total integrated $\overline{\nu}_e$ flux above 8 MeV. The results are reported on an absolute basis for the situation in which a similar experiment is designed. The results are reported on a per gram basis to help understand what core loading may be needed to achieve a certain amount of flux. The flux per gram can be considered relatively high at this loading as the inclusion of more targets will suppress the flux and therefore more production of ^{8}Li from ^{7}Li.

8.3.2 Reactor Performance Analysis

The inclusion on lithium targets in the flux trap has a significant impact on the cycle length due to the reactivity decrease from the large ^{6}Li thermal cross-section. The natural concentration of lithium contains 7.59%at ^{6}Li and 92.41%at ^{7}Li. In order to produce a sufficient amount $\overline{\nu}_e$ from ^{8}Li, a large amount of ^{7}Li is needed because its thermal cross-section is

low. However, the trade-off of lithium loading with the reactivity penalty from ^{6}Li makes it difficult. This will be discussed further in Appendix C.

8.4 Summary

The absolute $\overline{\nu}_e$ detection rate is important for understanding discrepancies between predicted and measured flux. The reactor power is directly proportional to the fission rate and is often one of the higher uncertainties in obtaining an absolute flux measurement (on the order of 2%). A calculation to obtain absolute flux using activation foils was not performed but the process for such a measurement at HFIR was outlined. However, the correlation between reactor power and $\overline{\nu}_e$ detection rate revealed difficulty in correlating power at percent level uncertainty. HFIR provides a challenge because the power level remains constant throughout the cycle, except for some short training startups that would not provide enough $\overline{\nu}_e$ detection statistics for correlation studies. Finally, a calculation was performed to quantify the amount of lithium loaded in the flux trap to artificially harden the spectrum and be used for absolute reactor power normalization. This work pushes the current work with PROSPECT to obtaining a greater understanding of the absolute flux measurement.

CHAPTER 9
CONCLUSIONS, IMPLICATIONS, AND FUTURE WORK

The focus of this work was to characterize the antineutrino source term coming from HFIR and to identify and quantify potential sensitivities that could impact analysis of the antineutrino spectrum. The goal of this section is to provide conclusions to the work, address potential implications of this work into the state-of-the-art in antineutrino detection, and identify potential future areas of work.

9.1 Conclusions

In Chapter 3, three research questions were asked. Conclusions to those research questions based on the work documented in Chapters 4-8.

The first question dealt with the traditional modeling and simulation of fission rates and distributions in HFIR. The fission rates and distributions were quantified. The PROSPECT experiment seeks to measure the pure ^{235}U spectrum from HFIR. It was confirmed that over 99.5% of fissions come from ^{235}U. The fission $\overline{\nu}_e$ spectrum decreases slightly with the buildup of the ^{239}Pu fraction, but no more than 0.3% in any energy bin for the two prediction methods discussed. The fission distribution flattens out over the cycle but has little impact on the change in $\overline{\nu}_e$ flux at the detector. The fission-weighted baseline concept is created, which may be useful for similar short-baseline experiments and/or larger cores. It confirms from radially-, axially-, and azimuthally-dependent fission rates that the reactor can be considerd as a near point source of $\overline{\nu}_e$.

The second question asked something that is unique to HFIR in its irradiation of different materials. A methodology for selecting non-fuel candidates for $\overline{\nu}_e$ emissions is created and candidates are selected from materials according to HFIR design and typical irradiation materials. The reaction rates and activities are quantified in a variety of regions in the

reactor. The results found that the ^{28}Al contribution is the highest and contributes as high as 8% in the lowest energy range above IBD threshold. ^{6}He and ^{52}V were both found to have non-negligible contributions below 1%. The contributions of ^{28}Al, ^{6}He, and ^{52}V are significant enough to be included in PROSPECT analysis. The loading of NpO_2 targets could have a substantial impact depending on the number loaded and number of previous cycles irradiated. Cycle 482 saw the highest rates of ^{239}Pu fissions due to the full loading of 9 VXFs with NpO_2 in their third irradiation cycle. The fission rate averaged 0.4% of the total fuel fission rate, even higher than the fission rate of ^{239}Pu in the fuel material itself.

The third question leveraged the research nature of HFIR along with computational tools to aid in contributing to other factors relating to the $\overline{\nu}_e$ spectrum measurement. Spent fuel contributions were quantified from correlations and internal HFIR data. The spent fuel impact on the $\overline{\nu}_e$ spectrum was found to be less than 0.2%. Some impacts were also made in the realm of theoretical predictions of $\overline{\nu}_e$ spectra. Reactor simulations were performed to understand the impact of fission neutron energy on summation predictions for various reactors. The results showed that the treatment of fission neutron energy is unlikely to be the cause of $\overline{\nu}_e$ anomalies. Power data from HFIR showed that it is difficult to notice percent-level power changes with current accuracies in equipment. Work was initialized to perform analysis on the reduction of uncertainty from absolute flux measurements. The beta capability in ORIGEN was also used to calculate expected spectra and compared to gold-standard predictions, illuminating the needs for some updates. This area of work provides the greatest opportunity for future development.

9.2 Broader Implications and Safeguards Impacts

The PROSPECT detector has made great strides in furthering the understanding of neutrino spectra and oscillations. The goal of this section is to contextualize the PROSPECT experiment as the state-of-the-art and antineutrino detectors (ADs) as a whole to analyze what gaps there are between the current technology and next steps for implementation of

ADs as potential monitors in the safeguards regime. This approach is designed to frame the current applicability of ADs into a broader context.

As discussed in Chapters 1-2, ADs serve many purposes that can serve the needs of the safeguards and nonproliferation community. These include the verification of operational status, determination of reactor power, and estimation of the fissile fuel inventory. The international community has and should continue to invest in antineutrino detectors and their technological improvements as they can achieve many of these objectives under varying time frames and level of precision. As of today, ADs have already been implemented around the world at reactors of various types and sizes. The technology is non-intrusive to the core, robust against tampering, and continuous in its data production. It is easy to tell if a nuclear reactor is undergoing operation with a properly-positioned antineutrino detector. Other experiments have also shown the reliability of antineutrino detectors in gaining information on fuel evolution and burnup. The demonstration so far of this technology has garnered interest from the international community for at least two decades.

In having a reliable power and burnup monitor, the IAEA seeks timely detection of any violation by a State of its safeguards obligations. They require the timely detection of diversion of nuclear fuel and the lack of undeclared production of nuclear material, primarily plutonium in the case of nuclear reactors. Covert plutonium production is cause for alarm because only eight kilograms of the material is necessary to manufacture a simple nuclear device, designated a significant quantity (SQ). Undeclared production of nuclear material could include several different paths, but has historically taken place at reactors fueled with natural or low-enriched uranium and moderators more conducive to increasing the likelihood of neutron capture on ^{238}U. The PROSPECT detector is unlikely to detect plutonium production at HFIR due to the breeding and fission rate of ^{239}Pu remaining relatively low.

PROSPECT is advancing the field of ADs by contributing its novel design and implementation to bridge the gap between the theoretical and experimental understanding.

PROSPECT is achieving what it sets out to do: 1) measure the nearly pure ^{235}U flux and 2) search for neutrino oscillations. Both of these have significant impacts in advancing AD technology. The precision of an isotope's known antineutrino spectrum is directly proportional to the time it takes to make conclusions regarding accordance with safeguards agreements; lower uncertainty breeds such in derived values. Knowing the spectra to high precision (addressed by goal 1) and explaining phenomena that could contribute to uncertainty in those predictions (addressed by goal 2) are both necessary given the current understanding of neutrino spectra.

From the detection side, PROSPECT has made a significant achievement in demonstrating AD technology at a short baseline near the surface. PROSPECT has achieved excellent background rejection capabilities and the best signal-to-background signal attained for a surface-level detector. The PROSPECT detector was also able to confirm reactor antineutrino production from HFIR at 5σ in under two hours. All of these provide demonstration of improvements of the technology from previous experiments.

Despite these advancements, the deficit and shoulder in the antineutrino spectrum have plagued physicists for many years. The understanding of the neutrino spectra is one of the major hurdles to wider implementation for safeguards applications; improvements in size, cost, and detector efficiency can also be improved. While the consensus on the cause of the neutrino flux deficit and bump is slowly narrowing, the state-of-the-art is not where it needs to be. Current and future experiments as well as work on theoretical models will continue to chip away at the uncertainty. Work in understanding the systematic uncertainty of neutrino predictions and measurements is necessary to advance them to be a reliable measure for safeguards verification.

ADs can also benefit from future reductions in size and cost without significant tradeoffs in efficiency. Much of this is expected to come with the higher sensitivities gained by reducing the uncertainties described previously. Mobile systems would also allow improvements in a wider range of applications. Full maturation of the technology could allow ADs

to be implemented early in reactor licensing and construction phases under a safeguards-by-design approach. Advanced reactors can benefit from this early in the licensing process and can demonstrate the technology at their more novel designs. Envisioning sufficient improvement in AD performance and agreement with theoretical predictions, the scalability and flexibility can enable a wider range of implementation. Experts have begun to examine the application of ADs to monitoring of clandestine nuclear reactors and nuclear weapons explosions. With continued support and advancement in the technology, ADs have a promising future in the field of safeguards and nonproliferation.

9.3 Future Work

This research illuminated many areas of potential work that would be significant for HFIR modeling, safety, neutrino analysis, and improvements in antineutrino predictions and applications.

1. In Chapter 7, it was discussed that the β^- spectra generation capabilities in the ORIGEN depletion code of SCALE could be updated. The code makes some assumptions, including the average energy of a β^- transition when lacking transition data. The update from ENSDF-95.1 to more modern data sets released through the Nuclear Data Sheets could have an impact on the reliability of β^- predictions, particularly at higher energies. To take it a step further, the $\overline{\nu}_e$ spectrum could also be calculated for isotopes that have known level schemes.

2. In Chapter 8, it was discussed how an absolute flux measurement could be achieved at HFIR using the pneumatic tube (PT). This capability allows for a range of experiments to be carried out at so that the flux spectrum can be characterized. With a highly characterized neutron flux and core configuration, it may be possible to get a higher precision on the reactor power. Additionally, because the power level was difficult to determine to under 2% precision, it would be beneficial to test a similar

method for a reactor that has a fluctuating power or is load-following.

3. In Chapter 8, it was also shows that lithium can be inserted in the core to artificially harden the $\overline{\nu}_e$ spectrum by producing neutrinos from ^{8}Li that are of higher energy than emitted in the nominal reactor spectrum. This can be used to test the efficiency of the detector at higher energies and be of potential use in calibration. The main issue with this proposition is the irradiation of ^{6}Li, which drastically reduces the cycle length on a per gram basis. Enrichment of lithium in ^{7}Li would be necessary to reduce the negative reactivity impact of ^{6}Li. Target design at HFIR could help achieve this. This work could be of potential interest for detecting weapons-related tritium production at nuclear reactors because lithium is primarily used as a target.

Appendices

APPENDIX A

FISSION DISTRIBUTIONS BY DAY

In Chapter 5, the fission distribution is calculated in the radial and axial directions. Here, the flattening of the distribution can be seen more clearly with the inclusion of the relative fission rate distributions for each day in the cycle. Figures A.1-A.4 show the relative fission rate distribution at each day in the cycle. All are plotted on the same scale so that the differences throughout the cycle can be seen.

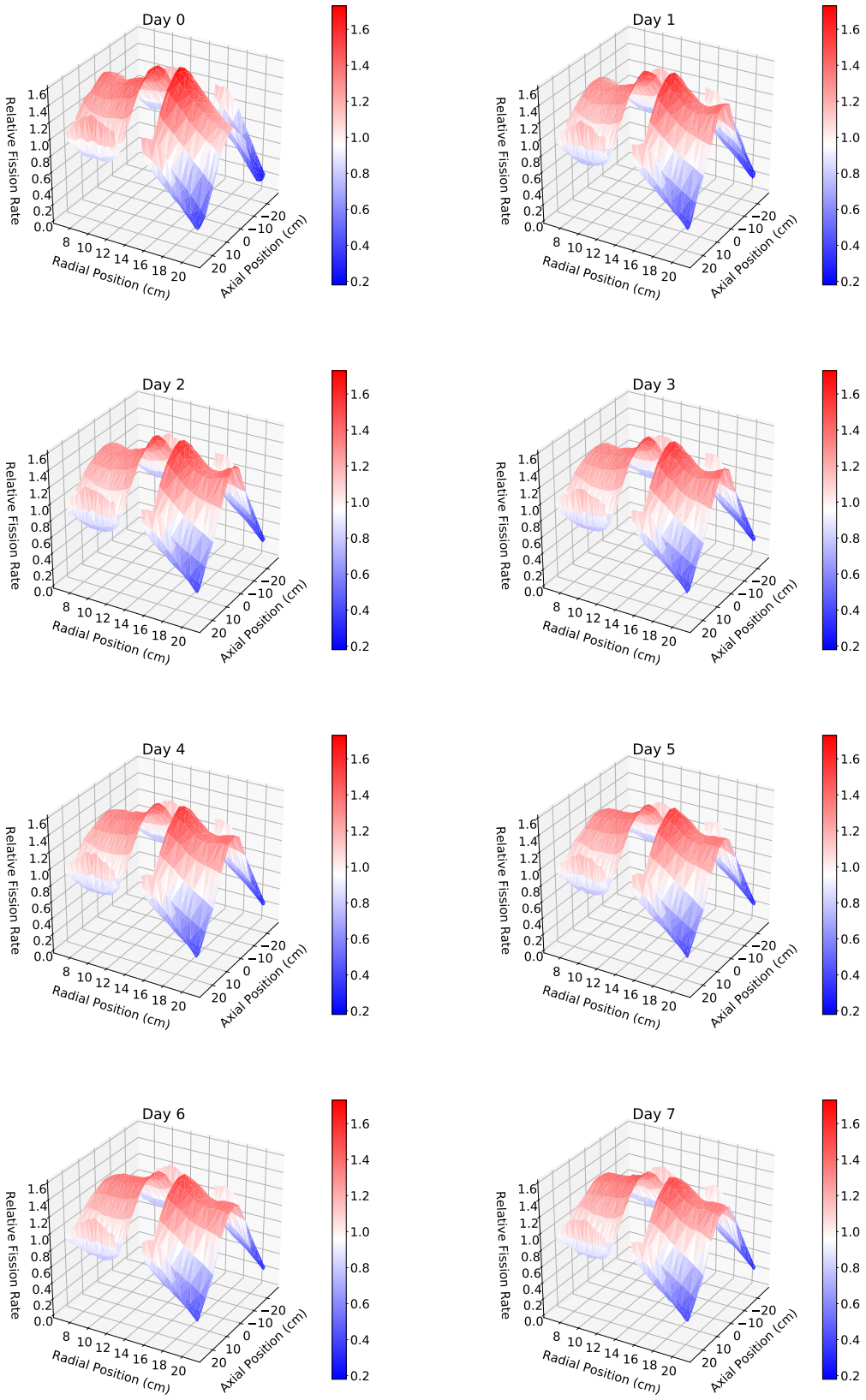

Figure A.1: Fission rate distribution for days 0-7

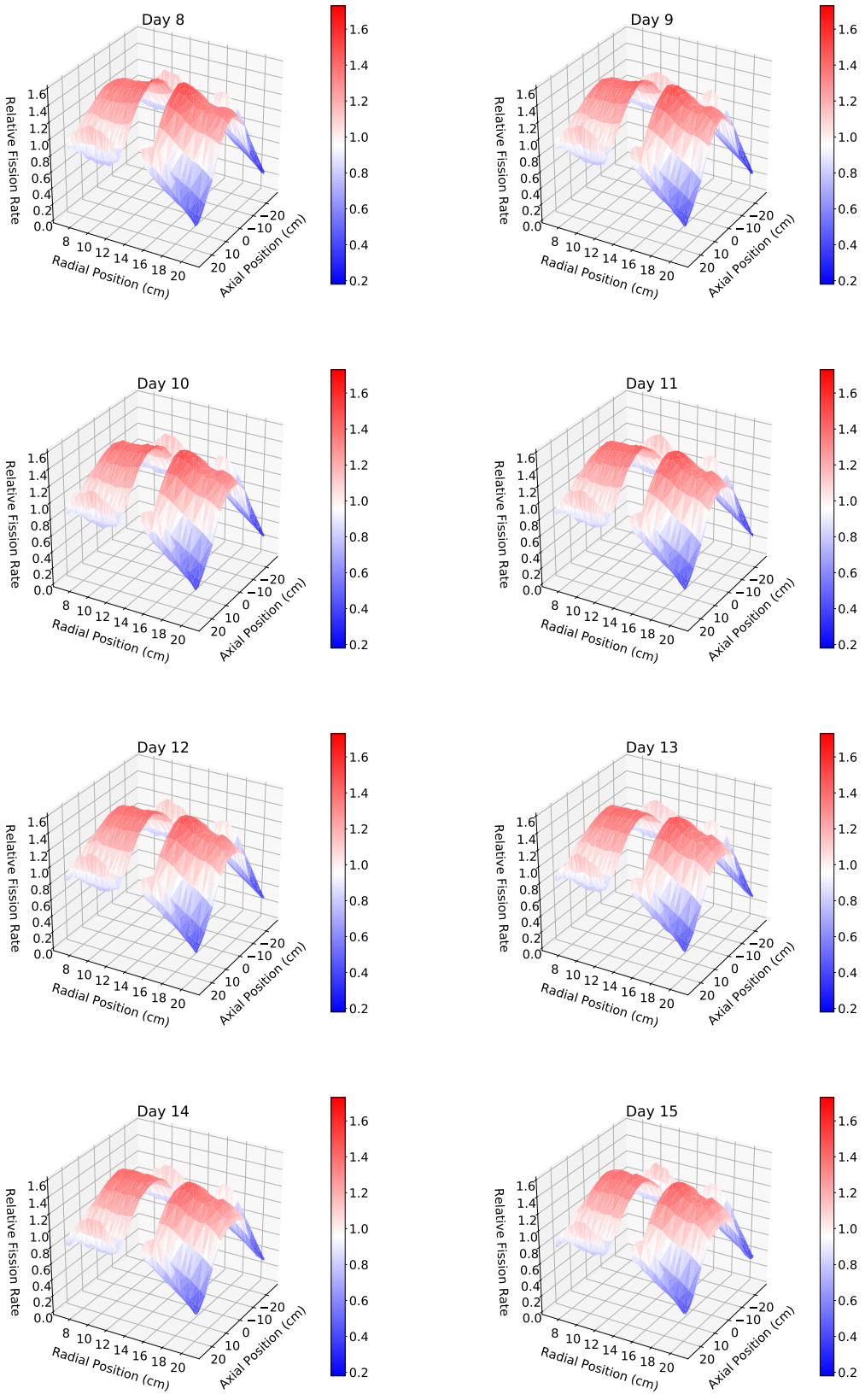

Figure A.2: Fission rate distribution for days 8-15

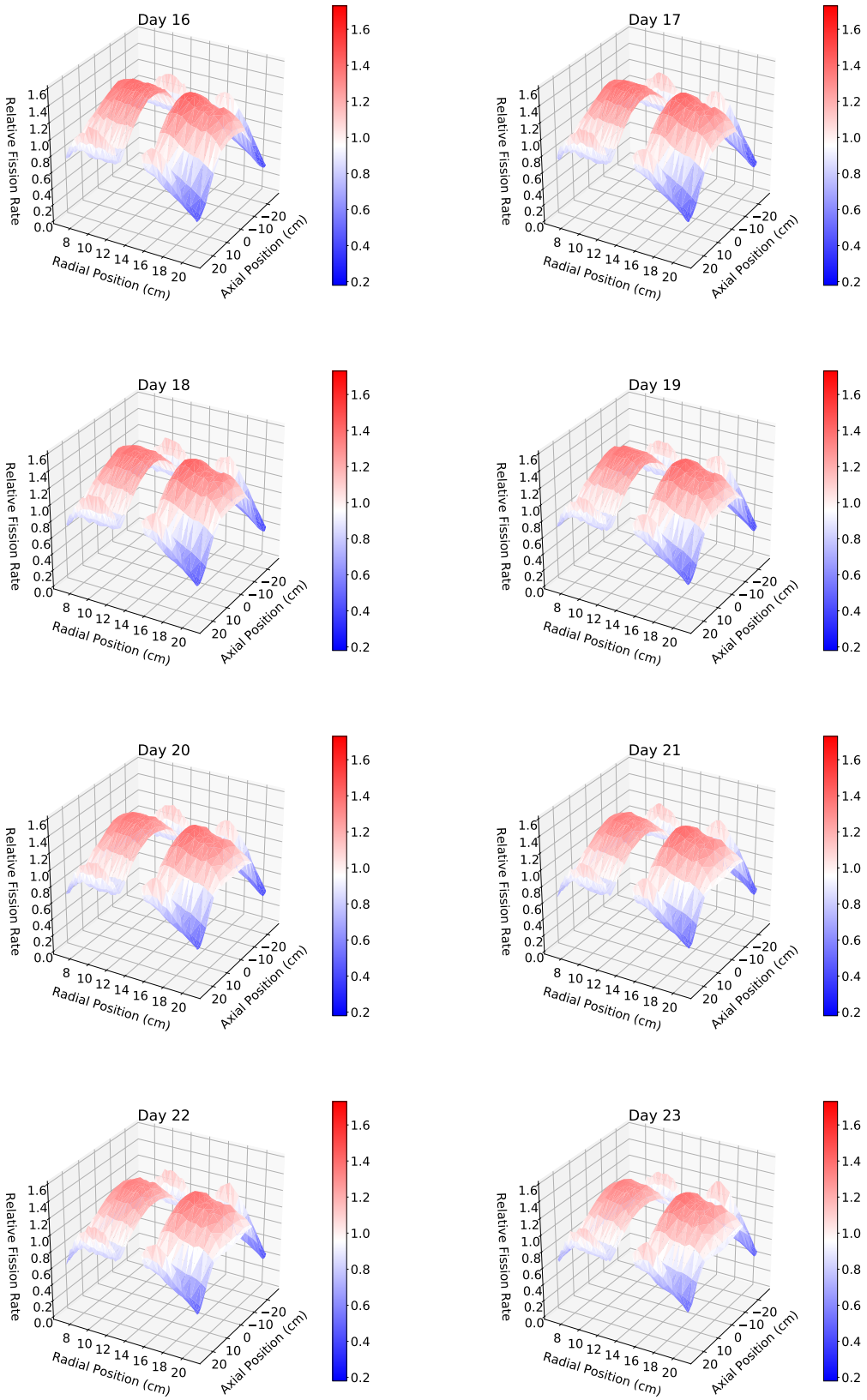

Figure A.3: Fission rate distribution for days 16-23

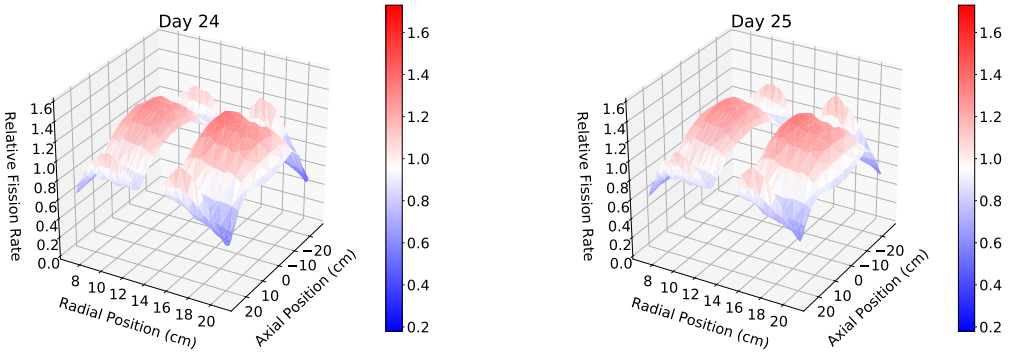

Figure A.4: Fission rate distribution for days 24-25

APPENDIX B

REFLECTOR POISON CONCENTRATIONS

The calculations for $\overline{\nu}_e$ candidates in the beryllium reflector in Section 6.4 can also benefit the HFIR Nuclear Safety and Experiment Analysis group in their calculation of the impacts of reflector poisons on beryllium degradation [82]. Increased ^{3}He and ^{6}Li concentration reduces reactivity and therefore cycle length with increased concentration. Buildup of gases such as tritium and ^{4}He can increase thermal stresses. The number of prior irradiation cycles of a fresh removable beryllium (RB) reflector is used in calculation for the estimated symmetric critical control element position (ESCCEP) calculation required for startup. Figure 6.10 shows the relevant reactions and decays that contribute to the creation of these isotopes. Some contributions to the knowledge of ^{6}Li and ^{3}He are discussed here.

B.1 Lithium-6

^{6}Li is one of the neutron poison products in the reflector. It is built up over the first few cycles and remains relatively unchanged due to core configurations and shutdown length. Figure B.2 shows the concentration of ^{6}Li relative to the equilibrium value as a function of axial position. It is shown for two cases, the first of which is when only the RB is assumed to be fresh. The other is when all regions (RB+SPB+PB) are fresh. The first situation is more common as the RB is replaced every few years. The PB, however, is only changed every two to three decades, but is expected to be replaced in the mid-2020s.

One phenomenon that this work found was a discrepancy in the ^{6}Li concentration as a function of axial position. Figure B.2 shows the axial concentration of ^{6}Li at the end of the first 10 cycles for the innermost radial ring of the RB. It can be seen that the ^{6}Li concentration is higher in the upper axial half of this region. The reason for this is that the outer control element, which moves upward throughout the cycle, has its black region closest to

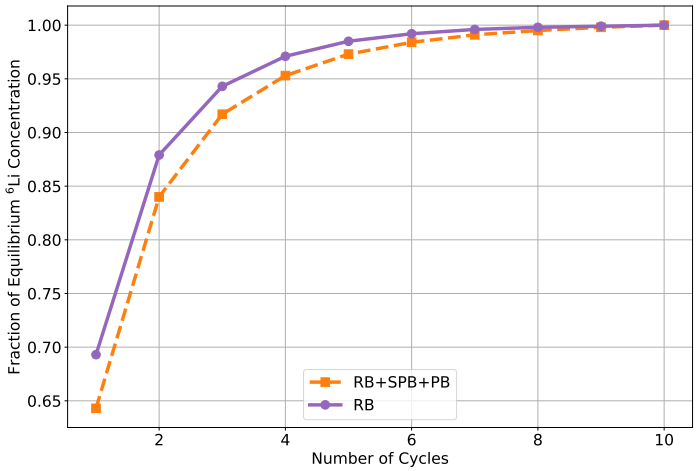

Figure B.1: Fraction of equilibrium ^{6}Li concentration as a function of cycle length for the entire reflector, in the cases of assuming the RB is fresh and assuming all regions (RB+SPB+PB) are fresh

the innermost radial ring of the reflector. Its presence hardens the spectrum, allowing for more ^{9}Be(n,α) reactions relative to ^{6}Li(n,γ). The production rate of ^{6}Li increases relative to its destruction rate when the control rod is near, resulting in a lopsided distribution. The equilibrium concentration over the first few cycles can also be seen in Figure B.2 as it tends to converge after 5-6 cycles.

Figure B.3 explains the control element effect more clearly in terms of neutron flux. It shows the relative difference in neutron spectra in the upper and lower half of the RB at BOC, when the black regions overlap the most with the RB regions. Region 1 is the upper- and lower-most cells, region 2 are the next two segments closer to the midplane, and region 10 are the two regions sandwiched around the central cell (19 total axially). The 'void' cases show the same difference if the black regions of the control elements are voided. This figure shows that the upper regions of the core have a 10-20% higher fast flux and a 30-50% lower fast flux. The regions closer to the center see less of this difference. These spectral differences can clearly explain the axial shape of the ^{6}Li concentration. In the future, this effect could potentially help explain axial variations in fuel fission rate or

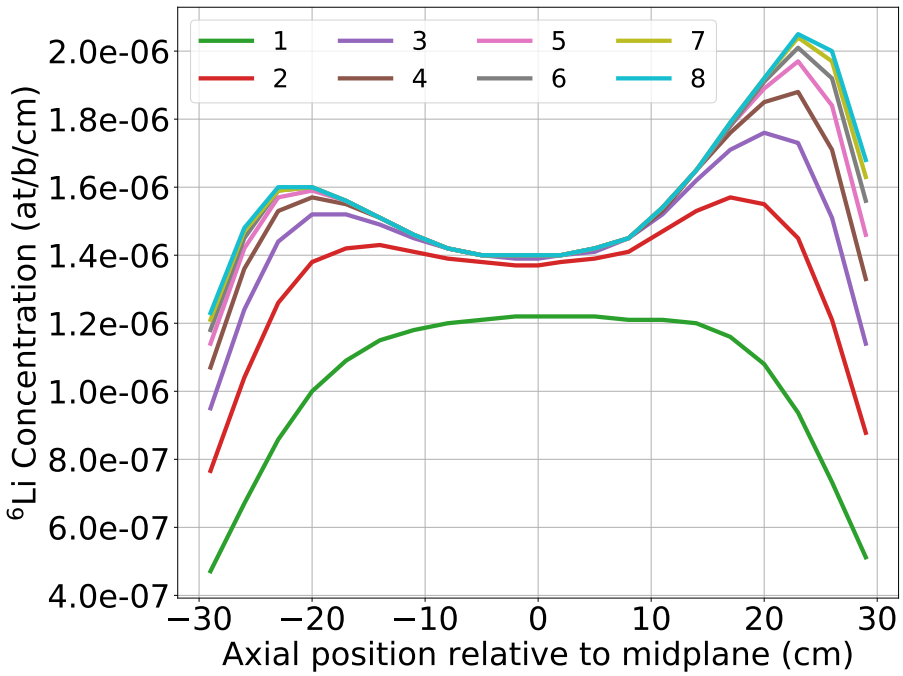

Figure B.2: Concentration of ^{6}Li in the innermost radial ring of a fresh removable beryllium (RB) reflector at the end of cycles 1-8

experimental facilities in the reflector.

B.2 Helium-3

The ^{3}He concentration in the core is created from the decay of tritium, ^{3}H, which is created from the large cross-section ^{6}Li(n,α) reaction. Due to the buildup of ^{6}Li over the first several cycles, the ^{3}H concentration also increases drastically over the first few cycles and then steadily with each cycle that follows. Upon shutdown of the reactor, the ^{3}H can decay into ^{3}He without sufficient neutron absorption on ^{3}He. ^{3}H has a half-life of 12.32 years [118]. Thus, the shutdown length has an impact on the amount of ^{3}He that has built up in the reflector regions. The shutdown length at HFIR varies from 18 or 19 days for a short outage to 45+ days for a long outage. Outages may be even longer for large maintenance activities.

The procedure developed in Section 6.4, shown in Figure 6.1, to calculate activities of

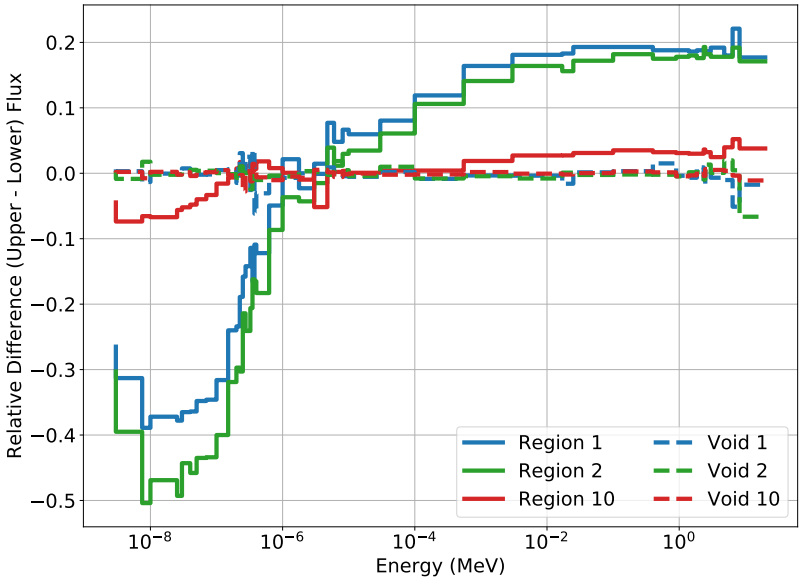

Figure B.3: Difference in neutron spectra in the innermost radial ring of the RB between symmetric axial position above and below the midplane, compared to voided cases

$\overline{\nu}_e$-emitting isotopes also accounted for shutdown length for the reason of calculating ^{3}He concentrations. The shutdown length is modified and run for many cases with the same cycle length of 25 days assumed. What is considered is the variation of ^{3}He with shutdown length once the ^{6}Li has built up over the first few cycles.

Figure B.4 shows the ^{3}He concentration in the entire reflector at the BOC and EOC of the first ten cycles of a fresh reflector for three specific shutdown lengths: 15 days, 25 days, and 50 days. The longer shutdown length allows for more of the ^{3}H to decay into ^{3}He. However, upon irradiation of the reflector during a cycle, all cases of the ^{3}He concentration reach roughly the same value, to within a few percent. The BOC concentration is what is considered for the ESCCEP due to reactivity penalty, therefore it is more important.

To more systematically understand the differences in ^{3}He between different shutdown lengths, the relative BOC concentrations are calculated relative to base cases. First, 19 days is considered as it is a typical shutdown length for HFIR. 25 days is also considered as this is what has been considered in previous analyses [82, 83]. Figure B.5 shows the relative

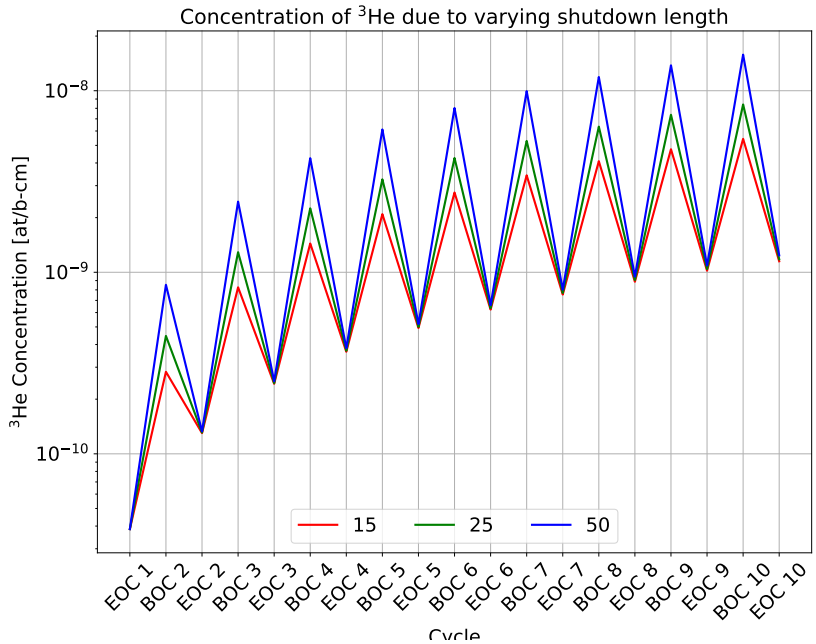

Figure B.4: Fraction of equilibrium ^{6}Li concentration as a function of cycle length for the entire reflector, in the cases of assuming the RB is fresh and assuming all regions (RB+SPB+PB) are fresh

difference in ^{3}He concentration relative to these cases. For example, consider the case of the HFIR 45 day shutdown that is typical at least once a year. A 45-day shutdown has approximately 125% more ^{3}He in its reflector compared to the 19-day shutdown case and 75% more compared to the 25-day case. Both of these relationships are roughly linear due to the half-life of ^{3}H being much longer than a normal HFIR shutdown length.

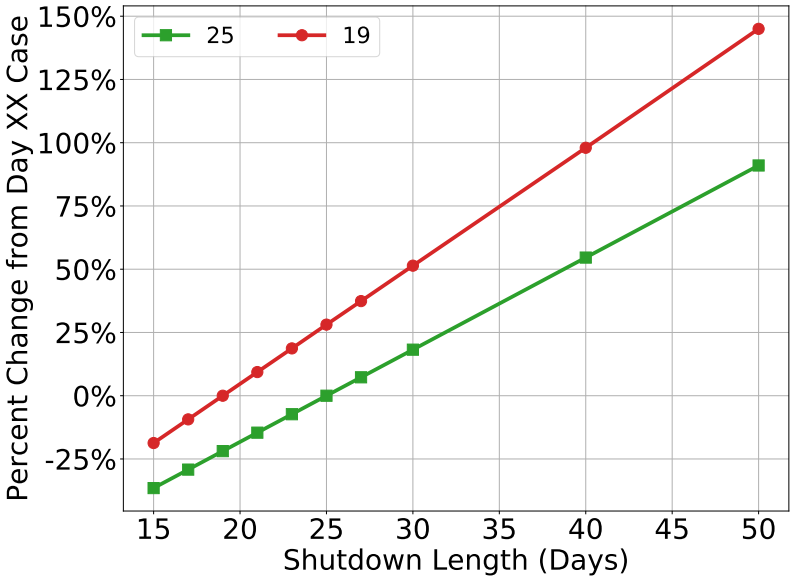

Figure B.5: Fraction of equilibrium ^{6}Li concentration as a function of cycle length for the entire reflector, in the cases of assuming the RB is fresh and assuming all regions (RB+SPB+PB) are fresh

APPENDIX C
REACTIVITY IMPACTS OF TARGETS

In this work, the loading of various isotopes in HFIR was analyzed. The operation of HFIR requires detailed calculations of reactivity impacts that impact startup and cycle length predictions. The goal of this section is to interpret the externalities of isotopes analyzed previously on these safety calculations for HFIR.

C.1 Vanadium

^{52}V was found to have a non-negligible contribution to the HFIR $\overline{\nu}_e$ spectrum in Section 6.5.1. Vanadium is a material that is commonly in the flux trap on the order of 100s of grams. The HFIR team keeps track of experiment loading for startup calculations of the ESCCEP, mentioned previously. Typically, the difference in gram loading of a particular element or isotope from one cycle to the next is calculated to have some reactivity impact on the next startup core.

Running cases of different gram loading in the FTT provided for criticality calculations to be analyzed. The k_{eff} of each case can be correlated with the gram loading of vanadium in the FTT. When vanadium was added/removed from the FTT, the material that was removed/added in its place was aluminum, a common material for dummy targets. Its reactivity impact is assumed to be negligible due to its significantly lower cross-section.

A linear fit of the k_{eff} value obtained from simulation ($\pm$ 9 pcm error) versus gram loading of the FTT is performed. The data is shown in Figure C.1 along with the maximum and minimum loading of vanadium from cycles 478-482 (Table 6.12). The fit can be described by the equation:

$$\Delta = \Delta M \frac{\Delta \rho}{\delta M} + C \tag{C.1}$$

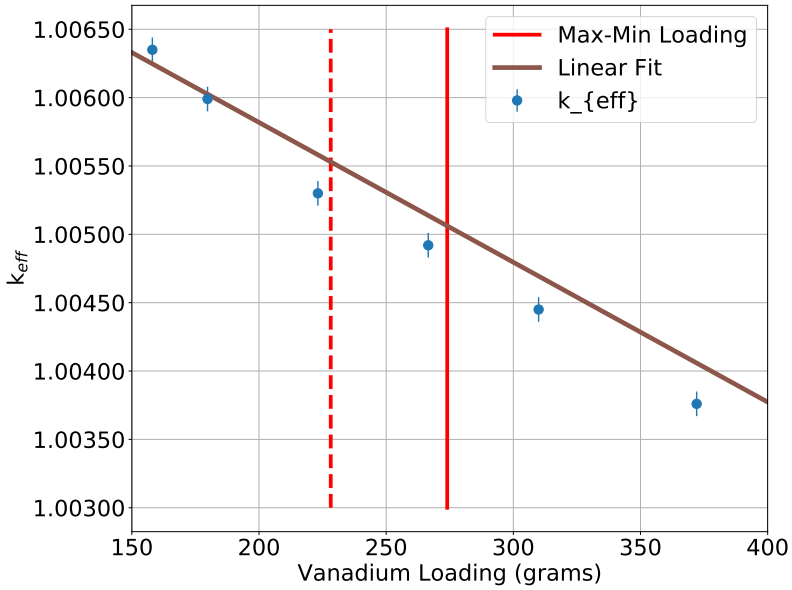

Figure C.1: Linear fit of criticality eigenvalue versus gram loading of vanadium in the core

The linear fit has an $R^2 = 0.99$. The value of $\Delta\rho/\delta M$ was found to have a value of -0.118 pcm. When accounting for the delayed neutron fraction at BOC, $\beta = 0.745$, the reactivity is -0.158 cents/gram. Because vanadium is often added or removed in larger quantities, this value makes more sense to interpret as -1.58 cents per 10 grams V added or 15.8 cents per 100 grams added.

C.2 Lithium-6 Targets

In Section 8.3, the use of lithium targets in the FTT was explored as a way to artificially harden the $\overline{\nu}_e$ spectrum with ^{8}Li production. While this may be of use for some application, the inclusion of lithium usually means loading ^{6}Li into the core, an important neutron poison. The goal here is to calculate the negative reactivity impact of loading of such lithium targets in an effort to maximize the ^{8}Li $\overline{\nu}_e$ contribution for high-energy calibration.

An approximation of reactivity worth of the lithium targets is calculated. Two cases of lithium targets were created in Section 8.3. Case 1 contained 4 lithium-loaded targets, 2 each of LiF and Li_2CO_3. Case 2 contained 6 lithium-loaded targets, 3 of each type.

Therefore, the difference between the two cases is one of each target type. The reactivity swing from Case 1 to Case 2 was $k_1 = 0.99094$ to $k_2 = 0.98714$, or $\Delta k = -380$ pcm ≈ -51 cents at BOC. Assuming that ^{6}Li is the largest contributor to the reactivity swing, the reactivity change per ^{6}Li alone is worth approximately 31 cents per gram. This value seems too high, as one target in these cases contained 0.6 to 1 gram of ^{6}Li. Several targets would decrease the reactivity to a few dollars. This would impact the cycle length of HFIR too greatly to get a sufficient ^{8}Li signal.

This approximation simplifies that there is a linear relationship between gram loading and reactivity, although some self-shielding effects will occur with increased FTT loading. Section 8.3 showed that the effect from loading two to three targets had a proper increase of about 90%. It is estimated that further gram loading in HFIR would exacerbate the flux suppression in the FTT. Therefore, at this point, it seems unfeasible to perform lithium calibration without enrichment in ^{7}Li. Considering different enrichment levels of ^{7}Li would allow for more gram loading of lithium in total and more conversion of ^{7}Li to ^{8}Li, therefore this should be examined further in the future.

APPENDIX D

VERSATILE TEST REACTOR (VTR) CALCULATIONS

Recently, the United States Department of Energy Office of Nuclear Energy (DOE-NE) has been pursuing the design and construction of a fast neutron spectrum research reactor. A test fast reactor is necessary to demonstrate advanced, innovative nuclear reactor designs and to examine the impacts of irradiation on new types of materials for those reactors. The DOE-NE began funding of such a design for a Versatile Test Reactor (VTR) at Idaho National Laboratory (INL).

The VTR project plans to implement an antineutrino detector an experimental capability at the reactor facility [119]. This is the first such "customer request" for an antineutrino detector to the author's knowledge. The $\overline{\nu}_e$ detector is supposed to be situated beneath or next to the core at a short baseline, under 20 meters. This would be the first IBD detector situated at a fast reactor with a short baseline.

The VTR would be unique for a neutrino measurement for a couple reasons. First, it fuel would indicate a large contribution of plutonium fissions. The current reactor design will use 5% LEU-20Pu$_{RG}$-10Zr metallic fuel with a high power density [120]. It is suspected that ^{239}Pu, ^{240}Pu, ^{241}Pu, and ^{242}Pu will contribute significantly to the fission fractions. Second, the reactor operates with a fast neutron spectrum. In the VTR, sodium is used as the coolant. The nominal cycle length is 100 days and average burnup reaches 54.4 GWd/t. The reactor power is supposed to be $\leq$ 300 MW$_{th}$ and will achieve a peak fast flux of $4 \times 10^{15} n/cm^2/s$ [120]. All of these different reactor parameters may have an impact on the expected $\overline{\nu}_e$ flux

Second, due to the low moderation of neutrons with sodium, fast neutron backgrounds at such a close detector would be large. Current concerns include activation of the sodium coolant in the secondary system [120]. It is also suggested that the VTR may not possess a

Table D.1: Concentrations of fissile and fertile isotopes for 5% LEU-20Pu$_{RG}$-10Zr metallic fuel in PRISM model

Isotope	Atom Fraction
^{235}U	0.95%
^{238}U	17.73%
^{239}Pu	3.65%
^{240}Pu	1.40%
^{241}Pu	0.18%
^{242}Pu	0.07%

load-following capability, which would change the magnitude of neutrinos produced with power level evolution [119].

The goal of this appendix chapter is to calculate the fission fractions experienced in the VTR. The second goal is to understand what fast neutron backgrounds may be experienced at a PROSPECT-like IBD detector.

D.1 Fission Fractions

The VTR core was based off a design of the General Electric (GE) PRISM Mod A core design [121]. A PRISM reference design is used for simulation. The views of the model are shown in Figure D.1. The composition of the fuel at BOC is shown in Table D.1. The PRISM MCNP model is modified to calculate fission rates and fractions for the various fuel cells in the core. As with HFIR modeling, phantom materials are used to calculate isotope-dependent fission rates. The rates are only calculated for the beginning-of-cycle, as fuel evolution expects the fractions to not change much [119].

The fission fractions for uranium and plutonium isotopes is shown in Table D.2. They are compared to previous estimates from Ref. [119]. The PRISM model has increased ^{235}U and ^{239}Pu fractions compared to the reference data while the ^{238}U, ^{240}Pu, and ^{241}Pu have all decreased significantly. This suggests that the fuel composition for the VTR may be slightly different than what is used in PRISM. The model needs to be updated for more accurate representation.

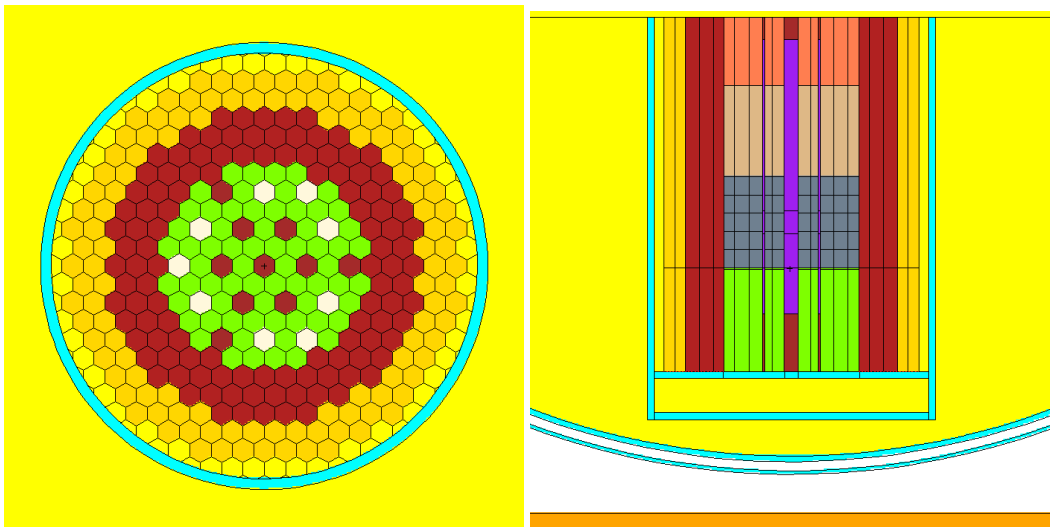

Figure D.1: Aerial (left) and side (right) views of the PRISM MCNP model

Table D.2: Fission fractions (%) calculated for the PRISM MCNP model at BOC compared with projections from Ref. [119]

Isotope	MCNP	Ref. [119]
^{235}U	15.8	13.2
^{238}U	9.4	12.6
^{239}Pu	64.2	61.8
^{240}Pu	1.4	8.4
^{241}Pu	0.2	2.7
^{242}Pu	0.1	0.3

D.2 Fast Neutron Backgrounds

One difference with the projected VTR IBD detector compared to PROSPECT is that the sources of fast neutron backgrounds will be different. PROSPECT has to manage cosmogenic fast neutrons while the VTR will have low cosmogenic backgrounds from the detector being underground. The VTR detector, however, will see more fast neutrons leaking from the core. Fast neutrons are problematic because they can cause false (non-IBD related neutron capture) signals in the detector if they reach the detector with sufficient energy. They can also produce high-energy gammas which can penetrate the detector too. The first is the capture reaction on hydrogen, which produces 2.1 MeV gamma rays. The second is the inelastic scatter off ^{12}C, which produces 4.5 MeV gamma rays. The iron concentration in stainless steel, a common reactor material, can also produce gammas from activation. The goal of this section is to understand the magnitude and specturm of neutrons that would reach a short-baseline $\overline{\nu}_e$ detector.

First, a simple spherical shell model is created to examine the attenuation of fast neutrons through sodium. The model includes concentric spheres of sodium up to 20 meters. Various source spectra for ^{235}U, ^{239}Pu, ^{238}U, and ^{241}Pu were found to have little impact on neutron spectra results. The ^{239}Pu spectra is displayed for most results since it maintains the highest fission fraction.

Figure D.2 shows the fraction of initial neutrons from their source that would reach through various distances of sodium. Only one in a 1,000 will make it through 1 meter while one in 100,000 will make it through 5 meters. Almost no neutrons get through 10 meters of sodium, although 2-3 meters is enough to attenuate most of them. The flux will depend on the exact distance of sodium through which neutrons have to traverse to leak out of the reactor vessel.

The fast neutron spectrum is calculated for a PROSPECT-like detector. In order to get an idea of the neutron magnitude and spectra at a detector, the neutron flux magnitude

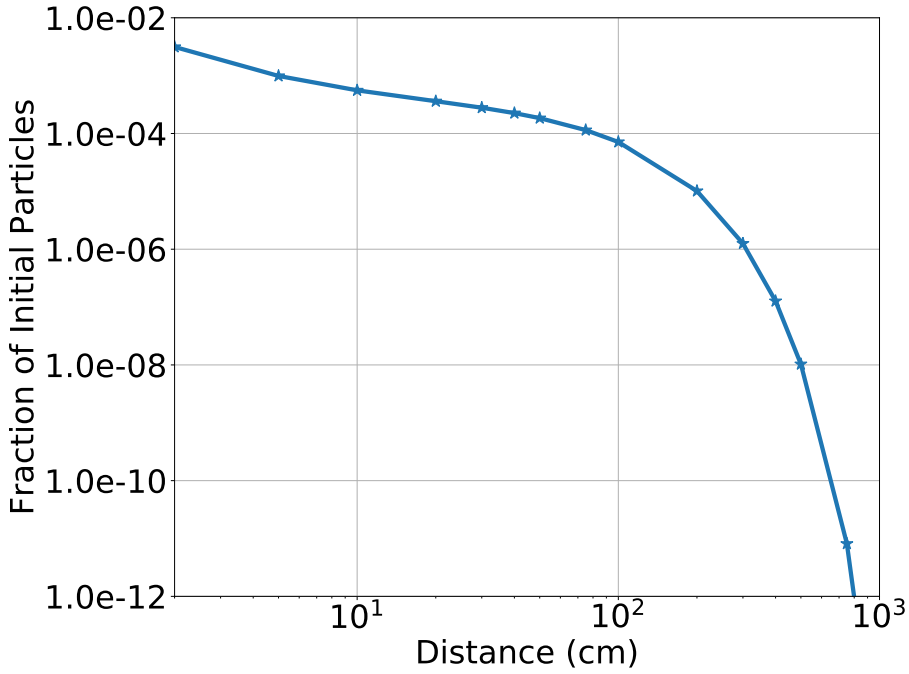

Figure D.2: Fraction of source particles reaching a certain distance through bare sodium using a ^{239}Pu Watt spectrum as a source

and spectrum from MCNP simulations is ray traced to the detector location. Here, a fast neutron flux at the edge of the core of $2 \times 10^{15} n/cm^2/s$ is used, which is consistent with initial predictions of VTR flux distributions. A baseline of 10 meters is assumed for the detector. Figure D.3 shows the reverse cumulative flux distribution of neutrons reaching the detector under these assumptions. This also assumed no other shielding between the sodium and detector, which is assumed to be conservative for the detector design. Two meters of shielding will reduce the neutron flux over 1 MeV to under $10^6 n/cm^2/s$. This data can be used for future studies in calculating flux and shielding requirements for an IBD detector at the VTR.

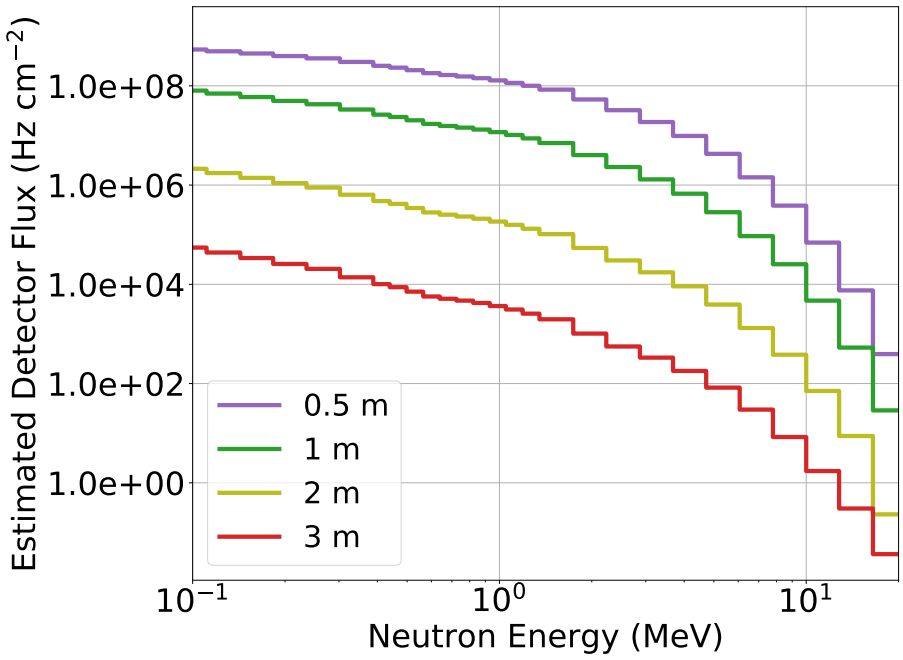

Figure D.3: Approximate neutron flux spectrum and magnitude at an IBD detector from VTR neutrons based on the length of sodium surrounding the core, 10 meter baseline, and neutron flux of $2 \times 10^{15} cm^{-2} s^{-2}$ at the edge of the core

REFERENCES

[1] World Nuclear Association, "World Nuclear Performance Report 2018," Tech. Rep., 2018.

[2] International Atomic Energy Agency, *IAEA Research Reactor Database (RRDB)*, Web, Accessed April 8, 2019.

[3] International Energy Agency, "Global Energy & CO2 Status Report," International Energy Agency, Tech. Rep., 2019.

[4] Nuclear Energy Agency, "Technology Roadmap Update for Generation IV Nuclear Energy Systems," Organisation for Economic Co-operation and Development, Tech. Rep., 2014, ORNL/TM-2013/416.

[5] Department of Energy/National Nuclear Security Administration, "Prevent, Counter, and Respond - A Strategic Plan to Reduce Global Nuclear Threats," Tech. Rep., 2018.

[6] International Atomic Energy Agency, "IAEA Safeguards Glossary: 2001 Edition," International Atomic Energy Agency, Vienna, Austria, Tech. Rep., 2002.

[7] ——, "Safeguards Techniques and Equipment: 2011 Edition," International Atomic Energy Agency, Vienna, Austria, Tech. Rep., 2011.

[8] ——, "IAEA Department of Safeguards Long-Term R&D Plan, 2012-2023," International Atomic Energy Agency, Vienna, Austria, Tech. Rep., 2013.

[9] Y. V. Klimov, V. I. Kopeikin, L. A. Mikaélyan, K. V. Ozerov, and V. V. Sinev, "Neutrino method remote measurement of reactor power and power output," *Atomic Energy*, vol. 76, no. 2, pp. 123–127, 1994.

[10] B. Achkar *et al.*, "Search for neutrino oscillations at 15, 40 and 95 meters from a nuclear power reactor at Bugey," *Nuclear Physics, Section B*, vol. 434, no. 3, pp. 503–532, 1995.

[11] Bernstein, A. and Wang, Y. and Gratta, G. and West, T., "Nuclear reactor safeguards and monitoring with antineutrino detectors," *Journal of Applied Physics*, vol. 91, no. 7, pp. 4672–4676, 2002.

[12] International Atomic Energy Agency, "Final report: Focused workshop on antineutrino detection for safeguards applications," International Atomic Energy Agency, Tech. Rep., 2008.

[13] P. Huber, "Reactor antineutrino fluxes status and challenges," *Nuclear Physics B*, vol. 908, pp. 268 –278, 2016, Neutrino Oscillations: Celebrating the Nobel Prize in Physics 2015.

[14] C. L. Jones, A. Bernstein, J. M. Conrad, Z. Djurcic, M. Fallot, L. Giot, G. Keefer, A. Onillon, and L. Winslow, "Reactor simulation for antineutrino experiments using dragon and mure," *Phys. Rev. D*, vol. 86, p. 012 001, 1 2012.

[15] C. Stewart, "Antineutrino-based Safeguards for Ultra High-Burnup Fast Reactors," PhD thesis, Georgia Institute of Technology, 2016.

[16] F. P. An *et al.*, "Improved measurement of the reactor antineutrino flux and spectrum at Daya Bay," *Chinese Physics C*, vol. 41, no. 1, p. 013 002, 2017.

[17] P. Vogel, L. J. Wen, and C. Zhang, "Neutrino oscillation studies with reactors," *Nature Communications*, vol. 6, 6935 EP –, 2015, Review Article.

[18] C. L. Cowan, F. Reines, F. B. Harrison, H. W. Kruse, and A. D. McGuire, "Detection of the Free Neutrino: a Confirmation," *Science (80-.).*, vol. 124, no. 3212, pp. 103–104, 1956.

[19] P. Vogel and J. F. Beacom, "Angular distribution of neutron inverse beta decay, $\overline{\nu}e+ \overrightarrow{p}\ e++n$," *Phys. Rev. D*, vol. 60, p. 053 003, 5 1999.

[20] H. Kwon, F. Boehm, A. A. Hahn, H. E. Henrikson, J. L. Vuilleumier, J. F. Cavaignac, D. H. Koang, B. Vignon, F. V. Feilitzsch, and R. L. Mössbauer,

[21] G. Zacek, F. V. Feilitzsch, R. L. Mössbauer, L. Oberauer, V. Zacek, F. Boehm, P. H. Fisher, J. L. Gimlett, A. A. Hahn, H. E. Henrikson, H. Kwon, J. L. Vuilleumier, and K. Gabathuler, "Neutrino-oscillation experiments at the Gösgen nuclear power reactor," *Physical Review D*, vol. 34, no. 9, pp. 2621–2636, 1986.

[22] Y. Kim, "Detection of Antineutrinos for Reactor Monitoring," *Nuclear Engineering and Technology*, vol. 48, no. 2, pp. 285–292, 2016.

[23] P.F. de Salas and D.V. Forero and C.A. Ternes and M. Trtola and J.W.F. Valle, "Status of neutrino oscillations 2018: 3 hint for normal mass ordering and improved CP sensitivity," *Physics Letters B*, vol. 782, pp. 633 –640, 2018.

[24] J. Choi *et al.*, "Observation of Energy and Baseline Dependent Reactor Antineutrino Disappearance in the RENO Experiment," *Phys. Rev. Lett.*, vol. 116, no. 21, 2016. eprint: 1511.05849.

[25] Y. Abe and others, "Improved measurements of the neutrino mixing angle θ 13 with the Double Chooz detector," *J. High Energy Phys.*, vol. 2014, no. 10, p. 86, 2014. arXiv: 1406.7763.

[26] F. An *et al.*, "New Measurement of Antineutrino Oscillation with the Full Detector Configuration at Daya Bay," *Phys. Rev. Lett.*, vol. 115, no. 11, 2015. eprint: 1505.03456.

[27] A. Hayes and P. Vogel, "Reactor Neutrino Spectra," *Annual Review of Nuclear and Particle Science*, vol. 66, no. 1, pp. 219–244, 2016.

[28] F. An *et al.*, "Evolution of the Reactor Antineutrino Flux and Spectrum at Daya Bay," *Phys. Rev. Lett.*, vol. 118, p. 251 801, 25 2017.

[29] T. Mueller *et al.*, "Improved Predictions of Reactor Antineutrino Spectra," *Phys. Rev.*, vol. C83, p. 054 615, 2011.

[30] "Neutron capture and the antineutrino yield from nuclear reactors,"

[31] D. A. Dwyer and T. J. Langford, "Spectral structure of electron antineutrinos from nuclear reactors," *Phys. Rev. Lett.*, vol. 114, p. 012 502, 1 2015.

[32] A. Sonzogni, E. McCutchan, T. Johnson, and P. Dimitriou, "Effects of fission yield data in the calculation of antineutrino spectra for $^{235}\mathrm{U}(n,\mathrm{fission})$ at thermal and fast neutron energies," *Phys. Rev. Lett.*, vol. 116, p. 132 502, 13 2016.

[33] P. Huber, "On the determination of anti-neutrino spectra from nuclear reactors," *Phys. Rev.*, vol. C84, p. 024 617, 2011, [Erratum: Phys. Rev.C85,029901(2012)]. arXiv: 1106.0687 [hep-ph].

[34] K. Schreckenbach, G. Colvin, W. Gelletly, and F. Von Feilitzsch, "Determination of the antineutrino spectrum from235U thermal neutron fission products up to 9.5 MeV," *Physics Letters B*, vol. 160, no. 4-5, pp. 325–330, 1985.

[35] F. von Feilitzsch, A. Hahn, and K. Schreckenbach, "Experimental beta-spectra from 239pu and 235u thermal neutron fission products and their correlated antineutrino spectra," *Physics Letters B*, vol. 118, no. 1, pp. 162 –166, 1982.

[36] A. Hahn, K. Schreckenbach, W. Gelletly, F. von Feilitzsch, G. Colvin, and B. Krusche, "Antineutrino spectra from 241pu and 239pu thermal neutron fission products," *Physics Letters B*, vol. 218, no. 3, pp. 365 –368, 1989.

[37] N. Haag, A. Gütlein, M. Hofmann, L. Oberauer, W. Potzel, K. Schreckenbach, and F. M. Wagner, "Experimental determination of the antineutrino spectrum of the fission products of ^{238}U," *Phys. Rev. Lett.*, vol. 112, p. 122 501, 12 2014.

[38] Mention, G. and Fechner, M. and Lasserre, Th and Mueller, Th A. and Lhuillier, D. and Cribier, M. and Letourneau, A., "Reactor antineutrino anomaly," *Physical Review D - Particles, Fields, Gravitation and Cosmology*, vol. 83, no. 7, 2011.

[39] A. C. Hayes, J. L. Friar, G. T. Garvey, G. Jungman, and G. Jonkmans, "Systematic uncertainties in the analysis of the reactor neutrino anomaly," *Phys. Rev. Lett.*, vol. 112, p. 202 501, 20 2014.

[40] C. Giunti, Y. F. Li, B. R. Littlejohn, and P. T. Surukuchi, "Diagnosing the reactor antineutrino anomaly with global antineutrino flux data," *Phys. Rev. D*, vol. 99, p. 073 005, 7 2019.

[41] A. C. Hayes, J. L. Friar, G. T. Garvey, D. Ibeling, G. Jungman, T. Kawano, and R. W. Mills, "Possible origins and implications of the shoulder in reactor neutrino spectra," *Phys. Rev. D*, vol. 92, p. 033 015, 3 2015.

[42] A. A. Sonzogni, E. A. McCutchan, and A. C. Hayes, "Dissecting reactor antineutrino flux calculations," *Phys. Rev. Lett.*, vol. 119, p. 112 501, 11 2017.

[43] M. Kellett and O. Bersillon and R. Mills, "The JEFF-3.1/3.1.1 radioactive decay data and fission yields sub-libraries," Nuclear Energy Agency, Organisation for Economic Co-operation and Development, Tech. Rep., 2009.

[44] M. Chadwick *et al.*, "ENDF/B-VII.1 Nuclear Data for Science and Technology: Cross Sections, Covariances, Fission Product Yields and Decay Data," *Nuclear Data Sheets*, vol. 112, no. 12, pp. 2887 –2996, 2011, Special Issue on ENDF/B-VII.1 Library.

[45] J. Ashenfelter *et al.*, "First search for short-baseline neutrino oscillations at hfir with prospect," *Phys. Rev. Lett.*, vol. 121, p. 251 802, 25 2018.

[46] ——, "Performance of a segmented 6 li-loaded liquid scintillator detector for the prospect experiment," *Journal of Instrumentation*, vol. 13, no. 06, P06023, 2018.

[47] ——, "The PROSPECT Reactor Antineutrino Experiment," *Nuclear Instruments and Methods in Physics Research Section A: Accelerators, Spectrometers, Detectors and Associated Equipment*, vol. 922, pp. 287 –309, 2019.

[48] D. Chandler *et al.*, "Modeling and Depletion Simulations for a High Flux Isotope Reactor Cycle with a Representative Experiment Loading," Oak Ridge National Laboratory, Tech. Rep., 2016.

[49] R. Cheverton and T. Sims, "HFIR Core Nuclear Design," Jan. 1971.

[50] G. Ilas *et al.*, "Modeling and Simulations for the High Flux Isotope Reactor Cycle 400," Oak Ridge National Laboratory, Tech. Rep., 2016, ORNL/TM-2015/36.

[51] D. Chandler, "Activation and Heat Generation Calculations to Support Pu-238 Fully Loaded Target Irradiations in Inner Small VXFs for up to Three Cycles," Oak Ridge National Laboratory, Tech. Rep., 2015, C-HFIR-2015-014.

[52] D. Chandler, "Development of an efficient approach to perform neutronics simulations for plutonium-238 production," PHYSOR Conference, 2016.

[53] C. Hurt, J. Freels, R. Hobbs, P. Jain, and G. Maldonado, "Thermal Safety Analysis for the Production of Plutonium-238 at the High Flux Isotope Reactor," Oak Ridge National Laboratory, Tech. Rep., 2016, ORNL/TM-2016/234.

[54] *MCNP6 Users Manual - Code Version 6.1*, LA-CP-13-00634, 2013.

[55] X-5 Monte Carlo Team, "MCNP - A General Monte Carlo N-Particle Transport Code, Version 5," *Los Alamos National Laboratory*, vol. I, pp. 2–71 –2–80, 2005.

[56] N. Xoubi and R. Primm, "Modeling of the High Flux Isotope Reactor Cycle 400," Oak Ridge National Laboratory, Tech. Rep., 2004, ORNL/TM-2004/251.

[57] W. Haeck, *VESTA User's Manual - Version 2.0.0*, ISRN DSU/SEC/T/2008-331, 2009.

[58] D. Chandler, G. Ilas, and E. Sunny, "Safety and Performance Metrics Calculations for a HFIR Cycle with Representative Target Loading," Oak Ridge National Laboratory, Tech. Rep., 2016.

[59] B. Rearden, M. Jessee, *et al.*, "SCALE Code System," Oak Ridge National Laboratory, Tech. Rep., 2016, ORNL/TM-2005/39.

[60] O. Hermann, "COUPLE: SCALE System Module to Process Problem-Dependent Cross Sections and Neutron Spectral Data for ORIGEN-S Analysis," Oak Ridge National Laboratory, Tech. Rep., 1998, ORNL/NUREG/CSD-2/V2/R6.

[61] O. Hermann and R. Westfall, "ORIGEN-S: SCALE system module to calculate fuel depletion, actinide transmutation, fission product buildup and decay, and associated radiation source terms," Oak Ridge National Laboratory, Tech. Rep., 1984, NUREG/CR–0200-VOL.2.

[62] S. Mosher *et al.*, "ADVANTG - An Automated Variance Reduction Parameter Generator," Oak Ridge National Laboratory, Tech. Rep., 2013, ORNL/TM-2013/416.

[63] S. Wilson and S. Mosher and C. Daily and D. Chandler, *HFIRCON Version 1.0 User Guide*, ORNL/TM-20XX/XXX, 2019.

[64] S. Mosher and S. Wilson, "Algorithmic Improvements to MCNP5 for High-Resolution Fusion Neutronics Analyses," *Fusion Science and Technology*, vol. 74, no. 4, pp. 263–276, 2018.

[65] D. Dwyer, *Oklo: A toolkit for modeling nuclides and nuclear reactions*, Github, https://github.com/dadwyer/oklo.

[66] N. Bowden, Personal communication, Oct. 13, 2016.

[67] J. Sterbenz, "Q-value (MeV/fission) Determination for the Advanced Test Reactor," Idaho National Laboratory, Tech. Rep., 2013.

[68] G. Zerovnik *et al.*, "On normalization of fluxes and reaction rates in MCNP criticality calculations," *Annals of Nuclear Energy*, vol. 63, pp. 126–128, 2014.

[69] M. Chadwick *et al.*, "Endf/b-vii.1 nuclear data for science and technology: Cross sections, covariances, fission product yields and decay data," *Nuclear Data Sheets*, vol. 112, no. 12, pp. 2887 –2996, 2011, Special Issue on ENDF/B-VII.1 Library.

[70] J. Favorite, "Using the MCNP Taylor series perturbation feature (efficiently) for shielding problems," *EPJ Web Conf.*, vol. 153, p. 06 030, 2017.

[71] V. Kopeikin, "Flux and spectrum of reactor antineutrinos," *Physics of Atomic Nuclei*, vol. 75, no. 2, pp. 143–152, 2012.

[72] A. Conant, H. Mumm, and A. Erickson, "Safeguards Impacts of Antineutrinos from Activation of Structural Elements in Power and Research Reactors," in *Proceedings of the 2018 PHYSOR Conference*, Cancun, Mexico, 2018.

[73] N. S. Bowden, A. Bernstein, S. Dazeley, R. Svoboda, A. Misner, and T. Palmer,

[74] "Evaluated Nuclear Structure Data File Search and Retrieval," *National Nuclear Data Center*,

[75] H. H. Schmidt, P. Hungerford, H. Daniel, T. von Egidy, S. A. Kerr, R. Brissot, G. Barreau, H. G. Börner, C. Hofmeyr, and K. P. Lieb, "Levels and gamma energies of ^{28}Al studied by thermal neutron capture," *Phys. Rev. C*, vol. 25, pp. 2888–2901, 6 1982.

[76] D. Diamond, J. Baek, A. Hanson, L-Y. Cheng, N. Brown, and A. Cuadra, "Conversion Preliminary Safety Analysis Report for the NIST Research Reactor," National Institute of Standards and Technology, Tech. Rep., 2014, BNL-107265-2015-IR.

[77] L. Cheng, A. Hanson, D. Diamond, J. Xu, J. Carew, D. Rorer, "Physics and Safety Analysis for the NIST Research Reactor," National Institute of Standards and Technology, Tech. Rep., 2004, BNL-NIST-0803.

[78] H. Junde, "Nuclear Data Sheets for A = 55," *Nuclear Data Sheets*, vol. 109, no. 4, pp. 787 –942, 2008.

[79] E. Browne and J. Tuli, "Nuclear Data Sheets for A = 66," *Nuclear Data Sheets*, vol. 111, no. 4, pp. 1093 –1209, 2010.

[80] H. Junde, H. Su, and Y. Dong, "Nuclear Data Sheets for A = 56," *Nuclear Data Sheets*, vol. 112, no. 6, pp. 1513 –1645, 2011.

[81] D. Tilley, C. Cheves, J. Godwin, G. Hale, H. Hofmann, J. Kelley, C. Sheu, and H. Weller, "Energy levels of light nuclei a=5, 6, 7," *Nuclear Physics A*, vol. 708, no. 1, pp. 3 –163, 2002.

[82] D. Chandler, *Reactivity Accountability Attributed to Beryllium Reflector Poisons in the High Flux Isotope Reactor*, CLUES, ORNL/TM-2009/198, 2009.

[83] D. Ilas, "Impact of HFIR LEU Conversion on Beryllium Reflector Degradation Factors," Oak Ridge National Laboratory, Tech. Rep., 2013, ORNL/TM-2013/441.

[84] B. Kendrick, *Estimated Symmetrical Critical Control Element Position (ESCCEP) for Cycle 482*, CLUES, C-HFIR-2018-022, 2018.

[85] Y. Dong and H. Junde, "Nuclear data sheets for a = 52," *Nuclear Data Sheets*, vol. 128, pp. 185 –314, 2015.

[86] D. Chandler, *Neutronics and Heat Generation Calculations to Support Pu-238 Fully Loaded Target Irradiations in HFIR VXFs*, CLUES, C-HFIR-2013-026-rev1, 2018.

[87] ——, *Nuclide Inventory and Decay Heat Calculations to Support Pu-238 Fully Loaded Target Irradiations in Inner Small VXFs for up to Three Cycles*, CLUES, C-HFIR-2015-025, 2018.

[88] D. Tilley, H. Weller, and C. Cheves, "Energy levels of light nuclei a = 1617," *Nuclear Physics A*, vol. 564, no. 1, pp. 1 –183, 1993.

[89] N. Nica, "Nuclear data sheets for a = 97," *Nuclear Data Sheets*, vol. 111, no. 3, pp. 525 –716, 2010.

[90] J. Ashenfelter *et al.*, "Measurement of the antineutrino spectrum from 235U fission at HFIR with PROSPECT," *Phys. Rev. Lett.*, vol. 121, p. 251 802, 25 2019.

[91] B. Zhou, X.-C. Ruan, Y.-B. Nie, Z.-Y. Zhou, F.-P. An, and J. Cao, "A study of antineutrino spectra from spent nuclear fuel at Daya Bay," *Chinese Physics C*, vol. 36, no. 1, pp. 1–5, 2012.

[92] V. Brdar, P. Huber, and J. Kopp, "Antineutrino Monitoring of Spent Nuclear Fuel," *Phys. Rev. Applied*, vol. 8, p. 054 050, 5 2017.

[93] E. S. Riyana, S. Suda, K. Ishibashi, H. Matsuura, J. ichi Katakura, G. M. Sun, and Y. Katano, "Calculation of low-energy electron antineutrino spectra emitted from nuclear reactors with consideration of fuel burn-up," *Journal of Nuclear Science and Technology*, vol. 56, no. 5, pp. 369–375, 2019.

[94] X. B. Ma, W. L. Zhong, L. Z. Wang, Y. X. Chen, and J. Cao, "Improved calculation of the energy release in neutron-induced fission," *Phys. Rev. C*, vol. 88, p. 014 605, 1 2013.

[95] N. Todreas and M. Kazimi, *Nuclear Systems Volume I: Thermal Hydraulics Fundamentals, year=2011, publisher=CRC Press*.

[96] K. Smith, "RELAP5 WCLOCA and LOOP Analysis - Scram/Safety Plate Timing Sensitivity Study," Oak Ridge National Laboratory, Tech. Rep., 1999, C-HFIR-1999-017.

[97] D. Chandler, G. Ilas, and E. Sunny, "Safety and Performance Metrics Calculations for a HFIR Cycle with Representative Target Loading," Oak Ridge National Laboratory, Tech. Rep., 2015, C-HFIR-2015-022.

[98] G. A. Cowan, A. Turkevich, and C. I. Browne, "Symmetry of neutron-induced $\mathrm{u235}$ fission at individual resonances," *Phys. Rev.*, vol. 122, pp. 1286–1294, 4 1961.

[99] G. A. Cowan, B. P. Bayhurst, and R. J. Prestwood, "Symmetry of neutron-induced $\mathrm{u235}$ fission at individual resonances. ii," *Phys. Rev.*, vol. 130, pp. 2380–2383, 6 1963.

[100] G. A. Cowan, B. P. Bayhurst, R. J. Prestwood, J. S. Gilmore, and G. W. Knobeloch, "Symmetry of neutron-induced $239\mathrm{Pu}$ fission at individual resonances," *Phys. Rev.*, vol. 144, pp. 979–983, 3 1966.

[101] ——, "Symmetry of neutron-induced $235\mathrm{U}$ fission at individual resonances. iii," *Phys. Rev. C*, vol. 2, pp. 615–620, 2 1970.

[102] B. R. Littlejohn, A. Conant, D. A. Dwyer, A. Erickson, I. Gustafson, and K. Hermanek, "Impact of fission neutron energies on reactor antineutrino spectra," *Phys. Rev. D*, vol. 97, p. 073 007, 7 2018.

[103] T. Kozlowski and T. Downar, "PWR MOX/UO_2 Core Transient Benchmark: Final Report," Nuclear Energy Agency, Organisation for the Co-operation and Development, U.S. Nuclear Regulatory Commission, Tech. Rep., 2007, NEA/NSC/DOC(2006)20.

[104] M. A. Kellett, O. Bernillon, and R. W. Mills, *The Jeff-31/6311 radioactive decay data and fission yields sub-libraries Jeff report 20*. Nuclear Energy Agency of the OECD (NEA): Organisation for Economic Co-Operation and Development - Nuclear Energy Agency, 2009, ISBN: 92-64-99087-6.

[105] Oak Ridge National Laboratory, "Beta-S: Code System to Calculat Multi-Group Beta Spectra," Oak Ridge National Laboratory, Tech. Rep., 2008, CCC-657.

[106] *Measured Results of Delayed Beta- and Gamma-Ray Spectra Due to Thermal Neutron Fission of U-235*, RSIC Data Library Collection, DLC-61, 2018.

[107] N. Tsoulfanidis, B. W. Wehring, and M. E. Wyman, "Measurements of time-dependent energy spectra of beta rays from uranium-235 fission fragments," *Nuclear Science and Engineering*, vol. 43, no. 1, pp. 42–53, 1971.

[108] M. Fallot, S. Cormon, M. Estienne, A. Algora, V. M. Bui, A. Cucoanes, M. Elnimr, L. Giot, D. Jordan, J. Martino, A. Onillon, A. Porta, G. Pronost, A. Remoto, J. L. Taín, F. Yermia, and A.-A. Zakari-Issoufou, "New antineutrino energy spectra predictions from the summation of beta decay branches of the fission products," *Phys. Rev. Lett.*, vol. 109, p. 202 504, 20 2012.

[109] K. Stelzer, "The absolute determination of nuetron flux with indium foils," *Nukleonik (West Germany) Discontinued with vol. 12*,

[110] W. N. McElroy, S. Berg, and G. Gigas, "Neutron-flux spectral determination by foil activation," *Nuclear Science and Engineering*, vol. 27, no. 3, pp. 533–541, 1967.

[111] B. Betzler, E. Davidson, G. Davidson, T. Evans, S. Wilson, S. Mosher, G. Ilas, C. Daily, A. Conant, and D. Chandler, "Reactor Physics Modeling of the Cycle 483 Event in the High Flux Isotope Reactor," Oak Ridge National Laboratory, Tech. Rep., 2018, ORNL/TM-2018/1102.

[112] Oak Ridge National Laboratory, *Guidelines for Control of Reactor Power*, Web, NOP-2020, 2018.

[113] ——, *NOP-2020 Accuracy Calculation*, Web, HFIR-IC-NOP-2020-01-16, 2018.

[114] V. I. Lyashuk, "High flux lithium antineutrino source with variable hard spectrum. How to decrease the errors of the total spectrum ?," 2016.

[115] J. Ashenfelter *et al.*, "Measurement of the Antineutrino Spectrum from ^{235}U Fission at HFIR with PROSPECT," 2018.

[116] F. Griffin, "LOOP Transient Analysis of RB-17J Irradiation Capsule," Oak Ridge National Laboratory, Tech. Rep., 2003, C-HFIR-2003-031.

[117] P. Vogel, "Analysis of the antineutrino capture on protons," *Phys. Rev. D*, vol. 29, pp. 1918–1922, 9 1984.

[118] J.E. Purcell and C.G. Sheu, "Nuclear Data Sheets for A = 3," *Nuclear Data Sheets*, vol. 130, pp. 1 –20, 2015.

[119] T. Hill, *Versatile Test Reactor Overview*, Web, Applied Antineutrino Physics Workshop, 2018.

[120] F. Heidet, G. Youinou, and J. Roglans-Ribas, "Overview of the Versatile Test Reactor Core Design Activities," in *Proceedings of the 2019 ANS Annual Meeting*, Minneapolis, MN, 2019.

[121] B. Triplett, E. Loewen, and B. Dooies, "PRISM: A Competitive Small Modular Sodium-Cooled Reactor," *Nuclear Technology*, vol. 178, no. 2, pp. 186–200, 2012.